AGH University of Science and Technology

FIELD OF SCIENCE Natural sciences

SCIENTIFIC DISCIPLINE Physical sciences

DOCTORAL THESIS

Study of novel precursors for Focused Electron Beam Induced Deposition of Metal Nanowires

Author: Jakub Mateusz Jurczyk

First supervisor: Prof. Dr. hab. Czesław Kapusta
Assisting supervisor: Dr. Ivo Utke

Completed in: AGH-University of Science and Technology, Faculty of Physics and Applied Computer Sciences, Department of Solid State Physics

Krakow, 2021

Declaration of the author of this dissertation: Aware of legal responsibility for making untrue statements I hereby declare that I have written this dissertation myself and all the contents of the dissertation have been obtained by legal means.

Declaration of the thesis Supervisor: This dissertation is ready to be reviewed.

What we know is a drop, what we don't know is an ocean.

Isaac Newton

I acknowledge the financial support from the European Union's Horizon 2020 research and innovation programme ELENA under the Marie Skłodowska-Curie grant agreement No 722149.

Acknowledgments

At the beginning, I would like to express my gratitude to both my supervisors: Prof. Czesław Kapusta and Dr. Ivo Utke for guiding me throughout years of our scientific collaboration. Starting with my B.Sc. studies, when I first met Prof. Kapusta, through my master internship at Empa, where I first worked with Dr. Utke and ending on this PhD project I always could count on their scientific support. Thanks a lot to Dr. Johann Michler for giving me opportunity to work in his laboratory.

I want to thank a lot for financial support of EU Horizon 2020 Marie Curie-Sklodowska Innovative Training Network “ELENA”, grant agreement No 722149.

I would like to thank a lot to all my collaborators: to Dr. Katja Höflich, who introduced me to silver FEBID, to Katarzyna Madajska and Prof. Iwona Szymańska, for their constant support in the field of chemistry. Thanks a lot to all PhD students and participants from ELENA ITN, especially to Prof. Lisa McElwee-White and her team, Chris, Olivia and Yu-Chi, for successful collaboration with Ru-complexes; to Prof. Mats Tilset and Cristiano Glessi for teaching me thermogravimetry and delivering gold compounds; to Dr. Felix Hermanns, Po-Yuan Shih, Rainer Becker and Dr. Klaus Edinger for helping me during my internship in Zeiss; to Prof. Petra Swiderek and Petra Martinovic for collaboration on review article and finally to the leaders of ELENA project.

I am very thankful to all my colleagues from EMPA. Special thanks goes to my closest colleague and friend, Luisa Berger, who was always there when I needed advice or help and support and thanks to whom even long hours in the laboratory were pleasant to work. Thanks a lot to Leo, Carlos, James, Thomas, Patrik, Gerhard, Lex, Agnieszka, Caroline, Remo for helping me with my experiments, articles and for teaching me new methods. Big "thank you" goes also to my officemates and other PhD students and post-docs from laboratory 206. You made my journey through PhD work a great experience.

I want to thank PhD students from Prof. Kapusta group at AGH, especially Kamil, Witek and Tomasz. Thanks also to all my friends from studies and PhD at AGH.

Thanks a lot to my longest-known friends: Patrycja, Joanna, Tomasz and Maciej for their support throughout years of my studies and later PhD. Even though we lived in different cities and countries, we stayed in closed contact.

I am really grateful to Doris and Herbert Kraft for all kindness and support I got from them living in Steffisburg during my work at Empa.

Last, but not least I want to thank a lot to my family: my mother Barbara and father Arkadiusz, for constant support with every choice I made in my life. Thanks to my sister, Weronika, for believing in me and thanks to my Grandparents. Without you, this Thesis would not have been possible.

Thank you all! Dziękuję wszystkim! Merci viel mall!

Abstract

Recent development of nanotechnology created a need to introduce reliable and reproducible methods of fabrication of structures in nanoscale. Focused electron beam induced deposition (FEBID) is a nano-structuring method, which allows for direct, mask-less deposition of three-dimensional, vertical structures with spatial resolution below 20nm, reaching even single nanometers. Direct approach and versatility are the main advantages of FEBID, thanks to which it was applied in various different fields, including nano-magnetism, plasmonics, manufacturing of sensor nano-devices or scanning probe microscopy tips or correction of lithography masks. Despite its advantages and various applications, there is still a lot of unresolved challenges concerning deposition with focused electron beam. The most prominent are the low metal content of deposited structures, coming mostly from using metalorganic (or organometallic) compounds to deposit metal or so-called proximity effects, which lower lateral resolution of the deposits.

This PhD Thesis addresses these challenges by presenting the results of systematic investigation of various novel metalorganic compounds as potential precursors for FEBID. The precursors are coming from three groups of complexes: silver carboxylates $Ag_2(\mu\text{-}O_2CC(Me)_2Et)_2$, $Ag_2(\mu\text{-}O_2C^tBu)_2$, $Ag_2(\mu\text{-}O_2CCF_3)_2$, $Ag_2(\mu\text{-}O_2CC_2F_5)_2$, $Ag_2(\mu\text{-}O_2CC_3F_7)_2$, ruthenium heteroleptic complexes $Ru(\eta^3\text{-}C_3H_5)(CO)_3Br$), $Ru(CO)_4Br_2$ and halogenated N-heterocyclic carbene compounds $Au(NHC)Me_2Cl$, $Au(NHC)Et_2Cl$. Chemical compositions of deposits obtained with silver carboxylates spanned from 34 at.% for $Ag_2(\mu\text{-}O_2CC_3F_7)_2$ up to 76 at.% for $Ag_2(\mu\text{-}O_2CC_2F_5)_2$. FEBID with ruthenium complexes resulted in metal contents around 23 at.% and with gold compounds not more than 16 at.%. TEM measurements have proven that for both Ag and Ru FEBID, the bonds between metal atoms and ligands have been successfully cleaved. Metal contents of Ru-containing structures were later enhanced with a forming gas based post-purification, which allowed for obtaining even 83 at.% of Ru without destroying the integrity of the deposit.

Important part of this PhD Thesis are characterisation methods. The thesis contains a first application of vacuum thermogravimetry as a method of pre-screening of thermal properties of low-volatility silver compounds. Secondly, focused electron beam induced mass spectrometry (FEBiMS) as a novel method to investigate volatile charged species leaving material due to irradiation with electrons was developed here. It was used to examine three solid compounds: $Ru_3(CO)_{12}$, $Ag_2(\mu\text{-}O_2CC_2F_5)_2$, $Cu_2(\mu\text{-}O_2CC_2F_5)_4$ and one gaseous compound adsorbed to the surface of the sample with constant gas supply: $W(CO)_6$. These both methods are novel in the

field of FEBID and provide new, important insight into thermal properties of precursor and the interaction between physisorbed precursor molecules and electron beam. Furthermore, WDS combined with EDX for elemental composition was developed as characterization for overlapping spectral peaks. TEM was used for establishing crystal structure, AFM for thickness determination of deposits and four-point probe method - for electrical resistivity measurements.

The last part of the thesis focuses on the development of FEBID modelling. It consists of two parts, first being the extension to characteristic rate (frequency) maps by introducing the shape resolution parameter and the surface diffusion rate. Second part considers modelling of co-deposition of ligands and its influence on metal content in the deposit. The model will be confronted with experimental results showing qualitative agreement between calculations and experiments.

Streszczenie pracy

Współczesny rozwój nanotechnologii stworzył potrzebę wprowadzenia godnych zaufania i powtarzalnych metod tworzenia struktur w nanoskali. Depozycja zogniskowaną wiązką elektronów (ang. Focused electron beam induced deposition – FEBID) to metoda naostrukturyzacji pozwalająca na bezmaskową depozycję trójwymiarowych struktur z rozdzielczością poniżej 20 nm, sięgającą nawet pojedynczych nanometrów. Prosta idea i wszechstronność to główne zalety FEBIDu, dzięki którym znalazł on zastosowanie na wielu różnych polach, włączając w to nanomagnetyzm, plazmonikę, budowę nanoczujników lub końcówek do próbników w mikroskopach ze skanującą sondą oraz do naprawy masek używanych w fotolitografii. Pomimo jej zalet i wielu zastosowań stawia ona wciąż wiele wyzwań związanych z depozycją zogniskowaną wiązką elektronów. Do najważniejszych problemów do rozwiązania należą niska czystość depozytów, mająca swoje źródło w używaniu metaloorganicznych (lub organometalicznych) związków do depozycji metali, oraz tzw. proximity effects (efekty bliskości), obniżające rozdzielczość z jaką można nakładać depozyty.

Ta praca doktorska próbuje odpowiedzieć na wyzwania FEBIDu przez pokazanie rezultatów systematycznych badań różnych związków metaloorganicznych jako potencjalnych prekursorów do depozycji wiązką elektronów. Pochodzą one z trzech grup kompleksów: karboksylanów srebra $Ag_2(\mu\text{-}O_2CC(Me)_2Et)_2$, $Ag_2(\mu\text{-}O_2C^tBu)_2$, $Ag_2(\mu\text{-}O_2CCF_3)_2$, $Ag_2(\mu\text{-}O_2CC_2F_5)_2$, $Ag_2(\mu\text{-}O_2CC_3F_7)_2$, heteroleptycznych kompleksów rutenowych $C_3H_5)(CO)_3Br)$, $Ru(CO)_4Br_2$ oraz halogenowanych N-heterocyklicznych karbenów złota $Au(NHC)Me_2Cl$, $Au(NHC)Et_2Cl$. Skład chemiczny depozytów wytworzonych przy pomocy karboksylanów srebra zawiera się pomiędzy 34 at.% dla $Ag_2(\mu\text{-}O_2CC_3F_7)_2$ aż do 76 at.% dla $Ag_2(\mu\text{-}O_2CC_2F_5)_2$. FEBID przy użyciu kompleksów rutenowych skutkował powstaniem depozytów z około 23 at.% metalu, a przy użyciu związków złota z nie więcej niż 16 at.% metalu. Pomiary TEM potwierdziły, że zarówno w przypadku srebra jak i rutenu, wiązania chemiczne pomiędzy atomami metalu a ligandami zostały zerwane. Procentowa zawartość metalu w depozycie zawierającym ruten została później zwiększona za pomocą metody oczyszczania bazującej na użyciu gazu formującego, co pozwoliło na uzyskanie nawet 83at.% rutenu bez utraty ciągłości strukturalnej depozytu.

Ważną częścią tej rozprawy były metody charakteryzacji własności depozytu: analiza WDS (Wavelength Dispersive X-ray Spectroscopy – spektroskopia rentgenowska z dyspersją długości fali) użyta łącznie z EDS-em (Energy Dispersive X-ray Spectroscopy – spektroskopia rentgenowska z dyspersją energii) do badania składu chemicznego, TEM (Transmission Elec-

tron Microscopy – transmisyjna mikroskopia elektronowa) do badania struktury krystalicznej, AFM (Atomic Force Microscopy – mikroskopia sił atomowych) do badania grubości depozytów oraz metoda czteropunktowa pomiaru oporności elektrycznej struktur. Ta praca przedstawia pierwsze użycie termograwimetrii próżniowej (VTGA Vacuum Thermo-Gravimetric Analysis) jako metody pre-selekcji nisko-lotnych związków srebra pod kątem ich własności termicznych. Ponadto, został zaprezentowany opis nowatorskiej metody badania lotnych, naładowanych elektrycznie fragmentów prekursora opuszczających powierzchnię próbki dzięki napromieniowaniu go wiązką elektronów: spektrometrii masowej indukowanej zogniskowaną wiązką elektronów (ang. Focused Electron Beam Induced Mass Spectrometry – FEBiMS). Metoda ta została zastosowana do zbadania trzech związków w stanie stałym: $Ru_3(CO)_{12}$, $Ag_2(\mu\text{-}O_2CC_2F_5)_2$, $Cu_2(\mu\text{-}O_2CC_2F_5)_4$ oraz jednego związku adsorbowanego na powierzchni próbki z fazy gazowej z ciągłą dostawą nowych molekuł gazu: $W(CO)_6$. Obie metody (VTGA i FEBiMS) są nowe w dziedzinie FEBIDu i dostarczają ważnych informacji zarówno o termicznych właściwościach prekursorów, jak i o interakcjach pomiędzy fizysorbowanymi cząsteczkami prekursorów, a wiązką elektronów.

Ostatnia część rozprawy doktorskiej skupia się na rozwoju matematycznego modelowania FEBIDu. Zawiera ona dwie części, z których pierwsza, to rozszerzenie map charakterystycznych częstości poprzez dodanie tzw. parametru rozdzielczości oraz częstości dyfuzji. Druga część analizuje modelowanie ko-depozycji ligandów oraz jej wpływu na procentową zawartość metalu w depozycie. Ten model został skonfrontowany z danymi eksperymentalnymi pokazując jakościową zgodność pomiędzy obliczeniami, a eksperymentem.

Table of Contents

List of Figures

List of Tables

List of Abbreviations and Symbols

AFM	Atomic force microscopy
ALD	Atomic Layer Deposition
η^3-allyl	C_3H_5 (ligand)
BF - STEM	Bright field scanning transmission electron microscopy
BSE	Backscattered electron
CVD	Chemical vapour deposition
DEA	Dissociative electron attachment
DF - STEM	Dark field scanning transmission electron microscopy
DI	Dissociative ionisation
DUVL	Deep ultraviolet lithography
e-beam	Electron beam
EBL	Electron beam lithography
EDX	Energy dispersive X-ray spectroscopy
EI-MS	Electron impact mass spectrometry
EUVL	Extreme ultraviolet lithography
Et	Ethyl (ligand)
FEB	Focused electron beam
FEBID	Focused electron beam induced deposition
FEBIE	Focused electron beam induced etching
FEBiMS	Focused electron beam induced mass spectrometry
FEBIP	Focused electron beam induced processing
FEG	Field emission gun
FIB	Focused ion beam
FIBID	Focused ion beam induced deposition
FW(99.9%)	Full width comprising 99.9% of all electrons (Gauss beam size)

FWHM	Full width at half maximum
GIS	Gas injection system
HR-TEM	High resolution transmission electron microscopy
HV	High vacuum
MC	Monte Carlo (Type of simulation)
Me	Methyl (ligand)
MS	Mass spectrometry
NHC	N-heterocyclic carbene (ligand)
PE	Primary electron
PVD	Physical vapour deposition
SAED	Small angle electron diffraction
SE	Secondary electron
SEM	Scanning electron microscopy
SIMS	Secondary ions mass spectrometry
TOF-SIMS	Time-of-flight secondary ions mass spectrometry
^{t}Bu	tert-butyl (ligand)
TGA	Thermogravimetry
UHV	Ultra-high vacuum
VTGA	Vacuum thermogravimetry
e^-	electron
f	Flux of electrons $\left(\frac{electrons}{m^2 s}\right)$
φ	Resolution parameter
J, J_{ML}	Flux of precursor molecules $\left(\frac{molecules}{m^2 s}\right)$
n	Number of molecules physisorbed on the unitary surface in a unit of time, ML – precursor molecules, L – ligands
n_0, n_{0ML}, n_{0L}	Maximum number of adsorption sites, for precursor molecules (ML)

	and ligands (L)
$\upsilon_{gas}, \upsilon_{des}, \upsilon_{diss}, \upsilon_{diff}$	Characteristic rates of gas supply (gas), desorption of molecules (des), dissociation (diss) and diffusion (diff) (1/s)
$\sigma, \sigma_{ML}, \sigma_{L}$	Cross-section for dissociation of precursor molecules (ML) and ligands (L) (m^2)
t_d	Dwell time (s)
t_r	Refreshment time (s)
$\tau, \tau_{ML}, \tau_{L},$	Average desorption time for precursor molecules (ML) and ligands (L) (s)
θ	Coverage of surface by precursor molecules

Motivation and composition of Thesis

Nanotechnology is a vast and very rapidly developing field of nowadays science. It contains novel nanoparticle based drug delivery methods, thin film coatings, micro- and nanorobots and nanoelectromechanic systems (NEMS), nanosensors, nanomagnetic, nanooptic and micro and nanoelectronic devices, where each of mentioned is wide field on its own, gaining the interest of scientists all around the world. As modern world needs more and more nanomaterials and nanostructures, it is of crucial interest to develop methods allowing for reliable and reproducible manufacturing in nanoscale. Focused electron beam induced deposition (FEBID) is one of these methods. Due to its incomparable precision, reaching single nanometers, direct approach and flexibility it is a number one choice for prototyping complicated-shape nanodevices. What is more, FEBID is still a developing technique, with many yet-not fully analysed and addressed scientific challenges. One of those challenges is purity of deposited structures. This work concludes years of research concerning physics and chemistry of electron induced processes governing dissociation and deposition of organometallic molecules adsorbed on conductive substrates.

The overall motivation of this PhD Thesis is to gain fundamental understanding about the creation of pure metal nanostructures by FEBID. In the course of the investigations, this goal further motivated the development of novel characterization and screening methods of FEBID precursors, the use of novel precursors as such, and the extension of existing FEBID models, which is schematically shown in Figure 0.1.

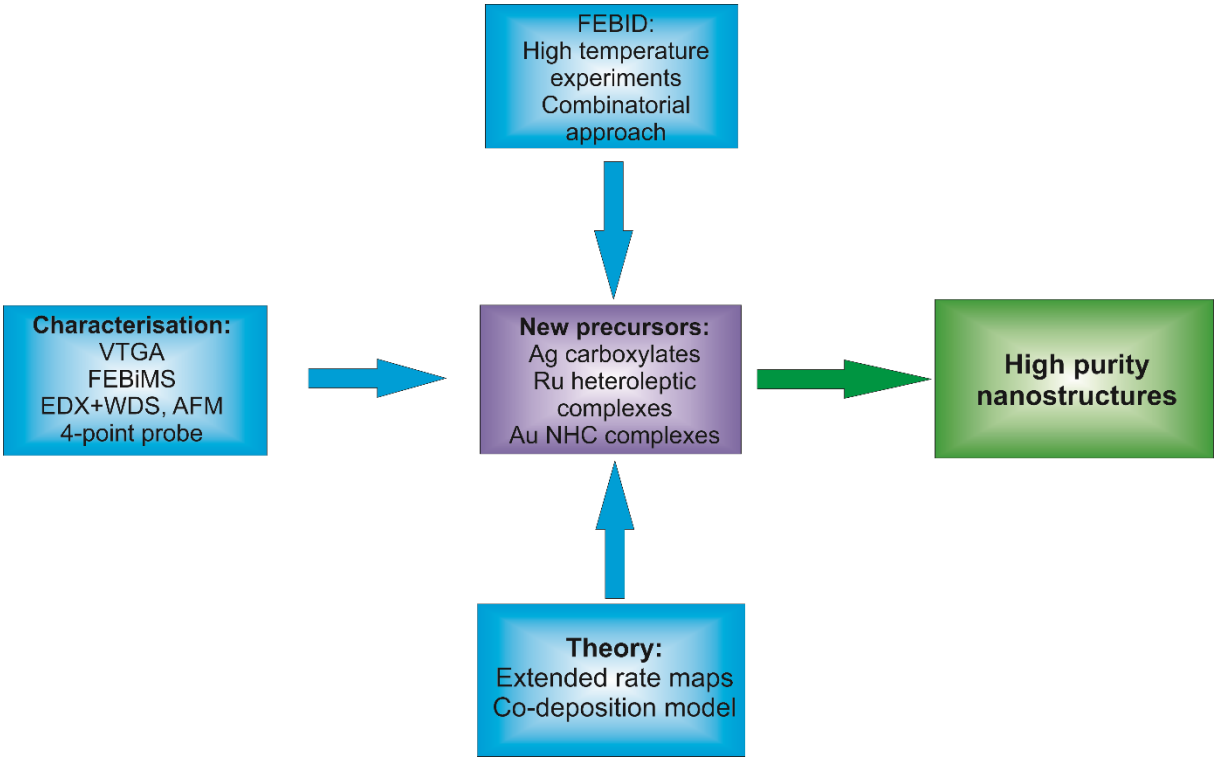

Figure 0-1 Schematic presentation of the systematic study of novel precursors using complementary methods to obtain high purity FEBID structures.

Chapter 1 consists of a comprehensive introduction to FEBID and state of the art results achieved with different precursors. Physics and chemistry governing the formation of the deposit, mechanisms of co-deposition of contaminants and its influence on achieved metal contents as well as proximity effects will be discussed. Moreover, methods of post-purification, their advantages and drawbacks will be presented. This chapter focuses also on basic modelling of FEBID, including recent development of rate (frequency) maps and the two-species model. Moreover, different characterisation methods and their specifics in context of applying them to investigated micro and nano-structures will be discussed. The chapter ends with challenges of FEBID which will be assessed in next parts of this work.

Chapter 2 contains a description of technical parameters of the experimental methods used in the work: starting with basics of the equipment used for FEBID experiments throughout scanning and transmission electron microscopy, methods of estimating the composition of the deposit with correction applied for thin film effects and finishes at thermogravimetry, mass spectrometry and four-point probe setups.

Chapter 3 shows the results of FEBID experiments with novel precursors. Chapter 3.1 focuses on deposition results using silver carboxylates. It starts from description of the precursor and investigation of their thermal properties using thermogravimetry. Then comes analysis of composition and morphologies of the FEB deposits, with special focus on their high metal content and halo effects. It is followed by investigation of electrical properties of deposited wires and examination of the possibility of creating 3-D vertical structures. Chapter 3.2 presents the results of FEBID using heteroleptic Ru complexes. Use of different chemical groups as ligands for deposition of ruthenium will be discussed, with a special focus put on the main source of carbon contamination. Deposition pathways will be proposed and discussed in the context of gas phase and condensed phase measurement results. Furthermore a post-purification protocols will be presented and assessed. Chapter 3.3 shows results of deposition using N-heterocyclic carbene gold precursors. Their chemical and thermal properties will be discussed, as well as their morphology and composition. The results will be compared with recently published work concerning Au(NHC)-halogen complexes and other results presented in this Thesis.

Chapter 4 focuses on the new method of investigation of volatile, charged species created due to irradiation of metalorganic compounds with the electron beam: focused electron beam induced mass spectrometry (FEBiMS). FEBiMS employs extraction of ionic species and does not involve post-ionisation. The method was used to investigate three solid state precursors, a carbonyl and two carboxylates as well as one physisorbed compound: $W(CO)_6$. Presented results show, for the first time, charged fragments of precursors dissociated during FEBID. Advantages and challenges of FEBiMS in context of its application to investigation of lithography methods will be discussed.

Chapter 5 presents two novel developments in modelling of FEBID. Firstly, the extension of recently introduced rate maps will be proposed to include the measurement of the size of the deposit and the influence of surface diffusion. Secondly, a ligand co-deposition model will be derived. The calculations will be confronted with experimental results, and the qualitative agreement between experiments and modelling will be shown.

The work will be summarised and concluded in chapter 6. This chapter will also show the outlook.

This PhD Thesis presents a systematic study using complementary experiments and measurements supported with calculations in order to reach an ultimate goal: creation of high purity nanostructures.

1. Introduction, state-of-the-art and challenges

1.1 Basics of focused electron beam induced deposition

Focused electron beam induced deposition (FEBID) is a method of manufacturing nanostructures, which allows for direct and local deposition of material onto any conductive substrate. It uses the focused beam of electrons from a scanning electron microscope (SEM) to locally dissociate adsorbed molecules of a compound, known as the precursor, to create the deposit. The precursor molecules are delivered in gas phase through a gas injection system (GIS) over the sample's substrate, where they should physisorb. Upon irradiation with the focused electron beam, the molecules should dissociate into a least two parts: volatile, which desorbs and leaves the SEM chamber and non-volatile, which chemisorb to the substrate, creating the deposit [1].

What distinguishes FEBID from other lithographic nanopatterning methods are its direct, single-step approach, possibility to manufacture three-dimensional and vertical structures of nearly any desired shape, and its very high spatial resolution, allowing for creating structures with lateral dimensions close to the size of the focused electron beam [2]. The smallest structures achieved with this method have sizes in the range of single nanometres [3], which is unreachable for any other micro- and nano-manufacturing techniques. As our understanding of electron-induced processes has progressed and the deposition regimes of FEBID have become described with more details, smaller and more complicated shapes have been deposited [4, 5]. Recent addition in the form of CAD based software for controlled deposition of multi-segment, highly complex shapes, pushed FEBID towards becoming a reliable and simple-to-use nano-3D-printing method [6-8].

A focused electron beam can be used also for very precise etching of the substrate. The precursor (etching gas) adsorbs onto the substrate's surface, where it is locally dissociated by the electron beam. The dissociated molecules bind with the atoms from the substrate, creating volatile moieties, which later thermally desorb and are evacuated from the vacuum chamber. This method is called focused electron beam induced etching (FEBIE) and, with FEBID, is a part of scientific and technological field named focused electron beam induced processing (FEBIP) [2].

Focused ion beam induced deposition (FIBID) is a method similar to FEBID, however, it uses an ion beam (i-beam) instead of electrons[9]. Ion beams are frequently installed in so-called dual beam systems and used most often for milling. The most popular are Ga^+ guns, however, He^+ ions have gained interest in recent years [10, 11]. Additionally, Xe^+ guns have been used for deposition of gold [12]. Using ion beams have certain advantages over electrons, such as higher structure growth rates or, in some cases, higher metal contents of deposited material. However, it can also generate problems, from which the most important is the implantation of ions from the i-beam into the substrate or deposit. Implantation can drastically change the properties of deposits. It is also important to properly set the beam's acceleration voltage and current, to avoid sputtering of the substrate's and/or deposit's atoms[13]. Despite the drawbacks, FIBID has been successfully applied to deposit various structures, including platinum [10, 14] and superconducting materials tungsten [15].

Standard FEBIP systems consist of an electron microscope, in most cases an SEM or environmental SEM (ESEM), however there are examples, where transmission electron microscopy (TEM) was used to deposit structures [16]. An SEM usually operates in high vacuum (HV) with a background pressure in the range of 10^{-7} – 10^{-5} mbar [9]. In some cases, ultra-high vacuum (UHV) systems have been used for deposition experiments [17, 18]. A FEBIP system is normally equipped with one or two gas injection systems: in-chamber and outside. Most commercially available GIS'es are from the second category [19], due to their easier handling. Sometimes, the gas injection system has more than one precursor line. In some cases, a heating stage can be used, especially when working with less volatile precursors that require heating to deliver the precursor molecules over the substrate. This kind of stage plays two major roles: it helps in avoiding condensation of heated precursor's vapours, as well as it can be used for *in situ* annealing experiments. One of the most important subsystems of a FEBIP setup is a beam control unit, usually equipped with specialised software, which allows for precise patterning. A schematic illustrating a typical setup for FEBIP/FIBIP is shown in Figure 1.1.

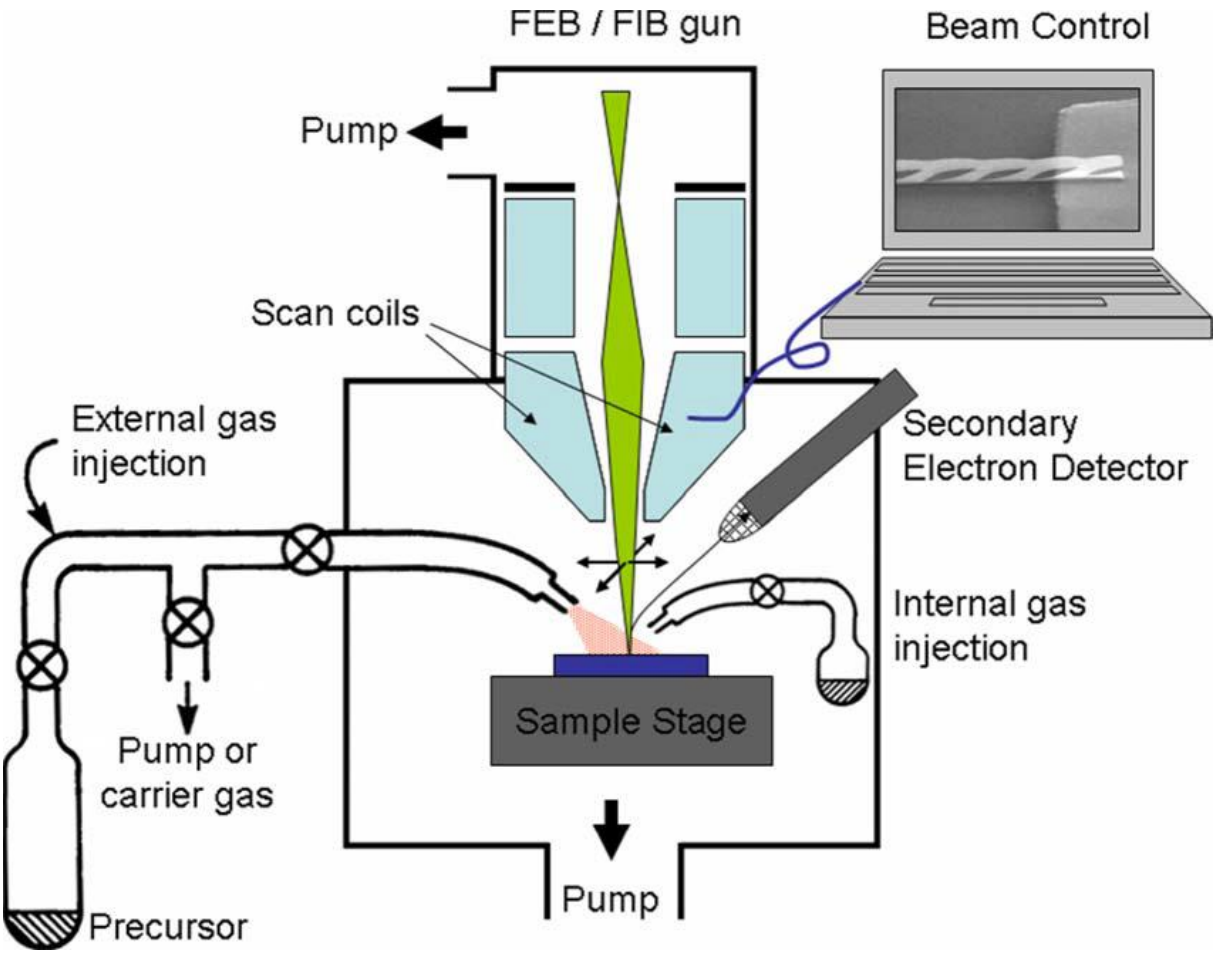

Figure 1.1 Schematic of a typical FEBIP/FIBIP equipment, reproduced from [2]

Even though FEBID is a single-step patterning method, it is very complex and has many parameters, which must be reviewed. Amongst them, there are four important patterning parameters, with great influence on the deposits' properties:

- dwell time (usually pixel dwell time) t_d: the time that an electron beam spend over 1 pixel of a pattern,
- point pitch: the distance between 2 neighbouring irradiated pixels,
- number of passes: the number of times a single pixel will be irradiated,
- Refreshment time t_r: average time between each to events of irradiation of the same pixel.

The last parameter, t_r, is connected to number of passes and point pitch. During that time, the depleted precursor molecules can be replenished by fresh ones, continuously adsorbing from the gas phase or delivered through diffusion from neighbouring areas. In several systems this

time can be directly set, in others it can be controlled by adding a "parking place" for the beam, far away from the actual deposition area.

A patterning strategy is another important element of the deposition process. The patterning strategy can be described as a beam trajectory on the irradiated area of the sample. In the case of FEBID, the three most common strategies of scanning are leading edge, serpentine and spiral. Each patterning strategy has an influence on the final shape of the deposit, as each may cause different artefacts. These artefacts were described in detail by Winkler et al. and are connected with certain properties of the deposition process [20].

Applications of FEBIP include prototyping structures used in nano-optics, plasmonics [5], nano-magnetics[21, 22], including magnetic sensors [23] and magnetic force microscopy tips[24], as well as gas-flow nano-sensors[25] and atomic force microscopy fine tips [26]. FEBID is also used to create micro-connectors and protective layers during (TEM) lamella preparation using focused ion beam (FIB). From an industrial perspective, the most important application of FEBID and FEBIE is the repair of photolithography masks [27, 28]. Photolithography is the main method for creating microelectronic devices, such as microprocessors, and the mask is a crucial part of the process. Defected masks cannot be used, as they would create faulty devices. FEBIP is the only method, which can repair many mask defects, lowering process costs and saving resources needed to replace defected masks. In recent years, a novel photolithography method has been introduced: extreme ultraviolet lithography (EUVL). The core of this method is to use a new source of radiation, electromagnetic waves of shorter than visible light wavelength of 13.5 nm. EUVL will help to move microelectronic engineering towards even smaller transistor sizes. This new method requires novel, specialised masks, which will work in reflection, rather than transmission mode (as nowadays photolithography masks). The most important part of such a mask is a mirror, made from multilayers of Mo and Si. To protect these stacks from oxidation, which could result in loss of reflectivity, a capping layer is required. One of the metal proposed for capping is ruthenium [29]. Ru does not oxidise easily and it is transparent to UV light. As FEBID is used to correct defects in masks, it is of crucial importance to develop methods for depositing pure Ru structures in micro- and nano-scale.

1.2 Interactions between electrons and material

The irradiation of a material with an electron beam leads to various outcomes [30]:

- the creation of secondary electrons (SE's),

- the creation of backscattered electrons (BSE's),
- the excitation and de-excitation of atoms and the release of characteristic X-rays,
- the excitation and de-excitation of atoms and the release of Auger electrons,
- cathodoluminescence.

Secondary electrons are created due to the ionisation of irradiated material by incoming electrons from the primary beam. If the energy of the incoming electron is high enough, the electron from substrate's atom can be ejected from the shell. If the secondary electron was generated close to the surface and its energy is high enough it can leave the substrate. SE's leaving the material are one of the basic signals detected in the SEM and most commonly used to investigate the morphology of a sample. For detector engineering purposes, the secondary electrons are considered the ones, which leave the sample's surface with energies less than 50 eV [31].

Backscattered electrons are created when electrons from the primary beam elastically scatter back from the surface of the material. Such electrons can undergo series of inelastic scattering events before they are reflected back. Their energy spectrum spans normally from tens of electronvolts up to the energy of primary electrons, which is typically on the level of keV. For engineering purpose, electrons leaving the sample's surface with energies above 50 eV are considered backscattered. As the number of emitted BSEs depends on the substrate material's atomic number Z, these electrons are used for material-based imaging via SEM. BSEs can also generate secondary electrons due to series of electron scattering before they leave sample substrate. This kind of SEs are called secondary electrons type II (SE II), while the ones generated by primary electrons (PE) are called type I (SE I) .

Characteristic X-rays are an effect of excitations of atoms from the material caused by the incoming primary beam of electrons. Excited atoms de-excite, emitting electromagnetic radiation with energies dependent on the differences between energy levels in irradiated atoms. As these differences vary, depending on the element, characteristic X-rays are often used to determine the elemental composition of a studied material in methods such as energy and wavelength dispersive X-ray spectroscopy (EDX and WDS, respectively), as well as X-ray fluorescence spectroscopy (XRF). For further information, proceed to the experimental chapter 2.3.

The mechanism behind the creation of Auger electrons is similar to the one leading to the generation of characteristic X-rays. Electrons irradiate a sample, exciting its atoms. The excited electrons from the inner shell de-excite and the released energy can cause the ejection of

one of the outer shell electrons. The energies of ejected electrons are dependent on the elements building the sample, so this method is also used for the examination of the elemental composition of materials.

Cathodoluminescence may happen during irradiation of semiconductors or non-metallic materials. Primary electrons cause the generation of a cascade of SEs, BSEs and X-rays, which may cause recombination between electrons from the conductance band and hole from valence band. Excess energy may be then emitted as a photon, which, for some materials, can be in the visible range.

1.3 Halo deposit

During FEBID, the primary electron beam, with energies usually in range of 1-30kV, irradiates a layer of molecules physisorbed on the substrate. However, cross-section for interaction between electrons and matter decreases with higher electron energy and the adsorbed layer is thin (roughly one monolayer). It is then unlikely that the primary beam would be the only responsible cause for electron induced dissociation processes. Literature sources [1, 32] point out low-energy electrons, mostly SEs as the main source of dissociation events. SE I are generated mostly inside the area irradiated by the primary beam, however SE II can be emitted from every place, where multiple-time scattered BSEs reached. These secondary electrons can also dissociate precursor molecules adsorbed on the surface, creating a so-called "halo" deposit. A halo is usually an unwanted effect, as it lowers the lateral resolution of the deposits. The size of halo is correlated with the energy of primary electrons, i.e. the higher the PE's energy, the wider the lateral range of the backscattered electrons. This dependence was described in detail by Kanaya and Okayama [33], amongst others. The thickness of the halo is usually much lower, than the thickness of a deposit, although there are several precursors, for which the halo is very pronounced. This has been mostly the case for recently investigated carboxylates, both copper and silver [34-36]. Deposition processes using silver carboxylates are an important part of this work and the origin of the halo will be discussed with more details in chapter 3.1. Moreover, for high-aspect ratio structures secondary electrons generated from the structure can widen its edge, further lowering the lateral resolution of the deposits. The origin of halo deposition is depicted in Figure 1.2a.

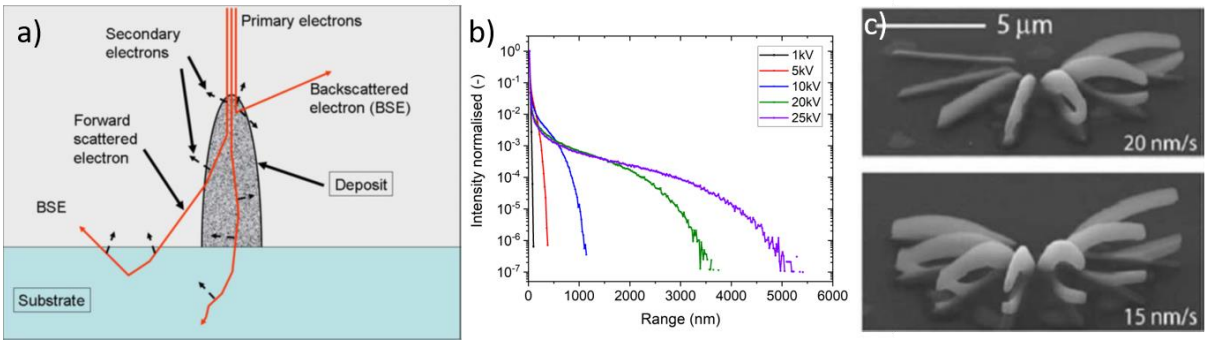

Figure 1.2 Influence of generated secondary and backscattered electrons on deposition of halo a) (taken from [2]). b) Simulated intensity ranges of BSEs. Parasitic deposition beneath the structure c) (taken from [2]).

Figure 1.2.b depicts the intensity ranges of backscattered electrons simulated using Monte Carlo CASINO simulations [37]. The simulations were performed on 20x20x20 μm^3 Si box of density of 2.33 g/cm^3, using 1 million electrons in a Gaussian-shape beam, with full width at 99.9% (FW(99.9%)) of 100 nm. The beam acceleration voltages were from 1 – 25 kV and are indicated in the legend. As can be noticed, the maximum range of BSEs varies a lot with acceleration voltage, starting from around 100 nm for 1kV ending on 5500 nm for 25 kV. The dependence between BSE range and primary beam acceleration voltage indicates, that range of halo can be quenched by using electron beams with low acceleration voltages.

Another effect, connected with the halo, is a parasitic deposition caused by forward scattered electrons. For structures with higher aspect ratios, incoming electrons can be scattered on the top of the structure and irradiate places, where the primary beam does not reach. If the number of forward scattered electrons in a single place is high enough, they may initiate deposition, creating unwanted structures in close proximity to the actual deposit. Parasitic deposition caused by forward scattered electrons is depicted in Figure 1.2c.

1.4 Purity of deposits

Ideally, e-beam induced dissociation would lead to the cleaving of bonds between the metal atom and the ligands, with desorption of the latter, leaving a pure deposit. In reality, however, this is a rare case, as found for various materials and summarised by review articles. In many cases, metal content in the deposit ranges between 5 and 25 at.%, with a handful of pure or close to pure deposits being reported. Further details on precursor chemistry can be found in section 1.4.

There are three main sources of impurities of FEB deposits, each depicted in Figure 1.3:

- incomplete dissociation

- co-deposition of adsorbed ligands
- co-deposition of residual gases from the SEM vacuum chamber.

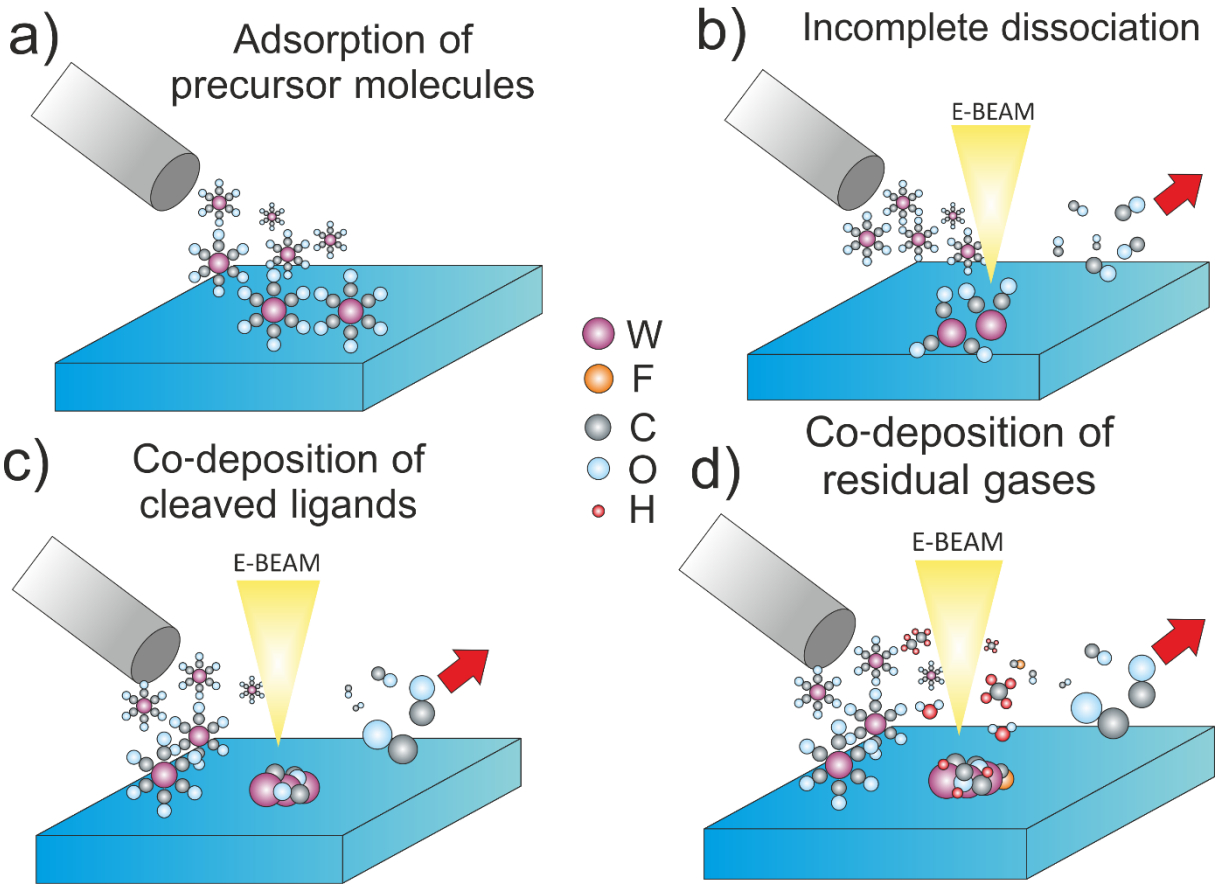

Figure 1.3 Adsorption of molecules on a substrate's surface, delivered through a GIS (a), incomplete dissociation of precursor molecules (b), co-deposition of cleaved ligands (c), co-deposition of impurities from residual gases from the SEM chamber (d).

The first situation happens, when the electrons do not cleave all metal-ligand bonds and the ligands are incorporated into the deposit [2, 38]. The deposited material then exhibits much lower metal content, as the ligands are usually long carbon-oxygen-hydrogen chains. The second situations occurs, when the number of incoming electrons per second is high enough to not only dissociate the metal-ligand bond, but also dissociate the cleaved ligands, which have not yet desorb from the substrate [2, 39]. The dissociation of ligands can create non-volatile species, which are incorporated into the deposit, lowering its purity. In some cases, the ligands, due to electron irradiation, may polymerize, losing their volatility and lowering deposit metal content. These two processes are responsible for most contaminations in the deposited structures. The third process, also related to the-co deposition of impurities is not connected with the beam parameters or the used precursor, but with the properties of the used vacuum system. In high vacuum systems, most commonly used for FEBID, the background pressure is

on the level of 10^{-7} – 10^{-5} mbar. According to work published by Bernau et al [40], this stands for maximally $1.6 \cdot 10^{15}$ molecules/cm^2 per second. Compared to precursor fluxes (e.g. $1.6 \cdot 10^{17}$ molecules/cm^2 per second of $Co_2(CO)_8$ from Bernau [40]) this effect should only have a minor effect on metal content of deposited structures, unlike the incomplete dissociation and co-deposition of ligands. However, this phenomenon cannot be completely neglected. Residual gases may also help increase the purity of deposited structures. Residual water molecules may, under irradiation with the e-beam, bond with carbon located in the deposit, purifying it. This effect, however, has never been properly quantified.

1.5 Chemistry of FEBIP precursors

The properties of the compounds used for deposition are crucial from the point of view of the properties of the deposited material. By now, dozens of different compounds have been tested as potential precursors with various effects: from deposits containing only few percent of desired material, up to nearly completely pure structures. There are certain requirements that a FEBID precursor must (or at least partially) fulfil, to increase the probability of successful deposition. First, it should be volatile enough to sublimate and evaporate at room (ideally) or moderately elevated temperatures (as a rule of thumb <250°C). Moreover, it should not decompose during evaporation (sublimation), so that full molecules are in the gas phase and can be delivered over the sample's surface. Molecules of the chosen compounds should dissociate under e-beam irradiation. Preferably, the bond between the central atom and the ligands should be the easiest one to cleave. Additionally the used ligands should have a short residence time on the surface, meaning, they should quickly desorb from substrate's surface after electron induced dissociation. Ligands should not cross-link on the surface, as this may create a non-volatile polymer. As the electron beam is not selective, short ligands are preferred. An important feature is also stability of the compound in vacuum and air. Stable compounds are easier to handle and provide more reproducible results. Furthermore, poisonous or potentially harmful compounds are most often avoided. More detailed analysis and design rules for the synthesis of optimal FEBID precursor can be found in recent papers written by McElwee-White et al. [41] and van Dorp et al. [42].

Compounds used in FEBID are mostly organometallics, although there are a few carbon-free precursors that have been successfully applied [43, 44]. The most important ones are WF_6 and WCl_6, which have given 66 at.% and 58 at.% of W content in the deposited material, respectively [45].It is worth noting, that WF_6 was used to fabricate deposits of much higher metal content of 85 at.% using an UHV setup [46]. Additionally germanium hydrate has been used

to deposit pure Ge structures [47]. XeF_2 is worth mentioning, as it is vastly used in FEBIE to etch Si with F [48]. Other examples of carbon-free precursors are tetrakis(trifluorophosphine)M(0), where M stands for Ni or Pt. Depositions using $Ni(PF_3)_4$ have lead to metal contents of around 36 at.%, however Ni probably oxidised, due to interaction with H_2O residual in the chamber [49]. $Pt(PF_3)_4$ was deposited with a focused electron beam in high vacuum with 82.6 at.% Pt [50], however the authors did not quantify elements not present in the precursor molecule. Another study showed deposition using this precursor, which gave 61 at.% of metal content [51]. A further example of short ligands, with little or no carbon atoms, are gold precursors, which are described in more detail within the next paragraphs.

The most popular organometallics are $Pt(CpMe)Me_3$, $W(CO)_6$, which are commercially available Pt and W precursors. Despite their popularity, the metal contents of as-deposited structures are typically on the level of 15-25 at.% for the former and 30-60 at.% for the latter. Carbonyls are a very popular group of precursors. The most important representatives of this group are $Co_2(CO)_8$ (95 at.% of Co) [52], $Fe(CO)_5$ (97 at.% of Fe) [17], the aforementioned $W(CO)_6$ [53], $Mo(CO)_6$ [54]and the recently developed heteronuclear $HFeCo_3(CO)_{12}$ [55]. The last one is well known for creating structures with very high metal content, up to 80at% of both Fe and Co [55].

Another, frequently used group of compounds are beta-diketonates. Representatives of this group have been used to deposit palladium from $Pd(hfac)_2$ and copper from $Cu(hfac)_2{\cdot}H_2O$. Recently, a beta-ketoestrate complex $Cu(tbaoac)_2$ has been applied in FEBID. $Pd(hfac)_2$ is characterised with relatively high vapour pressure, which enables deposition already at 36°C in high vacuum. The metal content of the obtained structures ranged from 5.4 at,% up to 28 at.% [56-58]. $Cu(hfac)_2{\cdot}H_2O$ is a green crystal air-stable solid decomposing at around 230°C. The maximum achieved metal content in deposited structures was 14 at.% [59] although other sources have reported lower values from 4 at.% [60] to 10 at.% [61]. It should be noted, that although the precursor molecules have 12 atoms of fluorine in all mentioned cases, their presence within the deposited material was below the detection limit of 1 at.%, suggesting, that they have been completely removed via e-beam irradiation. On the other hand, the removal of oxygen depends highly on the deposition parameters [59, 61]. $Cu(tbaoac)_2$ has the largest number of carbon atoms of all previously mentioned examples, with 16 C atoms per 1 Cu. Additionally, it has a substantially lower vapour pressure of 0.027 mbar at 100 °C in comparison to $Cu(hfac)_2{\cdot}H_2O$ (17.61 mbar at the same temperature). Despite this, the Cu content of

the deposited structure was reported to be higher, reaching 26 at.%. Moreover, for the first time electrically conductive copper structures were achieved without post-purification [62].

Copper has also been deposited using heteroleptic diketonate deriviates like Cu(hfac)VTMS, Cu(hfac)DMB and Cu(hfac)MHY. All three compounds are air-sensitive liquids. All of them have been studied under the same conditions (high vacuum, 500 pA beam current) by Luisier et al. for their comparative article [59]. In that work, the highest metal content of 25 at.% of Cu was achieved for Cu(hfac)DMB. Deposition with Cu(hfac)VTMS resulted in a material containing 20 at.% of Cu and the metal content of the deposits made using Cu(hfac)MHY was 13 at.%. None of the deposited wires were conductive [59]. From the three compounds, Cu(hfac)VTMS was studied the most. Deposits made from this precursor usually reach from 11 to 13 a.t% of Cu [63-65]. It is worth noting, that Utke et al. [66] have been able to obtain pure Cu deposits using this complex. However, this high purity was obtained only for free-standing rods and pillars via heat-assisted FEBID. Low heat conductivity of the growing pillars caused an increase in temperature at the growth front and, in turn, the thermal decomposition of the deposited material, resulting in the growth of rough, pure copper nanocrystals [66].

Beta-diketonate derivatives have also been employed in the deposition of Au, from $Me_2Au(acac)$, $Me_2Au(tfac)$ and $Me_2Au(hfac)$. The last is the most volatile, evaporating already at room temperature, however it is also the most unstable, making its application in FEBID limited. It has mostly been used in ESEMs in the presence of reactive gases. In water vapour and oxygen rich atmospheres, with even 50 at.% being achieved. Under standard HV conditions, this value is much lower, reaching only 2-3 at.% [67, 68]. $Me_2Au(acac)$ is the most frequently used compound among all gold diketonates. Typically, it gives deposits with Au content around 8 – 12 at.% [39, 69] and for high aspect ratio structures even up to 28 at.% of Au has been achieved, most probably as an effect of e-beam heating [70]. Similar purities of 30 at.% have been obtained with deposition at elevated stage temperature of 130 - 150°C [71]. The highest gold content for as-deposited materials without any reactive atmosphere were achieved using $Me_2Au(tfac)$, with values typically in the range of 15 – 30 at.% [72-74]. Even 39 at.% has been achieved for thermally decoupled substrate, milled using Ga^+ ions [75].

Following the intuitive rule to use short organic or inorganic groups as ligands, various short-ligand compounds have been discussed as potential gold precursors. With two of them, $AuCl(PF_3)$ and AuCl(CO) very high purity structures have been deposited, reaching 100 at.% of gold content for the former [76] and >95 at.% for the latter [57]. However, these com-

pounds are highly unstable and cannot be used for prolonged durations, limiting their applicability in industry [76, 77]. Another promising, short-ligand precursor is $Au_2Me_4(\mu\text{-}Cl_2)$, which allows obtaining metal contents of 41at% of Au [42]. As in the case of the previously-mentioned precursors, $Au_2Me_4(\mu\text{-}Cl_2)$ is unstable in HV. Alongside $Au_2Me_4(\mu\text{-}Cl_2)$, two other compounds have been tested: $AuCl(SMe_2)$, $AuMe(PMe_3)$. Using the first, no gold was found in the deposit. Most probably, the compound thermally decomposed inside the gas injection system. Better results were obtained with $AuMe(PMe_3)$, where 19-25 at.% of gold was found in the deposited material [42]. Recently, two precursors were studied using UHV surface science methods: $Au(CF_3)(CNMe)$ and Au(CF3)(CN^tBu). In UHV the compounds were deposited giving metal contents of 22 at.% and 14 at.%, respectively.

Recently, a new and highly promising group of compounds has been examined as FEBID precursors: carboxylates. These compounds have been known as CVD precursors, although in recent years, various examples of silver and copper FEB induced deposition using carboxylates have been reported. Carboxylates, in opposition to the aforementioned gold compounds usually have quite large carbon chains, however, they allow for the deposition of surprisingly high-metal-content structures, with around 25 at.% for Cu, and more than 50 at.% for Ag. The deposition process with silver carboxylates will be extensively discussed vastly within the next chapters of this Thesis (see chapter 3.1 and chapter4).

A vast compendium of FEBID precursors can be found in the new publication from Barth et al [43]. Moreover, coordinated complexes of atoms from groups 10 and 11 have been vastly discussed within recent work by Utke et al. [44]. The summary images from both publications are presented in Figure 1.4. Upper part of the figure shows the average and maximum metal content of the deposits achieved using FEBID with the number of potential ligands, which can be lost due to dissociative adsorption on surface. The lower part contains a summary of the behaviour of different functional groups as ligands in precursors used for FEBID. The highest purity was achieved for the ligands marked with green arrows.

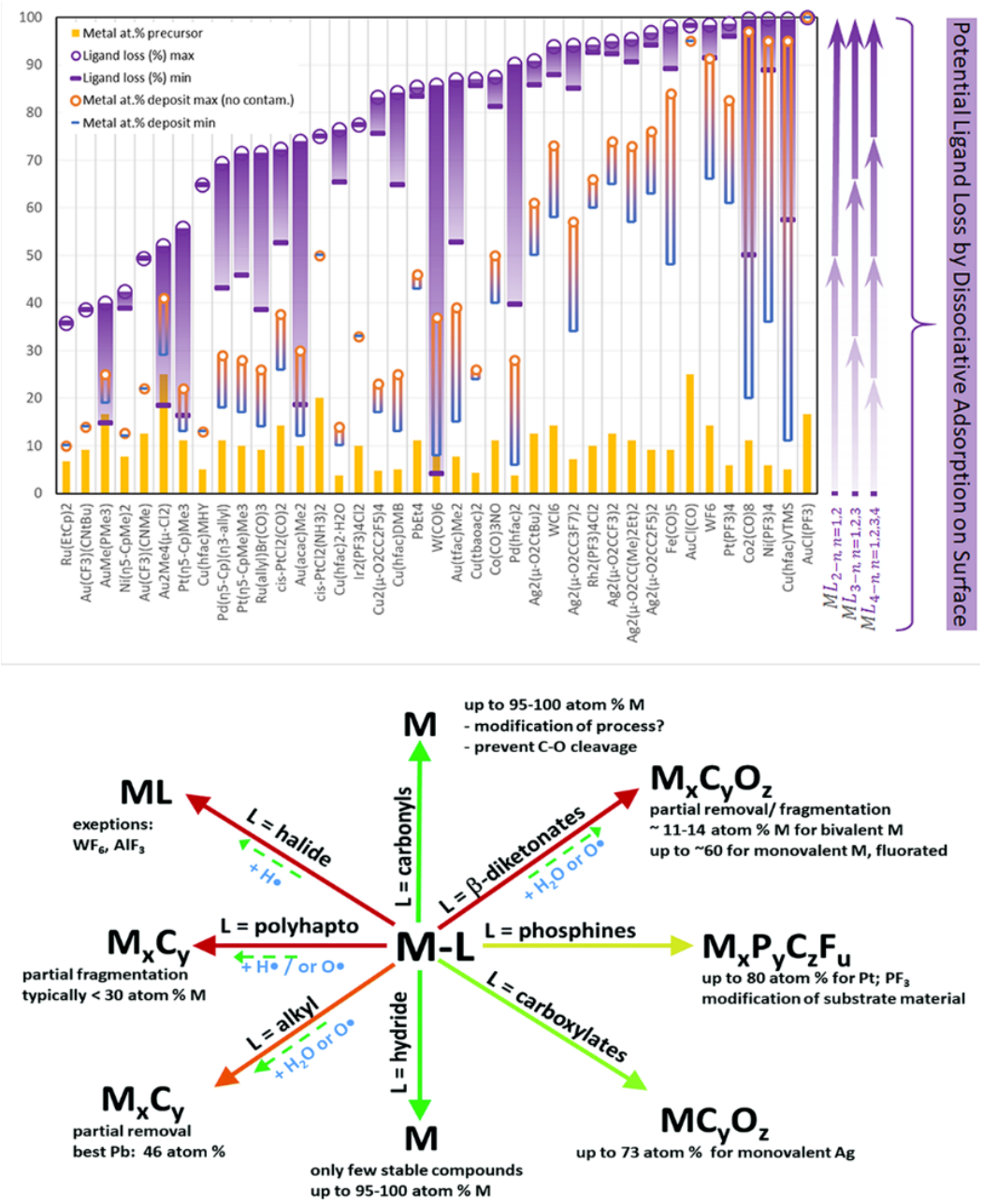

Figure 1.4 Average and maximum purities obtained with different precursors depicted alongside number ligands, which can be possibly lost (upper). Different chemical groups used as ligands for FEBID precursor (lower). Reproduced from [43] and [44] respectively.

1.6 Post-purification of deposited structures

Several post-purification procedures have been developed to tackle the issue of low metal content deposits. These procedures include *in situ* deposit curing, using electron beam and reactive gases. This method was applied to purify Pt deposits made with Pt(CpMe)Me3 and assisted by O_2 [78] and H_2O [79] as reactive gases. It has also been used to remove carbon from Ru-C deposits made with $Ru(EtCp)_2$ with H_2O [28]. A recently developed new protocol includes NH_3 as the purifying gas to clean $(\eta^3\text{-allyl})Ru(CO)_3Cl$. Although it has to be noted that

the experiments were performed in an UHV setup and the NH_3 was condensed on top of the deposited structures at 110 K. The results showed that NH_3 enhanced the removal of Cl upon electron beam irradiation. Sometimes the injection of a reactive gas was applied alongside the deposition process, which facilitated enhancing the metal content of the deposited structure. The deposition of gold using $Me_2Au(tfac)$ with the co-injection of water vapour resulted in an impressive purity of 91 at.% [80].

Additionally, *ex situ* purification methods can be applied. The simplest form is vacuum annealing at high temperatures, which has been applied, e.g. to increase the metal content of Co-O-C deposits made with $Co_2(CO)_8$ [81]. At higher temperatures, the cobalt oxide was reduced to metallic Co. This type of post-treatment, however, is not successful in all cases. For both $Me_2Au(acac)$ and $Cu(hfac)_2$ the metal content of the deposits increased only slightly, although, the grain size increased with the applied temperature [60]. Another form of thermal post-growth annealing is laser treatment, which has been used for Cu-C deposits, however, it led only to structural changes of the deposit, rather than an increase in metal content [61].

In some cases, high temperature annealing is coupled with reactive gas injection, such as H_2. This strategy was applied to Au-C deposits made with $Me_2Au(acac)$ [60]. Additionally, the metal content of Pt-C deposits increased from 15 at.% to 40 at.% by annealing at 500 °C in a forming gas atmosphere (5 % H_2/95 % N_2). H_2O-assisted high temperature (250°C and 400°C) annealing has been successfully applied to remove P contaminants from Pt deposits made with $Pt(PF_3)_4$ [82]. The combination of reactive gas e-beam purification with thermal post-annealing has been applied to purify Co-C structures made with $Co_2(CO)_8$, leading to pure Co layers [83]. In this work, purification via thermal annealing of Ru-Br-C deposits in oxygen and forming gas atmospheres will be discussed in chapter 3.2.

Purification is a powerful tool, however, it exhibits a major drawback. If successful, it removes most of the contaminants, however it entails the removal of a majority of atoms from the deposit, causing large volume losses. This may not be very problematic for simple, planar deposits, but it can cause damage to complexly-shaped, three-dimensional structures. This bottleneck can be addressed with the introduction of novel precursors, with which high-purity structures can be deposited. By increasing the purity of the deposited material, potential volume loss due to any post purification method, can be decreased, which helps to preserve the initial shape of the deposits.

To properly understand a surface physico-chemistry happening on the surface during irradiation of adsorbed molecules and hence be able to choose proper chemical group as a ligand for FEBID precursor it is of crucial importance to research and mathematically describe all processes contributing to the creation of deposit.

1.7 Physical processes governing FEBID and mathematical modelling

There are four main processes governing the behaviour of a molecule adsorbed to a substrate's surface upon electron beam irradiation:

- adsorption (physisorption) from the gas phase,
- desorption (both thermal and electron stimulated),
- surface diffusion,
- electron induced dissociation, creating volatile, desorbing moiety and non-volatile (chemisorbed) deposits.

Each of the aforementioned surface processes can be described with certain mathematical terms in differential equation. The following equation, which can be referred to as the fundamental FEBID equation, describes the time dependence of the number of precursor molecules adsorbed on a unitary surface and it takes on the form of [9]:

$$\frac{\partial n}{\partial t} = sJ\left(1 - \frac{n}{n_0}\right) + D\left(\frac{\partial^2 n}{dr^2} + \frac{\partial n}{r\partial r}\right) - \frac{n}{\tau} - \sigma f n \quad (1.1)$$

where

n – number of precursor molecules per unit of area,

n_0 – number of adsorption sites (maximum number of precursor molecules that can adsorb),

J – flux of incoming precursor molecules,

τ – average residence time (or desorption time),

σ – cross-section of electron induced dissociation,

f – electron flux,

D – coefficient of diffusion of molecules on a chosen surface,

t – time,

r – distance from the beam's centre,

s – sticking coefficient.

The first term, $sJ\left(1-\frac{n}{n_0}\right)$ describes the adsorption of molecules from the gas phase on the substrate's surface. These molecules, which reach the sample's surface, are represented mathematically by a flux J. The adsorption here is physisorption, where no permanent bonding between non-dissociated precursor molecules and the substrate is considered. The adsorption in the basic FEBID model follows Langmuir isotherm. Maximum equilibrium coverage $\theta = \frac{n}{n_0}$ established between adsorption and desorption cannot be greater than 1 and resembles a complete physisorbed monolayer. Other molecules cannot physisorb on top of physisorbed molecules.

The second term, $D\left(\frac{\partial^2 n}{dr^2}+\frac{\partial n}{r\partial r}\right)$, describes surface diffusion. Diffusion follows a concentration gradient. Adsorbed molecules will travel from regions with high concentration to places with less molecules per unitary surface. The speed of diffusion is represented by its surface coefficient D. Its values depend on the type of substrate and adsorbing molecule. As diffusion represents the mobility of molecules on the substrate's surface, it can be enhanced or quenched by the temperature of the surface. However, in FEBID modelling this dependence has not been vastly explored. Nevertheless, diffusion can play important role in the growth of the deposit, as it delivers new molecules in the case of constant depletion with no proper gas phase replenishment, e.g. during the stationary exposure of one spot. It is worth noting that diffusion in this model describes only surface transport of precursor molecules. The diffusion of dissociated species, although evidenced as feasible to play an important role [34, 36], is not considered.

Adsorption and diffusion are processes which "deliver" new molecules on a unitary surface, increasing their surface concentration. Two other processes, desorption and electron induced dissociation, act in an opposite way, lowering the number of precursor molecules per unitary surface area. In the case of FEBID, both thermal and electron stimulated desorption (TD and ESD, respectively) may play a role, as mentioned in the work of van Dorp [84]. Nevertheless, in the continuum FEBID model, desorption is a temperature controlled process, represented by an average residence (or desorption time τ [2, 85]. It's temperature dependence is expressed with the exponential function:

$$\tau = \tau_0 \exp\left(-\frac{E_0}{kT}\right) \quad (1.2)$$

where T is substrate's temperature and k is Boltzmann's constant. E_0 stands for the activation energy for desorption. τ describes only desorption of physisorbed precursor molecules. In the basic FEBID model, dissociated, volatile moieties are assumed to desorb immediately, without any chance of being dissociated again and co-deposited.

The last term represents electron-induced dissociation of physisorbed molecules. It linearly depends on two factors: flux of electrons, which, to some extent can be controlled and on cross section for dissociation, which depends on the energy of electrons and molecule type. In most of the cases, the electron flux can be described with a Gaussian function, representing the shape of used e-beam. Gaussian function parameters, such as amplitude and full width at half maximum (FWHM), can be either calculated or directly measured (e.g. with the well-known knife-edge method). The σ value used in this model is the total cross-section, which is the sum of cross-sections on different electron-induced processes. Estimating cross-sections for dissociation is still an ongoing challenge within the FEBID community, as there have only been a few compounds, for which theses values have been measured or calculated [86]. The most frequently used method involves measuring the interactions between electrons and gaseous precursor. This method is very selective and allows for differing between cross-sections on various dissociation pathways. There are four main dissociation channels, each basing on different physical effect and having different outcomes [87].

a) Dissociative electron attachment (DEA)

   It is a resonant process with the highest cross-section in the range from millielectronvolts up to single electronvolts. The electron attaches itself to the compound, creating excited non-stable meta-ion. If the energy of the attached electron exceeds the dissociation threshold, the ion will fragment into two parts: a negatively charged specie and a neutral, usually chemically active radical. It can be depicted with the following chemical equation:

$$AB + e^- \rightarrow AB^{(\ddagger)-} \rightarrow A^{(\ddagger)-} + B^{(\ddagger)} \quad (1.3a)$$

b) Dissociative ionisation (DI)

   It is a non-resonant process, where energy transfer from electron to molecule upon collision leads to removal of an electron from the molecule. The energy has to be greater than the ionisation energy of the respective molecule. The energy exceeding the ionisation threshold will be further transferred to created cation, resulting in its excited state (vibrationally and/or electronically). The excited state may lead to the

fragmentation of the ion into ionised and neutral parts. The maximum cross-section for DI is around 50 – 100eV. DI can be described with the chemical equation:

$$AB + e^- \rightarrow AB^{(\ddagger)+} + 2e^- \rightarrow A^{(\ddagger)+} + B^{(\ddagger)} + 2e^- \quad (1.3b)$$

c) Neutral dissociation (ND)

Similarly to DI, this dissociation channel is characterised by an energy threshold, i.e. incoming electrons should have energies higher than the dissociation energies of the certain bonds. The energy transfer causes excitation of atoms of the molecule. This excited molecule can then fragment, forming two neutral species. Neutral dissociation is not supposed to lead to as extensive fragmentation as DI [87]. However, quantum mechanics calculations suggest that in case of the $Pt(PF_3)_4$, it may play an important role, as excitations from bonding to antibonding states results in direct dissociation [88]. The authors of the cited study state that this conclusion may also apply to other FEBID precursors. ND is a very challenging process to investigate, as measurement methods, like mass spectrometry, require species to be charged to detect them and post-ionisation creates the risk of further dissociation of volatile moieties and therefore blurring the real image of the pathway. ND is represented by the following chemical equation:

$$AB + e^-(E_1) \rightarrow [AB]^* + e^-(E_2 < E_1) \rightarrow A^{(\ddagger)} + B^{(\ddagger)} \quad (1.3c)$$

d) Dipolar dissociation (DD)

The first stage of dipolar dissociation is similar to ND, i.e. incoming electrons electronically excite the molecule. If the transferred energy is high enough to overcome the Coulomb force between the positively and negatively charged parts of the molecule, a cation and an anion are created. The energy threshold for this process is higher than those of DEA and ND, however, lower than for DI. DD is most probably not a very efficient process [87], however it can play a role in electron stimulated desorption of $Fe(CO)_5$ ions [89]. DD follows the below-mentioned chemical equation:

$$AB + e^-(E_1) \rightarrow [AB]^* + e^-(E_2 < E_1) \rightarrow A^{(\ddagger)+} + B^{(\ddagger)-} \quad (1.3d)$$

Sticking coefficient is the most enigmatic factor from the presented model. It takes a value from 0 to 1 and represents the probability with which the molecule that flies towards the substrate from the GIS will "stick" to the surface. In contrast to thin film CVD and PVD processes, where the sticking coefficient defines the ratio of deposited versus impinging atoms/molecules, "sticking" in the FEBID model means the situation, that a molecule physisorbs for an average residence time τ before it desorbes. However, such a "physisorp-

tion" coefficient is barerly measurable and, to the best of my knowledge, nobody has ever published any value of it for any precursor-substrate combination. In most cases of FEBID modelling, it is either set to 1 or combined with *J*. Considering this, in this work the sticking coefficient will be set to 1 in all future analysis. This also includes the situation that no molecule physisorbs (its residence time on the surface will then go towards zero $\tau \to 0$).

The fundamental FEBID equation, in its general form, is a partial second order differential equation. Thus, the time-dependent, analytical solution of such an equation exist only in special cases. The simplest solution of the equation is for steady state, $\frac{\partial n}{\partial t} = 0$, without diffusion and under continuous spot exposure of the beam.

$$n = \frac{J}{\frac{J}{n_0} + \frac{1}{\tau} + \sigma f} \quad (1.4)$$

Continuous spot exposure is employed to grow vertical columns (pillars) in FEBID experiments. In other experiments, the beam is scanned over the area, spending on each pixel certain dwell time. When the beam is not irradiating a pixel, the depleted layer of adsorbed precursor molecules have a chance to be replenished, where the refreshment time is the time between each two exposures of one spot. In case of dwelled exposure, a time-dependent solution has to be used:

$$n = Ce^{-kt} + B \ (1.5)$$

where the parameters will have different values for the moment of exposure and for the refreshment. For the dwell time, where the certain area is exposed to the beam, the parameters are equal:

$$k = k_d = \frac{J}{n_0} + \frac{1}{\tau} + \sigma f \quad (1.6a)$$

$$B = B_d = \frac{J}{k_d} \quad (1.6b)$$

$$C = C_d = (B_r - B_d)(e^{-k_r t_r} - 1)(e^{-k_r t_r} e^{-k_d t_d} - 1)^{-1} \quad (1.6c)$$

where the electron beam is not irradiating a spot, and the layer of precursor molecules is refreshed and the parameters of the solution take the form of:

$$k = k_r = \frac{J}{n_0} + \frac{1}{\tau} \quad (1.6d)$$

$$B = B_r = \frac{J}{k_r} \quad (1.6e)$$

$$C = C_r = (B_d - B_r)(e^{-k_d t_d} - 1)(e^{-k_r t_r} e^{-k_d t_d} - 1)^{-1} \quad (1.6f)$$

1.7.1 Important model parameters:

One of the most important parameters, which is defined in FEBID modelling, is the growth rate. The vertical growth rate in units of dimension per time can be defined as an integral:

$$R = Vn(r) \int_0^{Ep} \sigma(E) f(r, E) dE \cong Vn(r) \sigma f(r) \quad (1.7)$$

where

V is the volume of the deposited molecule.

By integrating the growth rate over time (from 0 up to total exposure time) and spatial dimension, it is possible to calculate the theoretical shape of the deposit. The dependence of growth rate on the exposure (dwell) time and beam parameters is used in 3-BID, the FEBID CAD software, to create calibration files and estimate the total deposition time [90].

For pulsed-exposure deposition, an average growth rate per dwell time t_d can be defined as:

$$R = \frac{V \sigma f}{t_d} \int_0^{t_d} n(t) dt \quad (1.8)$$

Another parameter, connected with the shape of the deposited structure, is the resolution parameter, defined as the ratio between the FWHM of the e-beam and of the deposited structure (equation 1.9). This ratio is properly defined for dot deposits having an aspect ratio close to 1. It also applies to the tip region of a growing 3D deposit.

$$\varphi = \frac{FWHM_B}{FWHM_D} \quad (1.9)$$

where B and D indices refer to the beam and deposit, respectively.

The resolution parameter is associated with the deposition parameters by scaling laws, which describe how different deposition regimes influence the deposit's shape. This effect has been

comprehensively elaborated in the work of Szkudlarek et al. [91]. In this Thesis, only a brief description of the scaling laws will be presented.

The first scaling law describes the situation, when the deposition is performed in stationary exposure mode, neglecting surface diffusion.

$$\varphi = \sqrt{\log_2(1+\tilde{\tau})} \quad (1.10a)$$

where $\tilde{\tau} = 1 + \sigma f_0 \tau_{out}$ and $\tau_{out} = \left(\frac{1}{\tau} + \frac{J}{n_0}\right)^{-1}$

The second scaling law also considers the stationary exposure situation, however includes the influence of surface diffusion on deposit's shape.

$$\varphi = \sqrt{\log_2\left(2 + \frac{\tilde{\tau}-1}{1+\tilde{\rho}_{out}{}^2}\right)} \quad (1.10b)$$

where $\tilde{\rho}_{out} = \frac{2\sqrt{D\tau_{out}}}{FWHM_B}$

The third scaling law can be used in the case of pulsed exposure, with a dwell time of t_D, without surface diffusion:

$$\varphi = \sqrt{\log_2\left(2 + \frac{\tilde{\tau}-1}{1+\bar{t}_D^{-1}}\right)} \quad (1.10c)$$

where $\bar{t}_D = \frac{t_D}{\tau_{out}}$ and τ_{out} is defined the same as shown previously.

Finally, the fourth scaling law, considers both pulsed exposure and surface diffusion:

$$\varphi = \sqrt{\log_2\left(2 + \frac{\tilde{\tau}-1}{1+\bar{t}_D^{-1}+\tilde{\rho}_{out}{}^2}\right)} \quad (1.10d)$$

with the meaning of all symbols is as for the previous scaling laws. This fourth scaling law comprises all previous ones. From the scaling laws it can be determine that in all cases, the highest lateral resolution is obtained when the additive term under the logarithm goes to 0 ($\frac{\tilde{\tau}-1}{1+\bar{t}_D^{-1}+\tilde{\rho}_{out}{}^2} \to 0$ for fourth scaling law). This value can be reached by different means: 1) when the diffusion term is high enough to overcome the rest of the contribution (more molecules are delivered from the areas close to irradiated spot); 2) for very short dwell times (the molecules can be properly refreshed in the centre of exposed spot, where it is depleted the

most); 3) when the depletion term: $\tilde{\tau} = 1 + \sigma f_0 \tau_{out} \approx 1$, which corresponds to situation when $\sigma f_0 \tau_{out} \approx 0$. Mentioned requirements are fulfilled in the electron (reaction rate) limited regime. The deposition regimes were described in works of Toth et al. [85] and Szkudlarek et al. [91]. In mentioned papers depending on the deposition parameters, four deposition regimes were specified: 1) reaction rate limited (electron limited), where the number of precursor molecules is significantly higher than number of electrons; 2) diffusion enhanced where the deposit's shape and growth rate is determined by a diffusion of molecules from the sides; 3) mass transport limited (adsorbate limited), in which the physisorbed molecules are extensively depleted and the number of electrons is higher than molecules; 4) mixed between the two latter. Each deposition regime can associated with different shape of the spot deposit, as it was depicted in Figure 1.5.

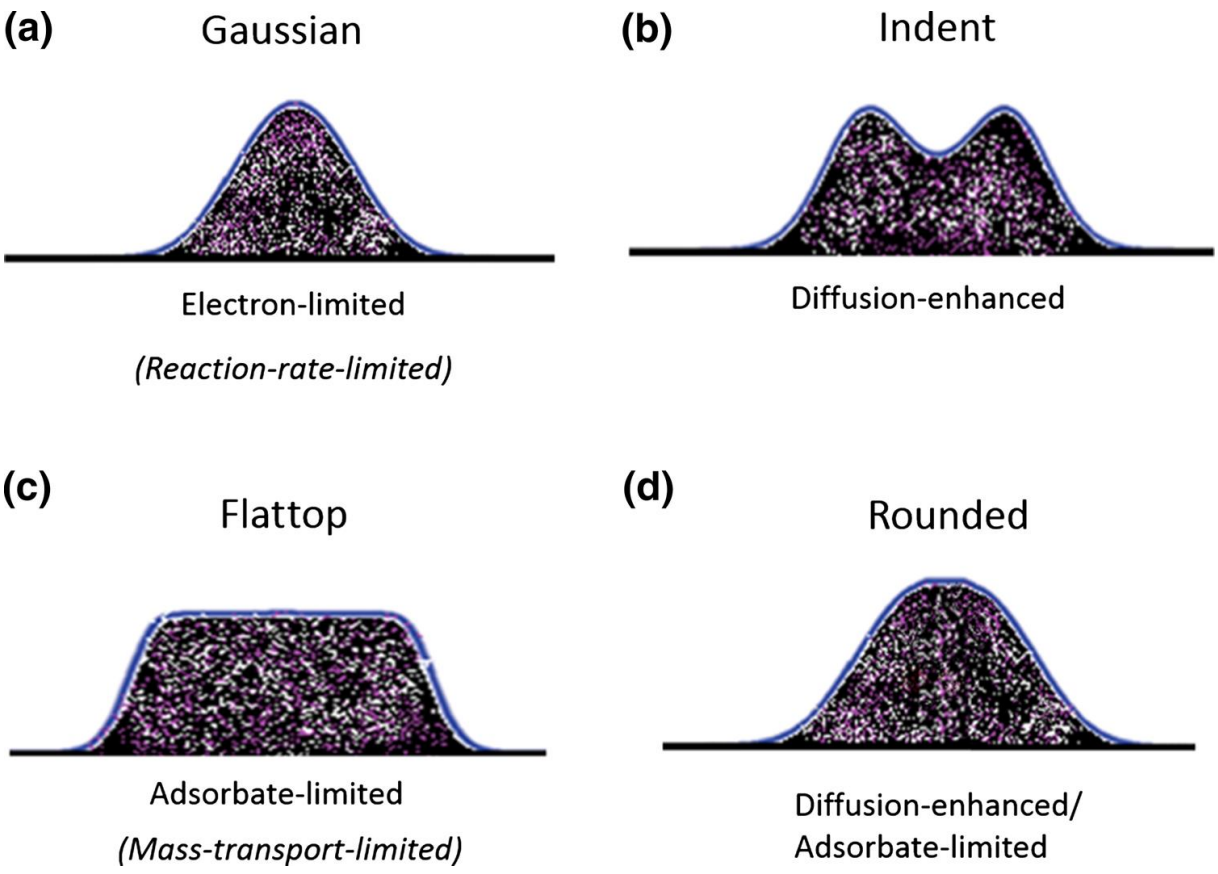

Figure 1.5 Shapes of deposits in different deposition regimes. A) Gaussian-shape deposit made in electron limited regime, b), indent shape deposit made in diffusion-enhanced regime, c) flattop shape deposit made in adsorbate-limited regime and d) rounded shape deposit made in diffusion-enhanced adsorbate-limited regime. Taken from [91].

As can be noticed, the best resolution achieved in electron-limited regime results in a Gaussian-shape deposit. Enhanced diffusion results in the presence of indent in the middle of the deposit. When the number of electrons overcomes the number of adsorbed molecules the shape

of the spot becomes a flat top. Adding the enhanced diffusion to adsorbate limited regime results in a rounded shape spots. Deposition regimes and their dependence on deposition parameters can be clearly visualised using rate (frequency) maps, which will be discussed more in next subchapter and also in chapter 5 of this PhD Thesis.

1.7.2 Rate (Frequency) maps

Rate maps can be used to visualise the FEBID model and were introduced by Sanz-Hernandes and Pacheco [92]. In the original work, they used a term "frequency" instead of rate, but frequency may have suggest a periodical value, which is not the case in the presented research. The fundamental equation is regrouped so that each contribution is represented by a specific rate. In their publication, they also used precursor coverage instead of unnormalised surface density, as is the custom. They extended their model beyond Langmuir adsorption and were additionally able to mathematically analyse the irradiation of multi-layered adsorbates (BET adsorption model). As in this PhD work, the modelling will include only Langmuir-type adsorption, the latter case will not be discussed. Moreover, to facilitate the calculations, in the first approximation, they did not include the rate of surface diffusion.

The basic equation (see Equation 1.1) in terms of rates is (with s=1):

$$\frac{\partial \Theta}{\partial t} = \nu_{ADS}\,(1-\Theta) - \nu_{DES}\Theta - \nu_{DISS}\,\Theta \quad (1.11)$$

where $\Theta = \frac{n}{n_0}$ is the surface coverage.

The first rate, ν_{GAS}, which from this point on will be referred to as the "gas supply rate" within this work, describes how many adsorption events happen in a unit of time on a unitary surface, and it can be expressed as:

$$\nu_{GAS} = \frac{J}{n_0} \quad (1.12a)$$

The desorption rate, ν_{DES}, can be expressed as the inversion of the average desorption time and describes the number of desorption events of precursor molecules from a unitary surface within a unit of time:

$$\nu_{DES} = \frac{1}{\tau} = \nu_0 \exp\left(-\frac{E_0}{kT}\right) \quad (1.12b)$$

In their work on the continuum model of FEBID, Toth et al. also introduced this value, calling it the "desorption rate".

The last frequency used in this model, the dissociation rate, stands for the number of dissociation events of adsorbed precursor molecules per unit of surface and time, and can be expressed as:

$$\nu_{DISS} = \sigma f \ (1.12c)$$

The steady state solution of the equation is similar to the equation (1.4) presented above, and, written with frequencies, has the form:

$$\Theta = \frac{\nu_{GAS}}{\nu_{GAS} + \nu_{DES} + \nu_{DISS}} \ (1.13)$$

The growth rate was also represented in units of 1/s:

$$\nu_{GR} = \frac{R}{Vn_0} = \nu_{DISS}\Theta = \frac{\nu_{DISS}\nu_{GAS}}{\nu_{GAS} + \nu_{DES} + \nu_{DISS}} \ (1.14)$$

The original maps present both the growth rate (in units of inverse time) and the coverage as a function of two normalised process rates. The third rate was kept constant and treated as a normalisation factor. Figure 1.6. presents an exemplary map, calculated using Matlab, based on the publication of Sanz Hernandez and Pacheco [92]. The map shows the case, where stage temperature is constant, which means that the desorption rate is constant. The colour scale refers to surface's the coverage, the lines and assigned numbers represent growth rate normalised to desorption rate.

The case presented on the Figure 1.6, with the desorption rate as the normalisation parameter, can be used in case of constant ν_{DES}, which requires constant substrate temperature. It is also possible to create the same map, but with another rate used as the normalisation factor. A constant gas supply rate describes the situation, where the flux of incoming precursor molecules does not change over time for a given deposition area. A constant dissociation rate means the constant flux of electrons. All mentioned maps can be found in original work of Sanz Hernandez and Pacheco [92] and were presented in Figure 1.7. The acronyms on the maps represent different deposition regimes: MTL stands for mass transport limited, DD for desorption driven and RRL for reaction rate limited (electron limited). The graph on the right shows the linear profiles of $\frac{\nu_{GR}}{\nu_{DES}}$ for two fixed values of $\frac{\nu_{DISS}}{\nu_{DES}} = 0.1$ and $\frac{\nu_{DISS}}{\nu_{DES}} = 10$. For higher $\frac{\nu_{DISS}}{\nu_{DES}}$ ratios, it can be seen that the growth rate also increases.

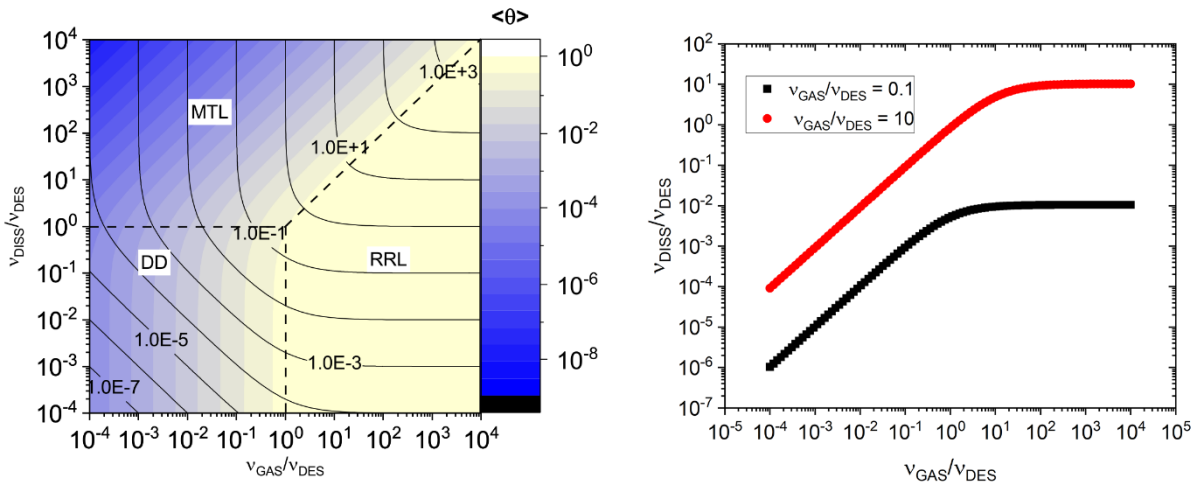

Figure 1.6 a) Example of rate map, plotted for the case of constant desorption rate, based on the map created by Sanz-Hernandez [92]. Dependences between normalised growth rate rate and normalised adsorption rate, plotted for two values of normalised dissociation rate : 0.1 and 10. : MTL stands for mass transport limited, DD for desorption driven and RRL for reaction rate limited (electron limited).

Mass transport limited (adsorbate limited) and reaction rate limited (electron limited) regimes are mentioned in the continuum model papers of Toth [85] and Szkudlarek [91]. The work of Sanz-Hernandez additionally underlines the role of desorption in deposition process. The central point of the map is the place where all characteristic rates are equal. Three regions of the map directly show dependencies between the parameters of the deposition process. An increase in the electron flux caused by either increasing the beam's current or decreasing the beam's FWHM (higher dissociation rate) drives the experiment towards lower coverages of the MTL regime, where the growth rate is limited by the number of adsorbed molecules. With higher molecule fluxes (higher adsorption rates) and lower number of electrons, the deposition process is kept in a reaction rate limited regime, where the whole surface is covered with molecules ($\theta = 1$) and the growth rate is controlled by the number of incoming electrons. Between those two regimes, there is a desorption driven regime, where both fluxes of molecules and electrons are low and the desorption rate is controlling the deposition growth rate.

Figure 1.7 presents two other maps made in Langmuir adsorption regime, reproduced from the work of Sanz-Hernandes et al. [92] : normalised to dissociation rate (denoted as ν_e; left side) and normalised to gas supply rate. These maps can be used to design or better understand experiments, which are conducted in different conditions: with constant beam current and with constant precursor molecules flux.

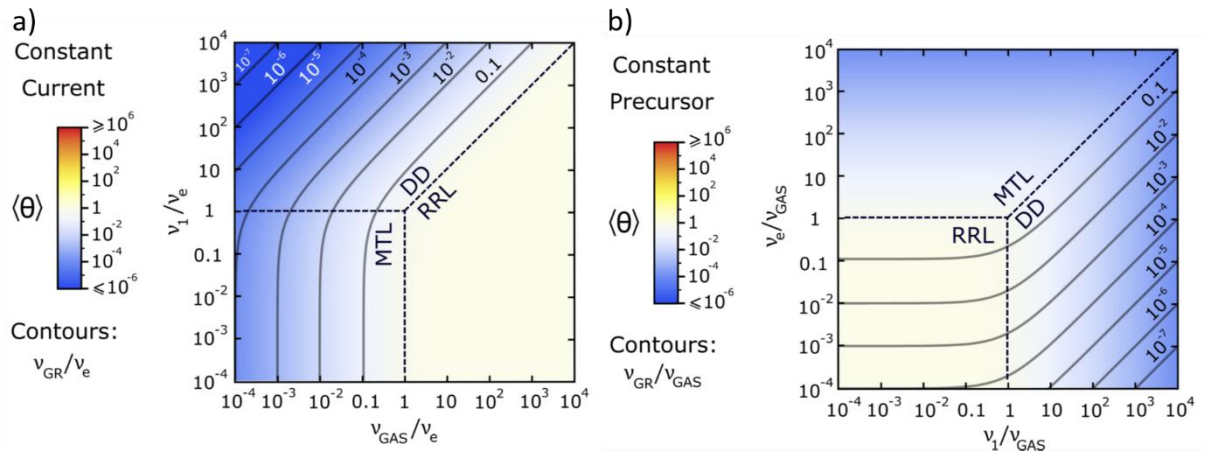

Figure 1.7 Rate maps plotted for two different cases: a) constant flux on electron (constant current) and b) constant precursor flux. Reproduced from [92].

All maps clearly visualise different deposition regimes. Taking example of the left map, it can be noticed that the growth rate increases with higher gas supply (increasing ν_{GAS}) until it reaches a maximum value at the border of reaction rate limited regime. In this regime, the number of electrons is significantly lower than number of adsorbed molecules and it is the limiting factor in the growth of deposit. Opposite situation is depicted on the right map. With growing flux of electrons (increase of ν_e) the growth rate also increase to reach is maximum value at the border of mass transport limited regime, where no matter how many more electrons will arrive to the surface, because the number of adsorbate is a limiting factor.

Although useful for visualisation of deposition regimes, the maps may be difficult to use to analyse the experimental results. To position an experiment on the map, all basic parameters of a used compound, like cross section for dissociation, average desorption time and number of sorption sites has to be known. To address this problem, the new variable has been added to the map in this PhD work: resolution parameter. Moreover, the influence of diffusion on the maps has been discussed. The expansion of the maps and discussion of the consequences can be found in chapter 5.

1.7.3 Two species model

In their work from 2010, Bernau and Utke modelled the FEBID with two different co-injected molecule flows; chamber's residual gas and FEBID of $Co_2(CO)_8$ [40]. Background gases were modelled using octane as an example of a hydrocarbon. The flux of incoming hydrocarbons was estimated based on the SEM vacuum chamber pressure. The schematics of the experiment were depicted on Figure 1.8.

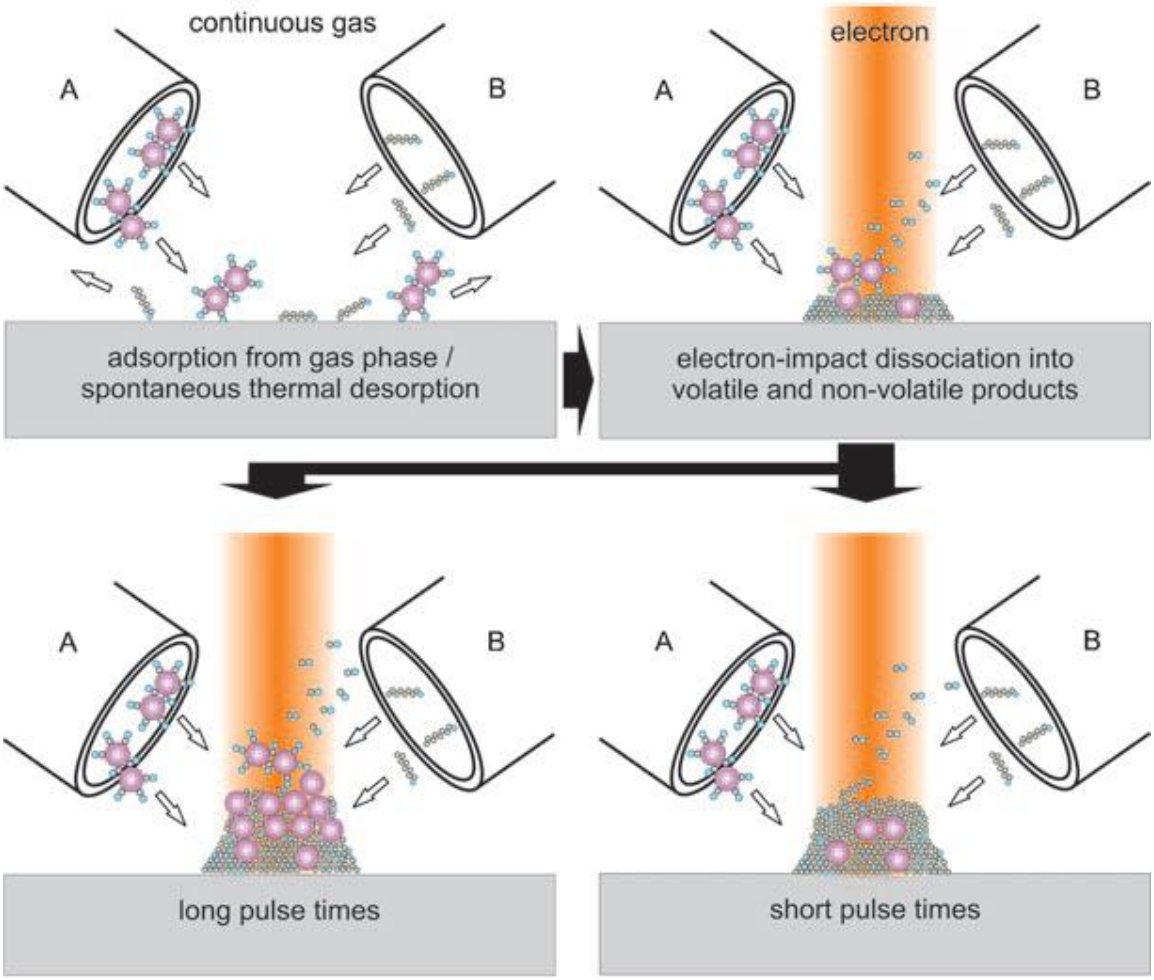

Figure 1.8 Schematics of the experiments performed by Bernau et al., where two-source gas supply was used, providing the metalorganic molecules and organic compound. Electron beam irradiation cleaves the ligands in both molecule type. Long dwell time pulses lead to more metal atoms incorporated into the deposit, while short pulses create lower metal content deposits. Taken from [40].

To model the deposition they used two differential equations, describing a system, where incoming precursor molecules are competing over the same adsorption sites. These equations, presented below are a base of two species model:

$$\frac{\partial n_1}{\partial t} = J_1\left(1 - \frac{n_1}{n_0} - \frac{n_2}{n_0}\right) - \frac{n_1}{\tau_1} - \sigma_1 f n_1 \quad (1.15a)$$

$$\frac{\partial n_2}{\partial t} = J_2\left(1 - \frac{n_2}{n_0} - \frac{n_1}{n_2}\right) - \frac{n_2}{\tau_2} - \sigma_2 f n_2 \quad (1.15b)$$

The explanation of the symbols is the same as for the basic FEBID model. The indices marks variables and constants concerning the first (1) and second (2) precursor. The first term of the equation has been changed, compared to the one-adsorbate model to correct the number of available sorption sites by subtracting the places occupied by the molecules of the second precursor. To simplify the calculations, surface diffusion is not considered in two species model.

In this model, which is based on the competition of two co-injected precursors over the same adsorption sites, one of the most important parameters are the average deposition yields of both species. The yields describes the average number of dissociation events during exposure time, given here with t_d.

$$Y_1 = \sigma_1 \int_0^{t_d} \frac{n_1(t)dt}{t_d} \quad (1.16a)$$

$$Y_2 = \sigma_2 \int_0^{t_d} \frac{n_2(t)dt}{t_d} \quad (1.16b)$$

The ratio of these values, given by $Z = \frac{Y_1}{Y_2}$, is directly correlated with the composition of the deposit. Assuming, that specie 1 is the precursor, dissociating ideally (all ligands are cleaved and desorb from the surface and the metal atom is deposited) and the second is some adsorbing organic contaminant, the metal content in the deposit can be described and precisely predicted. Furthermore, by tuning the deposition parameters, such as the molecule flux or dwell time, the metal content of final deposit can be controlled.

1.8 Basic characterisation methods used for structures deposited with FEBID

The mathematical description of FEBID is very important, however to properly understand all the surface processes, it is important to also characterise the deposited material. In this section, the most frequently used characterisation methods will be discussed, both their advantages and disadvantages.

The standard tool used in this study for both structure deposition and analysis is scanning electron microscopy. Every SEM consists of a vacuum chamber, equipped with a moveable stage, electron gun and various detectors, the most common being secondary and backscattered electrons detectors. Often, also energy and/or wavelength dispersive spectroscopy (EDX and WDS, respectively) detectors are available to measure the composition of the samples [30]. From the point of view of microscope performance, especially its resolution, the type of electron gun is very important [93]. The best resolutions are achieved using cold-cathode field emission guns (FEG's), where the spot size can be narrowed down to even single nanometres [2, 3]. The other type of a FEG is a Schottky FEG . It does not offer such brightness as the cold cathode one, however, it can work at lower vacuum [94] and the newer systems can achieve very high (single nanometres) image resolution [95] . In the context of deposition, the size of the beam is a crucial parameter, when manufacturing structures in the range of single

or tens of nanometres [2]. From scaling laws, we can see that the FWHM of the structures cannot be smaller than the FWHM of the beam, therefore more the electron beam is focused, the smaller the structures can be deposited [91]. However, there is a certain risk connected with using this type of electron gun to deposit novel precursors for FEBID. FEGs require ultra-high vacuum (at least in the gun compartment) and they are sensitive to injected gases and other contaminants. The vapour pressure and other gas phase thermodynamic properties of potential precursors are often not known prior to first deposition experiments, hence they can potentially be harmful to the equipment. Most of the compounds presented in this study were deposited using Hitachi S3600 (Hitachi, Japan), equipped with a thermionic-emission tungsten filament electron source. The resolution of thermal emission sources is not as good as FEG's or Schottky FEGs, however, their construction is simpler and it is easier to exchange broken electron source [96]. The sources are also considerably more cost-efficient. Their wide spot size is not a problem, as bigger structures are preferred for elemental composition measurements, which are crucial part of research with novel precursors. Further information regarding compositional analysis is provided in the following section.

1.8.1 Composition characterisation

Composition analysis of deposited structured is one of the key elements of researching novel precursors for FEBID. The chosen analytical method should be non-destructive, quantitative and relatively fast and easy to use. These requirements are fulfilled by methods based on analysis of characteristic X-rays emitted from the sample due to excitation [97]. Energy dispersive X-ray spectroscopy (EDX or EDS) is a method, which utilises the electron beam from a SEM to excite atoms from an irradiated area [98]. The detector (e.g. solid state Si), registers incoming X-rays, both Bremsstrahlung and characteristic X-rays, generated from the irradiated area through the de-excitation of atoms. The energies of the registered characteristic radiation depends on the differences between certain energy levels in irradiated atoms. As these values are specific for each atom, they allow to identify the elemental composition of the measured material [98]. The registered X-ray signal is represented as a graph of intensity versus energy, usually in eV. The plot is usually composed of a Bremsstrahlung background with high intensity peaks at energies of characteristic X-rays generated from the elements present in the investigated sample. As the peaks have certain dimensions (amplitude and FWHM), it may happen that two peaks overlap. This situation usually occurs, when the difference between two energy levels in atoms of one element (e.g. between K and L shells) is similar to the difference between different energy levels (e.g. L and M shells) in atoms of another ele-

ment from the same sample [99]. When there is only partial peak overlapping, it is possible to recognise both lines and even quantify the spectrum, using peak deconvolution algorithms. However, this is not always possible and peaks from two different atoms cannot be separated. A typical EDX detector has a spectral resolution allowing to distinct characteristic lines 100-125 eV apart from each other [100].

When it is not possible to distinguish individual X-ray peaks due to overlapping in EDS, it is necessary to find another composition analysis method. One such methods that's physical background is similar to EDS is wavelength dispersive X-ray spectroscopy (WDS) [98]. The difference between these two techniques lies in the detection method. WDS equipment uses different detectors and the obtained spectra are resolved using wavelength of the registered X-rays, not their energy (although commonly-used systems allow also for energy representation). WDS spectra have much better spectral resolution, allowing to differentiate peaks that are only separated by 50 eV on the energy spectrum. Figure 1.9 presents the EDX spectrum of Ru-C sample, in low energy range with overlapping CK and Ru M lines and WDS spectrum of the same sample with both lines resolved. The disadvantage of WDS is much longer measurement time then EDX and a much narrower energy range registered during one run. The WDS signal is registered one point after the other over certain energy ranges (usually no wider than few hundreds up to 1000 eV), resulting in a measurement time in range of few to several tens of minutes. This is a significant drawback, especially while analysing samples sensitive to e-beam irradiation. Moreover, unwanted simultaneous deposition of residual gases from the analytical microscope chamber may influence the result of measurement. EDS measurement of the full range between 0 eV and primary electrons' energy takes usually no more than one to several minutes [99].

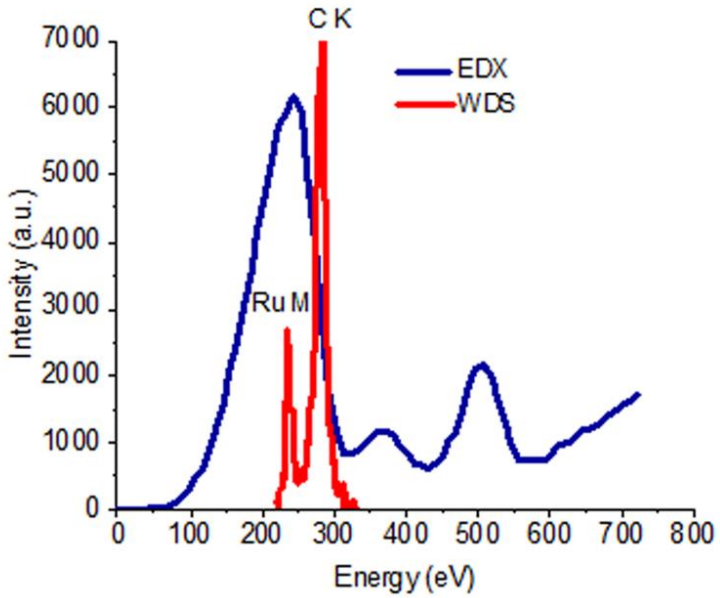

Figure 1 9 EDX and WDS spectra recorded for energy regions from 0-800eV (EDX) and 222-330 eV (WDS) on the sample containing Ru, C, O and Br. In EDX Ru M and C K lines overlap, giving one, blurred peak. Taken from supporting information from Jurczyk et al.[101].

1.8.2 Quantification of EDS and WDS spectra

Both EDS and WDS are quantitative methods, where the quantification of a spectrum is based on the intensity of the peak. The intensity is the area under the peak, calculated as a definite integral of the peak curve, after subtraction of the background curve. The background curve is usually estimated as an interpolation between known points from the background. In modern software, these points are automatically recognised and can be corrected by the user. The calculated intensity is then compared to the intensity of the same peak from a standard sample, giving the so-called k-ratio, as shown in the following equation:

$$k - ratio = \frac{I_{measured}}{I_{standard}} \quad (1.17)$$

The ideal standard should contain the same elements as the investigated sample, but in known amounts. It should be measured in the same conditions as the sample, meaning the same beam acceleration voltage and current. In some SEMs it is hard to set the exact same current values for two separate measurements which are not happening one right after another, therefore the spectrum should be normalised using the value of the current (or some derivate values, like number of incoming electrons in one second). In many EDX systems it is possible to performed so-called "standardless" quantification. This method uses the same fundamentals and

formula 1.17 for calculating the k-ratio, however, it uses the intensities of pure element standards, measured under the same condition and stored in built-in databases [99].

To calculate the amount of a given element in weight percentage, the k-ratio should be corrected. There are two main correction methods, i.e. ZAF and $\varphi\rho Z$. The first one corrects signal intensity alterations due to atomic number of measured element (Z), self- absorption of X-rays in the material (A) and emission of secondary X-rays due to self-absorption (F) [99]. The second uses X-ray take-off angle values (φ), the density of the material (ρ) and atomic number of the element (Z) [97]. The amount of element in atomic % can be calculated using the molar masses of all elements in the sample:

$$x_i(at\%) = \frac{\frac{w_i}{M_i}}{\sum_j \frac{w_j}{M_j}} \quad (1.18)$$

Where: $w_i = k - ratio(i) \cdot [corrections]$.

To be sure that all elements are properly quantified, the intensities of the lines should be saturated. The beam energy should be set approximately at double the energy of the last line we want to use to quantification. Furthermore, the EDX assumes that the elements are homogenously distributed in the sample. Both of those effects cause, that successful EDX and WDS analysis of thin or composite samples is challenging [99].

1.8.3 Thin film analysis

Thin films and nanostructures are not trivial samples from the perspective of EDX and WDS measurements. As was mentioned, the beam has to have a certain acceleration voltage to properly excite the atoms we want to measure. Acceleration voltage, alongside beam size, are crucial parameters, for measuring micro- or nano-structures and thin films. The incoming primary beam excites the atoms from the measured material in a certain volume. This volume, referred to as the excitation volume, depends highly on the energy of the primary electrons [97]. With increasing beam energy, the excitation volume also increases. For proper quantification, the spectrum volume of the measured sample must be bigger than the excitation volume. This is easily achieved for bulk samples, however, it is challenging for microstructures. In the case of FEBID, thick and planar samples should be chosen for EDX and WDS measurements. However, the thickness of the sample is often too small and a signal from the substrate is registered. In such cases, it is still possible to correct for the thin film effects using specialised software. In this work, the results were corrected using StrataGEM (SAMx,

France) [102]. The program is based on the k-ratio of elements, density of the examined material and the used acceleration voltage to correct quantification of the deposits. The program uses a $\varphi\rho Z$ method to correct k-ratio. To properly quantify the EDX spectrum with help of StrataGEM it is useful to know the thickness of the material. This can be obtained using atomic force microscopy (AFM).

1.8.4 Characterisation of deposit thickness and roughness

Atomic force microscopy is a basic method to measure thickness, shape and roughness of planar structures. A typical AFM works either in full contact or semi-contact (tapping) mode. As full contact could destroy some samples (especially carbon-rich structures), the latter was used in this work.

There are several artefacts that may occur during AFM measurements, which should be considered. The first and most common one comes from the placement of the sample on the holder. In some systems, the sample is placed on top of a sticky carbon tape on a standard stub. In such a case, the sample can be slightly tilted, which is sometimes not noticeable to the naked eye. This tilt causes that AFM scan to look like it was higher on one end. Fortunately, this artefact is quite easy to correct. In most analysis software (like Gwyddion, used in this study) the tilted background can be removed by subtracting a linear function from each line of the AFM map. Another artefact is caused by so-called creep of the scanner. When the tip encounters a steep edge, especially with high scanning speed, its vertical position readout will show higher values than the actual height of the step. It is caused by a slow response of the scanning unit to the fast and significant changes of position the tip (see, Figure 1.10.a). To correct this artefact, the scanning speed should be reduced. The shape of the tip can cause artefacts common for all AFM measurements, e.g. blurring of the sharp edges and widening of the measured structure. These effects can be noticed while scanning over both small trenches or vertical, steep-edge structures, see, Figure 1.10. b and c. These artefacts play a role in estimating of the deposit's volume, which is crucial to properly calculate volume loss during purification procedures. As these artefacts do not influence the deposit's thickness, it is possible to compensate for them, at least for planar structures, by using the measured thickness and angle of the tip cone. In addition, commercially available software provide ways to correct for this artefact, based on the shape of the tip.

Old, frequently used tips may be deformed, e.g. bent, split in two or shape lose. In all cases, such a tip cannot be used to properly image and analyse surface topography. The effects of

badly shaped tips on a scan profile are presented in Figure 1.9 d and e. To avoid artefacts from compromised tip shapes, the tips must be checked, using a standard sample. For this work, the tip quality was checked every time characteristic artefacts (like doubled structures for split tip) were noticed on the surface. Moreover, a routine checkout was performed every few weeks.

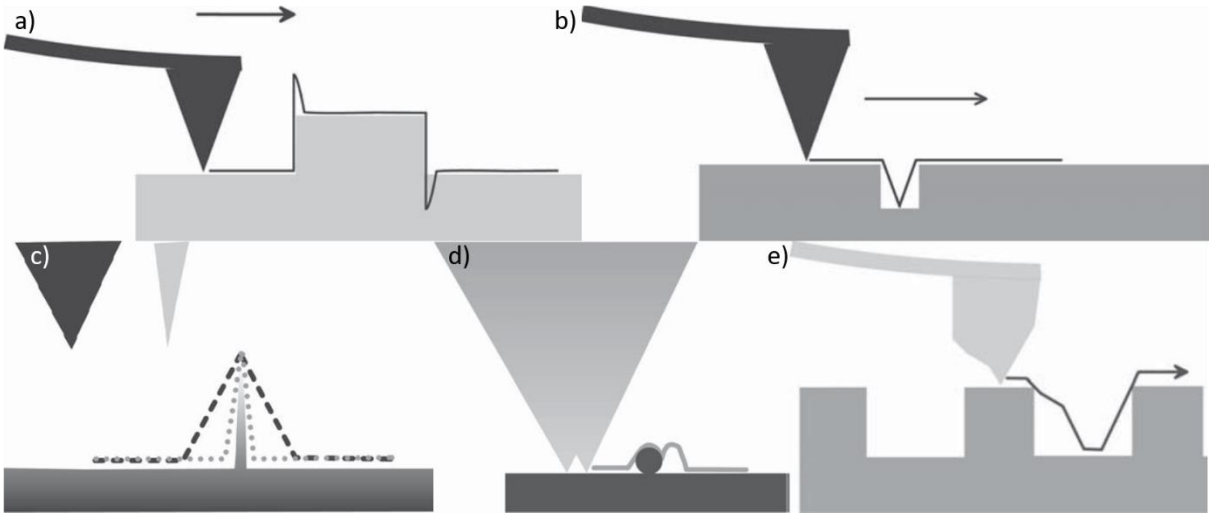

Figure 1.10 Schematics of the origin of common AFM artefacts. a) Creep artefact; b)blurring edges of the trench; c) widening sharp high-aspect ratio structure; d) split tip artefact; e) bad tip shape artefact. Compiled, basing on [103]

1.8.5 Characterisation of thermal properties of the precursors: thermogravimetry

Thermogravimetry is a measurement method, which allows for high precision measurements of mass changes in the sample induced by the heat [104]. It is vastly used to investigate different phenomena, such as evaporation, sublimation, sorption of gases or thermal decomposition, with the creation of volatile species. In addition, thermally-induced chemical reactions [105], especially oxidation[106] or oxidative decomposition [107] can be tested using this technique. Most frequently, TGA is used at atmospheric pressure, with a flow of protective gases, like nitrogen. TGA in vacuum was used to study oxygen sensitive materials [108, 109] or early stages of oxidation of metals [110]. TGA is commonly used to investigate organometallic precursors applied in both chemical vapour deposition (CVD) [111-115] and atomic layer deposition (ALD).

TGA instruments usually consists of high precision balance, placed inside a furnace and connected to a mass readout system. The samples are kept in crucibles made from chemically inert material. In the context of FEBID, TGA can be used as a method for evaluating the thermal properties of precursors. This possibility will be described extensively in chapter 3.1.2.

1.8.6 Mass spectrometry

Mass spectrometry (MS) is a widely used technique allowing for measuring volatile chemical moieties. Using mass spectrometer, all charged species, generated by electron-induced dissociation of the measured compounds can be detected. In the context of studying interaction between the electron beam and organometallic compounds, it is used in gas and condensed phase surface science methods. Both gas and condensed phase methods deliver significant insight to interactions between electrons and compounds used in FEBID.

The first method is based on the irradiation of a cloud of gaseous precursor with monochromatic, usually low energy, electrons [32, 87, 116]. Thanks to the attached mass spectrometers, researchers are able to trace dissociated, charged fragments and determine the cross-sections of various e-beam induced processes, such as dissociative ionisation (DI) or dissociative electron attachment (DEA). However, as there is no substrate involved, this type of measurement neglects any effects directly correlated with the presence of a surface, like adsorption and desorption, and their influence on the purity of the deposited material. If a ligand is cleaved from the metal atom, but does not have enough time to desorb from surface, it may be co-deposited, quenching the purity of the deposit. Moreover, secondary electrons, (SE I and SE II), produced during FEBID by incoming primary beam have a full spectrum of energies and are not monochromatic, which may also influence dissociation pathways.

The second method, based on e-beam irradiation of the condensed layer of precursors in UHV, is more similar to FEBID. On the one hand, the molecules are condensed on a cold substrate and are irradiated with a beam accelerated with voltages between 500 V and 1000 V, which is much closer to voltages of 5 and 25 kV used during FEBID, than mVs and single Vs used in gas phase [117, 118]. On the other hand, the beam used in surface science is much broader (1mm^2 vs hundreds of nm^2 used in FEBID) and less intense than during FEBID. The typical electron dose used during the irradiation of a condensed precursor for a few hours is usually lower than the number of electrons irradiating the same surface within one second of FEBID experiment (see results for surface science measurements [119] and FEBID for the same compound published by Jurczyk et al. [101]). Moreover, to condensate the precursor in UHV, temperatures of around -160 to -170 °C are used, which is significantly lower than room or elevated stage temperatures used in FEBID [120]. Stage temperature significantly influences desorption process, which is crucial in removing cleaved ligands from the substrate. The typical parameters for FEBID and surface science measurements are summarised in Table 1.1.

Table 1.1 Typical parameters used during deposition via using focused electron beam and in surface science studies.

Parameter	FEBID	Surface Science
***U* (kV)**	1 - 20	<1
***I* (nA)**	0.020 - 100	---
***p* (10^{-6} mbar)**	2.0 - 10	0.01 – 0.1
Substrate temperature (°C)	RT - 170	-168
Beam size	<35 0nm (usually ~20 nm)	Up to 1 mm
Electron flux (FEBID)/dose (surface science)	$10^{18} - 10^{20} \frac{1}{\mathrm{cm}^2 \cdot \mathrm{s}}$	$10^{16} - 10^{17} \frac{1}{\mathrm{cm}^2}$

The differences between FEBID, surface science and gas phase measurements are schematically depicted in Figure 1.11.

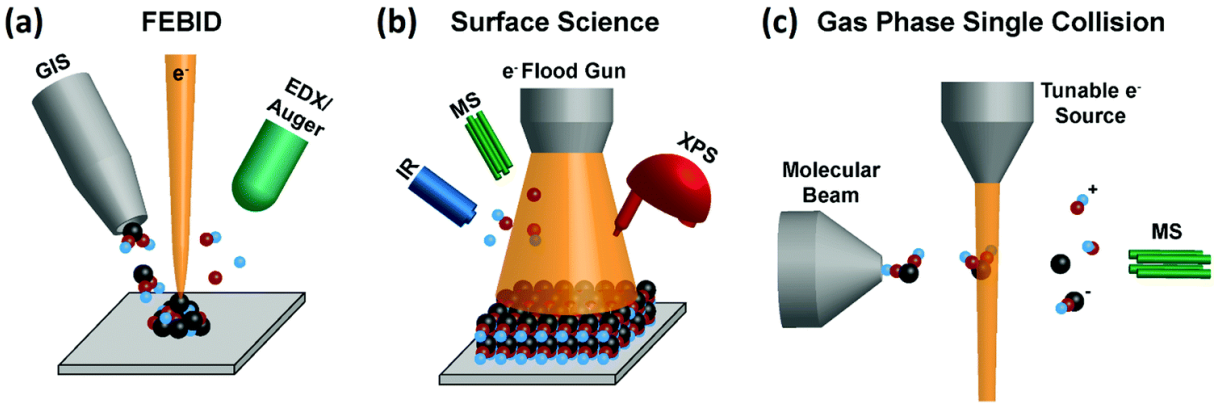

Figure 1.11 Schematics of differences between FEBID (a) and surface science approach (b) and gas phase studies (c). Taken from [43].

Both surface science and gas phase studies do not consider any influence of residual gases within the vacuum chamber. A UHV chamber used for the surface science approach has few orders of magnitude lower pressure, than HV SEM deposition chambers, which means significantly less contaminants adsorbing on the substrate. Although extremely valuable information can be extracted from both gas phase and condensate phase investigation methods on the behaviour of a potential precursor, their applicability is limited. The above-described differences in characterisation and FEBID methodologies do not allow to determine with certain-

ty the dissociation processes occurring during irradiation of physisorbed precursor with a focused electron beam.

One of the MS-related methods worth mentioning in the context of nanomanufacturing methods is focused ion beam secondary ion mass spectrometry (FIBSIMS). It is a destructive, but precise method of measuring elemental composition of a sample. An ion beam is used to sputter material from measured a volume. The sputtered ions are then registered by the time-of-flight (TOF) mass spectrometer, allowing for to determine the chemical composition of a sample [121, 122]. The method is only qualitative due to so-called matrix effects i.e. the dependence of the yield of sputtered ions on the chemical state of atoms from the substrate [123-125]. FIBSIMS can measure concentrations down to hundreds of ppms [122]. By using precisely focused ion beams and detection systems coordinated with an i-beam scanning control, it is possible to create precise elemental maps [122]. By estimating the sputtering rate either by *in situ* or *ex situ* AFM measurements, it is possible to create three-dimensional maps of distribution of elements in the sample. As it is destructive and not-quantitative, FIBSIMS is not commonly used to measure the elemental composition of FEB deposits. Most measurements rely on non-destructive and quantitative EDX (with WDS) and Auger electron spectroscopy (AES). In chapter 5, a new method, based on FIBSIMS is proposed and developed, namely focused electron beam induced mass spectrometry (FEBiMS).

1.9 Challenges and the scope of the Thesis

Despite all the advantages, there are still many challenges concerning the deposition with an electron beam. The most important of them are:

- low purity of deposited structures
- complex and still under-explored physics and chemistry governing deposition process.
- compromised resolution due to parasitic halo deposition

These challenges presently limit the application of FEBID. However, each of these issues comprises very interesting scientific questions, which will be addressed in this PhD work.

This work presents the results of systematic studies on new organometallic precursors for the deposition of metals, which have not been vastly studied before: silver and ruthenium. Furthermore, precursors that require further investigation, like for gold and tungsten, where previous studies have not researched all of the mentioned concerns. The precursors studied in this work allowed for examining the behaviour of different functional groups as ligands under electron beam irradiation.

The investigation of a novel precursor is a long and challenging process, starting with studies of its thermal properties (in case of low volatility compounds), through actual deposition experiments and possible post-purification, and characterisation of the deposited and purified material, and finally using the obtained results to expand and develop theories. The presented results from investigating five precursors from the carboxylate group, two heteroleptic ruthenium complexes, two NHC-based gold precursors and carbonyls, will shed new light on the physics and chemistry governing the process of FEB induced deposition. The precursors were chosen to test a variety of different ligand-metal combinations for metals of high interest in the field of nanostructuring. The performed experiments helped not only to learn more about novel precursor themselves, but helped with understanding the basic principles governing FEBID. Moreover, new analytical methods, such as pre-screening with vacuum TGA and focused electron beam induced mass spectrometry to determine the exact dissociation pathways during deposition with electrons. The obtained results allow to state what are the most valuable chemical groups to be used as ligands for FEBID precursors. Moreover, they help to understand what happens with adsorbed molecules due to irradiation with electron beam under FEBIP conditions.

2. Experimental methods

2.1 Scanning electron microscopy and FEBID

Most of the deposits presented in this work were produced using Hitachi S3600 SEM (Hitachi, Japan). The microscope was equipped with in-house built add-on sub-systems. An in-chamber gas injection system, made with chemically inert stainless steel no 1.445, equipped with a heating system, and fine needles, which could be mounted at the end of the nozzle to reduce the flux of the precursor. GIS heating was made using a Teflon heating container with a resistive wire wrapped around and connected with control system. The temperature of the GIS is monitored using a K-type thermocouple mounted between the outside wall of the GIS and the inner wall of the heating container. The thermocouple was electrically insulated using a thin layer of Teflon tape. The control over the heating consists of a hardware, a power supply connected with a feedback loop system, which adjusts the heating to reach and maintain selected temperature, and a labview software to program the temperature and adjust the proportional, integral and derivative (PID) controller's parameters when needed. The GIS was mounted on a 3-axis stage, allowing for precise positioning over the substrate. If it was not stated otherwise, the distance between lower edge of the GIS nozzle and the substrate was maximum 200 μm and the deposition area was around between 100 and 200 μm away from the upper edge of the GIS nozzle. For precursors, which required GIS heating, the deposition process was started not earlier than 10 minutes after reaching the GIS temperature set-point to stabilise the flow of precursor molecules. It is also possible to attach an external gas injection system to our SEM. This GIS injection system consisted of glass reservoir connected to a tubing system and a final needle. It had no heating system, so it could be used only for experiments with high vapour pressure compounds.

An additional subsystem available in the FEBIP microscope was a home-built heating stage. The stage is based on a ceramic heating element from Boralectric, connected to an external laboratory power supply. The stage temperature was monitored with thermocouple, and controlled by adjusting the voltage and current of the power supply. The sample was put not directly on the ceramic heater, but on the top of a copper piece. The piece had a flat surface and, as Cu is a good heat conductor, it was there to properly deliver the heat to the sample. Moreover, the thermocouple was mounted in a small hole in the copper piece. The sample was clamped directly on top of the piece using copper clamps. The size of the stage allows for using only one substrate at a time. For the experiments which required extensive stage heating (ramping from RT to 120 – 150 °C or more), the FEBID was performed not earlier than one

hour after reaching the stage temperature set-point to avoid thermal drifts. In case of silver carboxylates, the stage heating was usually switched on a night before the experiment and stabilised overnight. The stage heating was performed always prior to the GIS heating. Usually, 5 – 10 minutes spot deposition was performed prior to deposition of other structures to examine if there is a thermal drift. For experiments, which did not require stage heating, standard aluminium or stainless steel SEM stubs with copper clamps were used.

The standard substrates used for FEBID were Si <100> pieces with a native oxide layer, doped with boron to provide proper electrical conductivity in the SEM. Prior to FEBID, the samples were cleaned in ultrasonic bath using an acetone (5 minutes) and two times isopropanol (2 x 5 minutes). For each cleaning step the substrate was placed in a separate beaker, which was used only for this exact solvent. For four-point probe electrical conductivity measurements special substrates were used, see chapter 2.7.

The SEM was equipped with a pumping system containing a rotary backing pump and turbo molecular pump. The chamber pressure during experiments was monitored using a wide range gauge, connected with a pump control system (Edwards, UK). Typical background pressure was in the range of $1 - 1.2 \cdot 10^{-5}$mbar.

The electron beam was controlled using an external patterning system provided by Xenos (Xenos, Germany). The system consisted of a blanker and hardware to control the beam movement. It was connected with a software, which allowed for defining patterns and exposure parameters. The software uses a specific programming language. It is possible to define the pixel dwell time, point pitch, number of passes and patterning strategy: spiral or X and Y meanders. Additionally, basic programming elements, such as "for-loops" or pattern arrays are available. The software expose the patterns subsequently, one after another. Before each run, the exposure origin has to be mapped, to correlate SEM coordinates with the control software coordinates. The SEM Hitachi S3600 with external add-ons is depicted in Figure 2.1.

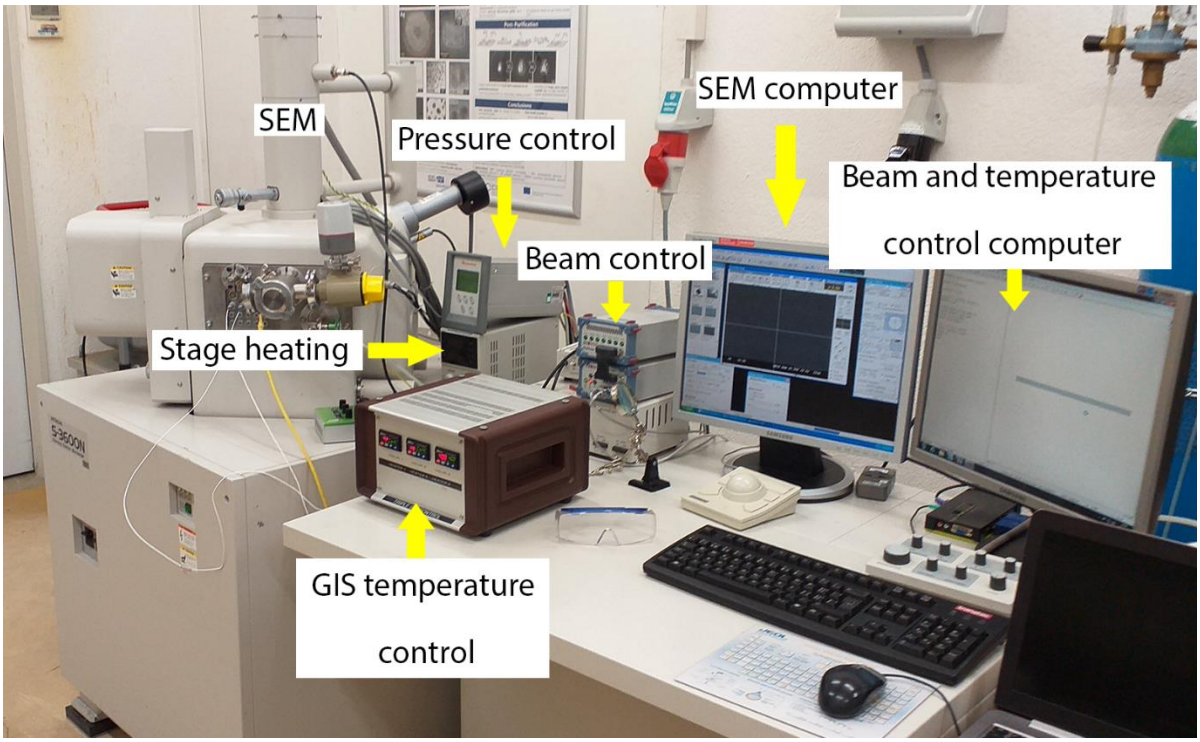

Figure 2.1 SEM Hitachi S3600 used for FEBID experiments, with labelled external subsystems.

High-resolution SEM images of the fabricated samples were mostly obtained using a Hitachi S4800 SEM (Hitachi, Japan) in secondary electron detection mode. Others were taken using a Mira3 SEM (Tescan, Czech Republic) and a Lyra3 dual beam system from the same producer.

2.2 Transmission electron microscopy

Transmission electron microscope (TEM) was frequently used to obtain high magnification images of the samples presented in this study. Modern TEMs can provide atomic-scale resolution in high-resolution imaging mode. In FEBID, they are often used to investigate the crystalline structure of deposited material vis electron diffraction methods. In this work, a JEOL JEM 2200FS TEM (JEOL, Japan) was used to both image and collect diffraction patterns of the produced samples. The operating acceleration voltage was set to 200 kV. Proper TEM sample preparation is crucial, as they have to be transparent for the high-energy electron beam to pass through. In this work, the measured structures (usually lines and spots) were directly deposited on the top of SiNx 50 nm film, purchased in the form of commercially available TEM grids (Norcada, Canada and TedPella, USA).

TEM measurements in chapter 3.3 were performed using FEI Titan TEM (ThermoFisher, USA). A lamella was cut out of one of the square deposits using GA^+ FIB from Lyra3 from TESCAN. Prior to ion beam cutting, the deposit was covered with protective layers of Pt (first

deposited with e-beam, and the second with Ga^+ ions) then thinned and polished and placed on copper TEM grid.

2.3 Compositional analysis: EDX and WDS

The composition of the deposited structures was measured using various EDX detectors. Silver and gold structures were measured using an EDX silicon(Li) detector from EDAX, attached to the Hitachi S4800 SEM. The detector had to be cooled down using liquid nitrogen at least 2 hours prior to operating. The results were analysed using EDAX Genesis software. A typical standardless quantification procedure included identification of the peaks, fitting the background signal and peak integration (with the fitted background being automatically subtracted).

As RuM and CK, as well as WM and SiK peaks have similar energies, they overlap in the EDX spectrum, compositions of these deposits were measured with combination of EDX and WDS, using a silicon drift detectors from EDAX, cooled down with Peltier elements, attached to the Lyra3 dual beam system or Mira3 SEM. The EDX spectra were analysed using EDAX team software. The spectra of the lines measured with WDS (RuM and CK, for Ru deposits, and WM and SiK for W deposits) were analysed using OriginLab Origin software, via the "peak analyser" option. This option enables recognising of the peak's centre, background subtraction and peak integration to obtain the peak's intensity. Prior to that, WDS spectra have to be normalised using the beam current measured in a Faraday Cup, to avoid the influence of small current changes on the intensity of the peaks. The intensities of peaks measured on deposits were divided by intensities of peaks coming from pure metal standard samples (purchased from Ted Pella). The standards were measured and analysed in the same manner as the deposits. Intensities of peaks from samples and standards were used to calculate k-ratios. In the case when on peak overlapping occurred, the k-ratios for other elements were measured with EDX.

For all presented deposits, the beam energy for EDX and WDS measurement was set to be at least twice the energy of last the analysed line to ensure. In most cases, deposits presented in this PhD work were so thin that the signal from the Si background was visible in the obtained spectra. When this occured, the results were corrected with SAMx Stratagem[102]. The software is based on the k-ratio of elements from the measured sample (both from deposit and substrate), the measurements beam's acceleration voltage, the take-off angle of the X-rays, and the type of measured lines. It is possible to set several lines and several acceleration volt-

ages for a single element, therefore the measurements were repeated a few times with different primary beam energies. The software can also estimate the thickness of the thin layer, however, the density of all measured materials must be known. The density of the substrate is usually not a problem, however, estimating the density of the deposits is not trivial. As deposit thickness can be measured directly using atomic force microscopy (see next section), StrataGem was used to estimate the deposits' densities. The procedure required adjusting the density of the thin layer until the estimated thickness matched the thickness measured with the AFM.

2.4 Morphology and thickness of depositions: atomic force microscopy

AFM was performed using a NT-MDT AFM and Raman system. For all AFM scans included in this work, RTESPA 300 tips (Bruker, USA) were used. Tips were made of Si with a reflective Al layer on top. The nominal diameter of the tip was 8 nm and maximal 12 nm for freshly changed. The tips are asymmetric with side angles of 17.5±2° and front and back angles of 15±2° and 25±2°, respectively [126]. The tip height was in the range of 10 to 15 μm. The data were processed using Gwyddion software (artefact corrections, 3D scans, extracting line profiles and estimating roughness parameters) and Origin (graph plotting, edge broadening correction).

2.5 Thermogravimetry

Vacuum TGA (VTGA) results presented in this work were obtained using Netzsch TG209 F1 Libra TGA equipment. The TGA was connected to an Agilent Technologies SH110 dry scroll pump. The minimum pressure obtained with this pump was $6.6 \cdot 10^{-2}$ mbar. No gas flow was applied during VTGA measurements. Mass has been read out with precision of 0.0001 mg. In this system there are two thermocouples, one attached to the furnace and the other to the sample holder. All measurements were performed using Al_2O_3 crucibles, with all VTGA experiments performed under low vacuum. Under these conditions, the thermal contact between the furnace and the sample was too low to use the thermocouples in the described way. Normally, the heating process is controlled by the furnace thermocouple and the one attached to the sample serves only for readout. For VTGA measurements, the heating process was controlled using the thermocouple attached to the crucible. The parameters of PID controller were adjusted to avoid signal oscillations, caused by the thermal feedback loop. Initial masses of the compounds measured with VTGA in this work were between 9 and 20 mg. The applied heating rate was 5 K/min. Comparative measurements were performed under ambient atmosphere with a protective flow of N_2. These experiments were conducted using a Netzsch STA 449 F3

Jupiter TGA. The heating rate was the same as for the VTGA experiments. The N2 gas flow was 40 mL/min and the masses of the measured compounds were between 15 and 16 mg.

2.6 Mass spectrometry

Focused electron beam induced mass spectrometry experiments were performed using the Lyra3 Dual Beam system from Tescan, equipped with a Ga+ ion beam and an electron gun. A HV compatible, synchronized high resolution (6000-1400 M/ΔM) time-of-flight secondary ion mass spectrometer (HTOF-SIMS) attached to the microscope was used to analyse the masses of volatile, charged species. TOF-SIMS system was provided by TOFWERK (TOFWERK, Switzerland). The results were analysed using the TOF-SIMS Explorer software from TOFWERK. The gaseous precursor was delivered through a 5-lines GIS (Orsay Physics, France). The GIS was kept around 0.2 mm from the sample. $W(CO)_6$ was used as a precursor. GIS was de-gassed before and after each use. Precursor was heated up to 90 °C before each experiment. Moreover three solid state precursors were used: $Ru_3(CO)_{12}$, $Ag_2(\mu\text{-}O_2CC_2F_5)_2$ and $Cu_2(\mu\text{-}O_2CC_2F_5)_4$. Grains of each compound were glued on different standard SEM stubs using a piece of carbon tape (Ted Pella, USA). Before entering the vacuum chamber, the excess of grains was blown using dry N_2 gas. The working distance of electron column was approx. 9.1 mm and the distance to the TOF extractor was around 6 mm. All results were obtained using 10kV acceleration voltage. The beam current varied from 5.2 nA for some deposits made with $W(CO)_6$ to 30 nA for MS spectra obtained on grains of precursors. The ionised molecules were detected using an ion extractor during 40 μs of dwell time. The maximum m/z value was 450. The scanning field for all samples was 20 μm × 20 μm, which was divided to 256x256 pixels, which resulted in a pixel distance of 78 nm. Serpentine scanning was used. As in previous cases the substrate was a piece of <100> Si wafer, p-doped to provide sufficient electrical conductivity. The sample was tilted at 55° with respect to the horizontal plane to maximise the intensity of the signal reaching the TOF ion extractor. The spectrum was recorded for every pixel. In this work, the spectra are cumulative, coming from the whole frame, as no spatially-resolved maps were needed. All spectra were mass-calibrated using the highest intensity peaks: m/z = 31 and m/z = 69 for both carboxylates; m/z = 28 and m/z = 32 for $Ru_3(CO)_{12}$; m/z = 28 and m/z=186 for $W(CO)_6$. The results were plotted using Origin software.

2.7 Four-point probe resistivity measurements

Electrical resistivity of the nanowires was measured using the four-point probe method. Two electrodes, placed on the outer parts of the wire, provide the electric current. Two inner elec-

trodes, placed in between the current electrodes, measure the voltage drop. Two types of wires were deposited directly between the contacts: 1) single pixel line, 30 μm long, 10 μs of a pixel dwell time, 6 nm of point pitch ; 2) a rectangle 30x1 μm^2 with 1 μs of pixel dwell time, 6 nm of point pitch, made with spiral patterning strategy. Number of passes was different for silver and ruthenium and it is listed in corresponding sections (3.1.5 for Ag and 3.2.5 for Ru). Figure 2.2 presents 6-contact design with marked current and voltage contacts and a single pixel line deposited in-between. The outer contacts were connected to electrodes providing current from the power source and a pair of inner contacts were connected to voltage probes.

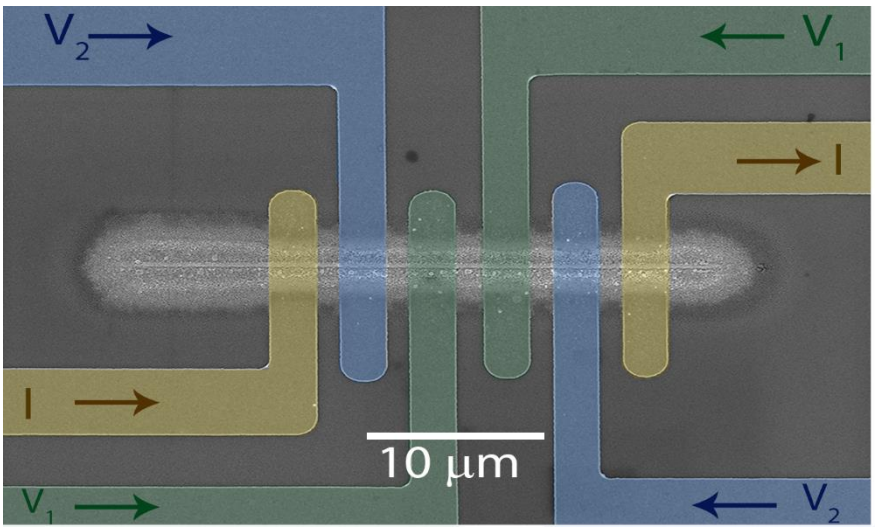

Figure 2.2 SEM image of a typical sample for the four point probe measurements. Yellow electrodes provide current and the voltage can be measure by each pair of four inner electrodes. Two possible arrangements are coloured green and blue.

The electrical resistance of the samples was measured using a home-built four-point probe setup, where each electrode was connected to an arm, allowing for independent movements along three axes. The electrodes were moved down to touch the connecting pads. For each wire, series of measurements were performed, starting from the lowest current, to avoid wire burning due to Joule-Lenz heating (especially important for low-conductive wires). The current was gradually increased until reaching the upper limit, which was estimated empirically. To ensure that the measured values were not a result of a poor connection between the electrode and the pad, the electrodes were positioned again and the resistance measurement for certain currents (usually the ones giving the best results) were repeated. For each voltage-current curve, 100 points were measured. Resistance of the wire was determined as the slope of the line fitted to experimental points. Resistivity of the wire was calculated using the formula:

$$R = \rho \cdot \frac{L}{S} \quad (2.1)$$

where R is the resistance of the wire, ρ the resistivity, and L and S are the geometrical parameters of the wire, length and area of the cross section, respectively. The length was measured using SE micrographs of the wire, as a distance between the inner edges of the voltage contacts. The distance was measured in 3 places between the contacts and the average was taken as the length value. The resistivity of the gold contacts was assumed to be negligible, compared to the resistivity of the nanowires. The cross-section was determined using the AFM scan of the wire with several profiles measured for each wire. The profiles were later analysed and integrated using a built-in integration function in MS Origin program. The area was then estimated as an average from the measured cross-sections.. The morphology of each wire was examined before and after electric measurements using electron microscopy to ensure, that the electric current did not affect the wire (e.g. did not melt it). The compositions of the wires was measured with EDX method, usually on the part of the wire laying on one of the outer gold pad connectors, to avoid influencing electrical measurements. Each measurement had to be corrected using StrataGem, due to low thickness of the wires. EDX measured on the part of wire laying directly on SiO_2 were unreliable, due to problems with oxygen level estimation. StrataGem was not able to assign the O content in wires laying on oxide substrate correctly.

Special substrates are needed to measure the electrical properties of the nanowires properly. Usually, these substrates have pre-patterned electrodes made with highly conductive metal. The micro- and nanowires are then deposited between the electrodes. The substrates have to be electrically conductive enough so that they do not charge during electron beam irradiation, however, they should have a non-conductive surface, so the current goes only through the electrodes and nanowires. In this work, the Si wafers with thermal, 100 or 200 nm thick layers of SiO_2 were used. Two types of substrate were used in this work, one with six electrodes per wire and one with four electrodes. The latter were designed especially to fit under the probe head of the Physical Property Measurement System (PPMS) delivered by Quantum Design, (San Diego, USA). The PPMS is a multi-method equipment, able to measure basic properties of materials, such as electrical or thermal conductance, magnetoresistance, magnetic permeability and susceptibility, in function of temperature and/or magnetic field. The temperature range used was from 4 K (liquid helium temperature) up to 300 K.

The PPMS-compatible substrates were prepared by methods of direct, positive tone photolithography, using a Direct Laser Writer (Heidelberg, Germany). Positive tone lithography uses

irradiation by light to make a resist locally more soluble. This resist is then solved, using a special solvent a called developer. The irradiated parts of the resist are then washed out, creating holes, in which another material can be deposited.

Si wafers with the thermal oxide were cleaned using an ultrasonic bath with acetone (5 min), isopropanol (2 x 5 min) and with oxygen plasma (5 min). The wafer was then transported to a cleanroom to coat it with the AZ ECI 3012 positive tone resist via spin-coating.

The spin-coater program was set to first accelerate to 500 rotations per minute (rpm) in one second, then to spin for 10 seconds with 500 rpm, accelerate to 2000 rpm in the next 2 s and rotate with this speed for 60 s. This protocol should give a coating thickness between 1 and 1.5 μm. As an exact value was not required, it was not measured. The coated wafer was then pre-baked at 90°C for 60 s and exposed with DLW.

DLW uses a laser beam to pattern the resist. The smallest patternable structures are around 1μm in lateral dimension. The power and duty cycle of the laser were adjusted through trial-and-error, and established to be equal 25 mW and 40 %, respectively. The wafers were exposed in 2x1 mode, meaning that each line was irradiated twice. The layout of the sample was designed in a way to adjust the placement of the contact pads to position of the probes of the PPMS probe-head. The layout was prepared using K-layout software.

After exposure, the wafer was post-baked at 110 °C for 90 s. A water solution of K-based AK 400, was used as the developer. The proportions of solvent and water were 1:5 (volumetric) and the development time was around 90 s. The sample was checked for patterning errors using optical microscopy. Next, the wafer was transferred from the cleanroom, to a PVD chamber (MANTIS Deposition Ltd., United Kingdom). Gold does not adhere properly to SiO_2, therefore up to 5nm of adhesive layer of Cr was deposited, followed by 100 nm of gold, covering the entire wafer. The non-irradiated parts, were then washed away during the lift-off process, using acetone in ultrasonic bath for 5 -10 minutes. Afterwards, the wafer was cut into pieces using a diamond tip.

3. Novel precursors:

In this chapter, the performance of three novel precursor groups will be analysed and assessed: silver carboxylates, heteroleptic, allyl-carbonyl-halide Ru complexes and NHC heteronuclear gold compounds. Their potential as FEBID precursor, as well as the properties of deposited material will be examined. Furthermore, some rules regarding using certain chemical groups as ligands will be proposed, basing on the achieved experimental results. As it was mentioned in chapter 1.5, development of new molecules, dedicated to FEBID is crucial for step to achieve pure three-dimensional structures.

3.1 Low volatility silver carboxylates

Silver was one of the metals gaining vast interest amongst researchers from the fields of photonics and plasmonics, due to its low optical losses in both the UV and visible light range. Plasmonic nanostructures find various applications, e.g. in light-based information technologies [127] and in sensors utilising surface-enhanced Raman scattering (SERS) [128, 129].

Silver is a metal, which for a long time has not been directly deposited with focused electron beam induced deposition. The first successful deposition experiments were reported by Ocola et al. [130], however, it was a liquid phase FEBID. First depositions using a gaseous precursor were reported by Höflich et al. and Berger et al. in the works from 2017 and 2018 [34, 35]. These works presented the successful utilisation of a novel class of precursors: metal carboxylates, specifically silver dimethylbutyrate $Ag_2(\mu\text{-}O_2CC(Me)_2Et)_2$ and silver pentafluoropropionate: $Ag_2(\mu\text{-}O_2CC_2F_5)_2$. Although known in the CVD society, carboxylates were never used before as FEBID precursors [113, 131].

In this study, we specifically investigate the dependence of the number of carbon atoms and size of the ligands on the metal content in FEB deposits prepared with five silver carboxylates: $Ag_2(\mu\text{-}O_2CC(Me)_2Et)_2$, $Ag_2(\mu\text{-}O_2C^tBu)_2$, $Ag_2(\mu\text{-}O_2CC_3F_7)_2$, $Ag_2(\mu\text{-}O_2CC_2F_5)_2$, $Ag_2(\mu\text{-}O_2CCF_3)_2$. As the electron beam is not selective with respect to bond breaking, it is expected that with the increase in the number of CF_x or CH_x groups in the molecule the metal content will decrease. Compositions of the deposits as well as their crystal structure and electrical properties were examined to better understand the electron-induced dissociation pathways and the role of ligands and their properties in deposition process.

3.1.1 Chemical formula

Silver carboxylates create the series with differing size and number of carbon atoms in ligands. In this work five silver precursors were used: three perfluorinated, with increasing

length of CF_x chains: $Ag_2(\mu\text{-}O_2CCF_3)_2$, $Ag_2(\mu\text{-}O_2CC_2F_5)_2$, $Ag_2(\mu\text{-}O_2CC_3F_7)_2$ and two without fluorine: $Ag_2(\mu\text{-}O_2CC(Me)_2Et)_2$, and $Ag_2(\mu\text{-}O_2C^tBu)_2$. The structural formulas of the precursors are depicted in figure 3.1.1; the complexes are ordered from left to right with decreasing number of carbon atoms in the molecule. The complexes were synthesised by Iwona Szymanska and Katarzyna Madajska from UMK in Torun, according to the process published by Szlyk et al. [115].

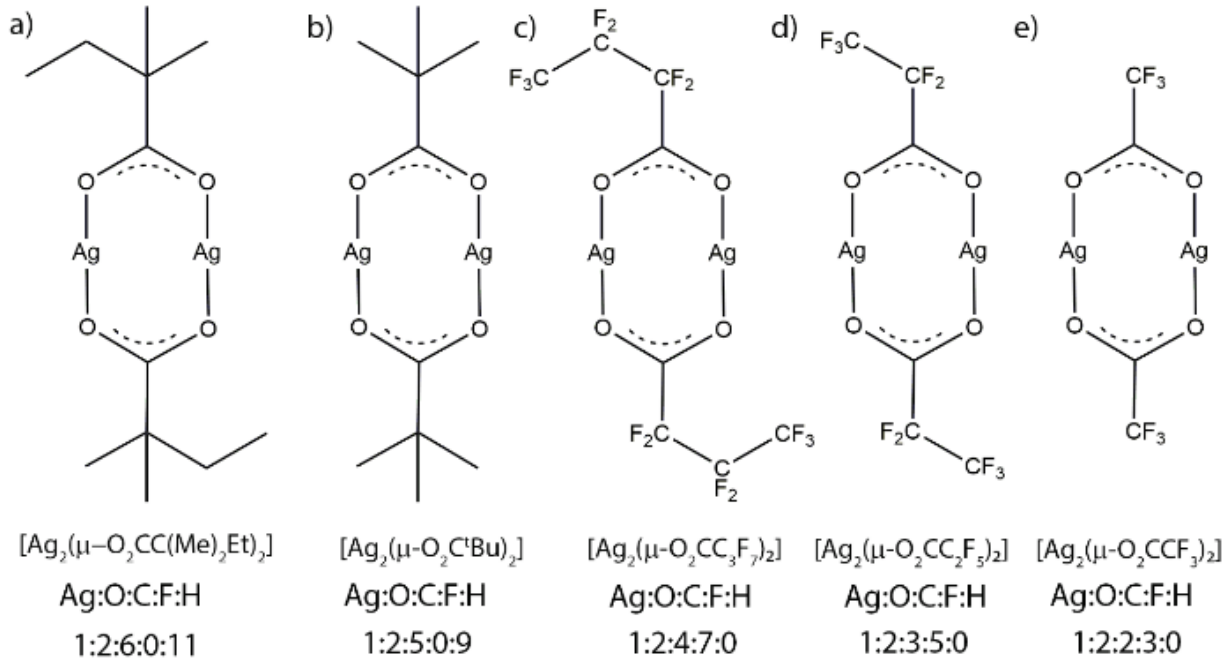

Figure 3.1.1 Structural formulae of the investigated precursors sorted by decreasing number of carbon atoms in the ligands from left to right. The fluorinated silver carboxylates form a series with carbon chain lengths of two to four carbon atoms and the carboxylates containing hydrogen continue with bulk ligands of five to six carbon atoms. Taken from Jurczyk et al. [132]

3.1.2 Thermal properties

Unlike many other precursors used for FEBID [1, 41, 43], silver carboxylates are not volatile at room temperature. It is then necessary to heat them up to sublime them and deliver through a gas injection system over the sample's surface. Increased process temperature creates two main difficulties: a risk of condensation of the precursor on the substrate, which could decrease both the metal content and lateral resolution of the created structures and thermal decomposition of the compound inside the reservoir, which can lead to sublimation of mainly ligands, lowering the metal content of the deposited material. The first challenge can be overcome by using substrate heating, although it complicates the process by adding another variable parameter. Moreover sample temperature cannot be too high, to avoid thermal decomposi-

tion of the precursor adsorbed on the surface. It is then clear that both the GIS and the heated stage temperatures have the same upper limit, namely the temperature of thermal decomposition of the used complex. The lower limit of the stage's temperature will be determined by the condensation of the precursor molecules on the substrate. In the case of GIS, the lower temperature limit is not precise. The only requirement is that the flux of the precursor molecules has to be sufficient enough to provide a proper growth rate. Table 3.1.1 summarises the applied GIS temperatures, as well as achieved throughputs (*Q*) and fluxes of molecules which arrived on sample surface (*J*).

Table 3.1.1 Summary of gas injection system (GIS) temperatures, molecule throughput Q through the heated GIS and impinging molecule flux J on the substrate at FEBID position for the silver carboxylates having the molar mass M (taken from Jurczyk et al. [132]).

Precursor	**GIS (°C)**	***Q* (molecules/s)**	***J* (molecules/(s·cm^2))**	***M* (g/mol)**
$[Ag_2(\mu\text{-}O_2CC(Me)_2Et)_2]$	145 - 175 °C	(0.2– 11)*10^{14}	(0.8– 45)*10^{14}	222
$[Ag_2(\mu\text{-}O_2C^tBu)_2]$	170 - 190 °C	(2.2–4.9) *10^{14}	(8.6 – 20)*10^{14}	209
$[Ag_2(\mu\text{-}O_2CC_3F_7)_2]$	175 - 190 °C	(4.4–6.0) *10^{14}	(1.7 - 2.4) *10^{15}	321
$[Ag_2(\mu\text{-}O_2CC_2F_5)_2]$	150 - 180 °C	(3.8–5.2) *10^{14}	(1.4 – 2.0) *10^{15}	271
$[Ag_2(\mu\text{-}O_2CCF_3)_2]$	170 - 185 °C	(2.8–2.9) *10^{14}	(1.1 - 1.2) *10^{15}	221

As can be noticed that the temperature for all used compounds ranged between 150°C and 200°C. These limits can be determined experimentally, through trial and error. It would, however, be extremely helpful to know these temperatures prior to any FEBID experiments. It would not only increase the efficiency of the experiments, by setting some starting points for the thermodynamical conditions, but also decrease the number of failed attempts and increase reproducibility of the experiments by determining the upper limit, i.e. decomposition temperature. We can then state that the use of increased temperatures for the GIS and stage during the FEBID process requires some pre-screening method for potential low-volatility precursors. This method should allow not only for eliminating compounds, the decomposition temperature of which is below sublimation point under given pressure, but also should help determining optimal thermodynamical conditions for FEBID.

Silver carboxylates were previously applied in chemical vapour deposition (CVD). [131, 133, 134].Their thermal properties were tested using various methods, including thermogravimetry [115, 135]. Although TGA looks very promising as a potential pre-screening method also for FEBID precursors, it has certain disadvantage, limiting its applicability. One can see that especially in the case of perfluorinated silver carboxylates. The sublimation temperatures measured using TGA were even 100°C higher than temperatures used during FEBID experiments. As will be shown in the next sections and what has been reported in our published works [34, 35, 101], the metal content of deposited structures in most cases exceeded 50 at.%. It would be impossible to achieve such high metal contents in deposited material without subliming Ag-containing molecules. The explanation of such discrepancies in process temperatures derived from FEBID and TGA can lay in the used pressures. Deposition experiments were performed in high vacuum, with pressures between 10^{-6} and 10^{-5} mbar, whereas thermogravimetry was conducted under atmospheric pressure of 1 bar.

To examine this hypothesis, in our recently published paper we used in-vacuum TGA (VTGA) to investigate the thermal properties of silver carboxylates. Experiments were performed in low vacuum, between 10^{-2} and 10^{-1} mbar. The graph on Figure 3.1.2 presents the mass of measured compound (as a percentage of the initial mass) inside the crucible as a function of temperature. We can directly see the difference between fluorinated and non-fluorinated carboxylates.

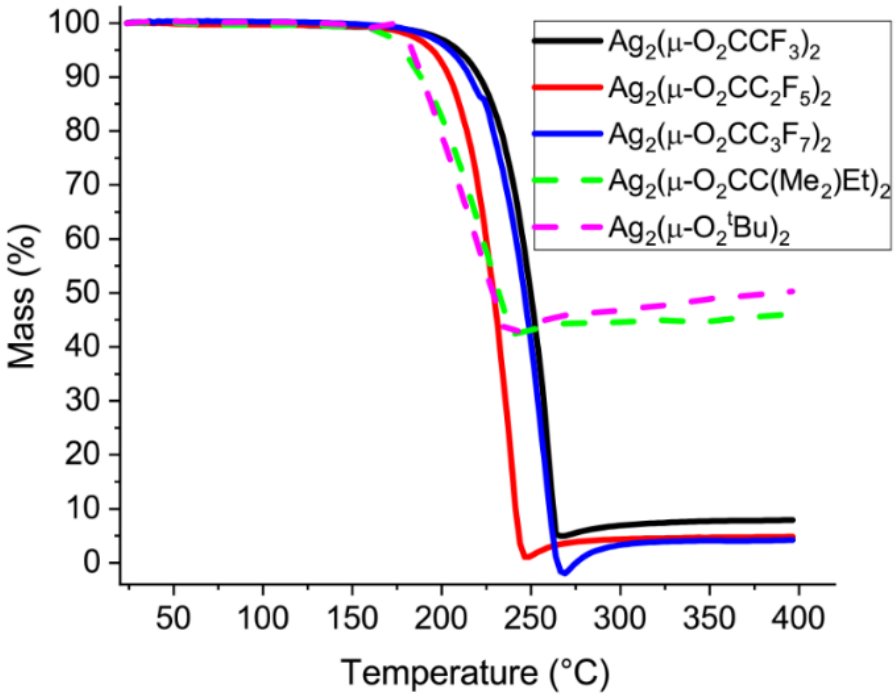

Figure 3.1.2 Results of VTGA measurements of various silver carboxylates. Taken from Jurczyk et al. [136]

On average, the first group leaves significantly less residuals inside the crucible than the second: maximum 8 % for $Ag_2(\mu\text{-}O_2CCF_3)_2$ vs around 45 % for $Ag_2(\mu\text{-}O_2CC(Me)_2Et)_2$. The mass loss, however, starts earlier on the temperature axis for both non-fluorinated species. Earlier start of mass loss indicates that the compound has a lower temperature of volatilisation. It is in qualitative agreement with GIS temperatures presented in Table 3.1.1. From all of the fluorinated compounds $Ag_2(\mu\text{-}O_2CC_2F_5)_2$ FEBID experiments were performed at the lowest temperature (down to 150 °C). Furthermore, the GIS temperature for $Ag_2(\mu\text{-}O_2CC(Me)_2Et)_2$ was significantly lower than those used to sublimate other compounds, where temperatures reached even up to 145 °C. The only exception is $Ag_2(\mu\text{-}O_2C^tBu)_2$, which was used with higher GIS temperatures. It is unknown exactly why this precursor needed a higher temperature to sublimate.

Low mass residues for fluorinated complexes indicate, that during VTGA measurements the precursors mostly sublimated, although 8±1 % of mass residues for $Ag_2(\mu\text{-}O_2CCF_3)_2$, 5±1 % for $Ag_2(\mu\text{-}O_2CC_2F_5)_2$ and 4±1 % for $Ag_2(\mu\text{-}O_2CCF_3)_2$ suggest small possibility of thermal decomposition during heating. In contrast, 45 ± 2% and 49 ± 1% of mass residues for $Ag_2(\mu\text{-}O_2CC(Me)_2Et)_2$ and $Ag_2(\mu\text{-}O_2C^tBu)_2$, respectively suggest that these compounds thermally decomposed during measurement. Silver amounts to 48.4% of molar mass of $Ag_2(\mu\text{-}$

$O_2CC(Me)_2Et)_2$ and 51.7% of molar mass of $Ag_2(\mu\text{-}O_2C^tBu)_2$. The differences between silver content in the molecule and mass residues are 3.4 ± 2% for the former and 1.7 ± 1% for the latter complex. It indicates that small amount of both non-fluorinated carboxylates sublimated alongside decomposition. The uncertainties of mass residue measurements were estimated based on the slight mass increase after the main mass loss event. Small local minimum just after the main mass loss event is an artefact of the measurement and was not considered neither in the discussion nor in uncertainties estimation. The TGA equipment allows for registering mass loss with a precision down to 0.0001 mg, which is 5 orders of magnitude lower than the masses of measured samples, which were between 9 and 20 mg. Hence, it was neglected in estimation of uncertainties of mass residues.

Figure 3.1.3 a-c presents the comparisons between VTGA and N_2-flow TGA of three compounds: $Ag_2(\mu\text{-}O_2CCF_3)_2$, $Ag_2(\mu\text{-}O_2CC_2F_5)_2$ and $Ag_2(\mu\text{-}O_2CC(Me)_2Et)_2$. In all three cases we can see significant differences between the results obtained in vacuum and at atmospheric pressure. These differences are most pronounced for perfluorinated complexes, where mass loss in vacuum starts at 130 °C lower temperatures, than for standard atmospheric pressure TGA. Additionally, mass residues at the end of the process are significantly larger for the N_2-flow TGA method. They reach around 40 % for $Ag_2(\mu\text{-}O_2CC_2F_5)_2$ and around 55 % for $Ag_2(\mu\text{-}O_2CCF_3)_2$. In vacuum, the mass left inside the crucible at the end of the process stands at around 8 % of the initial mass of each measured compound. For the non-fluorinated $Ag_2(\mu\text{-}O_2CC(Me)_2Et)_2$, this difference is much lower at around 4 % point between the mass residues recorded during VTGA and N_2-flow TGA. Furthermore, the difference in temperature between corresponding mass losses on the slopes of both curves is only around 39 °C.

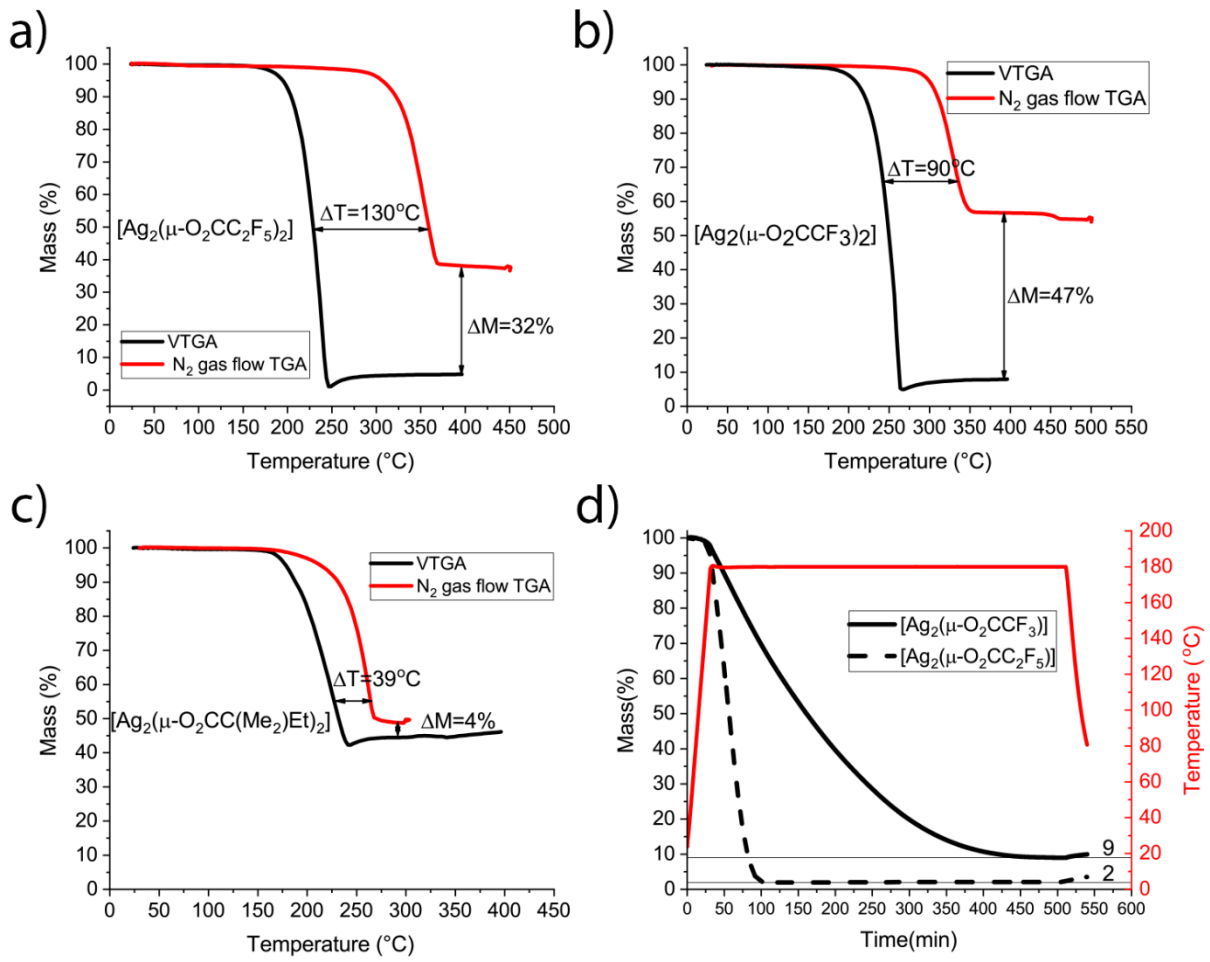

Figure 3.1. 3 Results of both in-vacuum (black) and gas-flow (red) TGA for a) $Ag_2(\mu\text{-}O_2CC_2F_5)_2$, b) $Ag_2(\mu\text{-}O_2CCF_3)_2$, c) $Ag_2(\mu\text{-}O_2CC(Me_2)Et)_2$ and d) comparison of isothermal TGA curves for two fluorinated compounds; Taken from Jurczyk et al. [136]

Figure 3.1.3d presents the isothermal VTGA for two fluorinated compounds: $Ag_2(\mu\text{-}O_2CC_2F_5)_2$, $Ag_2(\mu\text{-}O_2CCF_3)_2$. The measurements were performed at 180 °C, as it is one of the highest GIS temperatures used for depositions with these complexes. The difference in the slopes of mass loss curves of both compounds can immediately be noticed. $Ag_2(\mu\text{-}O_2CC_2F_5)_2$ sublimes relatively fast, leaving only 2 % of mass leftovers.

Comparison of both types of measurements, the one in vacuum and the one performed at atmospheric pressure clearly shows the importance of ambient condition during the measurement. The pressure used during VTGA was around 4 - 5 orders of magnitude lower than the one during N_2-flow TGA. From basic thermodynamics it is known that the sublimation process of a compound is driven by its chemical potentials both in solid and in gas phase. The chemical potential is a function of both the temperature and pressure, however it changes dif-

ferently for gases and condensed phases. As gases have a higher molecular volume, their chemical potential increases more with increase of pressure, than chemical potentials of solids and liquids. It means that more energy is needed to sublimate a compound under higher pressure, compared to low vacuum conditions. That is why fluorinated compounds decompose in ambient pressure measurements, while during VTGA they are mostly sublimating. Non-fluorintated complexes decompose both in atmospheric pressure and in low vacuum. High silver contents achieved during FEBID using non-fluorinated complexes (see next section) prove, that there are silver-containing molecules in gas phase. However, it should be noted, that FEBID is performed in high vacuum (around 10^{-5} mbar). Lowering the pressure further lowers the energy needed to sublimate the precursor molecules. It is possible then that non-fluorinated complexes may sublimate in high vacuum in temperatures lower than their thermal decomposition threshold.

The presented VTGA measurements have proved that this method can be used as a fast, pre-screening technique to examine potential FEBID precursors. The pressure is closer to high vacuum used in FEBID than the atmospheric pressure used in N_2-flow measurements applied widely to CVD precursors. Isothermal VTGA measurements are a promising method of checking the thermal stability of the precursor during several-hours heating, like it is commonly applied during FEBID. To make the TGA measurements conditions even closer to the ones of FEBID, it is necessary to apply high vacuum.

3.1.3 Morphology, composition and crystal structure

To determine the composition of the deposited material, series of square deposits were prepared. Each square had 10 x 10 μm^2 of defined dimensions and were made with 1µs of dwell time, using the spiral patterning strategy. The deposits are presented on figure 3.1.4. The edges of the defined squares are marked with blue dashed lines.

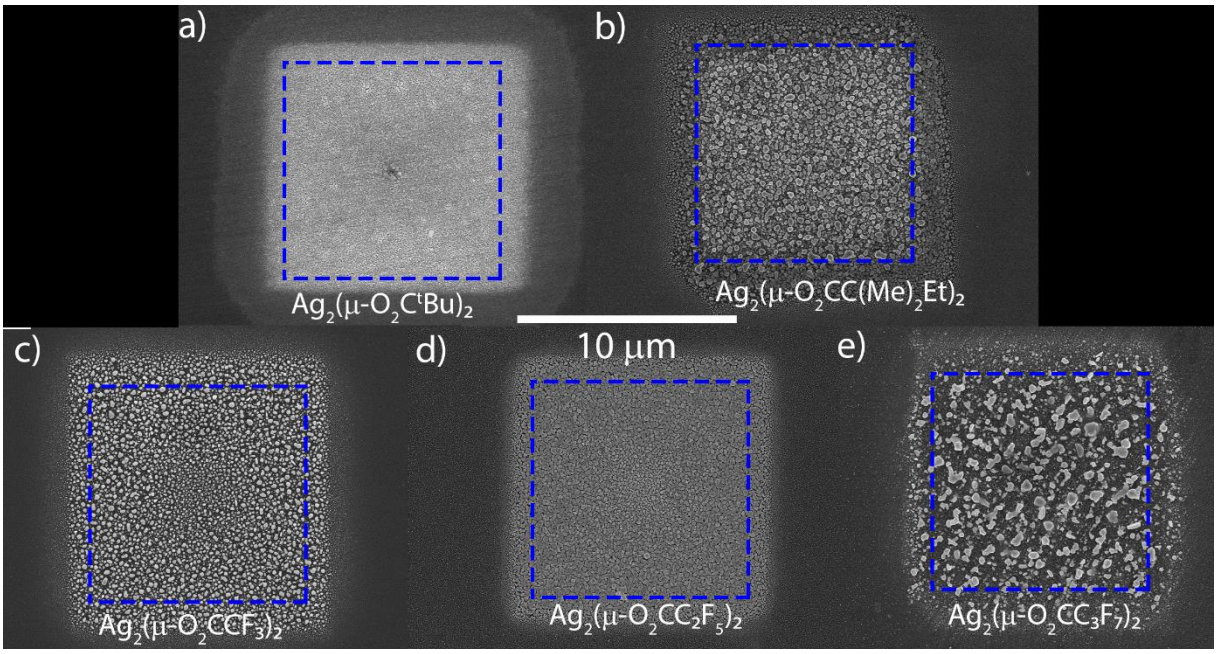

Figure 3.1. 4 SEM micrographs of square deposits made with 5 different carboxylates. Irradiated area of $10x10\mu m^2$ was marked with dashed blue line. Reproduced based on Jurczyk et al. [132].

All of the deposited squares were characterised with a rough, granular surface. As can be noticed, the real size of the square deposits is larger than the nominal values. There are three possible effects contributing to this difference. First is the size of the e-beam. For 20 kV of acceleration voltage, the width of the beam, comprising 99.9% electrons was around 450 nm, which adds to the nominal side length. The beam size was measured using a knife-edge method, see Appendix A1. Moreover, for deposits made with carboxylates, strong halo deposits can be observed. The largest halo region was observed for the deposit made with $Ag_2(\mu\text{-}O_2C^tBu)_2$. The deposition of halo region will be considered more thoroughly in next section of this chapter. The last effect, which can be noticed the most for the squares made with $Ag_2(\mu\text{-}O_2CC(Me_2)Et)_2$ and $Ag_2(\mu\text{-}O_2CC_3F_7)_2$, is a result of a slight thermal drift.

The compositions of materials deposited with different silver carboxylates is given in the table 3.1.2. The compositions were measured with EDX, using 8 kV of acceleration voltage. The results were corrected with Stratagem software. What is special about all the examined silver carboxylates is that most of the carbon has been cleaved and removed from the deposit. Compared to the complexes' stoichiometry, from 86 up to 91% of carbon atoms were removed (for the purest deposits). The removal of most of the carbon atoms resulted in high metal contents of deposited structures. For all compounds, except of $Ag_2(\mu\text{-}O_2CC_3F_7)_2$, even the lowest achieved Ag content was greater or equal 50 at.%. In all cases, the best achieved metal contents were around 60 and 70 at.%, depending on the compound. It has to be noted that for two

compounds, the purities reported in first publications were even higher, reaching 73 at.% for $Ag_2(\mu\text{-}O_2CC(Me)_2Et)_2$ and 76 at.% for $Ag_2(\mu\text{-}O_2CC_2F_5)_2$.

Table 3.1.2 Stoichiometry of silver carboxylates, atomic ratios of best metal contents, best and worst Ag content in at.% achieved and the rate of C removal. Reproduced basing on [132]

Precursor	**Precursor Stoichiometry Ag:O:C:F:H**	**Atomic ratio of best purity Ag:O:C:F:(H*)**	**Best Ag (at%)**	**Lowest Ag (at%)**	**C removal (best purity)**
$[Ag_2(\mu\text{-}O_2CC(Me)_2Et)_2]$	1:2:6:0:11	1: 0.08: 0.51: 0: (0.11)	63 (76)**	57	91%
$[Ag_2(\mu\text{-}O_2C^tBu)_2]$	1:2:5:0:9	1: 0.08: 0.57: 0: (0.12)	61	50	89%
$[Ag_2(\mu\text{-}O_2CC_3F_7)_2]$	1:2:4:7:0	1: 0: 0.52: 0.22	57	34	87%
$[Ag_2(\mu\text{-}O_2CC_2F_5)_2]$	1:2:3:5:0	1: 0.04: 0.27: 0.11	70 (76)***	63	91%
$[Ag_2(\mu\text{-}O_2CCF_3)_2]$	1:2:2:3:0	1 :0.02: 0.29: 0.03	74	65	86%

* H is not detected with EDS, it was estimated using C/H=9/2 from Bret et.al. [137]. **Metal content achieved by Höflich et al. [34]. *** metal content achieved by Berger et al. [35].

What can be also noticed is that for all investigated carboxylates the number of oxygen atoms per one Ag is very low. It suggests the cleaving of Ag-O bond in the carboxylate molecule. To further investigate this hypothesis, TEM measurements were performed. To conduct these measurements series of deposits were directly deposited onto 50 nm thick SiNx TEM grid. There were two types of deposited structures: continuous-exposure spots, with exposure times differing between 1 and 20 minutes, and single-pixel, 20 µm lines. The pixel dwell time was 1 µs and the point pitch was 6 nm. The lines differed with the number of passes: from 25000 up to 100 000. All deposits were prepared with 20kV acceleration voltage and 0.70 nA of beam current. Various exposure times (spots) and numbers of passes (lines) were used to ensure that for both types of deposits there will be at least a single structure both transparent to high kV e-beam and thick enough to give a clear signal in both scanning-transmission electron microscopy (STEM) and selected area electron diffraction (SAED) modes.

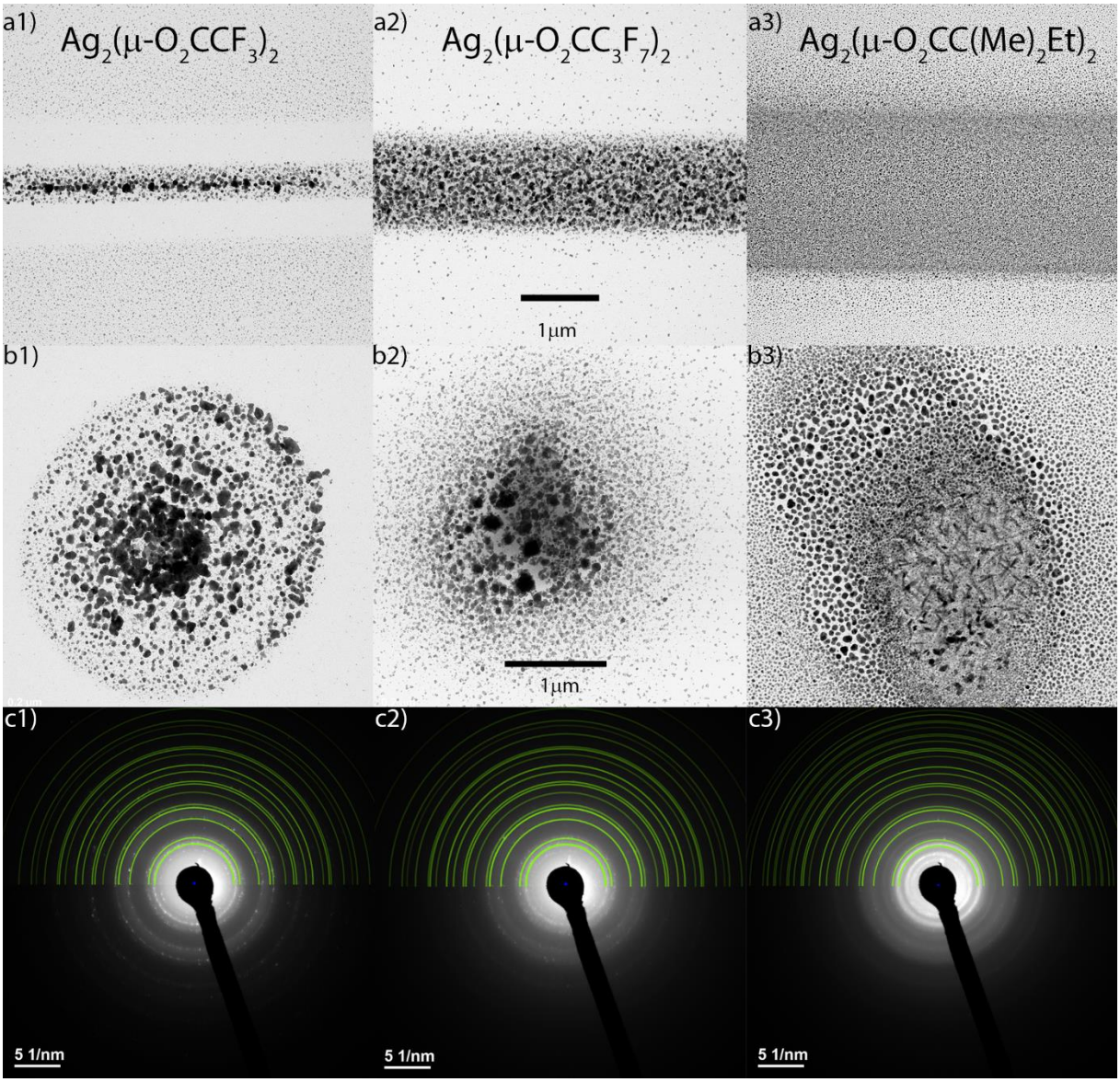

Figure 3.1.5 Upper row a): FEBID lines made on SiN_x membranes using 20 kV and around 0.70 nA of beam current. The number of passes spanned between 25000 to 100000 per line, with dwell time of 1µs and point pitch of 6nm. Middle row b): FEBID spots made on SiN_x membrane with 20 kV and around 0.70 nA. Exposure times used for these deposits were between 1 to 20 minutes Lowest row c): corresponding SAED pattern with matched pure silver patterns (light green rings). The formulas of precursors are given at the top of each column.

As was previously observed for structures made on Si, the deposited material is very granular, with particle sizes varying between tens and hundreds of nanometres. For each measured compound, SAED patterns showed clear and visible rings, indicating crystalline character of measured particles. The pure Ag pattern, presented as light-green half-circles in the upper part of SAED images, was in each case the best fit to the measured diffraction rings. This indicates that the deposited materials take form of Ag crystals embedded in a carbon-fluorine-oxygen matrix. This result stands in good agreement with the data previously reported by Höflich et al. and Berger et al. [34, 35]. The SAED results confirms the hypothesis, that the Ag-O bonds were cleaved under electron irradiation. Residual carbon and fluorine results most probably

from co-deposition of the dissociated ligands. Comparing the images in the row there are certain differences, which can be noticed. Firstly, even though all lines were created as single pixel lines, they have different width. For $Ag_2(\mu\text{-}O_2CCF_3)_2$ (Figure 3.1.5. a1) the biggest crystals are concentrated in the centre of the line and the smaller on the sides. From both sides of the line a depletion zone can be noticed, where no deposit was formed. Most probably, this effect can be attributed to surface diffusion. Physisorbed molecules travel towards the centre, where they are deposited. Another possibility includes the diffusion of metal atoms and the formation of bigger particles due to Ostwald ripening [138]. For $Ag_2(\mu\text{-}O_2CC_3F_7)_2$ (Figure 3.1.5.a2), the size distribution of the particles is more uniform throughout the width of the wire. The width of the beam used for this experiments was around 450 nm (FW(99.9%) – full width containing 99.9% of electrons). This means that the width of the lines cannot be explained only with interactions between the adsorbed molecules and secondary electrons of first type. As was shown in section 1.3, the widening of the lateral dimensions of deposit on the bulk substrate, called halo, is an effect of interaction between physisorbed molecules and secondary electrons of second type and/or backscattered electrons. The lateral size of the halo depends highly on the thickness of the sample, as we have explained before in the work of Höflich et al.[34] or in the review of Utke et al.[2]. It is due to reduced number and lateral range of escape of BSEs. The maximum range of BSEs escaping from the surface of 50 nm thick SiN_x was simulated using CASINO [37]. For 50 millions of electrons, 20 keV of primary beam energy and 450 nm of the beam size (FW(99.9%)) the most distant BSEs were registered around 2000 nm away from the beam's centre. It would explain the widening of the wire made with $Ag_2(\mu\text{-}O_2CC_3F_7)_2$. The wire made with $Ag_2(\mu\text{-}O_2CC(Me)_2Et)_2$ (Figure 3.1.5.a3), is the widest wire from all three. Such an increased width is probably not an effect of halo deposition, however, it may been caused by some vertical drift of the sample. The drift can be noticed also on the spot deposit made with the same precursor and presented in Figure 3.1.5.b3. The spot deposits made with both fluorinated carboxylates are qualitatively similar – the largest particles are concentrated in the centres, whereas in the halo, their size decreases. The size of the deposit made with $Ag_2(\mu\text{-}O_2CCF_3)_2$ is slightly smaller than the size of the spot deposited using $Ag_2(\mu\text{-}O_2CC_3F_7)_2$ (3.16 μm vs 3.37 μm).

Figure 3.1.6 presents for each precursor the average achieved composition, (from table 3.1.2), the error margin and the highest silver content with corresponding stage temperature. The amount of hydrogen for non-fluorinated compounds were estimated using the ratio of C:H=9:2, which was proposed by Bret et al. [137].

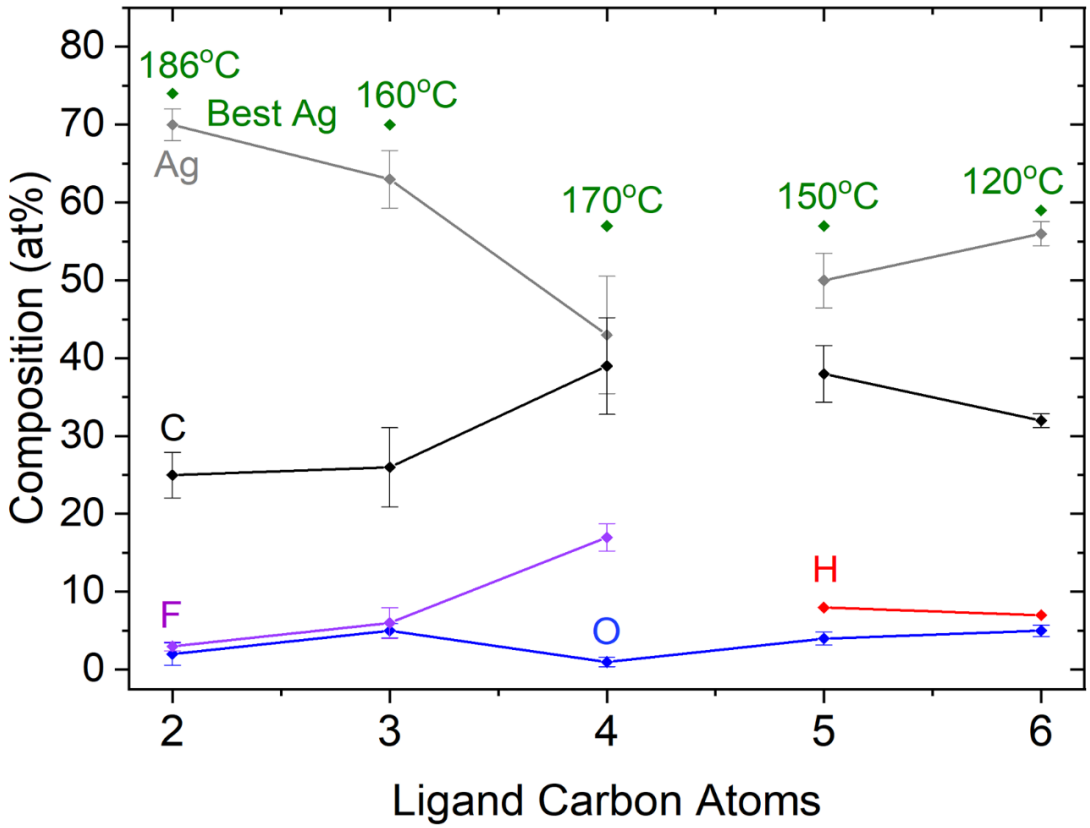

Figure 3.1.6 Average compositions achieved for different numbers of carbon atoms in ligand molecules. Highest silver contents were marked green, with corresponding stage temperatures. H was estimated using work of Bret at al. [137]. The lines connecting the points were added to better visualise the results. Reproduced from Jurczyk et al. [132]

What can be notice from the figure is that there is a slight trend between the number of carbon atoms in the molecule and the Au content of the deposits for perfluorinated carboxylates. The lowest average Ag content was achieved for $Ag_2(\mu\text{-}O_2CC_3F_7)_2$, which has the most carbon and fluorine atoms in the chain. This trend was not observed for non-fluorinated compounds.

There are several possible explanations, why such a high metal content of all deposits made with silver carboxylates was achieved. First of all, the stage and GIS temperatures were elevated during deposition. This provides additional energy to the molecules adsorbed on the substrate's surface. This additional kinetic energy may enhance dissociation of metal-ligand bonds, making a deposition process "thermally enhanced" as a result. Moreover, thermal desorption is driven by the stage temperature. This applies both to precursor molecules and ligands. With elevated stage temperatures, the cleaved ligands have shorter residence time, therefore a lower chance to be co-deposited. Furthermore, there is only one ligand per a single Ag atom in the precursor molecule. The bond between the carboxylate ligand and the silver

atom is weak [34]. Considering all the listed factors, it is understandable why such impressive metal contents can be achieved using silver carboxylates. Stage temperature may have yet another effect. It enhances surface diffusion, for both adsorbed precursor molecules and metal atoms, which resulted from the dissociation of metal-ligand bonds. Diffusion will enable the growth of big metal particles due to Ostwald ripening [138].

3.1.4 Single spot deposits – halo effect

Figure 3.1.7 presents series of deposits manufactured with 5 minutes of constant irradiation of a single spot with 0.5 – 0.76 nA of beam current and 20k V of beam acceleration voltage. The beam width containing 99.9% of electrons (FW(99.9) = 450 nm) is marked with green dashed-line circles. As can be seen, the diameter of each of the deposits vastly exceeds the beam size, reaching around 5 um for compounds and even 7 um for $Ag_2(\mu\text{-}O_2C^tBu)_2$. The material deposited outside of the primary beam region is characterised by a different morphology. The particle size is visibly higher than in the centre, especially for perfluorinated compounds. For non-fluorinated precursors, particle sizes do not differ too much along the radius of a spot. The halo regions are more homogenous.

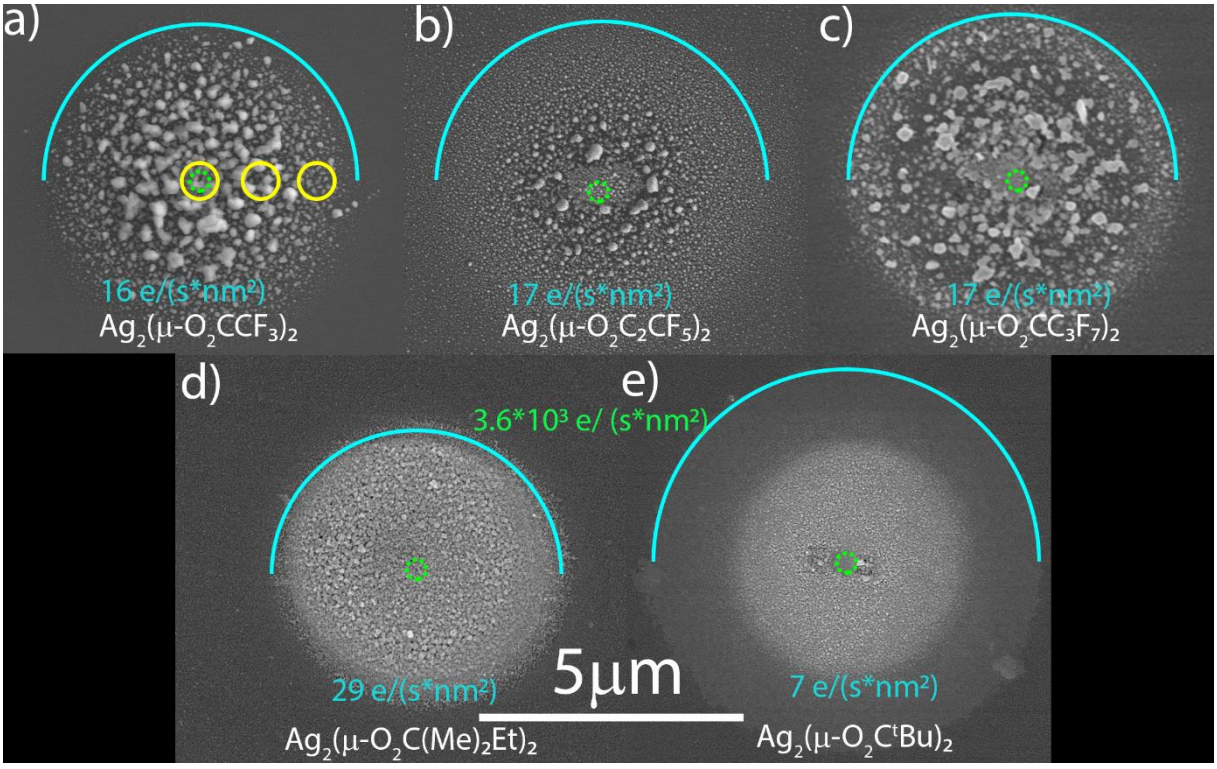

Figure 3.1.7 SEM top view images of FEBID spots taken at 8 keV. Irradiation was with 20 kV for 5 min. using different silver carboxylates, top: silver carboxylates containing hydrogen and bottom fluorinated silver carboxylates. Precursors are indicated. The primary electron beam (FW(99.9)) and the visible halo periphery are indicated by green and light-blue circles, respectively. Yellow circles indicate the spots were EDX measurements were taken. Size of the circles corresponds to maximum EDX excitation range. Note that there was a slight horizontal drift in (d). Reproduced based on Jurczyk et al. [132]

What is interesting, the composition of the deposited material also changes along the radius of each spot. The yellow circles in the figure 3.1.7 mark the places were the EDX measurements were taken. The size of the circles correspond to the maximum diameter of excitation volume during this measurement. For $Ag_2(\mu\text{-}O_2CC(Me)_2Et)_2$, $Ag_2(\mu\text{-}O_2C^tBu)_2$ and $Ag_2(\mu\text{-}O_2CC_3F_7)_2$ the metal content in the deposited material is the highest in the halo region (middle circle). The results are gathered in table 3.1.3. The term "centre" is used for the measurement, which was taken in the spot, where the primary beam was placed during deposition (left yellow circle on Figure 3.1.7); the term "halo" is used for the measurement taken in the middle of halo region (middle yellow circle on Figure 3.1.7) and the term "periphery" refers to the place at the border of halo region (right yellow circle on Figure 3.1.7).

Table 3.1. 3 Summary of compositions of spot deposits in atomic percent, measured in three spots marked with yellow circles on Figure 3.1.7 (centre, halo, periphery). The measurements marked with an asterisk were taken from our joint publication, Höflich et al. [34].

Precursor	**Ag:O:C:F**		
	Centre	**Halo**	**Periphery**
$Ag_2(\mu\text{-}O_2CC(Me)_2Et)_2$	42:7:51:0*	70:7:23*	---
$Ag_2(\mu\text{-}O_2C^tBu)_2$	38:7:55:0	65:33:2:0	43:12:45:0
$Ag_2(\mu\text{-}O_2CC_3F_7)_2$	50:0:49:1	60:0:39:1	58:0:41:1
$Ag_2(\mu\text{-}O_2CC_2F_5)_2$	45:1:51:3	46:0:51:3	35:1:58:6
$Ag_2(\mu\text{-}O_2CCF_3)_2$	73:0:27:0	76:0:24:0	56:0:43:1

The most possible reason of the differences in the metal contents between the central and halo regions is caused by the surface density of secondary electrons in these regions. In the centre, where the primary beam was placed, the electron flux is the highest, few orders of magnitude higher than in the halo region. The electron fluxes in the central and peripheral regions were simulated using Monte Carlo methods with Casino software. The simulation was run for 20 kV beam. It shows the radial distribution of BSEs from the centre of the primary beam up to several micrometres away (light-blue line on the graph on Figure 3.1.8). The primary electrons distribution was simulated as a Gaussian function using Origin software (light-green line on the graph on Figure 3.1.8). The intensity and FWHM of the simulated beam was adjusted to match the real values. The FWHM of the beam was measured using the knife-edge method

described more in the supporting information of papers: [34, 36] and Appendix A1. The intensity was estimated so that the total number of simulated electrons matched the total number of electrons calculated from the beam current. Although the simulations do not present the distribution of secondary electrons, the number of generated SEs is directly proportional to both the number of primary electrons and backscattered electrons. The distance between the centre of the deposit and the place, where the EDX measurements of halo were performed was around 1.4 μm, meaning, that in this region the flux of BSEs was around two orders of magnitude lower than the flux of PEs. In the centre, where a high secondary electrons flux is generated the dissociated ligand may not have time to desorb even if the ligand-metal bond has been cleaved. The ligands are further dissociated, creating non-volatile species and are incorporated into the deposit. This co-deposition concept is depicted in Figure 3.1.8 b and was suggested based on results of $Ag_2(\mu\text{-}O_2CC(Me)_2Et)_2$ [34]. The tendency of higher metal content FEBID at lower electron flux was also confirmed for $Ag_2(\mu\text{-}O_2C^tBu)_2$ and $Ag_2(\mu\text{-}O_2CC_3F_7)_2$, see table 3.1.3 when comparing the centre and halo metal contents For two other perfluorinated precursors, $Ag_2(\mu\text{-}O_2CC_2F_5)_2$ and $Ag_2(\mu\text{-}O_2CCF_3)_2$ there was no significant difference between the metal content in centre and in halo. The most possible explanation is that their ligands (or their fragments) desorbed still fast enough, in the central region so that they were not co-deposited by the corresponding high electron fluxes. In the periphery, the flux of electrons is a few orders of magnitude lower than in the centre and the halo. For all silver carboxylates lower metal contents were observed in this region, compared to the halo. As for now, there is no certain explanation of this observation. In case of $Ag_2(\mu\text{-}O_2C^tBu)_2$, where 12 at.% of oxygen is observed, it is possible that low metal content resulted from incomplete dissociation of precursor molecules. However, for the case of fluorinated precursors the oxygen was mostly removed, indicating the cleaving of Ag-O bonds. Long carboxylate ligands may undergo multiple dissociations under irradiation with electrons, creating several volatile C_xF_y (CO_2 or C_xH_y) species. This was observed for irradiation of pristine crystals of $Ag_2(\mu\text{-}O_2CC_2F_5)_2$, see chapter 4.2. It is possible then, that in the periphery, where the electron flux is low, dissociated ligands were not further fragmented, but rather deposited as longer C-F or C-H chains, hence low periphery metal content.

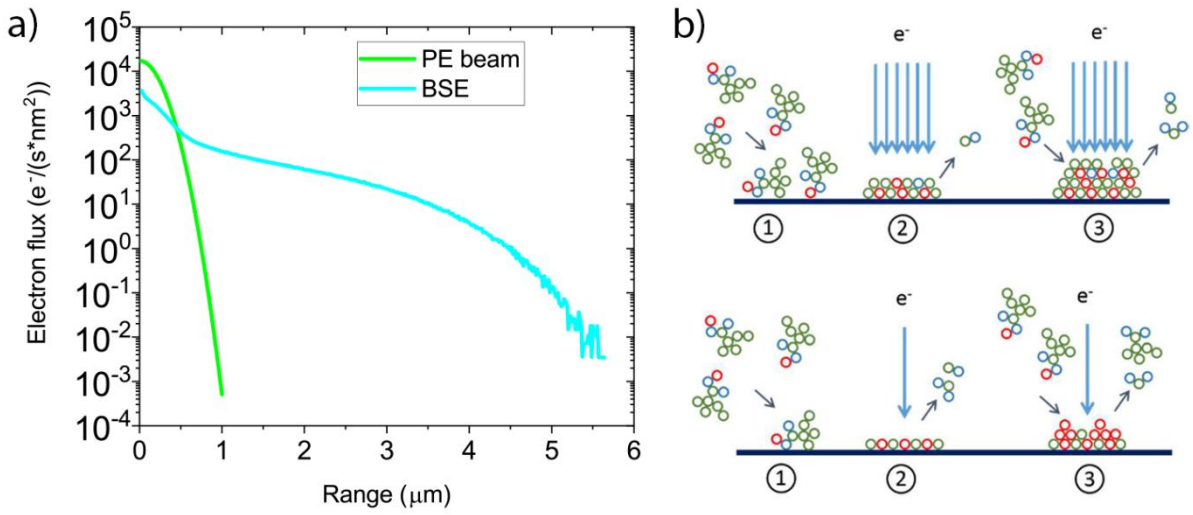

Figure 3.1 8 a) Electron flux as a function of distance from the beam centre for primary beam (blue, 0.5 nA, 20kV, $FWHM_B$ = 180 nm, FW(99.9%) = 450nm) and backscattered electrons. b) Schematic interpretation of the deposition process in the central region (upper row) and in halo region (lower row) taking into account ligand co-deposition. Taken from [34].

3.1.5 Electrical properties of nanowires

The resistivities of the nanowires, deposited using the methodology described in section 2.7 are presented in table 3.1.4. Two wires were deposited for each compound, one deposited a single-pixel line and one 30 x 1 μm^2 rectangle. FEBID parameters for each type of deposits were shown in chapter 2.7. Two types of wire were prepared to investigate the influence of FEBID conditions on obtained resistivities. The line was deposited with 500000 passes and 10 μs dwell time, resulting in the total dose of 1556 nQ/μm^2. Rectangles were deposited with 800 passes and 1 μs of dwell time, which resulted in a dose nearly two orders of magnitude lower: 19 nQ/μm^2. Although the size of the rectangle (30 x 1 μm^2) and the length of the single pixel line (30 μm) is bigger than the typical sizes of the nanowires (<100 nm) the intended thickness of the wires is in nanoscale, meaning ≤ 100 nm, thus the term "nanowires" was used. Each wire was measured several times, in at least five different current ranges, from 100 nA up to 700 μA. Higher currents were used only for the wires, which exhibited the lowest resistance, obtained in the lowest current range to avoid burning the wires due to Joule-Lenz heating. Some of the wires deposited between six electrodes were also measured by changing the probe electrodes. To each curve a linear function was fitted, the slope of which corresponds to the resistance of the wire. The resistances from all ranges were averaged and the resistivity of an individual wire was calculated using the dimensions of the wires with formula (2.1) given in section 2.7. Figure 3.1.9 shows a typical I-V results for one of the wires with the fitted curve.

The substrate for four-point probe measurements consisted of two sets of electrodes, which allowed for in two wires deposited per one precursor. However, not all of the wires could be measured due to electrode failures (scratches, lift-off problems) or melt-down during the measurements.

Table 3.1. 4 Average resistivities measured for different carboxylates and the range of achieved results. For first three compounds only one wire has been measured, for the two last precursors, the results come from the measurements of two wires, as it was explained above the table.

Compound	**Average Resistivity (μΩcm)**	**Resistivity range (μΩcm)**
$Ag_2(\mu\text{-}O_2CC(Me)_2Et)_2$	$3.2 \cdot 10^2$	$(1.42 - 2.21) \cdot 10^2$
$Ag_2(\mu\text{-}O_2C^tBu)_2$	$3.2 \cdot 10^3$	$(3.18 - 3.27) \cdot 10^3$
$Ag_2(\mu\text{-}O_2CC_3F_7)_2$	$2.0 \cdot 10^4$	$(1.92 - 2.08) \cdot 10^4$
$Ag_2(\mu\text{-}O_2CC_2F_5)_2$	$4.5 \cdot 10^2$	$(3.83 - 4.85) \cdot 10^2$
$Ag_2(\mu\text{-}O_2CC_2F_5)_2$	$7.3 \cdot 10^1$	$(7.09 - 7.34) \cdot 10^1$
$Ag_2(\mu\text{-}O_2CCF_3)_2$	$2.5 \cdot 10^1$	$(2.14 - 2.78) \cdot 10^1$
$Ag_2(\mu\text{-}O_2CCF_3)_2$	$9.3 \cdot 10^5$	$(7.33 - 10.68) \cdot 10^5$

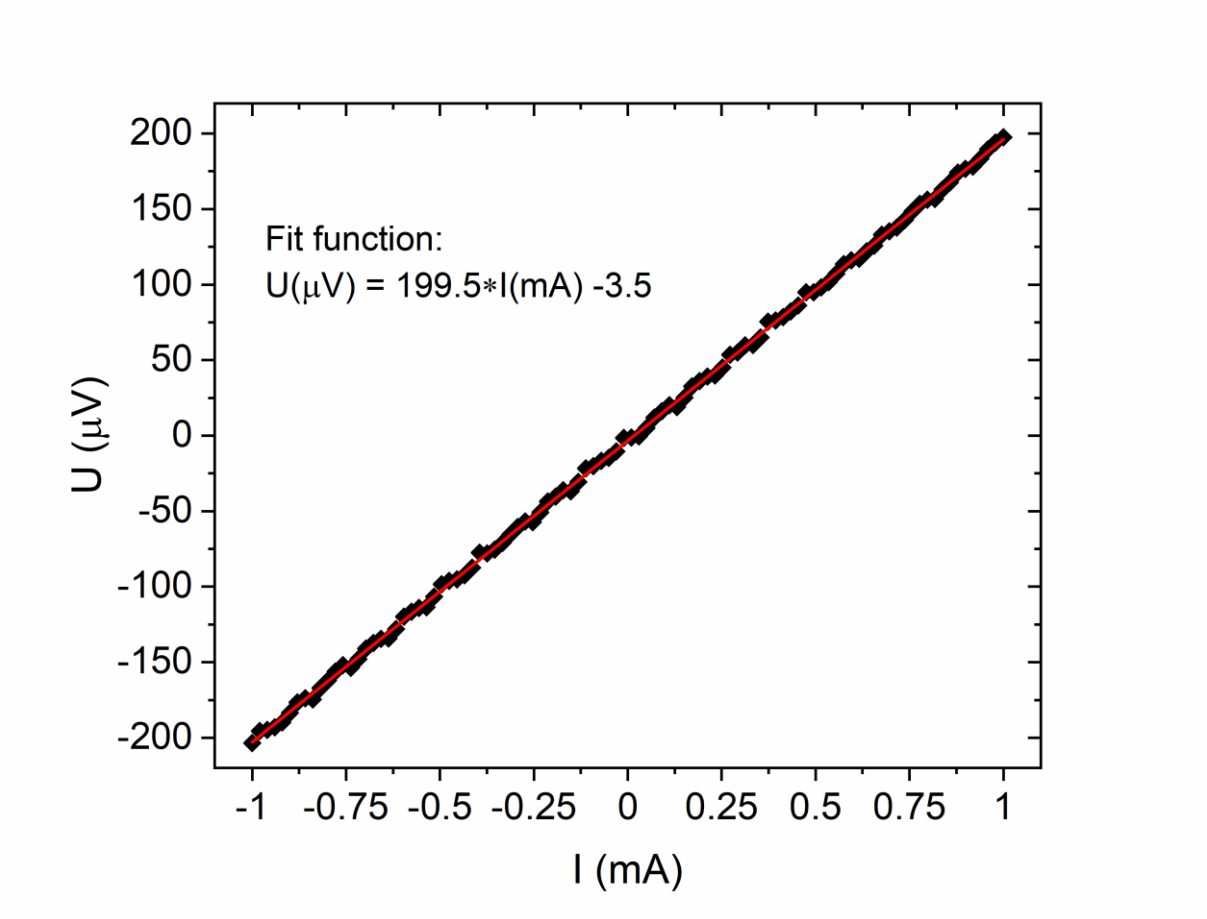

Figure 3.1.9 Exemplary voltage-current linear dependence (black) with fitted function (red line) for the deposit made with $Ag_2(\mu\text{-}O_2CCF_3)_2$. The resistance was $2.00 \cdot 10^1$ μΩcm.

The silver wires exhibited a linear voltage-current dependencies in the measured current ranges, indicating a metallic type of conductivity. The measured values for our wires, collected in the table 3.1.4, are one to even five orders of magnitude higher, than the resistivity of pure bulk silver, which is of 1.6 μΩcm at RT. There are two possible explanations of it: 1) low metal content in the material, 2) granular morphology of the deposited material. Both reasons can explain why all of measured resistivities are lower than the one of pure silver. For each silver microwire, the silver content was between 50 and 65 at.%. Synthetic graphite has a resistivity around $1.5 \cdot 10^4$ μΩcm [139]. An amorphous carbonaceous matrix co-deposited between the pure Ag crystals most probably has even higher resistivity than graphite, which is of four orders of magnitude higher than the resistivity of pure silver, 1.6 μΩcm. It can be concluded that the carbonaceous matrix is responsible for such a low resultant conductivity of the wire. The second reason is the granular form of the material. In such a case, the resistivity depends mainly on the occurrence (or not) of the percolation of grains. Tightly packed grains will have better conductivity, than those loosely connected. The size of the grains also plays a role, however, the most important factor is the contact surface between the grains. Granular,

percolated structure can be treated like a bulk, porous nanowire. The total contact surface between grains is usually lower than the surface area of a cross-section estimated from AFM profiles, thus corresponding to the higher resistivity. Low degree of percolation of silver grains may also influence the contact resistivity between the gold electrode and the wire, further decreasing measured resistance.

The evident example is the case of two different structures deposited with $Ag_2(\mu\text{-}O_2CCF_3)_2$. Both were deposited with different patterning strategies (single pixel line and rectangular deposit). The wires are shown in Figure 3.1.10. The resistivity difference between these wires reached four orders of magnitude, even though they were made with the same precursor and they have comparable silver content of 50 and 63 at.%. However, as can be seen in the Figure 3.1.10, wire a) is thicker and its grains are well-connected, while wire b) is composed of loosely connected grains. As a side note, it has to be explained why a single-pixel line is visibly thicker and wider than a rectangular deposit. The line was deposited with the total dose of 1556 nQ/μm^2. Rectangles were deposited with a dose nearly 2 orders of magnitude lower: 19 nQ/μm^2. For both deposits the same point pitch of 6 nm was used. Assuming similar thickness increment per dose of electrons this can explain why the single pixel line is thicker. As in previous experiments, the beam size was around 450 nm in diameter (FW(99.9%)). Slight thermal drift may have caused the increased width of the single pixel line. Furthermore, as the thickness of the line grew, some of the electrons were forward-scattered, broadening the deposit further.

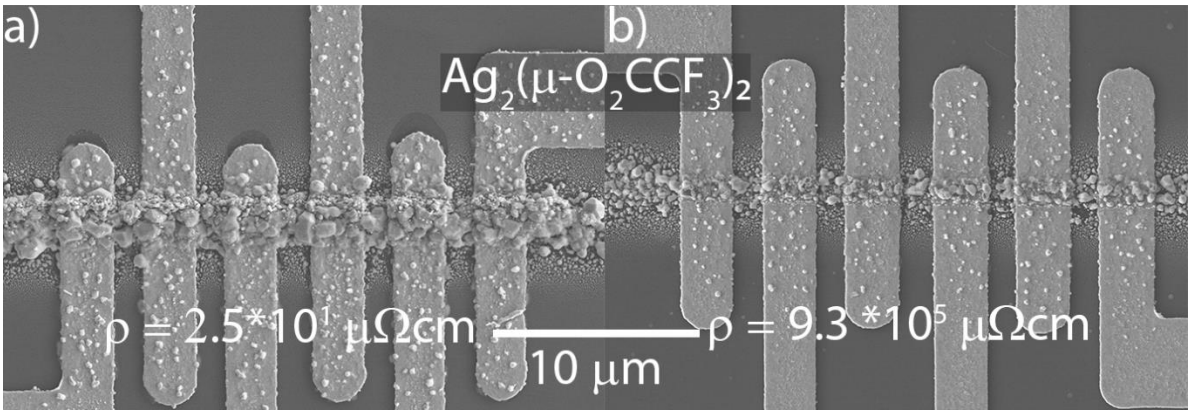

Figure 3.1.10 Nanowires deposited with $Ag_2(\mu\text{-}O_2CCF_3)_2$ and their resistivities measured with four-point probe method. a) A single-pixel line deposit; b) 30x1 μm^2 rectangle deposit. Both deposits were made at 20kV of acceleration voltage and current around 0.9nA. The exact FEBID parameters for both deposits are listed in Experimental section 2.7.

3.1.6 Temperature dependence of resistivity

The temperature dependence of resistivity was measured using PPMS apparatus. The wires were deposited on especially designed substrate, as it was described in the chapter 2.7. For each compound two wires were deposited, a single-pixel line and a rectangle. Out of ten wires, it was possible to measure seven. The most probable reason for this is that there was a slight mismatch between the position of probe electrodes and contact pads on the substrate, which was a result of cleaving 1x1 cm^2 Si pieces from the Si wafer. In the case of the three carboxylates $Ag_2(\mu\text{-}O_2CCF_3)_2$, $Ag_2(\mu\text{-}O_2CC_2F_5)_2$ and $Ag_2(\mu\text{-}O_2C^tBu)_2$ the resistivity versus temperature curve was a linear function, which confirms a metallic type of their electrical conductivity. A significant residual resistance at 4 K reveals a large number of defects in their crystal structure. The relative residual resistivities (RRR) for each compound are listed in Table 3.1.5. For a comparison, all of them were also normalised to the resistivity value for 273K (0°C).The exemplary graph depicting the normalised resistivity of $Ag_2(\mu\text{-}O_2C^tBu)_2$, $Ag_2(\mu\text{-}O_2CC_2F_5)_2$ and $Ag_2(\mu\text{-}O_2CCF_3)_2$ is presented in Figure 3.1.11.a. Figure 3.1.11.b shows the resistivity vs temperature graphs for a pure bulk silver sample.

What can be noticed, is that the values of resistivity at RT for all compounds is either the same as ($Ag_2(\mu\text{-}O_2CCF_3)_2$) or lower than the values measured before (see Table 3.1.4). The lower value may come from different grain sizes and/or defects content. Difference in deposition condition, even small, may cause the growth of bigger and better connected grains, which may result in lower resistivity of the wire. The wires were deposited using the same acceleration voltage and similar currents (0.95 nA for the ones measured only at RT vs 0.84 nA for wires used for temperature dependant studies). The stage and GIS temperatures were similar, with a differences in the range of 5 K. Dwell times and point pitch were the same. It is then possible that smaller thermal drift in the case of samples prepared for temperature dependent measurements could cause better percolation of grains and, thus, lower resistivity.

Table 3.1. 5 Relative residual resistivities for compounds showing metallic type of resistivity vs temperature and the value of resistivities at room temperature.

Compound	$\boldsymbol{RRR = \frac{\rho(273K)}{\rho(4K)}}$	$\boldsymbol{\rho(RT)}$ **(μΩcm)**
$Ag_2(\mu\text{-}O_2CCF_3)_2$	2.26	25
$Ag_2(\mu\text{-}O_2CC_2F_5)_2$	2.68	12
$Ag_2(\mu\text{-}O_2C^tBu)_2$	1.25	260

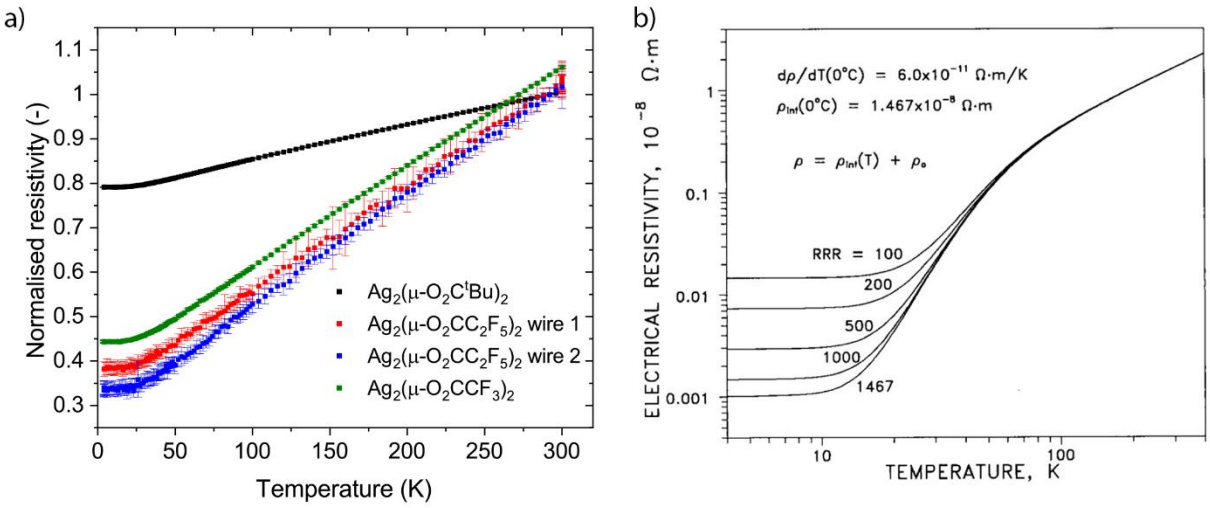

Figure 3.1.11 a) Normalised resistivity vs temperature measured for nanowires deposited with different silver carboxylates. b) Resistivity for different pure silver samples as a function of temperature; taken from [140].

The resistivity of metals has two components, as shown in the following equation:

$$\rho = \rho_L(T) + \rho_i \quad (3.1)$$

The first one, ρ_L, which decreases with decreasing temperature, comes from electrons-phonons interactions. As phonons are quasi-particles representing oscillations of the crystal structure of atoms, by reducing the temperature the amplitude of oscillation is also reduced, resulting in decreased material resistivity [141]. The residual resistivity is an effect of interactions between conduction electrons and defects or intrusions in the crystal structure. The more the real structure differs from the ideal crystal, the larger the residual resistivity will be. High value of relative residual resistivity ratio $\left(\frac{\rho(273K)}{\rho(4K)}\right)$ means that the contribution of the phonon-originated, temperature-dependent part of resistivity of the material is dominant. Low value represents the situation, where the crystal structure is full of defects, doping atoms or boundaries (e.g. grain boundaries) [141]. Comparing the RRR values from Figure 3.1.11.b to the ones from 3.1.5 it can be noticed that they are significantly lower, with the lowest obtained for $Ag_2(\mu\text{-}O_2C^tBu)_2$. Low $\frac{\rho(273K)}{\rho(4K)}$ values, compared to pure bulk silver, can be explained with the low metal content and developed morphology of the deposited nanowires. The produced structures are granular with, at best, around 76 at.% of silver (the best achieved value for square deposits, most probably the metal content in linear deposits is lower). Moreover, the diffraction pattern exhibits rings, which indicate a highly polycrystalline (or nanocrystalline) structure of the deposits. In such deposits, the electrons from the current are strongly scattered

on the grain boundaries, defects and co-deposited atoms of ligands, lowering the RRR value. Lower metal content of the deposits made with $Ag_2(\mu\text{-}O_2C^tBu)_2$ compared to deposits made using $Ag_2(\mu\text{-}O_2CCF_3)_2$ and $Ag_2(\mu\text{-}O_2CC_2F_5)_2$ (see Table 3.1.2) can explain why the nanowires fabricated with this compound had the lowest RRR value.

For the two other precursors, $Ag_2(\mu\text{-}O_2CC_3F_7)_2$, $Ag_2(\mu\text{-}O_2CC(Me)_2Et)_2$, the resistivity vs temperature graphs do not look similar to the ones plotted for other carboxylates. For all measured wires the resistivities actually decrease with the increase of the temperature, as can be seen in Figure 3.1.12.

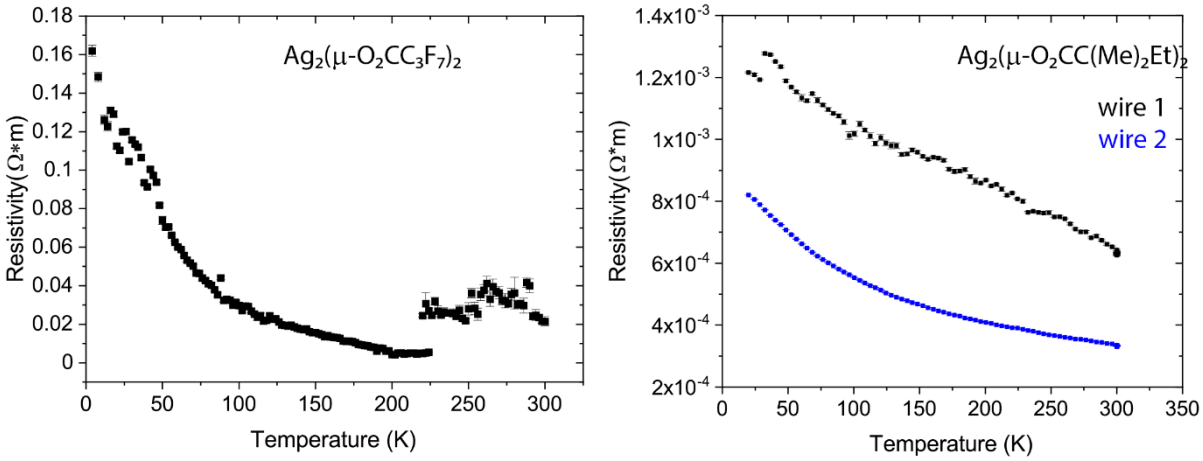

Figure 3.1.12 Temperature dependence of resistivity for FEBID nanowires made with $Ag_2(\mu\text{-}O_2CC_3F_7)_2$ (left) and $Ag_2(\mu\text{-}O_2CC(Me)_2Et)_2$ (right).

The behaviour of resistivity vs temperature curves resembles more a semiconductor type of electrical conductivity, rather than the metallic one. Resistivity at RT of a wire made with fluorinated $Ag_2(\mu\text{-}O_2CC_3F_7)_2$ is two orders of magnitude higher than the values measured for this compound on different wires. The same can be noticed for $Ag_2(\mu\text{-}O_2CC(Me)_2Et)_2$. It is not clear why, despite their linear U(I) characteristics, these compounds show an inverse dependence between resistivity and temperature. This kind of behaviour was observed previously by Huth et al. [53] for their nanogranular deposits. In their work, to describe the conduction-temperature dependence of their samples, they proposed a set of two functions. A stretched exponential dependence:

$$\sigma = \sigma_0 \exp\left(-\left(\frac{T_0}{T}\right)^{\frac{1}{2}}\right)$$

where σ is the conductance, σ_0 and T_0 are constants; and a power dependence:

$$\sigma = \sigma_0 + bT^{\beta}$$

with σ_0, b and β are constants.

The stretched exponential function corresponds to the conductance model, where the electrons are "hopping" (tunnelling) between grains of pure metal embedded in non-conductive matrix. However, they did not give a satisfying explanation of the power function. It is possible then, that in the case of granular silver deposits we also observe such a behaviour. The fluorinated $Ag_2(\mu\text{-}O_2CC_3F_7)_2$ exhibits the lowest silver content of all presented carboxylates and the highest fluorine content. The metal content of $Ag_2(\mu\text{-}O_2CC(Me)_2Et)_2$ was higher, although the connections between silver particles could be poor enough so the electrons had to tunnel between conducting silver particles. To address properly these issues, a direct systematic study would have to be further conducted, focusing on the dependence between FEBID conditions, purity, size of the silver particles and the electrical conductivity of the deposit.

3.1.7 Vertical pillars

For the application of silver in plasmonics, it is important to create three-dimensional high-purity silver structures. We reported 3D silver pillars created via constant spot irradiation [142]. In our work, FEBID experiments with two silver carboxylates, $Ag_2(\mu\text{-}O_2CC(Me)_2Et)_2$ and $Ag_2(\mu\text{-}O_2CC_2F_5)_2$, were performed. For each precursor, besides constant-irradiation spot, a serious of dots, with dwell times from 100 ns to 5 µs were created. For each one out of eight dwell times, a series of 10 dots were created. By measuring the height of the deposits made with different dwell times with AFM, it was observed, that in the case of non-fluorinated carboxylate there is no correlation between deposition exposure time and its height. Such a correlation was observed for the fluorinated complex – higher deposits were achieved for longer dwell times [142]. This fact suggests, that it may be impossible to grow three-dimensional structures using non-fluorinated carboxylates. Three continuous-exposure spot deposits are presented in figure 3.1.13. FEBID using $Ag_2(\mu\text{-}O_2CC(Me)_2Et)_2$ resulted in a completely flat structure, while for both $Ag_2(\mu\text{-}O_2CC_2F_5)_2$ and $Ag_2(\mu\text{-}O_2CCF_3)_2$ vertical, high aspect-ratio structures were deposited. The deposits were made with different exposure times (5 minutes for non-fluorinated, several hours for $Ag_2(\mu\text{-}O_2CC_2F_5)_2$ [142] and 70 minutes for $Ag_2(\mu\text{-}O_2CCF_3)_2$ however as it was proven, that exposure times do not correlate with the height of the deposit for $Ag_2(\mu\text{-}O_2CC(Me)_2Et)_2$, it can be assumed, that longer exposure times would not result in growing a pillar.

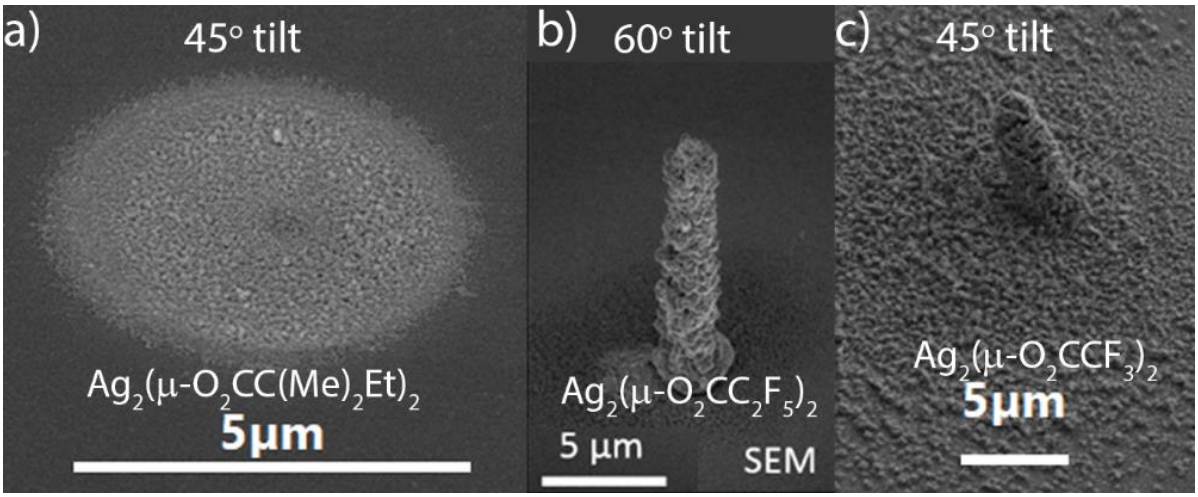

Figure 3.1.13 Tilt view SEM pictures of three continuous exposure spot deposits: a) completely flat made with $Ag_2(\mu\text{-}O_2CC(Me)_2Et)_2$ for 5 minutes of exposure time with 20 kV and 0.5 nA of beam current; columns deposited with b) $Ag_2(\mu\text{-}O_2CC_2F_5)_2$ with 15 kV and 0.5 nA of the beam current irradiated for several hours and c) $Ag_2(\mu\text{-}O_2CCF_3)_2$ with 20 kV and 0.6nA of beam current both with 70 minutes exposure time. Tilt angle is written on each picture. Image (b) taken from [142].

3.1.8 Comparison between carboxylate precursors

Silver carboxylates are a novel and very promising family of potential FEBID precursors. For all examined compounds the metal content of as-deposited structures was above 50 at.%. This is significantly higher than 15-25 at.% of metal typically obtained using commercially available precursors, like $Me_3CpPtMe$, $W(CO)_6$ or MeAu(acac). In all cases, the deposits had granular morphologies with particle size varying between different compounds, however, typically larger for fluorinated and smaller for non-fluorinated complexes. The granularity of the deposited material may limit its possible applications, as they would cause light scattering. Large, but non-percolated particles reduce the electrical conductivity of the deposited material, as was observed for two deposits made with $Ag_2(\mu\text{-}O_2CCF_3)_2$ and for deposits prepared with $Ag_2(\mu\text{-}O_2CC_3F_7)_2$ and $Ag_2(\mu\text{-}O_2CC(Me)_2Et)_2$ in the study of temperature dependence of resistivity. Diffraction measurements performed using TEM indicated the presence of pure silver, so the bonds between silver atoms and organic ligands were successfully cleaved. This is the first indicator that carboxylates are good candidates for precursor for FEBID, as the possibility to cleave the metal – ligands bonds reduces the possibility of incomplete dissociation of the precursor molecule. In a second step, the cleaved ligands must desorb to leave a clean silver deposit. To evaluate properly, which carboxylate is an optimal candidate for FEBID precursor, their properties have been collected in Table 3.1.6.

Table 3.1.6 Properties of materials deposited with silver carboxylates.

Compound	**Metal content range (at%)**	**Lowest electrical resistivity at RT (μΩcm)**	**Type of *R(T)* dependence**	**3D structures**	**Thermal decomposition in VTGA**
$Ag_2(\mu\text{-}O_2CC(Me)_2Et)_2$	57 – 76	$1.42 \cdot 10^2$	Non-metallic	No	Yes
$Ag_2(\mu\text{-}O_2C^tBu)_2$	50 – 61	$3.18 \cdot 10^3$	Metallic	No	Yes
$Ag_2(\mu\text{-}O_2CC_3F_7)_2$	34 – 57	$1.92 \cdot 10^4$	Non-metallic	No	No
$Ag_2(\mu\text{-}O_2CC_2F_5)_2$	63 – 76	$3.83 \cdot 10^2$	Metallic	Yes	No
$Ag_2(\mu\text{-}O_2CCF_3)_2$	65 - 74	$2.14 \cdot 10^1$	Metallic	Yes	No

Comparing all the properties of the carboxylates discussed in this chapter, it can be concluded that fluorinated compounds are better precursors on average. In VTGA they left the least amount of residuals, which indicates that they do not thermally decompose in vacuum (or at least they do not to such an extent as non-fluorinated complexes). Moreover, $Ag_2(\mu\text{-}O_2CCF_3)_2$ and $Ag_2(\mu\text{-}O_2CC_2F_5)_2$ exhibited the best metal content range out of five complexes measured and the lowest resistivity. The highest metal content may be an effect of the shortest ligands desorption time. The influence of ligands desorption time will be discussed in detail in chapter 5. Additionally, both compounds showed a metallic type of electrical conductivity in temperature dependent studies. Furthermore, both aforementioned complexes exhibited a possibility of direct writing of 3D structures, which is important from the point of view of the application of silver in plasmonic nanostructures. Lower metal content achieved with $Ag_2(\mu\text{-}O_2CC_3F_7)_2$ indicates that there is a certain limit in the length of the carbon-fluoride chain, which can be used for clean silver FEBID. It can be therefore concluded, that from the point of view of FEBID, the most promising precursors are $Ag_2(\mu\text{-}O_2CCF_3)_2$ and $Ag_2(\mu\text{-}O_2CC_2F_5)_2$.

3.1.9 Outlook

Although the presented results show a great potential of silver carboxylates as precursors for FEBID, there are still several challenges, which need to be addressed. First, there is most probably only very narrow, lower than 10 K temperature window, in which 3D growth was observed [142]. This makes the carboxylates hard to apply to processes needing high repro-

ducibility. Moreover, the deposited structures are granular, which also hinders the possibility of using them in nano-optics or plasmonics, as the silver particles would cause light scattering. Although TEM investigations indicated the cleavage of metal-ligand bond, it is unknown, what are the exact dissociation pathways, as there are no gas or condensed phase studies on these precursors until now. This issue will be addressed in chapter 4 of this Thesis, which introduces new measurement method referred to as focused electron beam induced mass spectrometry.

3.2 Heteroleptic Ru compounds

Results presented in the previous chapter are very promising from the point of view of metal content of the obtained structures. Despite the high metal content, results of FEBID using silver carboxylates exhibit several drawbacks, which in some cases can limit the application of such compounds in industrial processes. Deposited structures, although pure, are very granular, which can create problems in any photonic or plasmonic applications, as rough surfaces can cause light scattering. Moreover, due to their low volatility, both the gas injection system and the substrate have to be heated to temperatures often exceeding 150 °C. High sensitivity of silver carboxylates towards electron beam irradiation on one hand helps achieving impressive metal contents of as-deposited material, however, a halo forms around the deposit, which limits the locality of the process. All mentioned disadvantages could eliminate carboxylates as precursor for a metal, which can be potentially used for repairing photolithography masks. Masks repair is one of the most important applications of FEBID on an industrial scale. As was mentioned in Chapter 1, in new EUVL masks, Ru is considered as a potential capping layer, as it hardly oxidises in atmosphere and it is transparent for chosen extreme UV light. For this application, a smooth Ru layer surface is needed, as any roughness could create scattering of electromagnetic waves and result in decreased intensity of EUV used for the lithography process. As masks are created with extremely high precision, any halo deposition during FEBIB is a highly unwanted effect. Moreover, using stage heating can increase the time needed for deposition, as the substrate needs to stabilize after reaching a certain process temperature. It would further diminish the efficiency of the whole deposition process, which is significant drawback from the point of view of industrial applications. Taking into account all the mentioned effects, potential Ru precursor has to be volatile at room, or very close to room temperature. It should also create smooth-surface deposits, with negligible halos.

In this chapter, the use of $Ru(\eta^3\text{-allyl})(CO)_3Br$ and its derivate $Ru(CO)_4Br_2$ as FEBID precursors will be discussed. The first compound is not only interesting from the standpoint of potential industrial application, but also it creates an opportunity to examine the behaviour of three different ligand groups at the same time, under irradiation of a single electron beam. As this compound has been previously examined using both surface science and gas phase methods, FEBID experiments created the opportunity to discuss the results of three different electron-irradiation based types of experiments. Furthermore, the influence of different post-purification protocols on shape, morphology and metal content of the deposits made with $Ru(\eta^3\text{-allyl})(CO)_3Br$ will be discussed. By comparing the FEBID results using $Ru(\eta^3$-

allyl)$(CO)_3Br$ and $Ru(CO)_4Br_2$ the consequences of substitution of the allyl group by a halogen and carbonyl will be shown.

3.2.1 Chemical formulae and properties

The first compound, $Ru(\eta^3\text{-}C_3H_5)(CO)_3Br$ contains three carbonyl groups (CO), one allyl (C_3H_5) and one Br atom attached directly to the metal centre. The compound is volatile at room temperature therefore has to be stored in a fridge. It is not hygroscopic or and remains stable in air. It was evaporated with 80 mTorr of pressure at 30°C [119]. The compound was depicted on Figure 3.2.1 a).

The molecule of the second compound $Ru(CO)_4Br_2$ has a similar structure, however possesses four carbonyl groups instead of three and two bromine atoms instead of one. It also exhibits similar volatility as the allyl-containing compound, with 125 mTorr of pressure during evaporation at the temperature of 38 °C [143]. This compound is presented in Figure 3.2.1 b).

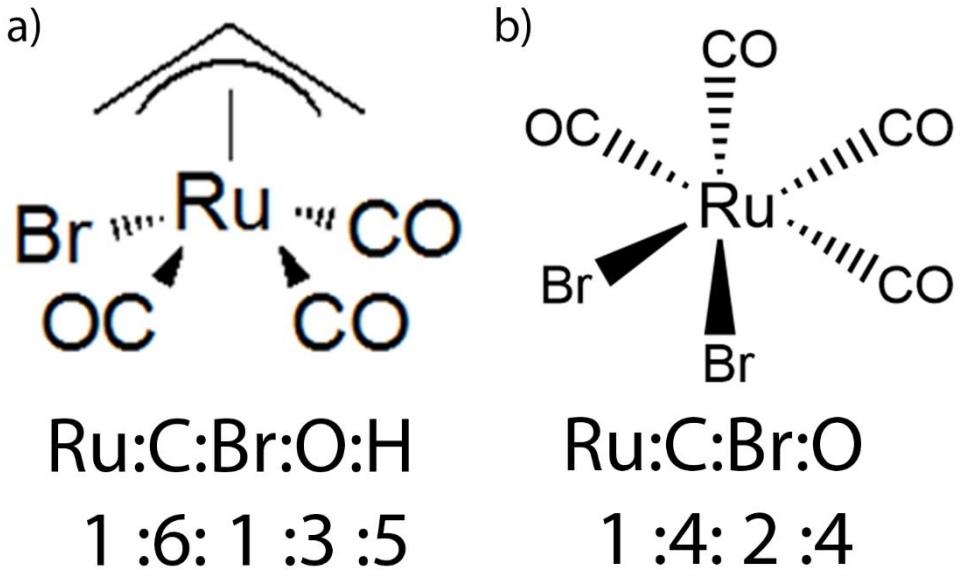

Figure 3.2.1 Structural formulae and proportions between the atoms of the ruthenium precursors studied in this chapter: a) $Ru(\eta^3\text{-allyl})(CO)_3Br$, b) $Ru(CO)_4Br_2$.

The first compound was investigated in gas phase by Thorman et al. [144]. In their crossbeam setup, they irradiate the gaseous precursor with a monochromatic, low-energy electron beam, to find possible dissociation pathways. These kind of measurements can even provide an energy dependence of relative dissociation cross section for different processes, namely DEA and DI. In their work, Thorman et al. proved that the most probable dissociation pathway is a loss of carbonyl ligands, for both DEA and DI processes [144]. Cleavage of the allyl-metal

bond was also observed, however, it was less effective than the cleavage of carbonyl. Per each precursor's molecule, 0.9 CO groups are lost due to DEA, when for allyl group it was only 0.2. The DI process resulted in the loss of 2.1 CO groups vs only 0.3 allyl ones, per one $Ru(\eta^3\text{-}C_3H_5)(CO)_3Br$. $[C_3H_5]^+$ ions were not observed leaving a substrate's surface during surface science studies as volatile species in the mass spectrum [119]. Spencer et al. condensed 2-3 nm of $Ru(\eta^3\text{-allyl})(CO)_3Br$ on amorphous carbon an polycrystalline gold in ultra-high vacuum at -168°C. The thin layer was then irradiated by a broad e-beam with 500V of acceleration voltage [119]. Using X-ray photoelectron spectroscopy (XPS), they observed a continuous decrease in intensity of both O (1s) and C (1s) peaks, indicating the dissociation and desorption of carbonyl groups. Bromine and three carbons (as much as in allyl groups) remained adsorbed. The very slow loss of Br atoms was observed only after 50 hours of additional irradiation [119]. However, the low stage temperature during these studies (-168 °C) should be noted, as it may have quenched desorption, compared to room temperature conditions used in FEBID experiments presented in this study. For the case of Br, it was observed in gas phase that the bond between the metal and halogen can be cleaved due to DI, however, like in the case of allyl, it was less effective than the cleavage of Ru-CO bonds (0.4 Br per one precursor's molecule vs 2.1 CO). We can expect then, the loss of all or nearly all carbonyl ligands due to e-beam irradiation. Bromine-ruthenium bonds should also be cleaved (at least for some molecules). In surface science experiments, Br atoms were removed due to interaction with a high dose of electrons during long-time exposure. As in FEBID, the doses of electrons are much higher and the temperatures of the stages (higher than -168 °C), it can be expected that the cleaved Br atoms will also desorb from the surface. The allyl group most probably will stay on the surface either due to incomplete dissociation or it will be co-deposited.

3.2.2 Morphology and composition of deposits made with $Ru(\eta^3\text{-}C_3H_5)(CO)_3Br$

Several FEBID experiments were performed using $Ru(\eta^3\text{-allyl})(CO)_3Br$. To measure the composition of the deposited material, square deposits with nominal dimensions of 3x3 μm^2 were prepared using the spiral scanning strategy. The deposition process was performed using 0.65 nA of beam current, 20 kV of acceleration voltage. The dwell time was set to 10 µm and the point pitch to 6 nm. The stage was kept at room temperature and the GIS was heated up to 35°C to increase the flux of molecules. The linear in-chamber GIS was used, to which a final needle with an inner diameter of 780 nm was attached. The flux of precursor was $3.54 \cdot 10^{17} \frac{\text{molecules}}{\text{s}\cdot\text{cm}^2}$, which using a GIS Simulator software [145, 146] was used to estimate the flux of the precursor impinging on the substrate, which was equal to $7.6 \cdot 10^{16} \frac{\text{molecules}}{\text{s}\cdot\text{cm}^2}$. A typical

deposit is presented in Figure 3.2.2.a. The red circle marks the position of the beam during the EDX measurement. The radius of the circle corresponds to the maximum radius of the area from which X-rays were collected. As can be noticed, there are two, very slight lines visible on the diagonal of the square. This is an artefact of the chosen patterning strategy. As was widely described by Winkler et al. [20], each scanning strategy has very specific effect on the morphology of the deposited material. Spiral scanning may result in triangular sub-structure on the top of the flat structure. The triangles can be observed using AFM (Figure 3.2.2.c). Square deposits made with $Ru(\eta^3\text{-allyl})(CO)_3Br$ also have visible halos. However, its thickness is much lower, comparing to the halos observed for silver carboxylates and it does not exceed 40 nm. It signalises that the used Ru compound is less susceptible towards halo formation than silver complexes. It can be explained by various effects including lower susceptibility of the Ru complex towards electron beam irradiation, as well as the influence of the stage temperature. High stage temperature used for Ag carboxylates enhanced the surface diffusion of precursor molecules towards irradiated area, however, due to their susceptibility towards e-beam irradiation, they were deposited already in the halo. Ru FEBID was performed with the stage kept at room temperature, which limited the influence of diffusion as a source of new precursor molecules, which combined with lower e-beam susceptibility resulted in significantly thinner halo. As Ru is a metal, which can be applied to EUVL masks corrections, small halo is an advantage, as it allows for creating high lateral resolution deposits. The average composition of a square deposit is presented in Figure 3.2.2.b. Ru stands only for around 23 at.%. The amount of Br equals that of Ru and there are twice as many C atoms than Ru atoms. Oxygen stands only for 8 at.% of the deposited material. All presented results were measured with 3 at.% of uncertainty margin. Although the obtained metal content is much lower, than values presented in previous chapter for silver, it is still double the metal content of materials deposited with $Ru(EtCp)_2$ [28, 147]. The thickness of the deposited material was around 550 nm, which, considering the 34 minutes of deposition time, gives in average 0.27 nm/s of growth rate. What can be noticed from the AFM scan, there is a pit around 75 ± 15 nm deep. The presence of the pit can be explained by the patterning strategy. When the beam is encircling the central area, it depletes the molecules from there. Additionally, the encircling beam prevents the molecules outside of irradiation area to diffuse to centre. The other possibility is that the effective dwell time, resulting from the real beam size and the point pitch is 14 times longer in the centre than on the sides. Longer dwell times may lead to denser deposits [148]. The average density of the deposit was estimated to be around 5.43 ± 0.26 g/cm^3.

The estimation is further described in detail in the experimental section and supporting information of Jurczyk et al. [101].

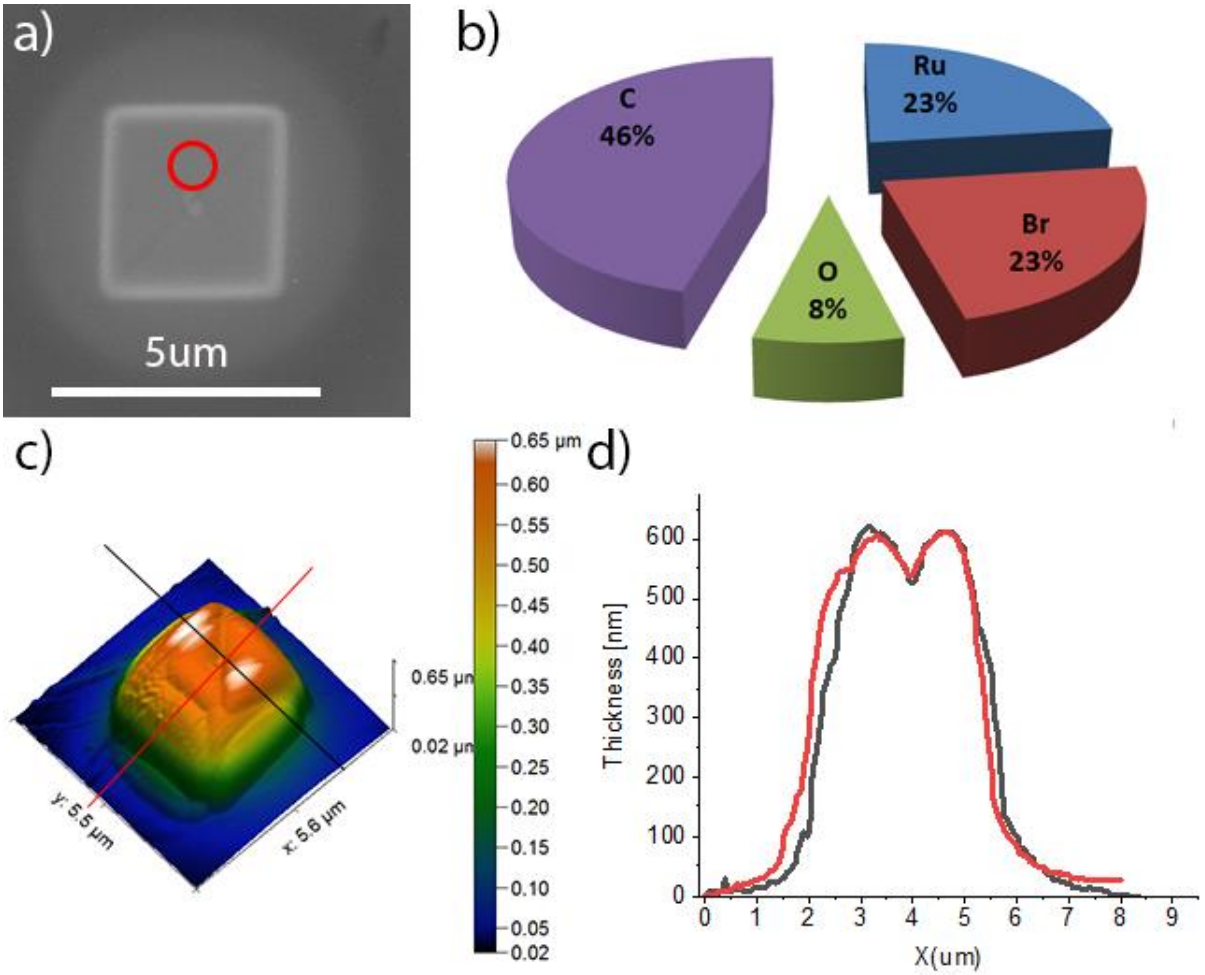

Figure 3.2.2 a) Top-view scanning electron micrograph of a typical 3 × 3 µm deposit on a native oxide Si substrate with the red circle symbolizing the EDX and WDS measurement area, with excitation range. b) Average composition of the deposit (in at. %, with uncertainty approximately 3 at.%). c) AFM 3D measurement of the shape of the deposit with marked line profile positions. d) AFM profiles measured through the centre of the deposit. Taken from Jurczyk et al. [101].

Normalising the obtained composition to one Ru atom, we can see that most of the oxygen (ca. 90%) and 4 out of 6 carbon atoms were lost compared to the stoichiometry of the pure precursor. The number of Br atoms is the same as in the pristine precursor molecule. Based on this result, we can state that carbonyl groups were mostly dissociated and desorb from the sample's surface. The rest of C atoms are most probably coming from the allyl group, although it should have 3 carbons per 1 Ru atom and in the deposit there are only 2. The cause of the removal of one additional carbon is more speculative. There are two main possibilities: either e-beam dissociated one of the bonds within the allyl group, creating volatile moiety with two carbons and one C being incorporated, or one of the three allyl groups was cleaved from the Ru atom and was able to desorb. Bromide was fully incorporated into the deposit,

meaning that the bond between Ru and Br was either not cleaved or the halogen was detached, however, it was co-deposited before it could desorb.

3.2.3 TEM measurements of $Ru(\eta^3\text{-}C_3H_5)(CO)_3Br$ deposits

Transmission electron microscopy measurements were performed using JEM 2200FS TEM from JEOL. Diffraction measurements were performed before imaging to avoid any changes in crystalline structure due to irradiation with the high-energy e-beam. Data from these measurements were analysed using C-spot software. The obtained diffraction patterns were fitted using C-spot database of patterns.

Special samples were prepared for TEM measurements. Series of pillars were grown at the edge of cut-in-half copper TEM grid. Each pillar was created with continuous exposure of one spot over 20 minutes with 25 kV of beam acceleration. The beam current was around 0.15 nA. The grown pillars were then coated with two protective layers of Pt-C, first one made using electron and the second using the focused ion beam. Afterwards, the pillars were thinned by the same Ga+ FIB, to electron transparency thickness. The pillars before and after e-beam and FIB pre-treatment are presented in figure 3.2.3.

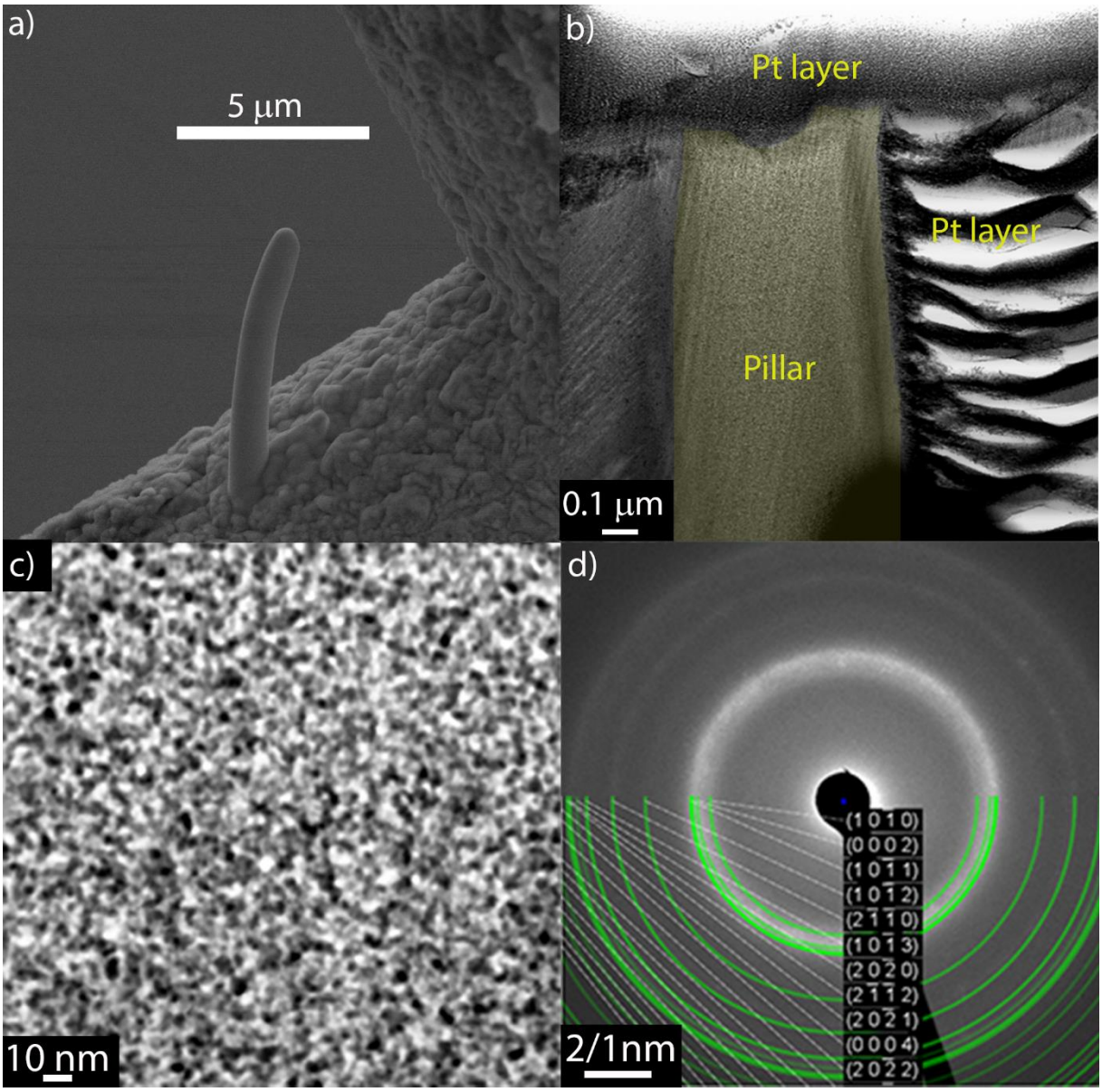

Figure 3.2.3 a) 70° tilt SEM image of one of the pillars prepared for TEM investigation; b) STEM image of the pillar (marked yellow) with protective Pt layer around; c) Bright-field STEM of pillar; d) electron-diffraction pattern of deposit matching the simulated pure Ru pattern (green lines).

Bright field scanning transmission electron microscopy image (BF-STEM) shows the nanogranular structure of the deposited material, with an average grain size around 2-3 nm. Electron diffraction revealed a nano-crystalline pattern. The measured rings match the ones of pure ruthenium. Thus, the visible grains are nano-crystals of pure Ru embedded in an amorphous C-O-Br matrix. The presented results indicate, that the ligand – metal bonds have been broken by electron induced dissociation. The low metal content of the deposited material is then rather an effect of co-deposition of cleaved ligands than incomplete dissociation of precursor molecules.

The comparison between stoichiometry, results of FEBID and condensed phase surface science measurements are gathered in table 3.2.1.

Table 3.2.1 Stoichiometry, composition of FEB deposit and condensed phase measurements, normalised to one Ru atom.

Element	Stoichiometry	FEBID	Condensed phase
Ru	1	1	1
Br	1	1.0	1→0.5
C	6	2.0	3.0
O	3	0.3	0

Comparing the obtained FEBID results with the aforementioned gas and condensed phase studies, there are certain similarities, which can be noted. For both types of measurement the loss of carbonyl groups was observed as well as in results obtained from FEBID. TEM results showing pure Ru grains suggest that bonds between the metal atom and ligands were cleaved. The possibility of bond cleaving between Ru and both the allyl and Br was presented in gas phase experiments reported by Thorman et al. [144]. Although no desorption of allyl groups has been observed in condensed phase (surface science) studies [119], they were performed in cryogenic temperatures, which limit the desorption (see formula 1.2), compared to FEBID performed at room temperature. Considering this and the gas phase measurement results, it can be stated, that the allyl ligands were cleaved, however, in most of the cases they were co-deposited. Only one allyl group out of three in average was able to desorb from the surface [101]. Other possibility is that the remaining carbon contamination is coming from dissociation of allyl ligands into some non-volatile moieties. The Ru-Br bond was most probably cleaved, however the Bromine was co-deposited on the surface [101]. No desorption of Br upon further irradiation with the electron beam was observed, which significantly differs from the observations made in condensed phase studies. On the other hand, FEBID was performed with constant gas supply which may have resulted in the burying of Br atoms below the incoming new precursor molecules [101].

3.2.4 Post purification of $Ru(\eta^3\text{-}C_3H_5)(CO)_3Br$ deposits

As the metal content of the as-deposited material was way below 100 at.%, which would be desired by EUVL mask reparation application, series of post purification experiments were performed to increase the metal content. The first post-irradiation treatment protocol included

heating up the samples to 450 °C and holding for 90 minutes in the pure oxygen atmosphere. The method successfully removed the bromine and most of the carbon from the deposit, although very high oxygen content reaching 60% indicated that the structure was partly oxidised. The morphology also changed, the deposit became more granular, compared to the flat top as-deposited structure. To reduce the oxide, the samples were heated for 180 minutes at 450 °C in an Advanced RICO MILA-5050 furnace in a forming gas atmosphere: 98 % N_2 and 2 % H_2. The oxide was reduced and the Ru content reached 83 at.%, however, the cracks appeared all over the surface of the deposit. As this could be an effect of oxygen leaving the volume of the structure due to forming gas reduction, the oxidation step was skipped in the next purification protocol. The sample was heated only in forming gas, with the heating time and maximum temperature set as previously stated. This post-purification protocol resulted in even higher-metal-content structure, with Ru content reaching up to 89 at.%. However, probably due to rapid and significant volume loss resulting from the removal of all bromine and most of the carbon, the structure cracked and started to delaminate from the substrate. The SEM micrographs, presenting the results of applied post-purification protocols, are shown on Figure 3.2.4.

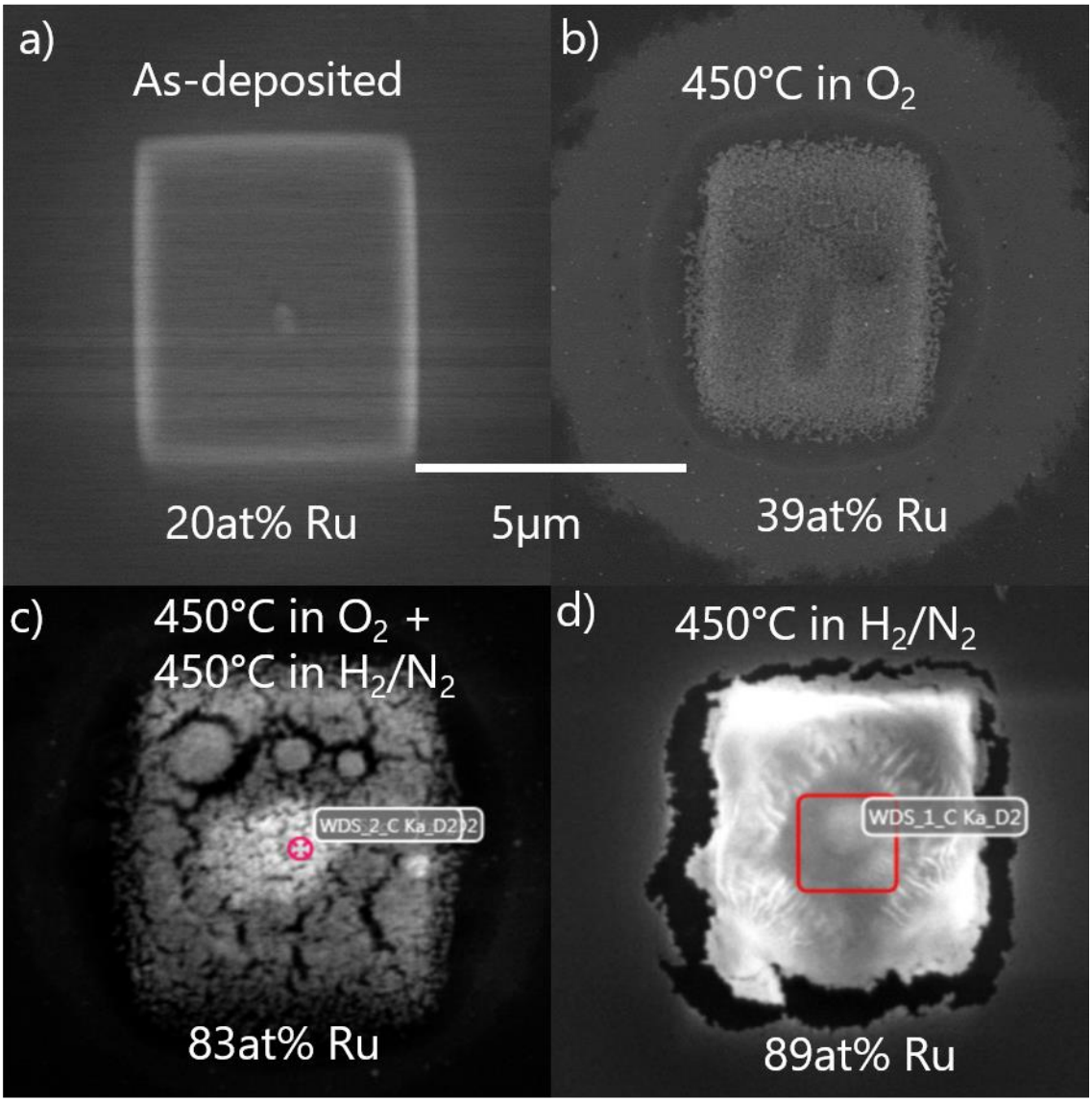

Figure 3.2.4 Morphology of 3x3 µm^2 squares deposited with Ru(η^3-C_3H_5)$(CO)_3$Br: a) as deposited; b) purified with heating at 450 °C in oxygen atmosphere for 90 min; c) heating subsequently in oxygen atmosphere and in forming gas at 450 °C for 90 minutes in each gas; d) heating up only in forming gas at 450 °C for 180 min. The darker substructures on image b) and brighter place on c) are the areas where WDS and EDX measurements were performed.

The deposit has a rectangular shape due to slight vertical drift. Images from Figure 3.2.4 b) and c) were made after EDS and WDX measurements and the substructures visible in the middle of the squares (darker for b) and brighter for c)) are spots where the beam was placed during these measurements.

Figure 3.2.5 gathers the compositions of the deposited and purified material, measured with quantified from EDX + WDS analyses.

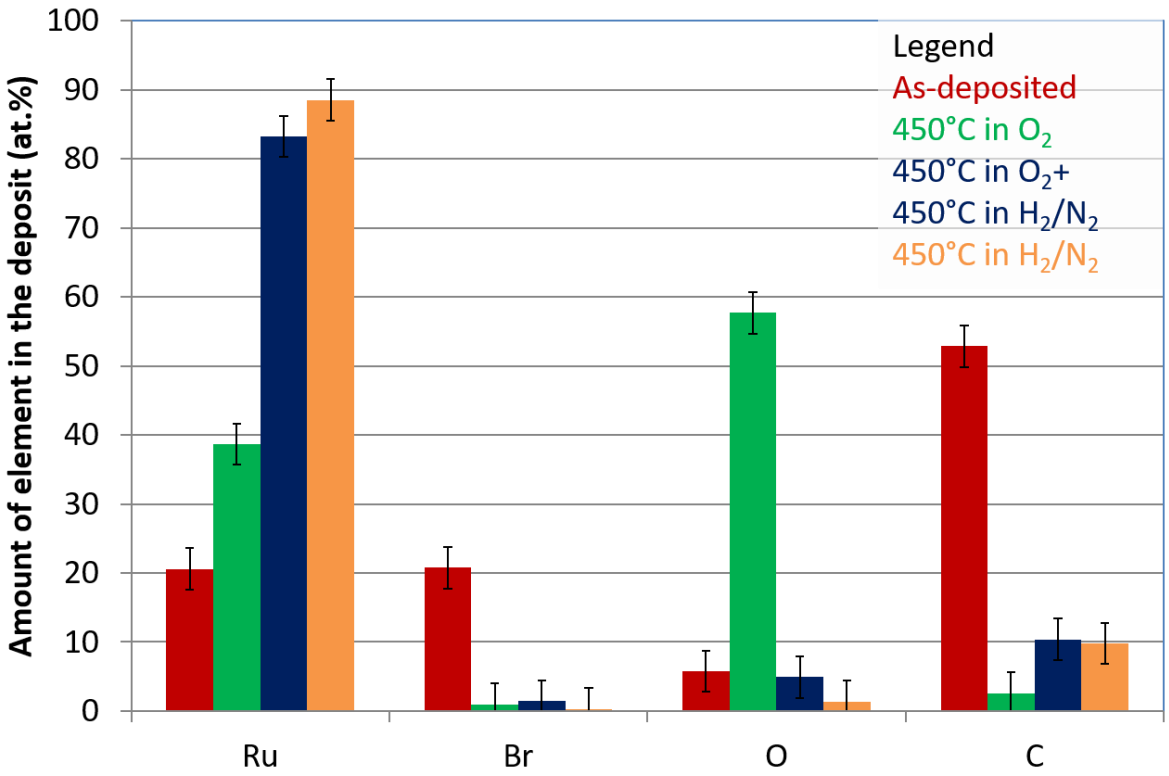

Figure 3.2.5 Comparison of compositions of as-deposited structure and compositions achieved due to different post-purification methods. The uncertainty was estimated to be 3 at.%, basing on the results for as-deposited structures.

As can be noticed, all purification protocols almost completely removed bromine from the deposit. The lowest Br content was observed for the one-step forming gas protocol. The final C-contents were comparable for both the one and two-step protocols. Despite achieving high deposit metal content, the deposit cracked during post-treatment, which is an important limiting factor in the possible application of the described process to create pure Ru structures. As the speed of the chemical reactions is often controlled by the temperature of the process, reducing the furnace temperature could slow down the purification process and in result help in avoiding cracks in the deposited material.

The most successful post-purification experiment was performed using Advanced RICO MILA-5050 furnace in reactive atmosphere of forming gas: 98 % N_2 and 2 % H_2, as this protocol proved to provide the highest Ru-contents. The process temperature was 300°C to slow down the purification reaction. The deposit was heated for 180 minutes.

Figure 3.2.6. presents the results of the optimised post-purification. The deposit preserved its square shape with only 9 ± 5 % of lateral dimensions shrinkage. However, the thickness of the structure decreased significantly, by 75 ± 1%. Therefore the total volume loss amounted to 79

± 2 %. Despite the large volume loss, no cracks were observed on the sample's surface, proving that using the one-step forming gas based purification enables obtaining high metal content flat structures.

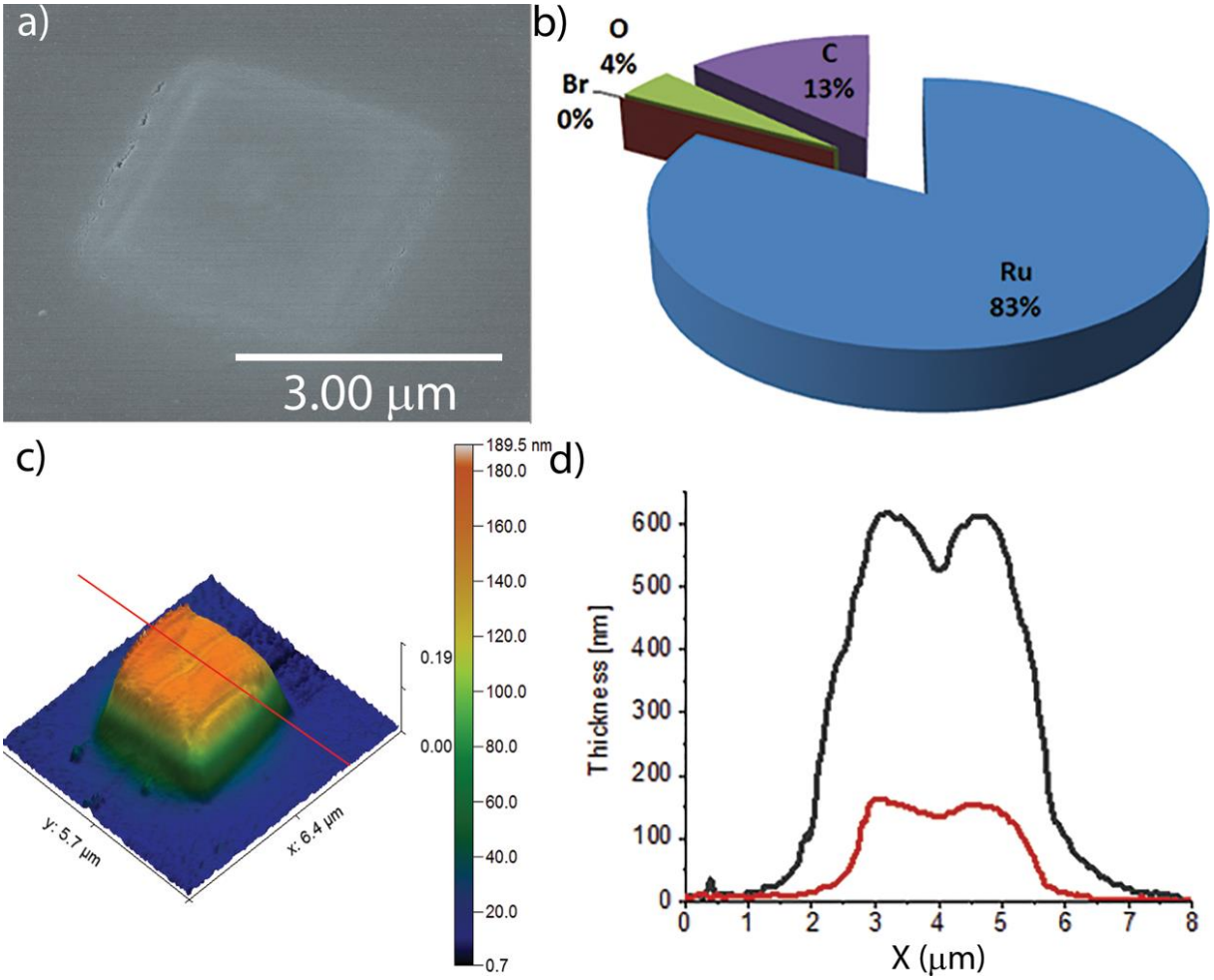

Figure 3.2.6 (a) 45° tilt view SEM of a typical square deposit purified with forming gas at 300 °C. (b) Results of EDX + WDS quantification. (c) AFM 3D measurement of the shape of the deposit after purification. The red line marks the position of the line profile in part d. (d) AFM profile measured before (black) and after (red) purification.

The significant volume loss was caused by the removal of most of the contaminants. Bromide desorbed completely, carbon was reduced to only 13 at.% and oxygen to 4 at.%. Ru content was on the level of 83 at.%. What should be highlighted, Ru did not oxidise, as it was in the case of water-vapour purification of Ru-C deposits made with $Ru(EtCp)_2$ [28]. In recent studies, a novel NH_3-based purification method has been reported to give similar metal content [120].

The entire deposition and purification process is depicted n Figure 3.2.7. The ongoing chemical reactions are also provided in reactions 3.1 (summarizes the electron induced dissociation reaction) and 3.2 (summarizes thermal purification). The volatile fragments proposed in the

second reaction are HBr and hydrocarbons. However, there is not enough data to state which exact fragments are leaving the surface due to heat-assisted forming gas purification.

$$Ru(\eta^3 - C_3H_5)(CO)_3Br \xrightarrow{e^-} RuBrC_2O_{0.3}(H_{0.44})^* + 3CO^{\uparrow} + C_xH_y^{\uparrow}\ (reaction\ 3.1)$$

$$RuBrC_2O_{0.3}(H)^* + N_2/H_2 \xrightarrow{450°C} RuC_{0.2}O_{0.05}(H_{0.04})^* + \left(HBr^{\uparrow} + C_xH_y^{\uparrow}\right)(reaction\ 3.2)$$

*H is not detectable with EDX nor WDS, thus its amount was estimated using the ratio C/H=9/2 by Bret at el. [137].

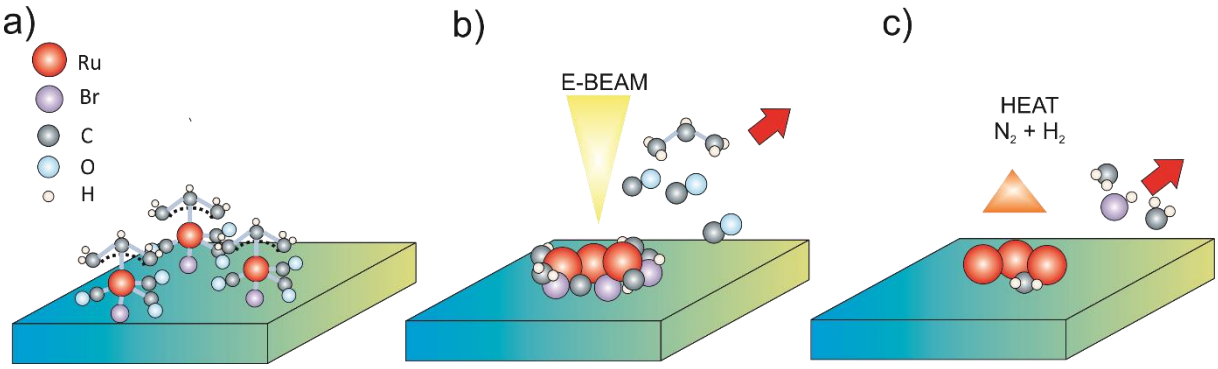

Figure 3.2.7 Schematic of (a) physisorbed precursor molecules covering the surface in an adsorption−desorption equilibrium surface concentration, (b) electron beam dissociated material and desorbing carbonyl and allyl species, and (c) material obtained after heating in reducing forming gas atmosphere creating volatile HBr and CHx species, leaving ruthenium on the surface. Taken from Jurczyk et al. [101]

3.2.5 Electrical properties of nanowires deposited with $Ru(\eta^3\text{-}C_3H_5)(CO)_3Br$

Two types of nanowires were deposited to investigate their electrical properties. The first type was a 30 µm long single pixel line, deposited with 20 kV of acceleration voltage, 0.6 - 0.7 nA of beam current, 10 µs of dwell time, 6 nm of point pitch and 100 000 passes. The other pattern was a 30x1 μm^2 rectangle, patterned with the same voltage, beam current, and point pitch. The dwell time was set to 1 µs and 800 passes were used. The rectangle was deposited with a spiral patterning strategy (outside to inside). Both patterns were used to examine the influence of FEBID parameters on the resistivity of deposited materials. Although the size of the rectangle (30 x 1 μm^2) and the length of the single pixel line (30 µm) is bigger than the typical sizes of the nanowires (<100 nm) the intended thickness of the wires is in nanoscale, meaning ≤ 100 nm, thus the term "nanowires" was used. Total dose used to deposit a line was 2407 nQ/μm^2 and for the rectangle 14 nQ/μm^2. The deposits are presented in Figure 3.2.8 a and b.

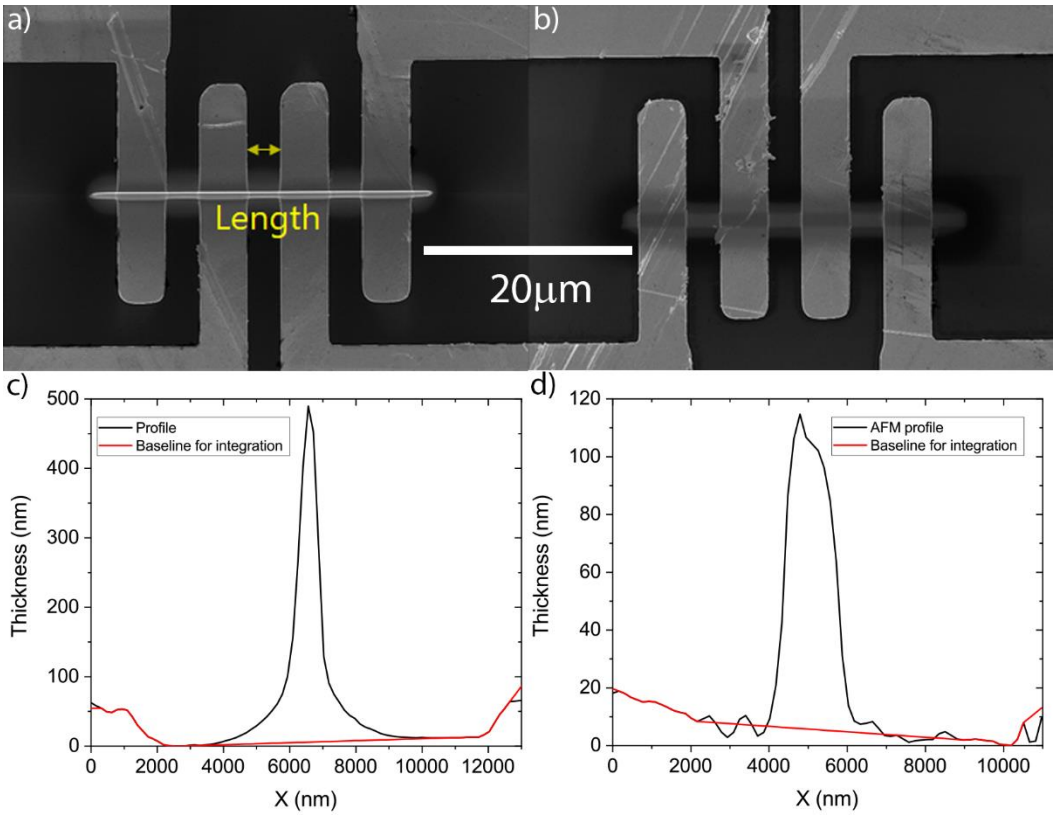

Figure 3.2.8 Upper row: micro-wires deposited for four-point probe electrical conductivity measurements: single pixel line a) and a 30x1 μm^2 rectangle b). Lower row: corresponding cross section profiles measured with AFM c) and d).

Prior to the measurements, the samples were studied with an AFM in tapping mode to extract the cross section profiles. Single-pixel lines were around 500 nm thick and the rectangles - around 100 nm. Cross section profiles were extracted using the procedure described in chapter 2.7. AFM scans were corrected for possible artefacts (tilt, scars) and then 2 pixel wide line profiles were extracted orthogonal to the wires. The cross sections with marked baselines are shown in Figure 3.2.8 c and d. The length of the wire was measured as a distance between the inner edges of the closest voltage electrodes (marked on figure 3.2.8. a). Resistivity was calculated using formula (2.1).

Figure 3.2.9 presents electrical conductivity vs. temperature graphs for both types of wires. As can be noticed, both graphs are non-linear and (except for the first few measurement points from the right graph), the conductivity of the wires increases with increasing temperature.

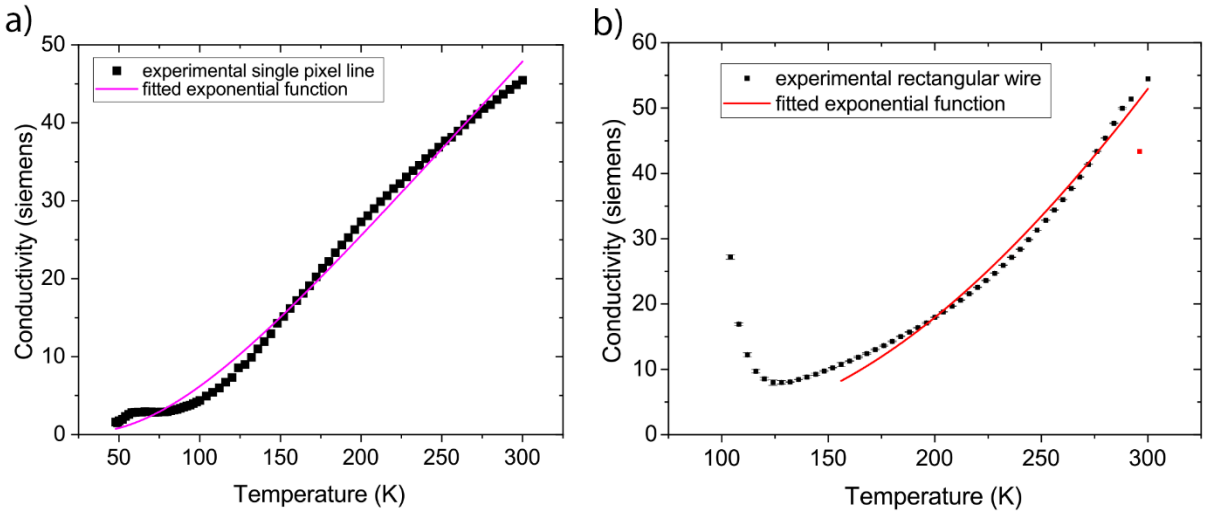

Figure 3.2.9 Electrical conductivity versus temperature for both type of measured deposits: a) single-pixel line and b) the rectangle with exponential formula fitted to data (magenta line on the a) graph).

Unlike most of the silver micro-wires presented in the previous chapter, ruthenium wires exhibit only non-metallic type of electrical conductivity. The exponential fit function has the form:

$$\sigma = \sigma_0 \exp\left(-\left(\frac{T_0}{T}\right)^{\frac{1}{2}}\right) \quad (3.2.1)$$

where both σ_0 and T_0 are constants, used as fitted parameters: $\sigma_0 = 783 \pm 40$ siemens and $T_0 = 2342 \pm 77$ K. As it was mentioned in the previous subchapter 3.1.5, this kind of function was proposed by Huth et al. [53] to describe conductivity of one type of their nano-granular W-C deposits: for the wires, where the grains of conductive material are dispersed in a non-conductive matrix, the electrons cannot travel freely through the wire and, instead, they have to overcome the distance between the conductive grains. This electron transport behaviour is called "hopping" and has been described before [149, 150]. To overcome the distance between two conductive Ru grains in such a way, the electron needs a certain energy, dependent on the average distances between the grains. This is the reason why the conductivity of the sample increases with temperature. In the work of Huth et al. [53], hopping was present for W nano-grains dispersed in C-O matrix, when the metal content was around 19 – 22.5 at.% of W [53]. In the case of Ru deposits presented here, the average metal content was on the level of 23 at.%, and the structure was similar to the wires investigated by Huth et al. [53]; pure Ru grains embedded in C-O-Br matrix. It can be then concluded, that for single-pixel as-grown Ru-C-Br wires the electrical conductivity is driven by hopping between conductive pure Ru grains embedded in a non-conductive matrix.

The rectangular wire deposit exhibits a more complex conductivity vs. temperature curve. In general, for temperatures between 100 K and 120 K, the conductivity decreases, above 120 K it grows with increasing temperature. Exponential formula could be fitted only to the growing part of the data. Fit parameters have significantly larger error bars than for the graph presented in Figure 3.2.9.a: $\sigma_0 = 6528 \pm 729$ siemens and $T_0 = 6954 \pm 300$ K. The problem of the conductivity upturn ate low temperatures needs, however, a further study. .

3.2.6 FEBID using Ru carbonyl halide complexes without allyl

As the allyl group from Ru(η^3-allyl)$(CO)_3$Br was most probably co-deposited with the e-beam under conditions described in previous chapter, a new allyl-free precursor was synthesised and tested with FEBID, namely $Ru(CO)_4Br_2$. The allyl group is replaced by an additional carbonyl group and one more halogen. As the carbonyl groups were removed from the previous Ru(η^3-allyl)$(CO)_3$Br compound, the following reaction upon e-beam irradiation is expected:

$$Ru(CO)_4Br_2 + e^- \rightarrow RuBr_2 + 4CO^{\uparrow} \ (reaction\ 3.3)$$

Without the allyl, there should be no more carbon detected in the deposit, as it was the co-deposition of this group, which most probably caused carbon contaminations in the deposits shown in previous section. As Br is a liquid at room temperature at atmospheric pressure, it is possible that in high vacuum of the SEM chamber it can desorb from the substrate, leading to an even more optimistic scenario of deposition of pure Ru structures:

$$Ru(CO)_4Br_2 + e^- \rightarrow Ru + Br_2^{\uparrow} + 4CO^{\uparrow} (reaction\ 3.4)$$

For $Ru(CO)_4Br_2$ there are no gas phase or condensed phase studies, however these kinds of measurements were performed on a similar compound, $Ru(CO)_4I_2$ [143]. In gas phase, the most probable dissociation pathway due to DEA is the loss of 2 carbonyl groups. Dissociative ionisation produced many more ionised fragments than DEA, with also RuI_2^+ and pure Ru^+ ions being observed in the spectrum [143]. In surface science study, 1.3-1.9 nm of the $Ru(CO)_4I_2$ precursor was condensed at -100 °C in UHV on gold substrate. Due to irradiation with the electron beam, subsequent loss of all carbonyl groups was observed. However, due to similar electronegativities of Ru, I and Au, the fate of Ru-I bond was hard to determine by the X-ray photoelectron spectroscopy (XPS) method, as the cleaving of the Ru-I bond would not produce any change in the peak positions of Ru(3d) and I($3d_{5/2}$) [143]. Nevertheless, the halogen stayed on the surface (peak position did not move and its intensity did not decrease) [143], which stands in contradiction to the fate of Br atoms from Ru(η^3-allyl)$(CO)_3$Br irradiated under similar conditions in some previously published work [119]. $Ru(CO)_4Br_2$ was also

used in gas assisted electron beam induced deposition experiments. The experiment was conducted in UHV (10^{-9} Torr of background pressure and 10^{-7} Torr during experiment with injection of gas through leak valve), using a very high (comparing to typical FEBID) current of 2 mA and 3 kV of beam acceleration voltage. The authors did not state the size of the beam, however, as they are using static exposure its diameter can be estimated from the provided SEM image, which shows that it was around 1 millimetre. The composition of the deposit was: 27 at.% of Ru, 54 at.% of Br, 15 at.% of C and 4 at.% of O. It should be noted that WDS was not used for quantification, therefore the amounts of Ru and C may not be fully correct [143]. Based on provided information, it can be expected, that during FEBID, similar metal content can be achieved. Moreover, most of the CO groups are expected to desorb from the substrate after Ru-(CO) bond cleavage.

To examine the aforementioned hypothetical electron-induced reactions, several deposits were prepared using $Ru(CO)_4Br_2$. The typical square deposit and its elemental composition are shown in figure 3.2.10 a and b. The square structures were deposited with the stage being at room temperature and slightly heated up to 48°C, the gas injection system temperature was 48°C. The spiral patterning strategy was used, with 20 kV of acceleration voltage and 0.76 nA of beam current. As in the case of previous Ru depositions, the nominal side length was 3 µm. The precursor was delivered through the short linear open gas injection system, with 3 mm of the inner diameter. This resulted in the flux of molecules about $2.1 \cdot 10^{15} \frac{\text{molecules}}{\text{cm}^2\text{s}}$, at the nozzle which was around two orders of magnitude lower than for the allyl-containing Ru compound.

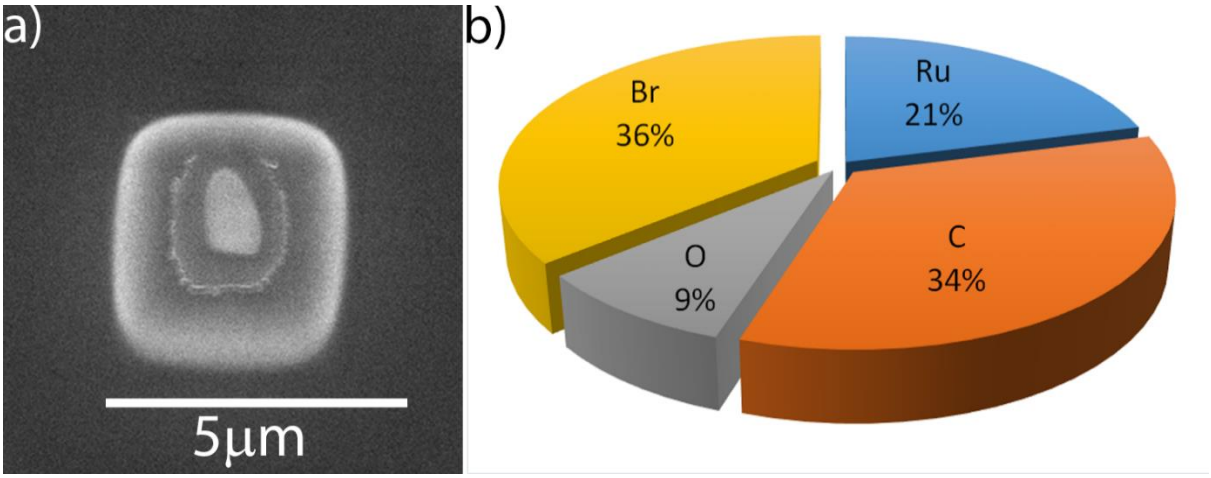

Figure 3.2.10 a) SEM image of typical square deposit made with $Ru(CO)_4Br_2$. b) Average composition of the deposited square structures in at%. Uncertainty was estimated to be 3 at.%. The sub-structure in the middle of the deposit was caused by long, around 25 minutes irradiation during WDS.

The composition of the deposited structure was very similar to the one achieved using Ru(η^3-allyl)$(CO)_3$Br (compare to Figure 3.2.2). Best achieved Ru content was 23 at.% and the average around 21 at.%. In the case of contaminants, the lowest achieved carbon content was 28 at.% and the lowest bromine content was 32 at.% (but in different deposit). The oxygen content was always in the range of 9 - 10 at.%. What can be noticed is that the average Ru content is slightly lower than the one reported before by Thorman et al.(27 at.%) in UHV FEBID [143]. However, our carbon content doubles the reported value of 15 at.%. Furthermore, in this work the amount of Br (36 at.%) is lower than the 54 at.% reported by Thorman et al. [143]. This can be explained by the significantly different used deposition parameters: the square-shaped deposits prepared for this study were made with the beam moving over the area in a spiral pattern with a short, comparing to constant exposure, dwell time of 10 µs. Thorman et al. used a very broad (comparing to SEM) beam of around 1 mm diameter, combined with a beam current of 2 mA, orders of magnitude higher than the current used in this study for FEBID. This resulted in an electron flux of $1.6 \cdot 10^{22} \frac{\text{electrons}}{\text{m}^2\text{s}}$, which is in the same order of magnitude as the flux of electrons used in this study: $2.9 \cdot 10^{22} \frac{\text{electrons}}{\text{m}^2\text{s}}$. Unfortunately, Thorman et al. does not provide the exact value of the flux of molecules they used in their study. The chamber pressure during their experiment was at the level of $1.33 - 2.66 \cdot 10^{-7}$mbar [143], which is 2 orders of magnitude lower than $1.5 \cdot 10^{-5}$ mbar recorded in this study. Without direct gas supply (no GIS) the precursor flux is directly proportional to the difference between the background chamber pressure and the pressure during deposition experiment [2]. For Thorman et al. this difference was around the pressure during experiment (background pressure of around $4 \cdot 10^{-9}$mbar). In the experiment described in this PhD Thesis the difference was around $2 \cdot 10^{-6}$mbar, which is an order of magnitude higher than the value of Thorman et al. It can be assumed then that the flux of molecules was also an order of magnitude higher, which may explain the different composition of the deposit reported here and by Thorman et al.

Table 3.2.2 shows compositions of different squares deposited with various dwell times and beam currents, normalised to one Ru atom. For all deposits, the GIS temperature was 48 °C.

Table 3.2. 2 Normalised composition of 20kV FEBID deposits made with $Ru(CO)_4Br_2$ and Ru content in at% in dependence of deposition's current, stage temperature and pixel dwell time. The uncertainty of the measurement was estimated to be 3 at.%, which translates to 0.2 in case of normalised values. (RT=room temperature, approx. 24°C)

Deposition current (nA)	**Stage temperature**	**Dwell time (µs)**	**Ru (at. %)**	**Ru**	**C**	**O**	**Br**
0.74	RT	10	17	1	2.4	0.5	1.8
0.73	RT	1	22	1	1.4	0.5	1.7
0.76	RT	0.5	23	1	1.2	0.4	1.7
0.19	RT	0.5	19	1	2.2	0.5	1.6
0.72	48	10	22	1	1.7	0.4	1.5
0.72	48	1	23	1	1.3	0.4	1.6
0.72	48	0.5	23	1	1.2	0.4	1.7

Removing the allyl group from the precursor did not significantly improve the metal content of the deposit. As in the case of the previous Ru compound, bromine has proven to be very hard to remove from the deposited material. In the best case, only 0.5 Br atom for every Ru atom desorbs from the substrate and was not incorporated into the deposit. In worst case, only 1 Br per 5 Ru. It is a slight improvement and shows that halogens (bromine) can be removed under FEBID conditions, compared to the allyl-containing counterpart, where all Br was incorporated into the deposit at the pristine precursor ratio of Ru:Br:1:1. The fate of carbon depends strongly on the deposition parameters. As the amount of oxygen is nearly the same in all measured samples and the bromine content changes only slightly, the metal content of the deposits depends mostly on the achieved carbon content. The worst metal content, 17 at.% of Ru was reported for the highest current (0.76 nA) and longest dwell time combination (10 µs). However, using 4 times lower current (0.19 nA) and 20 times shorter dwell time also resulted in low metal content structure: 19 at.% of Ru. Using shorter dwell times with low current was supposed to move the deposition regime closer to the reaction rate limited, to check how it influences the metal content. However, applied change may have not been big enough to cross the regimes border. Changing the regime may have an effect on the metal content, as using less electrons may lead to lower co-deposition of ligands. Concerning the best metal content of 23 at.%, the best combinations of deposition parameters are short dwell times and higher

currents. Judging by the C/Ru ratio, a maximum of 3 (out of 4 in the precursor molecule) CO groups per each Ru atom are cleaved and desorb from the substrate surface. Considering that the O/Ru ratio is constant and, for the purest samples, 3 times lower than the C/Ru ratio, it is very probable that C-O bonds were dissociated and that carbon was co-deposited, while oxygen could have desorbed. In contrast to the expected electron induced reactions 3 and 4, the FEBID reaction leading to highest Ru content can be summarised as:

$$Ru(CO)_4Br_2 \xrightarrow{e-} RuBr_{1.7}C_{1.2}O_{0.4} + 0.15Br_2^{\uparrow} + 2.8CO^{\uparrow} + 0.8O^{\uparrow} (reaction\ 3.5)$$

Increasing the stage temperature to equal the GIS temperature can improve the metal content of the deposits, since the desorption of the both precursor molecules and the cleaved ligands depends on the substrate temperature. Increasing the stage temperature should then reduce the co-deposition of ligands but also decrease the deposition rate.

A series of three squares, deposited with different stage temperatures, was performed. The GIS was kept at a constant temperature of 63 °C and the stage temperature was gradually lowered, starting from 51 °C and ending close to room temperature, at 30 °C. The beam acceleration voltage was 20 kV, and the current was around 0.67 nA. The pixel dwell time was set to 10 µs and the distance between pixels (point pitch) was 6nm. As previously, a spiral patterning strategy was applied and the nominal side length was 3 µm. The composition of the deposits was measured using a combination of WDS and EDX. The results of the experiments are gathered in table 3.2.3. For these experiments, the gas injection system nozzle was equipped with final needle with an inner diameter of 0.76 mm (0.9 mm of outer diameter), to limit precursor flux and decrease the possibility of burying not yet desorbed ligands under incoming precursor molecules. However, the exact value of the flux was not noted, due to a small error in the GIS handling after the measurement.

Table 3.2. 3 Normalised composition of deposits made with $Ru(CO)_4Br_2$ and Ru content in at% for the same beam current and pixel dwell time, however, at different stage temperatures. The uncertainty of the measurement, was estimated to be 3 at.%, which translates to 0.2 in case of normalised values.

Stage temperature	**Ru (at.%)**	**Ru**	**C**	**O**	**Br**
51	7	1	10	2.8	0.7
42	17	1	3.5	0.9	0.6
30	19	1	2.2	0.7	1.2

Interestingly, in all deposited structures the number of Br atoms per 1 Ru atom was reduced, compared to the previous deposits made with this precursor. This effect cannot be attributed to stage temperature, as in previous case for comparable stage temperatures the number of Br atoms was still higher. The highest Br/Ru ratio was 1.2, where previously the lowest achieved value was 1.5. It means, that reducing the flux of precursor helps the electron stimulated desorption of Br atoms. Unfortunately, the deposits exhibited still relatively low metal content, due to high carbon contents. The lowest achieved C/Ru ratio was 2.2, which is comparable to the values obtained previously for this dwell time and stage temperature (2.4, see table 3.2.3). At higher stage temperatures more carbon content was detected. As no material was deposited in-between the squares, we can exclude thermal decomposition or condensation of adsorbed precursor molecules. Although, as the number of C atoms is much higher than the number of O atoms per 1 Ru atom, we may speculate that the heat promoted the dissociation of CO groups and desorption of oxygen, leaving carbon to be incorporated into the deposit. The C/Ru ratio of the deposit made with the highest stage temperature of 51 °C exceeds more than twice the C/Ru ratio of the pristine precursor molecule, which can indicate that with the help of stage heating, electron induced dissociation creates volatile Ru-containing moieties. Other possibilies of such a high C/Ru ratio include the co-deposition of carbon from residual SEM chamber gases or co-injection of contaminants either coming from precursor impurities of the leftovers of solvent used to clean the GIS. As the deposits, which compositions are presented in Table 3.2.3, were done subsequently, with constant GIS temperature and decreasing stage temperature, thermal decomposition of the precursor inside the GIS probably did not cause the higher than stoichiometric C/Ru ratio in the deposit. The highest Ru content reported in Table 3.2.3 can be summarized by the following proposition of an electron induced chemical reaction:

$$Ru(CO)_4Br_2 \xrightarrow{low\ molec.flux, e^-} RuBr_{1.2}C_{2.2}O_{0.7} + 0.4Br_2^{\uparrow} + 1.8CO^{\uparrow} + 1.5O^{\uparrow} \ (reaction\ 3.6)$$

3.2.7 Deposition of Ru: conclusions

Both heteroleptic Ru complexes used for deposition exhibit very similar properties under irradiation with an electron beam. They both exhibit around 20-23 at.% of Ru in the deposited material. Furthermore, for both complexes, the halogen bonded directly to Ru atom is incorporated into the deposited material, despite the cleavage of Ru-Br bond evidenced by Ru grain formation. In the case of $Ru(\eta^3\text{-}C_3H_5)(CO)_3Br$, most probably all of the carbonyl groups are cleaved from the metal atom and desorb from the surface. The carbon incorporated into the deposit comes mostly from the allyl group. However, even using an allyl-free compound re-

sulted in the deposition of 1.6 C atoms on average per each Ru. With only a few atomic percent of oxygen in the deposit, it would mean that using more carbonyl groups resulted in electron induced dissociation of CO into carbon, which was then co-deposited and oxygen, which mostly desorbed. Comparing the results of deposition using $Ru(\eta^3\text{-}C_3H_5)(CO)_3Br$ and $Ru(CO)_4Br_2$ it can be stated that the replacement of the allyl ligand, which is the main source of the contamination, with a volatile carbonyl and halogen did not increase the metal content (in the FEBID conditions used). To properly design a precursor molecule for FEBID, it is crucial to know the real electron induced dissociation pathways, which are happening during a FEBID experiment. To address this issue, a new analytical method of focused electron beam induced mass spectrometry will be proposed in chapter 4. Moreover, in both cases, using Br directly attached to Ru atom has led to the incorporation of halogen into the deposit, indicating that bromine is a difficult ligand for FEBID. However, it may be removed during FEBID at higher stage temperatures where the Br/Ru ratio was reduced to 0.6, indicating that in certain conditions it is possible to successfully remove at least part of this halogen. Further, systematic studies would be needed to investigate this deposition window, however, such investigations venture beyond the scope of this Thesis.

3.3 Gold(I) N-heterocyclic carbene precursors

Gold is a metal with many interesting properties. It is very good electrical conductor and it is not very reactive – it does not oxidise easily. Due to the presence of free electron gas, it can be used for plasmonics [70]. Gold has been successfully deposited using electron beam before. The best purity, around 100 at.%, was achieved using $Au(PF_3)Cl$ and Au(CO)Cl, but the compounds are unstable in vacuum and spontaneously decompose [76, 77]. The other, well established precursor MeAu(acac) is stable, but it gives deposits with the metal content around 15-20 at.% [42, 60]. It is then important to still develop novel gold precursors, which will be both stable and give high purity deposits. In this chapter, results of deposition using two new heteroleptic gold compounds with NHC based and halogen ligands are presented. The composition of deposits and their crystal structure will be discussed and compared to other NHC based gold precursors. Furthermore, metal contents of deposit and halo will be analysed and correlated with deposition parameters.

3.3.1 Chemical formulae and properties

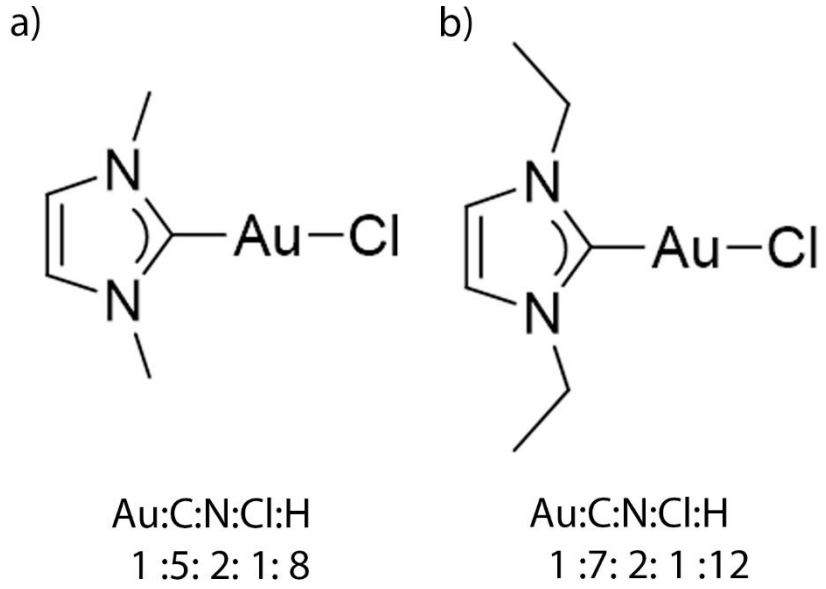

Figure 3.3.1 Precursors used to deposit gold by FEBID with a) $Au(NHC)Me_2Cl$ and b) $Au(NHC)Et_2Cl$.

The gold precursors used for experiments are imidazolium based N-heterocyclic carbenes (NHC). They differ with one CH_2 group. They were synthesised at University of Oslo by Cristiano Glessi. In a cold finger apparatus under 10^{-3} mbar of pressure the $Au(NHC)Me_2Cl$ sublimed at 86-87°C and $Au(NHC)Et_2Cl$ at 87°C of reservoir temperature, which implies that these compounds also need heating in FEBID to be delivered over the sample substrate.

3.3.2 Morphology and composition

All deposits were prepared using 20 kV of beam acceleration voltage. Point pitch was 6 nm. Rectangular spiral patterning strategy (outside to inside) was used for deposition. Nominal side size was 3 μm, dwell time, beam current and the number of passes were changing depending on the experiment. The stage temperature was kept at 125 °C – 130 °C Au(NHC)Me_2Cl and between 120 °C and 140 °C for Au(NHC)Et_2Cl, depending on the experiment. The GIS temperature was in the range of 120 °C – 150 °C for the former and in the range of 140 °C – 150 °C for the latter compound. The GIS position and the times used for thermal stabilisation of the stage and the GIS were described in Chapter 2.1. Figure 3.3.2 presents 2 typical deposits prepared with Au(NHC)Me_2Cl and Au(NHC)Et_2Cl.

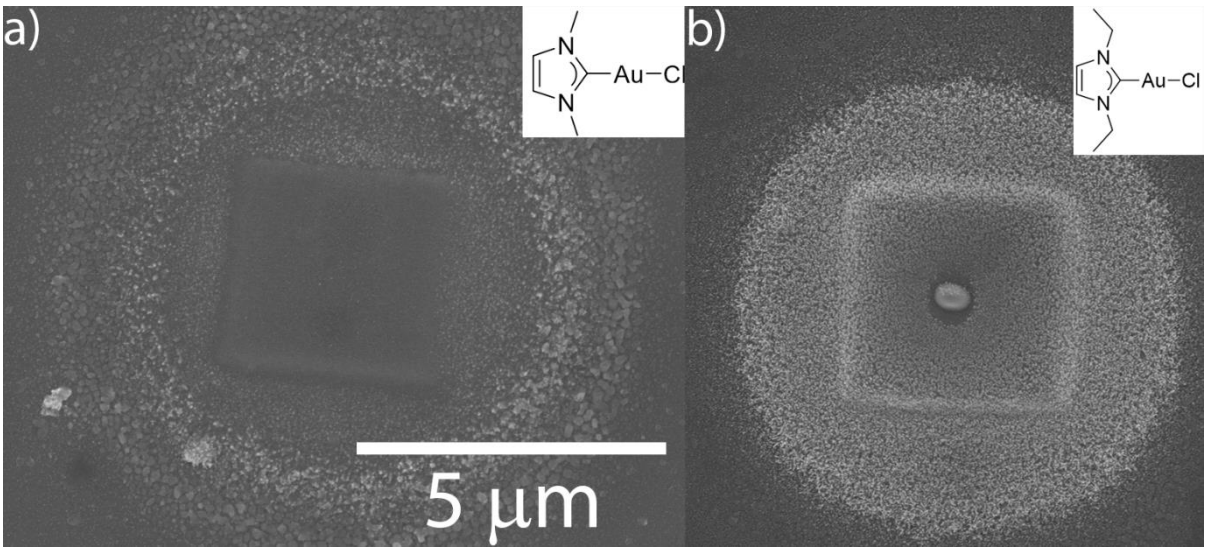

Figure 3.3.2 Typical square deposits of nominal dimensions of 3x3μm^2 deposited with NHC$(Me)_2$AuCl a) and NHC$(Et)_2$AuCl b). Insets show the formulas of the precursors.

As it was in the case of structures prepared with silver carboxylates, deposits prepared with gold NHC compounds exhibit visible halo around scanned area. In case of deposits made with the precursor containing methyl groups, the halo was around 3.1 μm from the edge of the deposit and for the other precursor it was around 1.8 μm from the edge of the deposit. In case of NHC$(Me)_2$AuCl the halo area is visibly more granular, than the deposit. In case of a structure deposited with NHC$(Et)_2$AuCl, both deposit and halo are made of very small, but distinguishable particles. The big particle in the centre of the square is most probably a result of used spiral patterning strategy. The beam has most probably spent more time in the centre of the deposit than in the outer part, hence growth of the spot deposit. What can be noticed, is that despite the square shape of the deposit, the halo regions are circular. This can be attributed to the proximity effect, which results in a lower accumulative dose for peripheral pixel positions

in exposed structures, like the two ends of a line deposit and the corners of squares. In high precision e-beam lithography this effect is counteracted by increasing the pixel dose at these positions. The specific circular halo shape in figure 3.3.2 arises from the comparable dimensions of the square and backscattered electron range. For the silver deposits, see Figure 3.1.4 where $10x10\mu m^2$ structures have been deposited, the halo is not circular around the larger squares. Moreover, for the structure from Figure 3.3.2.a, the halo looks like it was made out of two distinguishable rings. Halo around the structure on Figure 3.3.2.b is more uniform. It is most probably an effect of different deposition regimes. The halo in case of deposition with $(NHC)(Me)_2AuCl$ is larger than in case of $(NHC)(Et)_2AuCl$, which means, that lower surface flux of electrons is needed to dissociate adsorbed molecule. Lower fluxes may shift the deposition towards electron-limited regime and promote growing of larger grains, hence, visible rings at the outer edge of halo. In case of $(NHC)(Et)_2AuCl$ such low doses of electrons do not cause dissociation. The deposit is formed only in mass transport limited regime, hence uniform morphology of deposited square and halo.

Average, best and worst purities achieved were gathered in table 3.3.1. Compositions of deposited material were measured using EDX. The average was calculated over the results coming from deposits made with the same acceleration voltage of 20 kV, but with different beam currents (0.55 nA for all structures made with $(NHC)(Me)_2AuCl$ and 0.6 nA and 0.16 nA for $NHC(Et)_2AuCl$) and different dwell times in range from 0.5 μs up to 100 μs.

Table 3.3.1 Average normalised composition (EDX) of deposits made by FEBID with both compounds. The compositions are given with an uncertainty of ±0.8 for $Au(NHC)(Me)_2Cl$ and 0.5 for $Au(NHC)(Et)_2Cl$. The stoichiometric composition of the pristine compounds are given in the table.

Precursor	**Average composition**					**Best Au content (at.%)**	**Worst Au content (at.%)**	**Average Au content (at.%)**
	Au	C	N	Cl	O*			
Stoichiometry	1	5	2	1	0			
$Au(NHC)(Me)_2Cl$	1	8.5**	1	0.1	0.4	15±4	5±4	9±4
Stoichiometry	1	7	2	1	0			
$Au(NHC)(Et)_2Cl$	1	4.5	0.8	0.5	0.1	16±3	12±3	15±3

*O was not present in the precursor molecule. ** Note that the FEBID material contains more carbon than the pristine molecule.

Average gold amount for both compounds does not exceed 20 at.% in the deposit and equals to 9 ± 4 and 15 ± 3 at.% for Au(NHC)$(Me)_2$Cl and Au(NHC)$(Et)_2$Cl, respectively. Reported metal content is comparable or lower than the values achieved with other organometallic precursors used for FEBID, MeAu(acac), MeAu(hfac). In case of Au(NHC)$(Me)_2$Cl most of the Cl atoms were successfully dissociated and removed, for Au(NHC)$(Et)_2$Cl one Cl per 2 Au atoms was incorporated into deposit. For both precursors from 2 nitrogen atoms 1 was successfully removed, while the second was mostly co-deposited. Very interesting is the comparison of carbon content for both deposits. Despite having less C atoms in the molecule, Au(NHC)$(Me)_2$Cl, average number of carbon per one Au is nearly twice higher than for Au(NHC)$(Et)_2$Cl (8.5 vs 4.5). Most probably, fragments of dissociated ligands created due to irradiation of Au(NHC)$(Me)_2$Cl are not volatile enough and they are dissociated again and co-deposited. The effects of e-beam irradiation on the precursor can be noted in form of reactions.

$$(NHC)Me_2AuCl + C_xH_y \xrightarrow{e^-} AuNC_{8.5}Cl_{0.1}O_{0.4} + N\uparrow + 0.9Cl\uparrow \ (reaction\ 3.7)$$

$$(NHC)Et_2AuCl + \xrightarrow{e^-} AuN_{0.8}C_{4.5}Cl_{0.5}O_{0.1} + 1.2N\uparrow + 0.5Cl\uparrow \ (reaction\ 3.8)$$

The results are comparable with recently published data from Glessi et al. [151]. In their work, they have tested various NHC based gold compounds as potential FEBID precursor. Out of seven compounds, the highest metal content was achieved for (N,Et)AuCl compound (compound 6 from their study) and was around 14.6 at.% [151]. In their work Glessi et al. presented possible dissociation pathway of this compound (Figure 5 from [151]), which contained cleaving of Au-Cl bond and also fragmentation of the part of N-heterocyclic carbene ligand, which led to losing some nitrogen and one of attached ethyl groups. It stands in agreement with the results obtained using Au(NHC)$(Et)_2$Cl, presented in this Thesis. The Au content of the six other gold(I) N-heterocyclic carbene compounds, which have been tested by Glessi et al. [151] varied between 7.3 and 10.3 at.%. This is comparable to the average metal content achieved for Au(NHC)$(Me)_2$Cl (9 at.%) and lower than the average value of deposits obtained with Au(NHC)$(Et)_2$Cl (15 at.%).

What is interesting, in the deposits made with the Au(NHC)$(Me)_2$Cl compound there were significantly more carbon atoms per one Au than in the precursor's molecule. This can be attributed to several reasons; (i) volatile Au-containing species are created due to irradiation of adsorbed molecules while the carbon is deposited, (ii) there is a significant co-deposition of hydrocarbons from residual gases from the SEM vacuum chamber, (iii) there was thermal de-

composition of the precursor in GIS, or (iv) there were carbon-containing impurities in the precursor material. Figure 3.3.3. shows the chronology of the deposition process and the obtained C/Au.

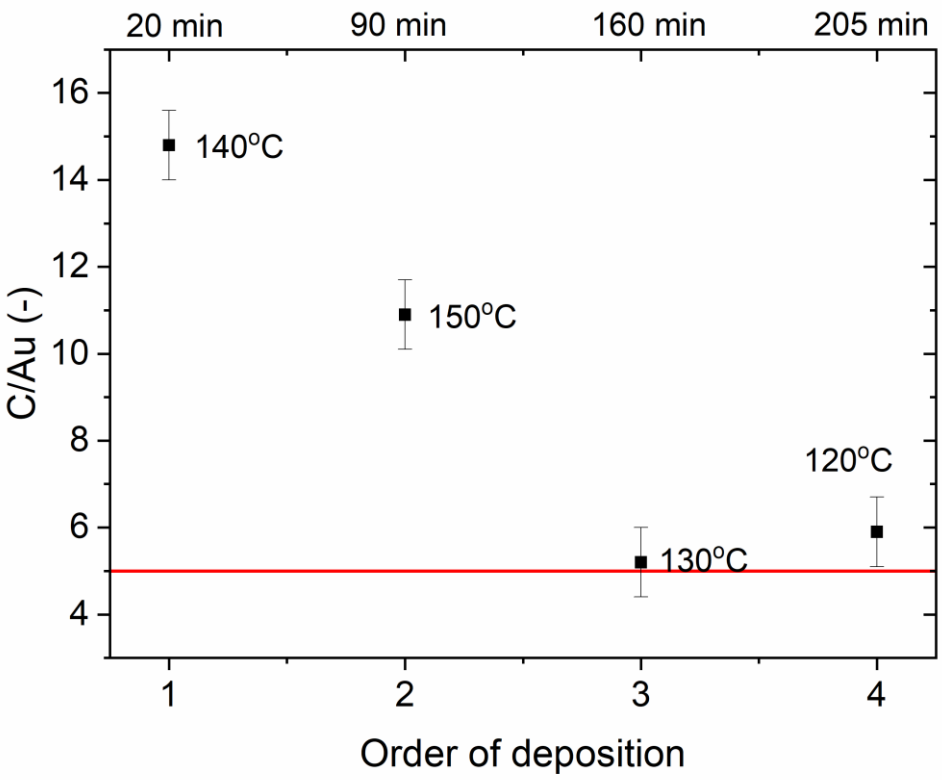

Figure 3.3.3 C/Au ratios for deposits made with Au(NHC)$(Me)_2$Cl. The order of deposition refers to chronological order in which the deposits have been prepared. GIS temperatures as well as 0.8 error bars are marked on the graph. The substrate temperature was 125°C - 130°C. The red line indicates the stoichiometric precursor C/Au ratio. The time values on the upper axis mark the time, which passed from the beginning of the experiment until the start of deposition of this structure. The time values are labels, the axis is not at scale.

The GIS has been heated up first to 140 °C and 20 minutes after the temperature stabilised (stabilisation of GIS temperature marks the start of the experiment) first structure was deposited. It was followed by heating the GIS further to 150 °C and further FEBID experiments. The first structure at this GIS temperature was deposited around 90 minutes from the start of the experiment. The GIS was later cooled down to 130 °C and finally to 120 °C. The time which passed from the start of experiment until the square structure was deposited at corresponding GIS temperature was marked on the upper axis of Figure 3.3.3. As can be noticed, the C/Au ratio was first about three times higher than the stoichiometric value to fall down to close to 5. If the precursor has been thermally decomposed at 150 °C the C/au ratio should not have decreased at lower temperatures.

Although the thermal decomposition can be excluded, other possibilities listed above Figure 3.3.3 can still explain the higher than stoichiometric C/Au ratios.

3.3.3 TEM measurements

To examine the crystal structure of the grains of the deposit, a TEM lamella was prepared with the procedure described in chapter 2.2. The lamella was prepared from a square deposit fabricated with $Au(NHC)(Et)_2Cl$. The lamella was measured using TEM and the results are presented in Figure 3.3.4.

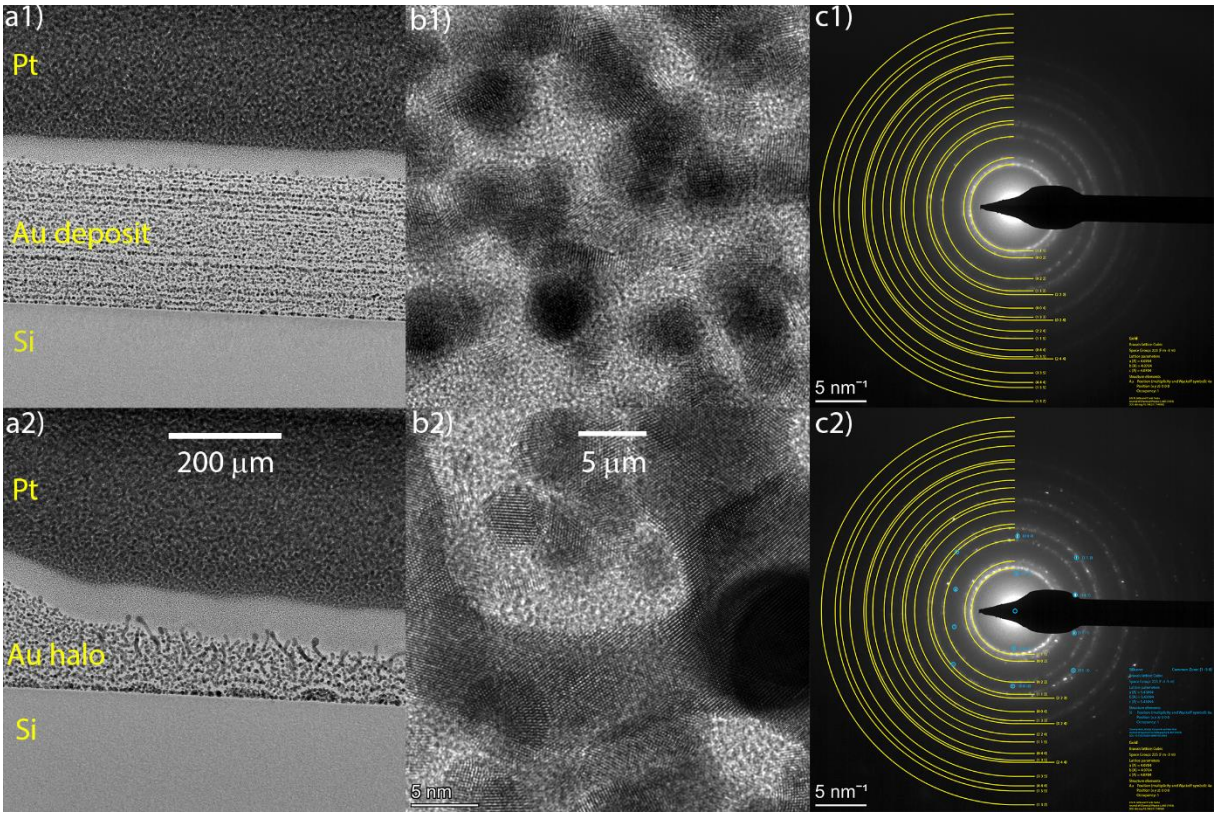

Figure 3.3.4 TEM results of a lamella made from a square deposit prepared with $Au(NHC)(Et)_2Cl$. 1st row refers to the results coming from the deposit centre and 2nd row from halo. a) BF-STEM images of the lamella, b) HR-TEM images of the particles of the deposited material c) SAED patterns of the deposited material.

Figure 3.3.4 a1 and a2 present BF-STEM images of the central part and the halo, respectively, of the square deposit from Figure 3.3.2.b. Interestingly, the centre of the deposit exhibits a layered structure, where the gold nanocrystals (black spots) align in the horizontal layers with matrix material. The layered structure is not preserved in the halo region, where the grains of gold start to grow, creating a "hair-like" structure. HR-TEM images (Figure 3.3.4 b1 and b2) show the crystalline structure of the Au grains with visible atomic planes, especially in the halo region. The size of Au nanocrystals in the centre of the square was around 5 nm. SAED diffraction pattern confirm the crystalline character of the grains with the pattern matching that of pure gold (Figure 3.3.4 c1 and c2). The diffraction pattern in Figure 3.3.4 c2 contains also

spots which can be attributed to the pattern of pure Si. They are originating from the Si substrate and they do not come from the deposited material. Pure gold particles embedded in C-O-N-Cl matrix suggest, that also in the case of $Au(NHC)(Et)_2Cl$ metal-ligand bonds have been dissociated. The layered structure of the deposit, may be an effect of diffusion of gold atoms, but its origin is not fully understood.

3.3.4 Halo deposits

Metal content of halos visible around square deposits was measured using EDX. The results for $Au(NHC)(Me)_2Cl$ are gathered in Table 3.3.2. All deposits were made with 0.55 nA of beam current. For low GIS temperatures, the difference between metal content of halo and square deposit is not significant on the level of uncertainty. The most significant difference is visible for GIS temperatures of 140 °C and 150 °C, where metal content in halo is around twice as high as for the metal content measured inside the deposit. Metal content of deposited material did not vary in the dwell time range of 1-100 µs examined. As it was described in chapter 3.1 for silver, the mechanism behind the varying metal contents of halo and deposit is due to different fluxes of electrons. In the centre, high electron flux, which can be translated to high ν_{DISS} co-deposits ligands, hence lower metal content. In halo region, where the electron flux and thus ν_{diss} is much lower (see results for silver in chapter 3.1), the deposition process is conducted in electron limited regime. In this regime, the ligands cleaved off from the metal atom can thermally desorb before being further dissociated into non-volatile fragments. Rising GIS temperature increases further the flux of molecules impinging on the substrate surface (increase of ν_{GAS}). These molecules then may adsorb on freshly dissociated molecules and bury the volatile fragments before they can desorb thus creating a low-metal-content deposit. The exact values of molecule flux are not straightforward to determine. The GIS temperature was changing during one run of experiment. As the background pressure did not increase significantly due to change of the temperature, the only way to estimate the flux of molecules would be by using the mass difference of precursor inside the GIS before and after the experiment. Such estimation gives a value of $5.4 \cdot 10^{15} \frac{\text{molecules}}{\text{cm}^2\text{s}}$ of the flux of molecules leaving the GIS nozzle. It is around 2 orders of magnitude lower than the value for $Ru(\eta^3\text{-allyl})(CO)_3Br$ presented in chapter 3.2. However, this would give only an average value and would not show any influence of the GIS temperature change. It indicates that in the beam centre the deposition happens in mass transport (adsorbate) limited regime. In halo region, where the number of electrons per unit of surface and unit of time is few orders of magnitude lower (see results for silver in chapter 3.1), the deposition process is conducted in elec-

tron limited regime. In this regime the ligands cleaved off from the metal atom can thermally desorb before being further dissociated into non-volatile fragments.

Table 3.3.2 Metal contents of deposit and halo region for the structures made with $(NHC)(Me)_2AuCl$ in dependence on dwell time and GIS temperature. All contents are given with 4 at.% of uncertainty. Note that a higher GIS temperature signifies higher flux. The substrate temperature was 125-130 °C and the beam current 0.55 nA.

$(NHC)(Me)_2AuCl$	**Deposit (at.%)**	**Halo (at.%)**	**Dwell time (µs)**	**GIS temperature (°C)**
	15	16	10	120
	13	16	10	130
	5	12	10	140
	8	16	1	150
	7	14	10	150
	9	16	100	150

In the case of $(NHC)(Et)_2AuCl$, all of the measurements were performed for the deposits made at 140°C. For all measured structures, but one, there is significant difference between the metal content of the deposited material and the metal content of halo. The results are presented in Table 3.3.3. For all deposits, the metal contents of material in the region which was irradiated are comparable. For first two deposits made with 1µs of dwell time, the metal contents of both deposits and halo regions are almost the same, despite different beam currents used to produce both structures. It suggest, that changing the beam current (and that way changing the ν_{diss}) with constant dwell time does not influence the dissociation pathways, meaning that the deposition regime was not changed. In this case the deposition regime was determined by the dwell time. Lowering the dwell time by 50% reduced the metal content of the halo region from 23 to 13 at.%, which further support this hypothesis. The most interesting part is the difference between first and last deposit presented in the table. They are made with the same beam current and dwell time. The only difference between the conditions of two deposits was the distance from the upper edge of the GIS nozzle end. First three deposits were made 170 µm from the upper end of the nozzle, while the last deposit was made at the distance of 260 µm. As it is known from results of GIS simulations [146], higher distance to the nozzle decreases the flux of impinging molecules. However, as it was shown for the same GIS and similar geometry in our joint paper [34] changing the position of the deposition area

just by 100 µm should not change significantly the impinging precursor flux (change less than 2% points). This may point to a narrow window of optimal ratio between the fluxes of precursor molecules and electrons, which needs to be installed for high metal content FEBID with this precursor. The metal content is then determined by the competition between ν_{DISS} and ν_{GAS}. When the flux of electrons was too low (which translates to low ν_{DISS} values), as in the case of the shortest dwell time and lowest beam current, the metal content of halo decreased. The possible explanation of this decrease is an incomplete dissociation of the precursor molecule in the halo region, which is then buried by the incoming gas molecules. Lower flux of molecules (low ν_{GAS}), combined with the highest electron current resulted in the halo deposit with the highest metal content. Changing the conditions of the deposition did not affect the metal contents of the deposited squares, only halos. It can be explained using a ligand co-deposition model, presented in chapter 5. In some cases, namely for low ligand desorption time (or high cross section of deposition of ligands) and high electron fluxes (as in the beam centre) the composition is not affected by small changes (below 2 or 3 orders of magnitude) of electron flux (see Figure 5.11.b, black curve). The deposition is performed in mass transport limited regime, with ν_{diss} dominating over other characteristic rates.

Table 3.3.3 Metal contents of deposit and halo region for the structures made with (NHC)$(Et)_2$AuCl in dependence on dwell time . All contents are given with 3 at.% of uncertainty. The substrate temperature was 135-140°C.

(NHC)$(Et)_2$AuCl	**Deposit (at.%)**	**Halo (at.%)**	**Dwell time (µs)**	**Beam current (nA)**
	16	23	1	0.63
	15	22	1	0.16
	13	13	0.5	0.16
	16	30	1	0.64

3.3.5 Au deposition – conclusions

Deposition results shows that maximal achieved metal content in the deposits made with both compounds was around 16 at.%, which is not better than what was previously achieved for compounds listed in chapter 1 in comparable FEBID conditions. Moreover, the deposits exhibit the presence of halo, which limits the applications of the compounds in nanostructure preparation. However, the size of halo depends on the range of backscattered electrons, which

is correlated to the energy of the primary electrons (see figure 1.2b). In such a case, similarly to silver carboxylates, the unwanted halo deposition can be limited by using lower beam acceleration voltages. In this PhD work, the presence of halo provided important information about the influence of electron flux on deposition regimes. The same as for silver craboxylates, the gold NHC compounds need to be heated to sublime, which complicates a FEBID process, but they do not allow for such high metal contents. Considering the facts listed above, it can be concluded that NHC ligands are the least optimal groups from all tested FEBID precursors – they are not as easy to use as ruthenium complexes and they do not provide as high metal contents as silver carboxylates.

3.4 New precursors – summary and conclusions

In presented chapter, nine compounds with three different atomic core atoms and representing three different groups of complexes have been examined as potential FEBID precursors. In total nine different ligand-metal combinations were tested, giving a broad spectrum of results.

The best metal content was achieved for silver carboxylates, which in average resulted in FEBID with > 50at.% metal. The presence of a pronounced halo around structures deposited with carboxylates indicates that these compounds are very sensitive towards irradiation with electrons. Even though fluxes of electrons in halo are orders of magnitude lower than the flux in the beam centre, the deposit was still created. The dose, which resulted in deposition of tens of nanometre size Ag crystals in the peripheral region of the spot deposit was in the range of $(3.4 - 14) \cdot 10^{-2} \frac{\mathrm{C}}{\mathrm{cm}^2}$, which is at least twice smaller than the dose used by Hari et al. to deposit single nanometre thick lines using Pt(η^5-CpMe)Me_3 [152]. Doses in the halo region are in the same order of magnitude as critical doses for organic ice lithography [153] but still at least one order of magnitude higher, than critical doses used in electron beam lithography [154]. The sensitivity of the silver carboxylates towards irradiation with electrons may contribute to overall high metal content of deposited structures, as the metal-ligand bonds are easily cleaved, it also, due to deposition in halo region, limits potential applications of silver carboxylates FEBID, because of the limited spatial resolution of created deposits. However, as can be noticed in Figure 1.2b, the BSE range depends on the energy of the primary beam, so the halo size can be decreased by using low kV acceleration voltages (<1kV). In this work, the presence of halo created a unique opportunity to investigate the FEBID in different deposition regimes, starting from MTL at the beam centre, finishing on RRL for halo area. The morphology of the deposited material consisting of relatively large (size from several tens of

nm up to few hundreds nm, depending on the compound), loosely percolated metal particles degrades, the electrical conductivity in comparison to bulk silver. The granular morphology may be also a limiting factor for future application of Ag FEBID structure in plasmonic nano-devices and is definitely an open issue, which needs further research to be able to control it.

$Ru(\eta^3\text{-allyl})(CO)_3Br$ and $Ru(CO)_4Br_2$ provided similar purity of 23 at.% of Ru while deposited using focused electron beam. Both compounds gave smooth deposits with thin halos around. For $Ru(\eta^3\text{-allyl})(CO)_3Br$ the deposited material contained of pure Ru nanograins embedded in C-O-Br matrix. What is the most important, from a point of view of application in repair of photolithography masks is that deposits made with this precursor can be successfully ex-situ purified with heat and forming gas. The biggest drawback of this method of purifications lies in a huge volume loss of 79%. But this volume loss happens mostly due to loss of the thickness. It could be then applied for corrections of flat masks.

Sensitivity towards electron beam irradiation of precursor molecules may play important role in deposition of high-purity FEBID structures, but it does not grant high purities only by itself, as can be concluded comparing the results from silver and gold. Gold NHC compounds also exhibit large halos, but their purities are at 15 at.% at best. The similarity between structures made using gold and silver FEBID is that purity of halo regions is higher than the purity of material deposited inside irradiated area. Basing on results on these two groups of precursors it can be stated, that the most important in order of achieving high purity deposits is to choose proper chemical groups as precursors. It is not only important to cleave metal-ligand bonds by electron irradiation but also to ensure that these intact ligands will desorb off the surface before they are further co-deposited. It was also confirmed by results obtained with ruthenium precursors. Although most probably all of the three ligand groups from $Ru(\eta^3\text{-allyl})(CO)_3Br$, allyl, carbonyl and bromine have been detached form metal atom, the purity of the deposit was only 23 at.% in average, mostly due to co-deposition of cleaved ligands: allyl and Br.

Judging just by the results of deposition using $Ru(\eta^3\text{-allyl})(CO)_3Br$ and silver carboxylates it could be concluded that the best candidates for ligands for FEBID are CO and carboxylate groups (especially fluorinated). However, it cannot be omitted, that even using preferable chemical groups as ligands may not be enough to deposit pure FEBID structures. Exchanging allyl group with a carbonyl and bromine did not prevent the carbon contamination, during FEBID using $Ru(CO)_4Br_2$.

Studied gold NHC precursors do not seem to be the most optimal choice for gold FEBID. Their metal contents are not higher than values reported before, and the exhibit halos limiting their application in nanostructurisation. Comparing the results presented here with the one showed by Glessi et al. [151] it can be stated, that in general NHC ligands are not a favourable for FEBID.

To properly address these issues, further investigations have to be conducted. The most important is to properly understand the pathways of electron-induced dissociation and desorption. Although there are methods like gas and condensed phase studies, which can help understanding the electron-induced fragmentation of metal-organic compounds, as it was shown for the case of Ru deposits, their results are not always in agreement with results of FEBID experiments. Differences between experimental condition, like no presence of any substrate in gas phase studies or lower electron flux, much lower substrate temperature and lack of constant gas supply in case of condensed phase studies result, in some cases in staggering differences in observed composition of the deposits. Next chapter of this dissertation will focus on introducing a novel measurement method, which can be of help in such cases: focused electron beam induced mass spectrometry.

4 FEB induced Mass Spectrometry as a method of examining dissociation pathways

Previous chapter presented results of electron-induced deposition using precursors with various metal cores and ligands, from simple carbonyl groups or halogens to longer carbon – fluorine chains. As was presented, chemistry of precursor molecules was one of the main factor determining metal content and structure of deposited material. Finding proper ligands, which provide both good volatility in moderate temperature range and can be easily dissociated with electron beam is one of the main interest of chemists working in field of FEBID. Recent years, there has been some attempts to determine a simple set of rules which a promising precursor candidate should fulfil [41, 42, 117], but this task is not simple and straightforward. Compounds containing the same ligand groups but different metal cores have not only different thermal properties, but also may give deposits with significantly different metal content. Deposits made with $Ag_2(\mu\text{-}O_2CC_2F_5)_2$ reach 76 at.% of silver [35], while its copper equivalent, $Cu_2(\mu\text{-}O_2CC_2F_5)_4$ gives only around 25 at.% of copper [36]. Various metal carbonyls tested previously also exhibits significantly different purities, starting from very high obtained for $Co_2(CO)_8$[52, 155] and $Fe(CO)_5$[17] (97 and 100 at.%, respectively), 66 at.% obtained with $W(CO)_6$ down to around 15 at.% achieved with $Mo(CO)_6$ [54].

To evaluate, whether a compound can be promising FEBID precursor it is crucial to determine its electron dissociation pathways. By now, there are two main methods of investigation e-beam dissociation processes, both mentioned in first chapter: electron irradiation of precursor in gas phase and irradiation of few monolayers of compound condensed on surface in ultra- high vacuum. Both methods can give very valuable information about electron-induced processes, but due to measurement condition which are usually significantly different than the ones used for FEBID, their results have only limited applicability of predicting the outcome of e-beam irradiation of a compound in HV SEM chamber used for e-beam induced deposition, which was discussed in previous chapter.

In this chapter, novel method of investigation of dissociated precursor fragment during e-beam induced deposition will be presented. Focused electron beam induced mass spectrometry (FEBiMS) allows for tracing all charged species desorbing from sample surface due to irradiation with electrons. This method employs the time of flight secondary ion mass spectrometer (TOF -SIMS), attached to the SEM vacuum chamber. Recently, these type of spectrometers are increasingly used in focused ion beam induced secondary ions mass spec-

trometry (FIBSIMS). FIBSIMS is a destructive but highly sensitive method of determining the occurrence of chemical elements as well as trace elements in a material. Due to its high sensitivity and high lateral and depth resolution, FIBSIMS was used in investigation of various materials, such as Li batteries [156], thin films [157] and nanocomposites [158]. In presented case, high spectral resolution of TOFMS detector was used to register all charged species leaving the substrate during standard electron beam induced deposition process. As there is no post ionisation involved charged fragments from dissociative ionization events can be directly traced. Neutral dissociation fragments may be detected using a post ionisation add-on, but this was not scope of this Thesis.

4.1 Geometry of measurement

Figure 4.1 presents the visualisation of the inside of vacuum chamber of the SEM used for experiments with an inset with infrared camera picture for comparison. Experimental conditions were described in chapter 2.6 of this Thesis.

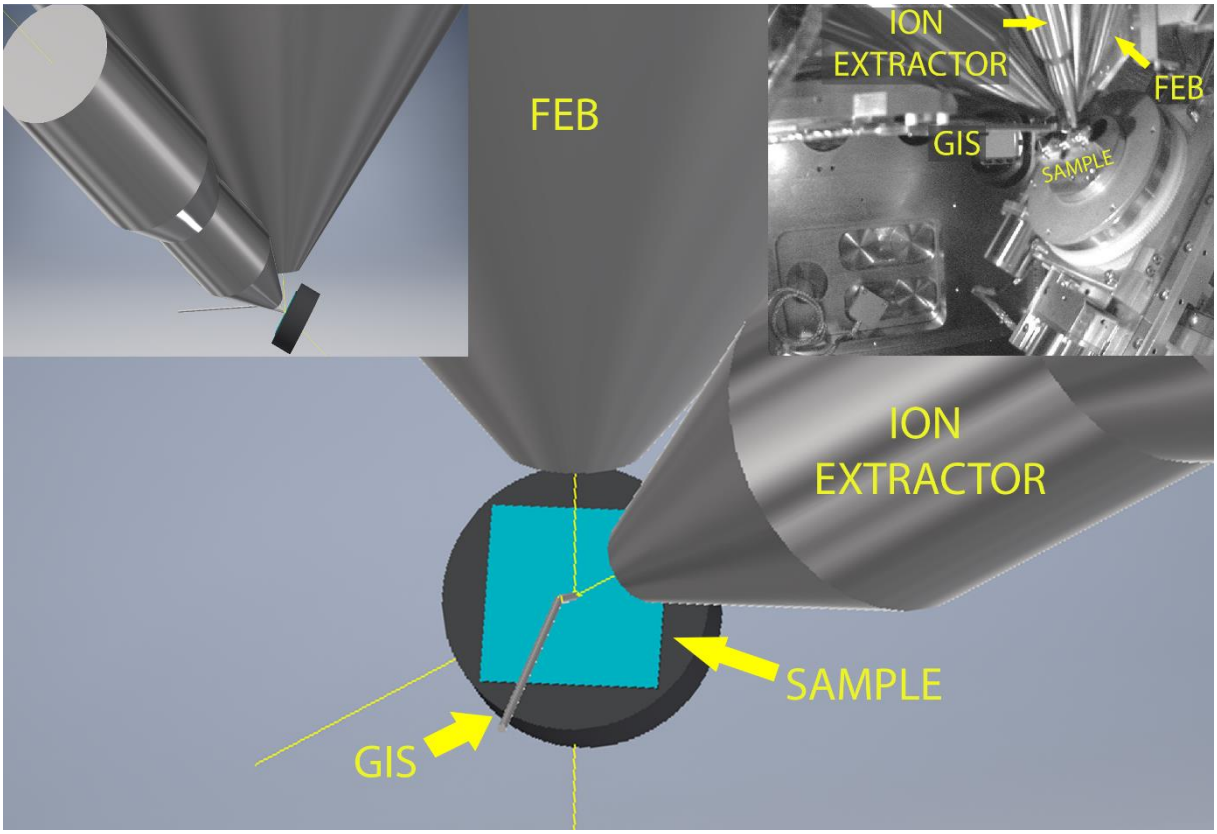

Figure 4.1 Schematics of the geometry of the FEBiMS measurements: top view. Inset, left: side view of the schematics; right: infrared camera image of the inside of the SEM chamber

4.2 Irradiation of grains of the precursors

The first experiment included irradiation of grains of three compounds: $Ru_3(CO)_{12}$, representing of carbonyls and two carboxylates: $Ag_2(\mu\text{-}O_2CC_2F_5)_2$ and $Cu_2(\mu\text{-}O_2CC_2F_5)_4$. All three compounds were applied before in FEBID. $Ru_3(CO)_{12}$ was used to prepare first Ru-containing deposits [159], $Ag_2(\mu\text{-}O_2CC_2F_5)_2$ was widely described in publications and in chapter 3.1 [34, 35] and $Cu_2(\mu\text{-}O_2CC_2F_5)_4$ is a novel precursor, used to deposit structures reaching 25 at.% of Cu in as-deposited material [36]. Copper carboxylate was also recently applied in room temperature lithography [160]. The grains of precursor were placed in the SEM chamber using the protocol described in chapter 2.6. Schematic representation of the experiment was depicted in figure 4.2.a. For all measured compounds, it is expected to detect mostly relatively light fragments, coming from fragmented ligands. For $Ru_3(CO)_{12}$ the most ions should come from carbonyl groups. CO groups are known to be volatile and they are easily leaving the surface, even in condensed phase measurements, which are conducted with samples at cryogenic temperatures below -160 °C. Post ionised CO^+ groups from the substrate were detected in surface science measurements for $W(CO)_6$ [161], $Mo(CO)_6$ [162], $Fe(CO)_5$ [163, 164] and $Ni(CO)_4$ [165]. No metal containing ions are expected to appear in the spectrum, as they are heavy and not easy to volatilise. In the measured m/z range from 1 to 450, ionised parent molecule $Ru_3(CO)_{12}^+$ cannot be detected, although a double-ionised specie could be visible. Ru has five isotopes with higher abundance, above 0.1 and another two with abundance above 0.01. In the spectrum it should result in a group of five to seven peaks at m/z = 96, 98, 99, 100, 101, 102, 104.

Upon irradiation with electron beam $Ag_2(\mu\text{-}O_2CC_2F_5)_2$ and $Cu_2(\mu\text{-}O_2CC_2F_5)_4$ during high-temperature FEBID metal contents of 76 at.% and 25 at.%, respectively have been obtained. They correspond to 95% and 80% of elemental ligand loss. For both carboxylates it is expected then to detect the presence of various $C_xF_y^+$ groups. It is also possible to detect the entire (ionised) ligand in the spectrum or some oxyfluorocarbons. The measurement range would allow to detect ionised parent molecules for both copper and silver complexes. However, as it was for $Ru_3(CO)_{12}$ it is not expected to see any metal containing species desorbing from the substrate. In their work, Berger et al. presented different pathways of fragmentation of physisorbed $Cu_2(\mu\text{-}O_2CC_2F_5)_4$. These pathways, based on EDX results are listed below:

$$Cu_2(\mu\text{-}O_2CC_2F_5)_{4\,(ads)} \xrightarrow{e-} 2Cu\downarrow + C_2F_4\downarrow + 3(\mu\text{-}O_2CC_2F_5)\uparrow + CO_2\uparrow + F\uparrow \quad (reaction\ 4.1)$$

$$Cu_2(\mu\text{-}O_2CC_2F_5)_{4\,(ads)} \xrightarrow{e-} 2Cu\downarrow + C_2F_4\downarrow + 5CF_y\uparrow + 4CO_2\uparrow \quad (reaction\ 4.2)$$

Upward pointing arrows represent desorbing species and downwards pointing arrows stand for fragments deposited on the surface. It has to be noted that these pathways have been proposed for high-surface-temperature (about 120°C), gas-assisted FEBID. On the other hand experiments with electron irradiation of $Cu_2(\mu\text{-}O_2CC_2F_5)_4$, condensed at room temperature showed similar metal contents [160], so proposed dissociation pathways may also apply to irradiation of solid state grains.

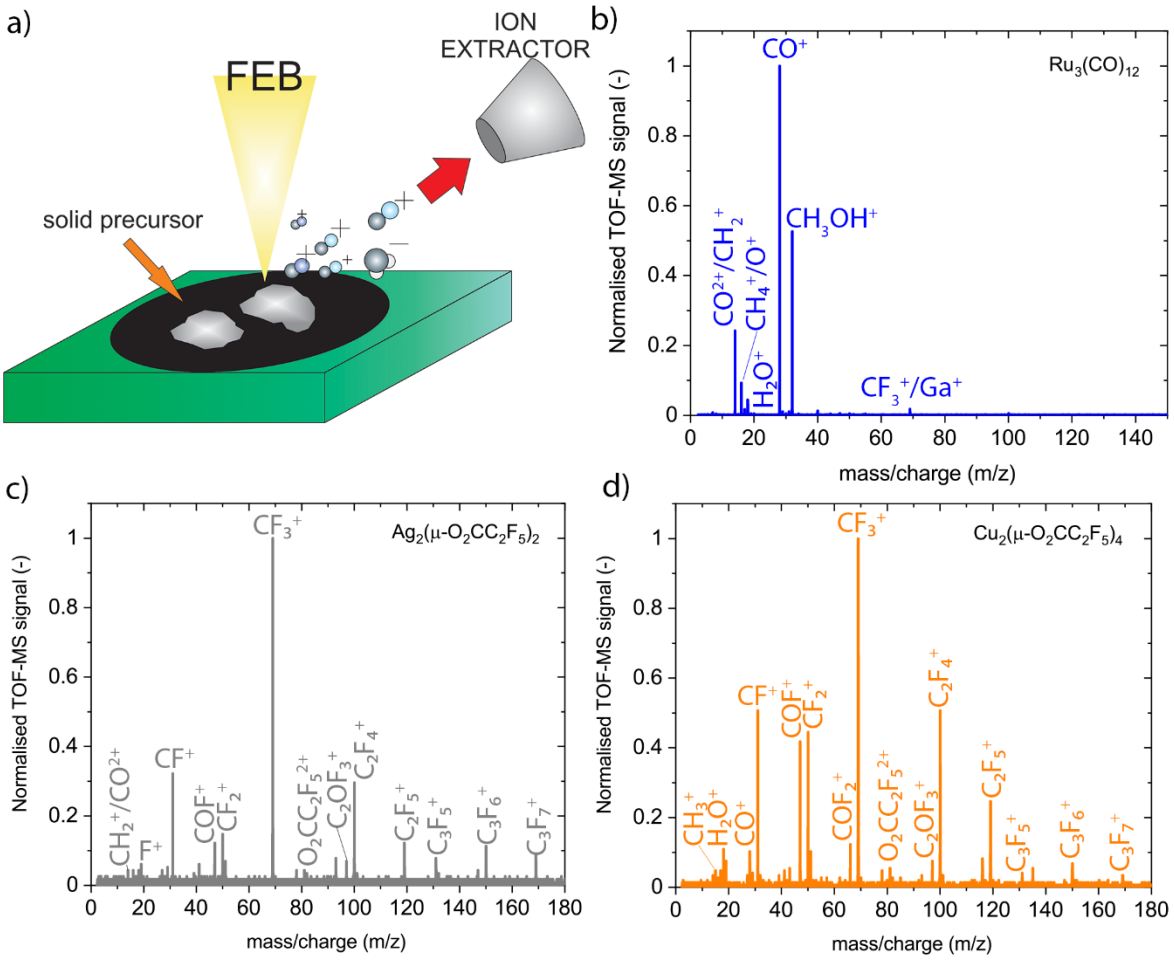

Figure 4.2 a) The schematic representation of irradiation of precursor grain, tilt of the stage and neutral ions are omitted for clarity. Spectra of irradiated grains of precursors: b) $Ru_3(CO)_{12}$, c) $Ag_2(\mu\text{-}O_2CC_2F_5)_2$ and d) $Cu_2(\mu\text{-}O_2CC_2F_5)_4$.

Figure 4.2 b, c and d present spectra detected during irradiation of $Ru_3(CO)_{12}$, $Ag_2(\mu\text{-}O_2CC_2F_5)_2$ and $Cu_2(\mu\text{-}O_2CC_2F_5)_4$ respectively. For the carbonyl, the peaks are contained to low m/z part of spectrum, below 150. The most intense, m/z = 28 comes from ionised carbonyl groups. There is also a peak of m/z = 14 which is probably doubly ionised CO^{2+} moiety (or a CH_2^+). Second most intense, m/z = 32 most probably originates from ionised methanol groups CH_3OH^+. Methanol may be either a gas residing in the vacuum chamber or it is an effect of reaction between carbonyl groups and residing water. This peak may also be an effect

of ionisation of oxygen molecule O_2^+. Water ions were also detected (m/z=18). Neither high m/z peaks nor peaks grouped in families of five to seven were detected, indicating that no ruthenium containing ions desorbed from the surface.

In the case of carboxylates, the spectra are qualitatively similar, containing mostly peaks representing different fluorocarbon groups of $C_xF_y^+$, with x = 1…3 and y = 1…7. In both cases, the most intense one appears at m/z=69, which corresponds to CF_3^+ ions. In addition, other fragments of fluorocarbon ligand are present in the spectrum: CF^+ (m/z=31), CF_2^+ (m/z=50), $C_2F_4^+$ (m/z=100), $C_2F_5^+$ (m/z=119), $C_3F_5^+$ (m/z=131), $C_3F_6^+$ (m/z=150), $C_3F_7^+$ (m/z=169). As it was for the carbonyl, there are no metal containing species presented in the spectra of both compounds. Also full ligand molecule $O_2CC_2F_5^+$, is not visible in any of the spectra. On the other hand, small peak at m/z=81.5 indicates the presence of doubly ionised $O_2CC_2F_5^{2+}$ moiety. The main difference in the results of irradiation of both complexes lays in the presence of small peaks, which appear near the main fluorocarbon signals in spectrum of Cu carboxylate. Zooming in, one can notice, that these signals differ by m/z=3 from the main $C_xF_y^+$ peaks. They are coming from oxygenated fragments, with general formula of $C_xOF_{y-1}^+$. Majority of the peaks are much less intense than their fluorocarbon counterparts. The only exception is COF^+, which intensity is nearly as high as the intensity of CF_2^+. This peak appears for both, Cu and Ag spectra. Although the origin of this peak cannot be directly measured, it can be hypothesised that because copper compounds have twice more ligands per metal atom, there are higher chances to create oxygen-containing moieties with electron beam irradiation.

Irradiating electron beam creates a square or rectangular hole in the irradiated grain. Deformation of $Ru_3(CO)_{12}$ grain was depicted in figure 4.3.

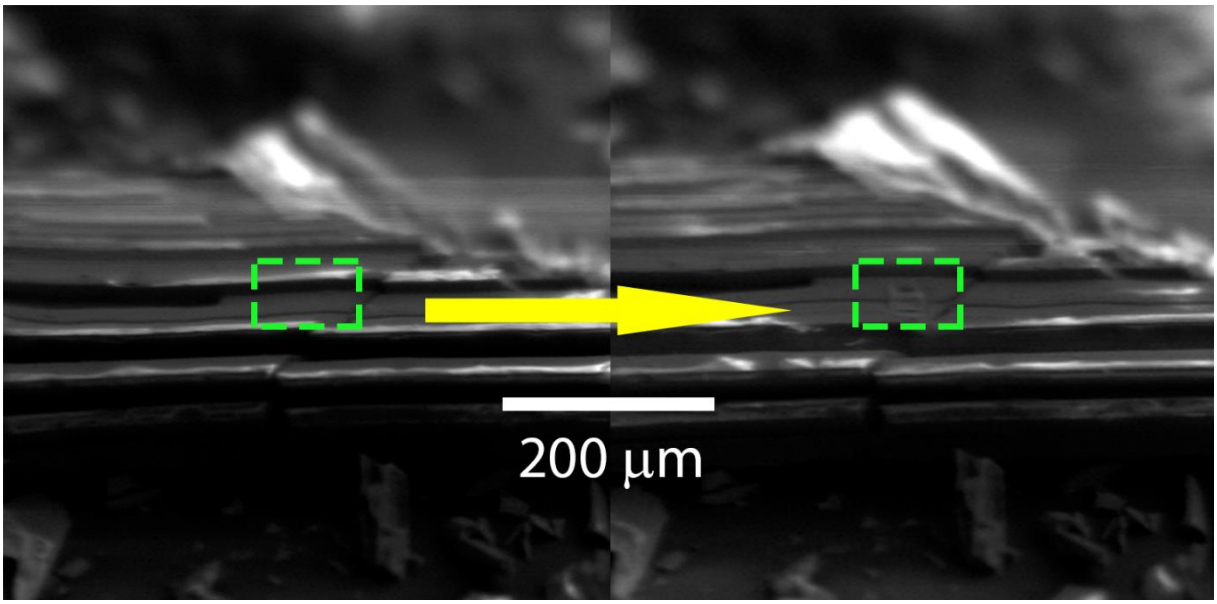

Figure 4.3 Deformation precursor grain due to the irradiation with electrons. The place, where the beam was irradiating is encircled with the green frame. Left image was taken before irradiation, right image after irradiation. Small square-shaped structure visible on the right image is the irradiation area.

4.3 FEBiMS during FEBID

The experiment was divided into three parts, which were done directly after each other with no breaks between. First, pure, cleaned Si wafer was irradiated with electron beam. Recorded spectrum showed volatile, charged species created during deposition of residual gases from the chamber – potential contaminants in FEBID process. After around 300 frames, GIS valve was opened and incoming precursor started adsorbing on the substrate. Electron beam dissociation of physisorbed precursor molecules was creating a deposit, while charged moieties leaving sample's surface were registered using MS. After another 300 frames were irradiated, the GIS valve was closed. The same area was irradiated for next 300 frames, to investigate how fast precursor molecules are removed from the chamber and also to check a possibility of electron induced desorption. The experiment has been schematically depicted on figure 4.4.

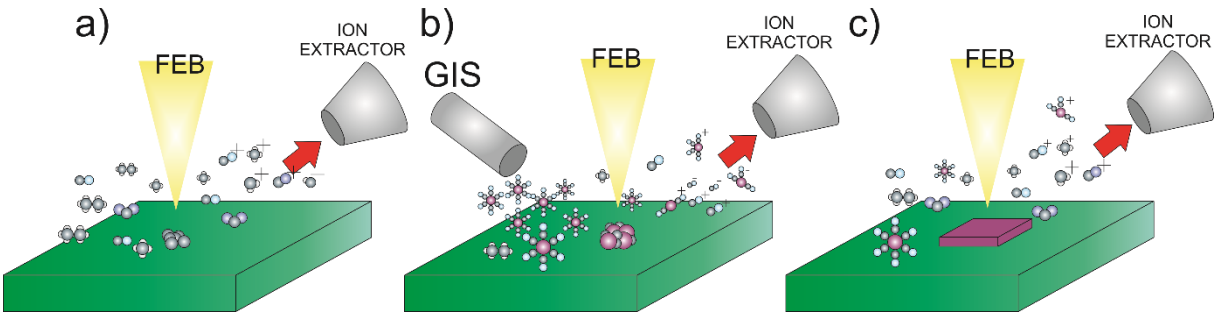

Figure 4.4 The schematic presentation of 3 stages of experiments: a) Mass spectrometry during irradiation of the bare Si wafer b) mass spectrometry during FEBID of $W(CO)_6$ precursor, delivered in gas phase through GIS; c) irradiation of deposited material with GIS valve closed to investigate post irradiation processes.

Condensed phase studies performed by Rosenberg et al. [161] on $W(CO)_6$ in UHV at cryogenic temperature of the sample and beam energy of 500 eV suggest two reactions happening on the surface; presented below:

$$W(CO)_{6(ads)} \xrightarrow{e-} W(CO)_4 \downarrow +2(CO) \uparrow (reaction\ 4.3)$$

$$W(CO)_{4(ads)} \xrightarrow{e-} WO_x \downarrow + 4C \downarrow +(4-x)O \uparrow (reaction\ 4.4)$$

The arrows up mark volatile fragments and arrow down represents deposited fragments. First, the bonds between metal and carbonyl groups are cleaved, leading to desorption of two CO^+ ions per parent molecule (in average) and deposition of partly de-carbonylated molecule. The second reaction leads to dissociation of adsorbed carbonyl ligand. The fragmentation of CO leads to deposition of carbon and oxidation of tungsten or release of volatile oxygen. After irradiation of the condensed phase, mainly WO_3 and C were left on the substrate. Other condensed phase studies conducted by Spencer et al. on $W(CO)_6$ and $Co_2(CO)_8$ confirmed observations presented above [117]. The first reaction, they observed, also has led to partial removal of carbonyl groups. The second reaction, fragmentation of CO groups, has led to either oxidation of metal, release of volatile oxygen or creation of volatile CO_2 due to reaction of oxygen and carbonyl groups. Van Dorp et al. performed FEBID experiments on $W(CO)_6$ using 300kV electrons. Presented results proved that irradiation with e-beam has led to lowering of activation energy of desorption by 2-3 times in comparison to thermal desorption of this compound [84]. The authors stated, that most of the $W(CO)_6$ molecules desorbed from area irradiated with electrons, but they could not identify the composition of desorbing fragments with their setup. It is then expected to observe mainly CO ions in FEBiMS spectra, although, judging from van Dorp experiments, it may be possible to also observe ionised parent molecule $W(CO)_6^+$.

Figure 4.5.a presents positive ion spectrum recorded during FEBID using $W(CO)_6$ as a precursor. The spectrum was recorded in range m/z from 0 to 450, but as the last visible peaks have m/z < 375, only this part of the spectrum was presented. The most pronounced peak is m/z=28, coming from CO^+ ions. It is not surprising, as these are the ions produced both by dissociative ionisation and dipolar dissociation processes of tungsten hexacarbonyl. This peak, as well as H_2O^+ and CF_3^+, were observed also in the spectrum registered during irradiation of pure silicon with GIS valve closed. But, as the peak intensity of m/z=28 is much higher than intensities of H_2O^+ and CF_3^+ peaks, which are not coming from dissociation of precursor it can be suspected that it was produced mostly by dissociation of $W(CO)_6$ and not from SEM's chamber residual gases. Moreover, the intensity of CO^+ ions increases rapidly with opening of gas injection system, which proves that this moiety comes mostly from dissociation of $W(CO)_6$ molecules, see graph 4.6. Second most intense peak is m/z = 12, which can be attributed to C^+ ions. High intensity of this peak suggests, that it origins from further dissociation of ligands, carbonyl groups. Peaks from the high-mass region of spectrum are grouped in families of four, with certain distribution of peak intensities among one family. These all peaks come from tungsten-containing moieties. Starting from four peaks around m/z = 354, which corresponds to ionised full $W(CO)_6^+$ molecule, going down to m/z = 326 ($W(CO)_5^+$), m/z = 298 ($W(CO)_4^+$), m/z = 270 ($W(CO)_3^+$), m/z = 242 ($W(CO)_2^+$), m/z = 216 ($W(CO)^+$), m/z = 188 (W^+). Intensities of the peaks inside one family correspond to abundance of tungsten isotopes. Group of peaks around m/z = 200 comes most probably from $WC(CO)^+$ moieties. Group of peaks in central part of the spectrum, between m/z = 69 (residual gases peak) and m/z = 184 (lowest-mass W^+ isotope) is also grouped in families of four. Closer look on this peaks reveals, that each family from this group has a corresponding family in high-mass part of the spectrum, with double the mass. It means that peaks from this region are most probably also tungsten containing moieties, but doubly ionised.

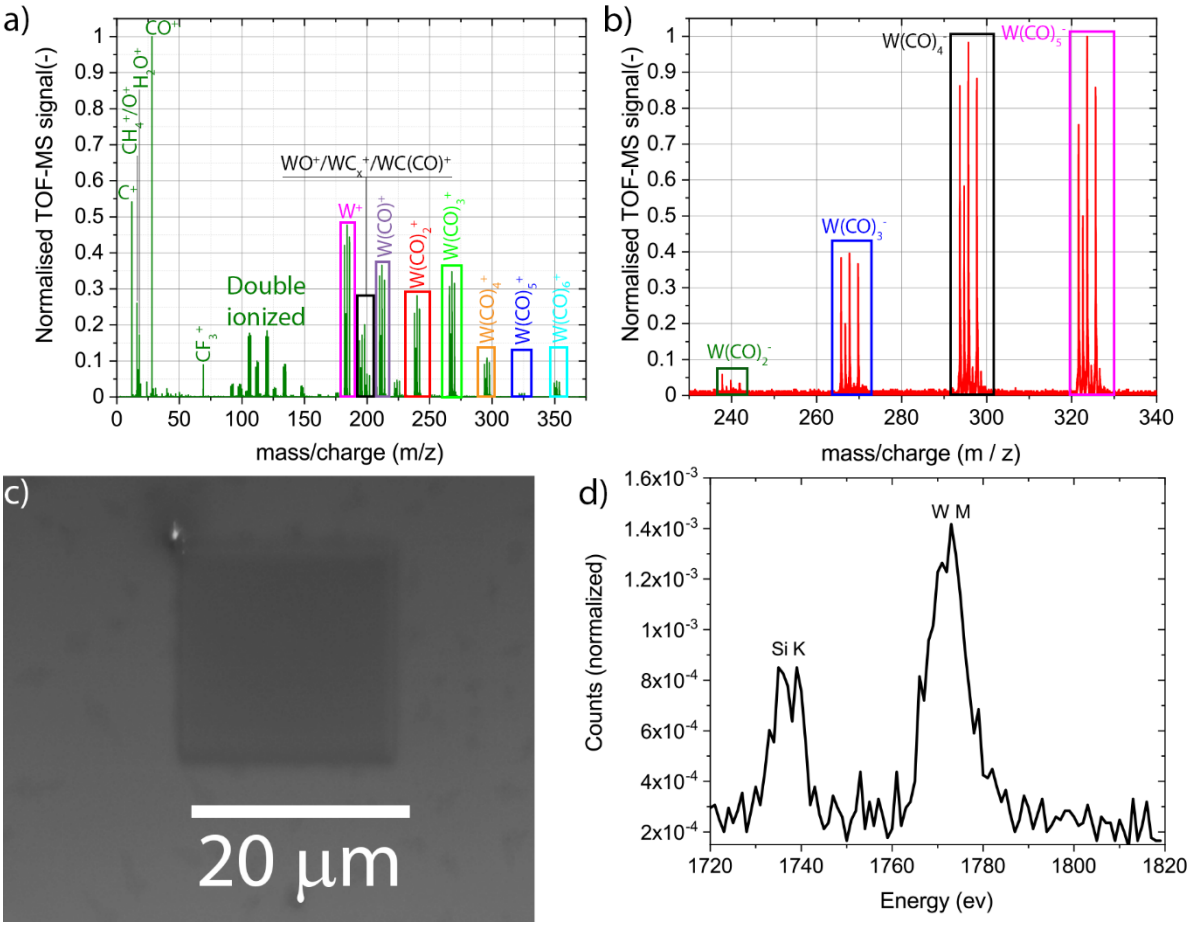

Figure 4.5 Positive a) and negative b) ion spectrum during FEBID with $W(CO)_6$ over. SEM image of deposit obtained during FEBiMS c), typical WDS spectrum in the region between 1720 and 1820 eV d).

Figure 4.5.b shows part of negative ions spectrum recorded during FEBID of $W(CO)_6$. As in previous cases, spectrum was recorded for m/z between 0 and 450. Lower mass (m/z<230) part of the spectrum contains only one peak, m/z = 19, which most probably comes from ionisation of fluorine molecules, residual in SEM chamber. There are no visible peaks for m/z>340, so this part of the spectrum is not shown on the graph. Similar to positive ion spectrum, peaks are grouped in the families of four. It means, that all peaks are coming from ionised tungsten-containing moieties. There are only four families visible, corresponding to four moieties: $W(CO)_5^-$, $W(CO)_4^-$, $W(CO)_3^-$, $W(CO)_2^-$. There are no peaks coming from ionised complete tungsten hexacarbonyl molecule $W(CO)_6^-$, as well as no $W(CO)^-$ and W^- peaks. Interestingly, there are no CO^- molecules, which means, that these fragments are produced only as positive ions, most probably due to dissociative ionisation.

Presence of heavy, tungsten-containing ions in the spectrum is counterintuitive, however, it is in agreement with observations of van Dorp et al. [84] discussed above. Figure 4.5.c presents the SEM image of a deposit made during FEBiMS monitoring of charged, volatile species.

Composition of deposited material was measured using combination of WDS and EDX. As deposits were not thicker than 250 nm, and beam acceleration voltage during measurement was 4 kV it is possible to see SiK peak in the EDX spectrum. Characteristic X-ray lines of SiK and WM lays close to each other (1.739 eV and 1.775 eV, respectively), so they overlap in EDX spectrum. WDS spectrum of W and Si lines and EDX spectra for other elements were quantified using the protocol described in chapter 2. Average composition of deposited material was 1.5 at.% W, 87.5 at.% C, and 11 at. % O. It is below purities achieved before, when metal content reached up to 30 at.% [53]. Uncertainty of the measurement was around 0.5 at.% (estimated as standard deviation of the tungsten content).

It is possible that presence of electric field of TOF detector, can influence deposition process, by simply dragging the charged species from sample's surface towards the detector. It could cause lower than expected metal content of the deposit. If the electric field from TOF detector would have any influence the deposition process, it would also affect both composition and growth rate of the deposits. In order to examine this, another experiment was performed. Three squares were deposited with TOF detector inserted, but without any electric field applied. Next two deposits were made with electric field adjusted to record positive ions spectrum and last two deposits with electric field adjusted for negative ions. Deposits' compositions and average thicknesses are shown in Table 4.1. Thicknesses of the deposits were measured using AFM in tapping (semi-contact) mode. Composition was measured using combination of EDS and WDS, because of overlapping between W M and Si K lines in EDS spectrum, like it was described before.

Table 4.1 Average composition of deposits made in each mode and their measured thicknesses. "w/o TOF" marks deposits made when there was no voltage applied on the TOF detector. All values are given with 0.5 at.% of uncertainty.

Mode	**W (at%)**	**O (at%)**	**C (at%)**	**Thickness (nm)**
w/o TOF	1.3	10.5	88.2	146/137/198
Positive	1.5	11.0	87.5	189/163
Negative	1.3	10.6	88.1	204/194

What can be noticed is that there is no significant difference in composition of deposits made in each mode. All structures have around 1.4 ± 0.5 at.% of tungsten inside. Thicknesses of de-

posits varies much more from 137 nm measured for the deposits made without any voltages applied on ion extractor from TOF and up to 204 nm for the deposit made in negative ion extraction mode. Although the results are spread, there is no clear trend between them, indicating that electric field of the TOF ion extractor does not cause desorption of charged molecules created due to e-beam irradiation. Furthermore, if, hypothetically, electric field of the TOF would drag the charged molecules and cause their desorption from the surface, observed effect would be opposite to the one observed. Deposits made without any field applied would have been thicker, due to increased desorption and decreased growth rate, than the ones made with electric field. Which is clearly not the case.

In condensed phase, surface science studies carried out in cryogenic conditions of 40 K of sample's temperature, Massey et al. observed presence of Fe-containing ions, which desorb from the layer of $Fe(CO)_5$ due to low energy (4 - 22 eV) electrons exposure [89]. Their experiment, alike FEBiMS have not involved post-ionisation. Moreover, van Dorp et al. pointed out the importance electron stimulated desorption during FEBID using $W(CO)_6$ [84]. In condensed-phase studies conducted using $W(CO)_6$ by Rosenberg et al. no tungsten containing species have been observed [161]. Similar spectrum to the one obtained in positive ions detection mode was obtained also by Neustetter et al. for their gas phase cross beam experiment using 70 eV e-beam [166]. Presence of positive ions was explained as an effect of dissociative ionisation. Also gas phase studies performed by Wnorowski et al. showed similar spectrum obtained in negative ions detection mode [167]. In this case, physical process responsible for detection of negative ions was dissociative electron attachment. It is possible then that tungsten-containing ions are not created due to dissociation of species adsorbed on the surface, but by interactions between gaseous $W(CO)_6$ above the substrate and incoming electrons, either from primary beam and/or secondary electrons created on the substrate.

However, simple estimation of ionisation events on the surface and in gas phase is not trivial. One could estimate the concentration of molecules both on surface and in the gas right above the surface, knowing the density of the compound and also its pressure above the surface. Then, it is possible to estimate ratios between the travel paths in gas and condensed phase and using them to estimate the ratio between ionisation events. Ionisation events I depends on concentration of molecules in a volume n, cross section for ionisation sigma and the length of the path, which travels the electron inside this volume:

$$I \sim n\sigma l \quad (4.1)$$

In first estimation it is assumed, that the volume is filled uniformly with molecules. Concentration of molecules in the gas phase n_{gas} depends on the pressure p and temperature T:

$$n_{gas} = \frac{p}{kT} \quad (4.2)$$

where k is the Boltzmann constant. Concentration of molecules which are adsorbed on the surface n_{ads} depends on their density and molar mass:

$$n_{ads} = \frac{\rho N_A}{M} \quad (4.3)$$

where N_A is an Avogadro number. Pressure over the substrate can be calculated knowing the flux of molecules leaving the gas injection system through the nozzle exit J:

$$J = PN_A(2\pi MRT)^{1/2} \quad (4.4)$$

Where R is the universal gas constant and other variables are explained above. J can be calculated using a throughput of the precursor Q through the GIS and the area of the nozzle exit. The throughput is proportional to pumping speed S and the difference of pressure during FEBID and SEM background pressure. The difference is denoted Δp.

$$Q = S \cdot \Delta p \quad (4.5)$$

Background pressure in the SEM chamber was $2 \cdot 10^{-6}$ mbar. After opening of GIS valve, the pressure stabilised around $6 \cdot 10^{-6}$ mbar, after short jump to the value of $1 \cdot 10^{-5}$ mbar. This corresponds to a local pressure of $p = 5 \cdot 10^{-3}$ mbar on the substrate, over the irradiation area of the FEB. Entering other parameters like density: $\rho = 2.65\ \mathrm{gcm^{-3}}$, $W(CO)_6$ molar mass: $351.85\ \frac{\mathrm{g}}{\mathrm{mol}}$ and the temperature of reservoir and the nozzle $T = 100°C$, the ratio between concentrations in adsorbed and gas phase can be estimated: $n_{ads}/\, n_{gas} \approx 5 \cdot 10^7$. As desorption of ionised fragment from adsorbed phase most probably will occur only from the two first monolayers, the path of the electrons in through condensed phase can be estimated to be about the size of the metalorganic molecule $l_{ads} \approx 1\ nm$. In gas phase, the travel path (without collision) of electrons can be estimated to be around $l_{gas} \approx 100\ \mu m$. Using the ratio between travel paths it can be estimated that in this experimental conditions was about: $I_{ads}/I_{gas} \approx 5 \cdot 10^2 \cdot \sigma_{ads}/\sigma_{gas}$.

To continue the quantification one needs to know the cross sections for dissociations, both in gas phase and on surface. Up to now, for $W(CO)_6$, there are only relative gas phase cross sec-

tion measurements available, which prohibit further quantification [167]. Although de Vera estimated the absolute values basing on relative cross section and by means of dielectric formalism [86], these results were not confronted with the experiments. Thus, it is not possible to properly quantify how much of the signal comes from the gas and how much from the adsorbed phase in the FEBiMS spectrum. Yet the travel-path of electrons through the gas "cloud" can be minimized by the arrangement of detectors, GIS, and FEB and in this way the gas contribution can be minimized. To address the knowledge gap in absolute cross section values of adsorbed phases or the quantitative ratio of $\sigma_{ads}/\sigma_{gas}$ further experiments or simulations would be desirable but they were not in the scope of this PhD Thesis.

4.4 Signal time evolution

Figure 4.6 presents the time evolution of signals, coming from different peaks present in $W(CO)_6$ spectrum. As it was described in the previous section, the GIS valve was opened after 300 frames of irradiation of empty Si wafer. After opening the valve, rapid and sharp increase of signal of the ions was observed. Then the signal fluctuated until 600th frame, when the valve has been closed. After closing the valve, the average intensity of signal stayed on the same level for some time, called delay time t_D and then started exponentially decreasing, reaching the level of background. This delay time comes from the fact, that after closing the valve, the gaseous precursor will stay for some time above the surface, adsorbing and desorbing before it starts to be depleted with e-beam. As all of the signals go exponentially down, it can be stated, that there are no post-deposition changes to the structure due to electron beam stimulated desorption or beam damage to the structure. The time evolution of signals coming from different ions from $W(CO)_6$ spectrum are presented in Figure 4.6a.

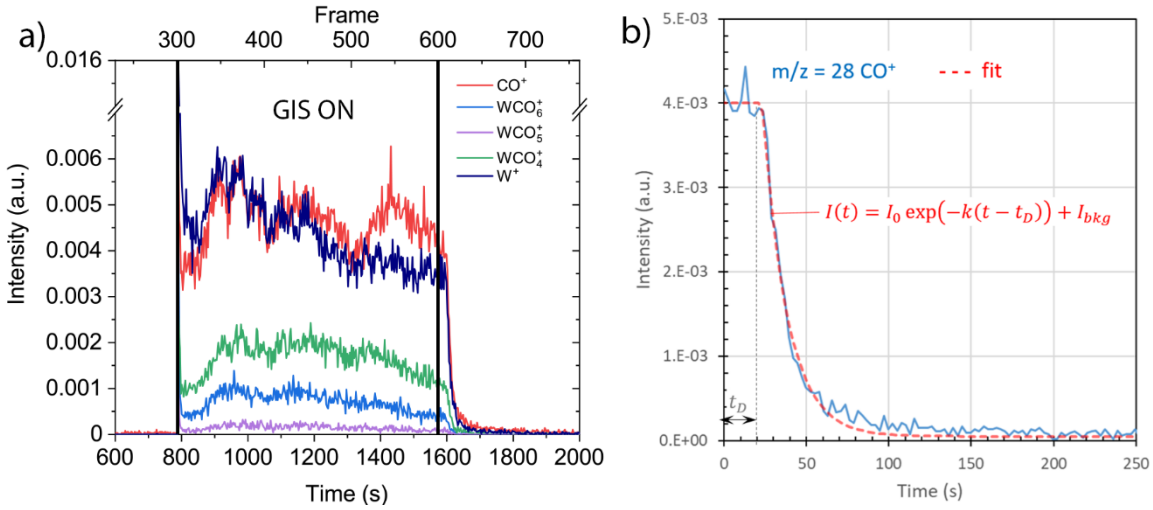

Figure 4.6 Signal time evolution of intensities of chosen peaks coming from $W(CO)_6$ positive ions spectrum (a). Close up on the signal time evolution of CO^+ ions. The curve was biased, so the time of the 600th frame was moved to 0. Red dashed line represents a curve fitted to experimental data.

The decay of a signal coming from CO^+ ions is presented in Figure 4.6b. The data were fitted with exponential function with formula: $I(t) = I_0\, exp\big(-k(t - t_D)\big) + I_{bkg}$, where I_{bkg} is a background signal level, k represents the decay rate of the signal, t_D is a delay time, I_0 is a signal amplitude. The values coming from fitting the curve are: $I_{bkg} = 5 \cdot 10^{-5}$, $I_0 = 0.04$, $t_D = 23$ s, $k = 0.067$ s^{-1} (which represents the time of 15s which is needed to reduce the signal intensity by $1/e$). Parameter k^{-1} depends on the dimensions of the chamber, efficiency of pumping system and temperature.

4.5 Discussion of the FEBiMS results

Concerning the results presented in chapter 4, especially obtained with silver carboxylates and ruthenium complexes FEBiMS delivers new insight into electron-induced dissociation processes.

All FEB induced deposits made with carboxylates and presented in this study characterise with, unusual, for FEBID metal contents, especially $Ag_2(\mu\text{-}O_2CC_2F_5)_2$. Irradiated grain of this precursor produced various different volatile ions, which can be described by general formula C_xF_y. What is interesting, full ligand molecule was not detected as single ionised specie, although there was a low intensity signal coming from doubly ionised $\mu\text{-}O_2CC_2F_5$ moiety. The most probable explanation is that non-selective electron beam cleaves many bonds, including the one between silver and oxygen atoms and also bonds within the ligand. Although in some cases cleaving of the inter-ligand bonds may lead to lowering the metal content of the deposit, for silver carboxylate majority of the produced fragments are volatile fluorocarbons, which may explain high silver content of the deposits. On the other hand, the same spectrum was ob-

tained for $Cu_2(\mu\text{-}O_2CC_2F_5)_4$, which gave much lower metal content while deposited with electron beam, both from gas phase as well as from condensed layer of precursor[36, 160]. However, copper carboxylate has twice more ligands per one metal atom, which makes it more probable to create non-volatile species due to e-beam irradiation. Furthermore, one has to understand, that results coming from irradiation of a grain of compound cannot be compared directly to actual FEBID experiment. To really asses the problem with differences in metal content between these two compounds, FEBiMS measurements during FEBID with these two compounds would have to be conducted. This implies using heated stage and short, in-chamber GIS, which was applied to experiments described in chapter 3.1. As the TOF mass spectrometer is installed on a multi-user FIBSEM with TEM lamella preparation and EBSD facilities, these technical modifications could not yet be realised due to space limitations.

The results obtained for $W(CO)_6$ can help with understanding of the FEBID results obtained with both $Ru(\eta_3\text{-}C_3H_5)(CO)_3Br$ and $Ru(CO)_4Br_2$. Although for the first compound, the allyl group seem to be the most problematic and causing the low metal content in as-deposited material, replacing it with more volatile carbonyl and another Br atom did not change the metal content. The carbon content was still relatively high. In the FEBiMS spectrum of $W(CO)_6$ peaks of C and O could be observed, supporting the assumption made in section 3.2 that volatile carbonyl groups can still be dissociated and some carbon may be co-deposited, lowering the metal content of the FEBID material.

4.6 Conclusions

Comparing the FEBID results with MS spectrum obtained it can be concluded that it is not only important to use volatile groups as ligands, but also to use ligands, which, upon irradiation, dissociate into other, volatile moieties, rather than co-deposit. FEBiMS is a very versatile and powerful method which allows for detection of any ionised species desorbing from the substrate due to irradiation with electrons. Considering this, it gives incomparable insight into electron-induced processes happening on the surface. It was applied to detect volatile parts of ligands dissociated with electron beam during FEBID, as well as the ions desorbing from irradiated precursor grains.

Focused electron beam induced mass spectrometry provided additional information about electron induced dissociation pathways. For fluorinated carboxylates it has shown a spectrum of different C_xF_y species, suggesting that even fragmentation of dissociated ligand can create a volatile moieties, which can explain high metal content of deposits made with $Ag_2(\mu\text{-}$

$O_2CCF_3)_2$ and $Ag_2(\mu\text{-}O_2CC_2F_5)_2$. Moreover, FEBiMS measurement provided proof that in FEBID conditions carbonyl groups can dissociate into C and O ions, which explains why replacing an allyl group with additional halogen and carbonyl did not lead to carbon-free deposits. Potentially, it can be used to detect also ions desorbing from the adsorbed layers of resist used for electron beam lithography. It does not require ultra-high vacuum, like typically used in condensed phase surface science methods, which makes it easier to apply and also closer to real condition of both FEBID and electron lithography. As it is novel method it has some disadvantages, like a problem with the origin of the metal-containing ions detected in the spectrum, but further development of this technique can provide a powerful measurement method, which will be of interest for electron-beam nano-structuring community.

5 Development of FEBID modelling

5.1 Rate maps with resolution parameter and influence of diffusion

In chapter 1, a standard FEBID model has been shown. This model allows for mathematical description of the fate of the molecule of the precursor, which has adsorbed on the surface. Such a molecule can desorb or be dissociated, contributing to the growth of the deposit. In its primary form, the model was developed for Langmuir type of adsorption (coverage < 1), but it was further developed by Sanz-Hernandez et al. to describe also a multilayer adsorption (BET adsorption) [92]. They proposed a new tool of visualisation of the results of modelling: rate maps (in original work called frequency maps).

One of the biggest drawbacks of rate maps is that to properly locate the experiment on the map. The exact set of parameters have to be known before, to calculate characteristic rates for all three surfaces processes (excluding surface diffusion so far). Growth rate frequency also cannot be directly measured. It can be a serious problem, as to calculate rates it is required to know the basic properties of used precursor, like the size of its molecule (to estimate n_0), average desorption time and cross section for dissociation. As was mentioned before, these parameters are difficult to measure, hence it is not easy to find all three values for a precursor. To properly address this problem, modification of original maps is proposed, by adding resolution parameter φ to the maps. This parameter can be easily calculated for created deposits as it requires to measure only FWHM's of the beam and the spot deposit. By using aforementioned scaling laws, the resolution parameter can be expressed in the units of characteristic frequencies and directly plotted on maps, giving new insights into deposition process. Figure 5.1 depicts a rate maps with the coverage plotted on the colour scale and resolution parameter as lines. The parameter was calculated using formula (1.10a), for the case of stationary exposure without diffusion.

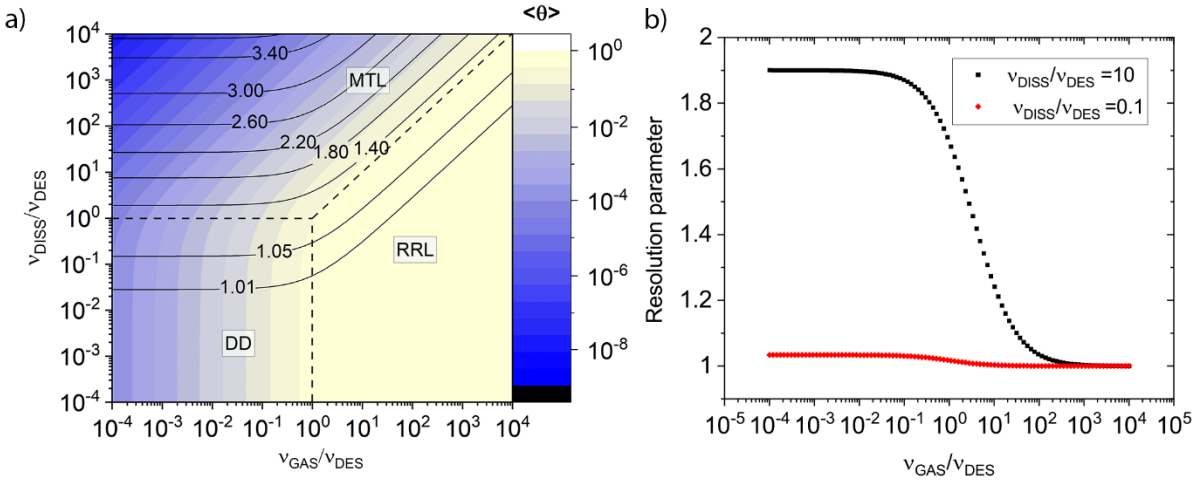

Figure 5.1 a) Characteristic rate map with coverage on the colour scale and resolution parameter on the line scale with numbers. b) Dependences between resolution parameter and normalised adsorption rate plotted for two values of normalised dissociation frequency: 0.1 and 10. DD, RRL, MTL stand for different deposition regimes, i.e. desorption driven, reaction rate limited, mass transport limited, respectively.

By adding this parameter, it is much easier to position the experiment on the map. It is enough to know only one rate, in case of map from figure 5.1 it would be desorption frequency and then perform experiment, where the size of the deposit is measured depending on different dissociation frequency. This frequency is relatively easy to change, as most of the modern SEMs allow for changing the beam current over relatively large range of few orders of magnitude.

Figure 5.2 presents modified map from Figure 5.1. It is still made for the case of constant desorption frequency. The colour scale presents normalised growth rate frequency and line scale with numbers shows resolution parameter. As can be noticed, for high adsorption frequencies and low dissociation frequencies (reaction rate limited regime), the resolution parameter is close to 1. By increasing dissociation frequency (e.g. by using higher beam currents or better focused beam), resolution parameters grows, reaching the highest value in mass transport limited regime. In this regime, there precursor is depleted before it can be fully replenished. For the Gaussian-shape beam, the highest depletion occurs in the centre, where electron density is the highest. In the case of MTL regime, even further from the beam centre there is enough electrons to successfully deposit, increasing the lateral size of the structure. This effect was observed in the work of Pablo-Navarro [168]. In their experiment, they were changing the flux of $Co_2(CO)_8$ precursor molecules and observing the growth rate and shape changes in function of the pressure in the chamber. Even though the aspect ratios of their deposits is larger than 1, they observed, that for higher pressures, the deposits are taller and thinner (higher

growth rate and lower resolution parameter). With lower precursor fluxes the deposits are thicker and shorter.

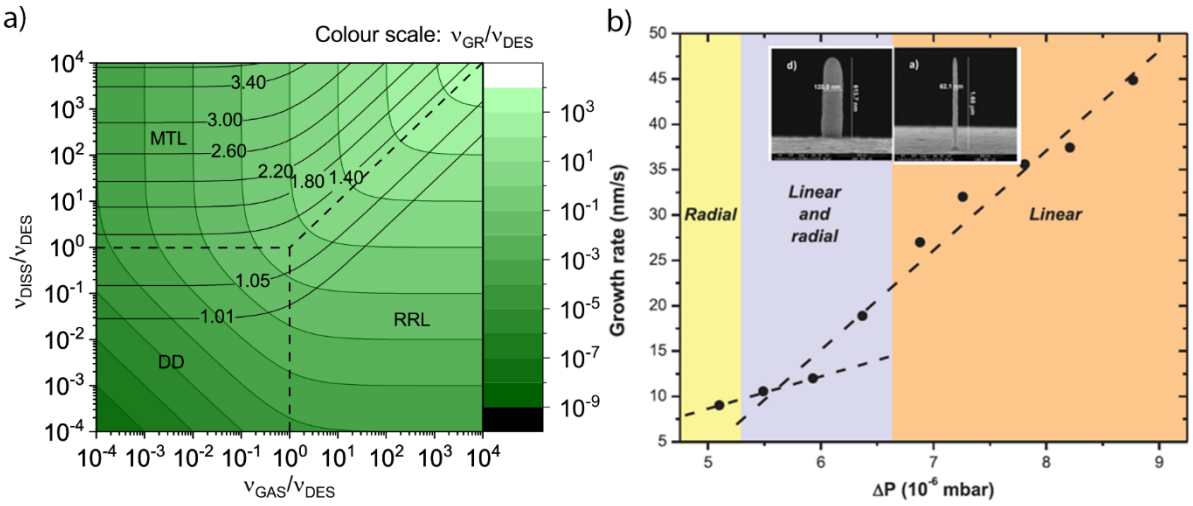

Figure 5.2 a) Modified characteristic frequency map with normalised growth rate frequency on the colour scale and resolution parameter on the line scale with numbers. b) Dependence between growth rate and the difference between background vacuum pressure and operational pressure during FEBID of $Co_2(CO)_8$ with marked growth regimes. The inset presents the deposits made in each regime. Reproduced basing on [168].

5.1.1 Rate maps including surface diffusion

By solving the main FEBID equation (1.1) including diffusion influence, it is possible to create another set of rate maps. To do so, there is a need to define so called diffusion rate, which would inform, about a number of diffusion events happening on the unitary surface during unitary time. Diffusion rate can be expressed as the ratio between surface diffusion coefficient of the molecule on the surface and the beam's FWHM squared:

$$\nu_{Diff} = \frac{D}{FWHM_B^2} \quad (5.1)$$

Using so defined diffusion frequency, maps were prepared using Matlab® for calculation and Origin software for plotting for Langmuir adsorption model and are presented in figure 5.3. The solution of the FEBID equation, using which the maps with the diffusion influence were prepared can be find in Appendix A3. The maps were plotted for the point on the surface, where the centre of the electron beam was placed. The maps were normalised to desorption frequency (constant stage temperature case) and are showing coverage of surface on colour scale and normalised growth rate frequency on the line scale. The first map (a) is very similar to the one from Figure 1.7, without any influence of diffusion. It was plotted for the case when diffusion rate was equal to desorption rate. This case can be treated as a threshold,

above which diffusion starts to play more significant role. Increasing the diffusion rate further, to effects can be observed:

1) Increase of the area of the region of the full surface coverage. Moreover, surface is fully covered for higher dissociation rates.
2) The high-growth-rate region moves towards lower adsorption rates.

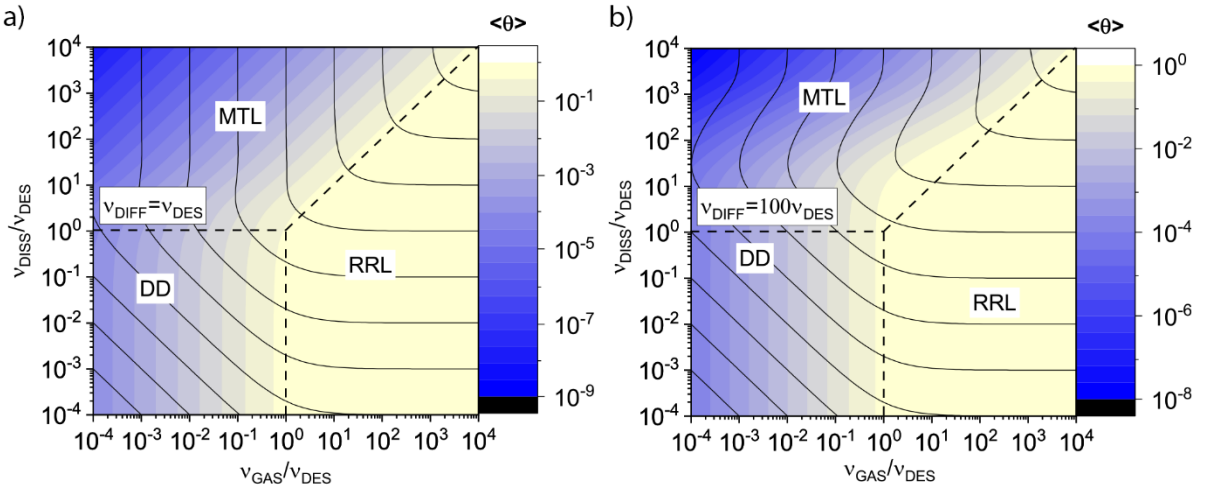

Figure 5.3 Characteristic frequency maps with introduced normalised diffusion frequency in the centre of the beam.

Figure 5.4 presents the influence of the diffusion on the resolution parameter. As can be noticed, by increasing diffusion rate, resolution parameter decreases for the same normalised adsorption frequency. This effect is even more pronounced than the change in growth rate. Figure 5.4 c and d present respectively resolution parameter and normalised growth rate in the function of normalised adsorption rate, for single dissociation vs. desorption frequency ratio of 100. What can be noticed, for the diffusion to desorption rates ratio of 1, the growth rate behave the same as if no diffusion was applied. For the same $\frac{\nu_{DIFF}}{\nu_{DISS}}$ ratio, the resolution parameter changes significantly, compared to the no-diffusion case.

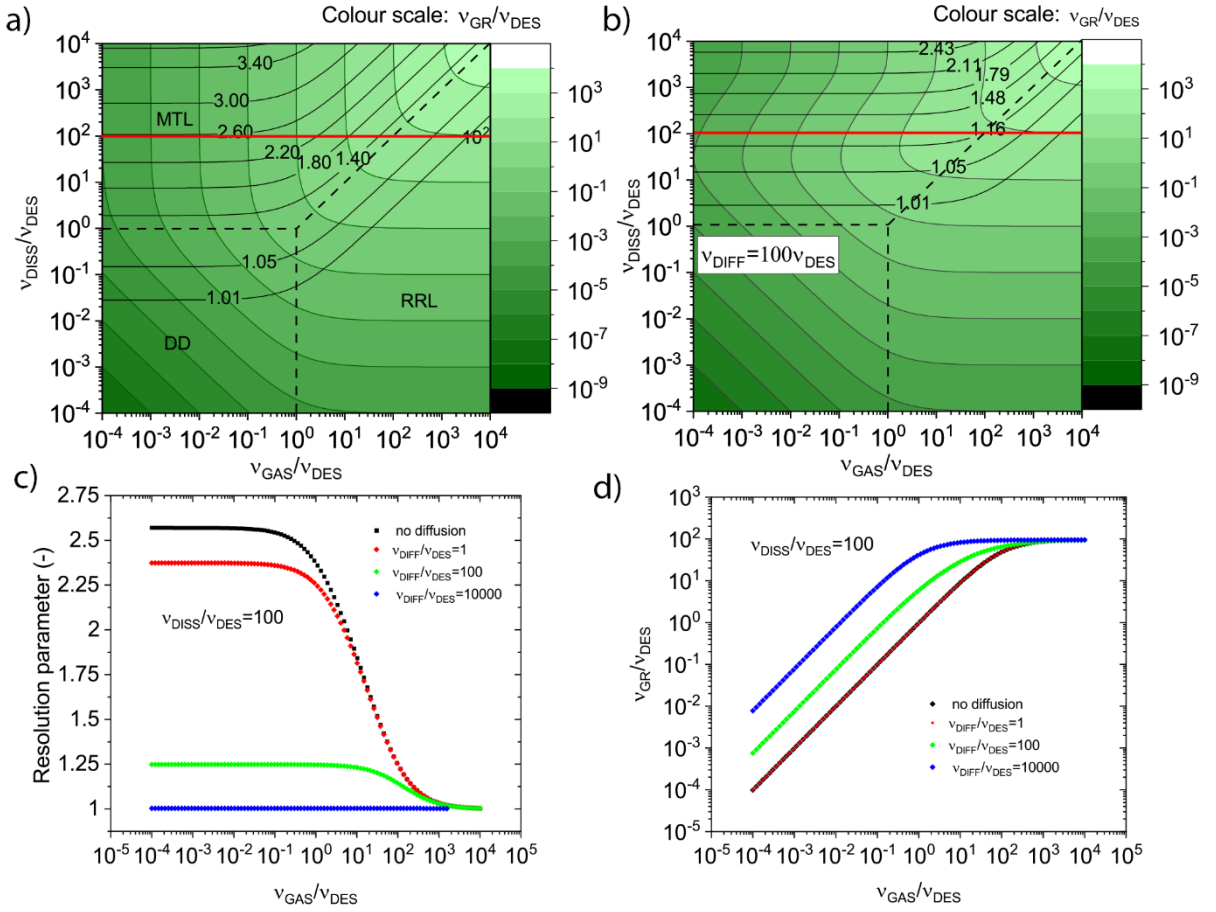

Figure 5.4 The influence of the diffusion on the modified frequency maps. a) The map without any diffusion influence, b) the map for $\nu_{DIFF} = 100\nu_{DES}$. The red lines on both maps present the place, from where the linear profiles were extracted; c) Linear profiles of resolution parameter for $\nu_{DISS} = 100\nu_{DES}$; d) Linear profiles for normalised growth rates for $\nu_{DISS} = 100\nu_{DES}$.

Both of these effects – enhancement of growth rate and decrease of deposit site can be explained as a direct effect of increased number of molecules in the beam area, delivered there by surface diffusion. In the central point, the depletion of the molecules due to the e-beam irradiation is the highest, creating large gradient of lateral density of molecules, which also enhance the diffusion. Diffusion delivers more precursor molecules, increasing the growth in the centre. Moreover, when more molecules travels towards the centre in the unit of time, there is lower probability that they will be dissociated by the electrons from the outer part of the beam. Higher the ν_{DIFF}, more molecules will travel towards centre in the one second, further decreasing the FWHM of deposited spot.

5.2 The ligand co-deposition model

Current FEBID model, extended with rate maps discussed in detail in chapter 1 and in previous subchapter has proven to be very useful in helping understanding and describing the mutual dependences between multiple parameters of deposition process and their influence on final size and shape of the deposit. Despite it, the model has certain limitations, among which, one of the most important is that it does not specifically consider electron-induced cleavage of ligands from the metal atom and their subsequent fate which can be their desorption and co-deposition.

In this subchapter, a co-deposition model, which analyses the fate of ligands adsorbed to the surface will be presented. Not only results of the calculations will be shown, but also an experimental evidence, qualitatively confirming the assumptions of the model. Moreover, further extensions to the model will be discussed.

5.2.1 Basics of the model

The main original part of this model is that it individually follows the fate of ligand upon electron-induced fragmentation. A homoleptic (metalorganic) molecule M-L composed of a (metallic) core element (M) and its (organic) ligands (L) is considered. The ligand L stands for a certain family of ligands e.g. carbonyl, beta-diketonates, carboxylate, depending on the molecule used for FEBID. Precursor examples of these would include $W(CO)_6$, $Cu(hfac)_2$ and $Ag(\mu\text{-}O_2CC_2F_5)_2$. The adsorption type of the molecule is modelled as physisorption – the molecule stays intact on the surface. To simplify the calculations, surface diffusion was neglected. What is different to the standard FEBID model is that now also the fate of the ligands dissociated from the metal core can be modelled. They can either thermally desorb from the surface or be further dissociated. Such dissociated ligands create non-volatile sub-fragments, which are co-deposited on the surface and volatile sub-fragments, which were considered to desorb immediately. For instance, a carbonyl ligand dissociated into carbon and oxygen atoms $CO \xrightarrow{e^-} C \downarrow + O \uparrow$. In this example, carbon is deposited and oxygen desorbs and is pumped out from the chamber. Any potential reaction of the volatile sub-fragments (in this case atomic oxygen) with the surface is neglected. The model assumes no second electron dissociation of once dissociated ligand. Also, possible re-adsorption of ligands after they desorb is not considered. The ligand co-deposition model bases on two differential equations:

$$\frac{\partial n_{ML}}{\partial t} = J_{ML}\left(1 - \frac{n_{ML}}{n_{0ML}} - \frac{n_L}{n_{0L}}\right) - \frac{n_{ML}}{\tau_{ML}} - \sigma_{ML} f n_{ML} \quad (5.2)$$

$$\frac{\partial n_L}{\partial t} = \sigma_{ML} f n_{ML} - \frac{n_L}{\tau_L} - \sigma_L f n_L \quad (5.3)$$

All variables are the same as for standard FEBID model, just the indices differentiate between the precursor: ML and the ligand: L. As can be noticed, in both equations ligands are described by the same three parameters, which depend only on the properties of the molecule and cleaved ligand: σ, τ and n_0. Electron flux is the same for both precursor and ligands. Molecules ML are supplied at a rate of $\frac{J}{n_{0ML}}$ to the surface from the gas phase and ligands are formed on surface as a result of electron induced dissociation of the intact molecule ML, at the rate $\sigma_{ML} f$. As ligands and the pristine molecule can have different sizes, they have also different maximal number of physisorption sites ($n_{0ML} \neq n_{0L}$). The situation is depicted schematically in Figure 5.5. The molecules are depicted as consisting of two parts, the metal atom M (red) and ligand atom L (green). The adsorption sites are represented by square mesh, dividing the surface of the substrate. After the molecule physisorb on the surface, it is dissociated by the electrons leaving chemisorbed (red rectangles) metal atom and physisorbed (green rectangles) ligands. Then ligand can be also dissociated with the electron beam leaving chemisorbed part L1 and a volatile part L2, which desorbs.

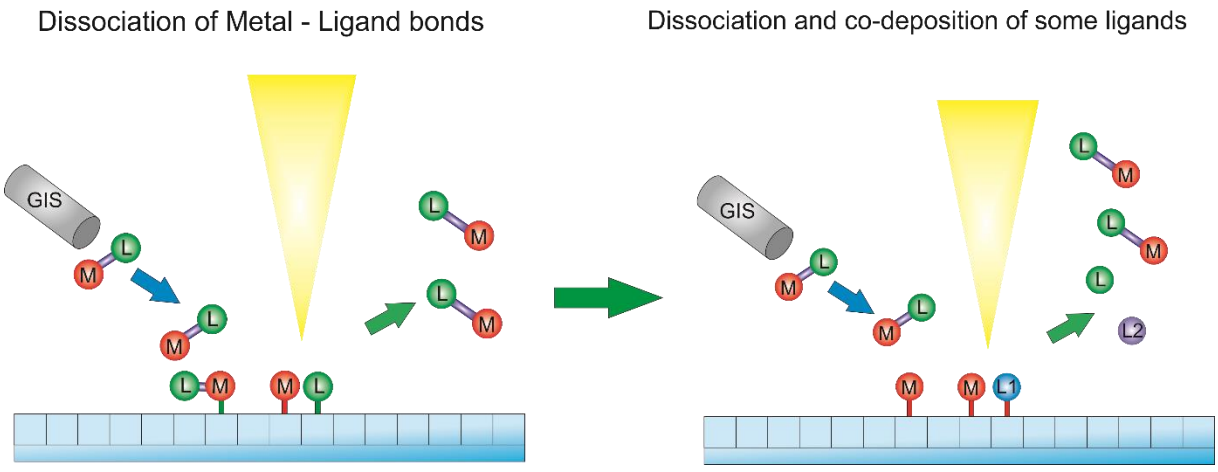

Figure 5.5 The schematic representation of ligand co-deposition. The substrate square mesh represents the adsorption sites. Chemical bonds are presented as sticks with colour code; grey: metal-ligand bond, green: physisorption (van der Waals force, moiety can still desorb), red: chemisorption (moiety is deposited).

Although, on the schematic representation in figure 5.5 it was depicted like this (for clarity reason), co-deposition model is not limited only to the compounds which have one ligand per a precursor molecule. Generally speaking, it can be applied also to any homoleptic compound

of a general formula $M(L)_N$, like carbonyls which are frequently used in FEBID. To consider more ligands, the second equation has to be re-written in the form of:

$$\frac{\partial n_L}{\partial t} = N \cdot \sigma_{ML} f n_{ML} - \frac{n_L}{\tau_L} - \sigma_L f n_L \ (5.4)$$

as each dissociation of precursor molecule can create up to N ligand parts. The set of equations has two solutions: one for precursor and one for ligands. Analytical solution and its consequences have been discussed thoroughly in master Thesis of Leo Brockhuis [169]. In this work, the equation was solved numerically, using self-written script in Matlab®, basing on Euler's method.

$$\frac{\partial n}{\partial t} = g\big(t, n(t)\big) \ (5.5.a)$$

$$t_i = t_0 + i \cdot \Delta t \ (5.5.b)$$

$$n_{i+1} = n_i + \Delta t \cdot g\big(t_i, n_i(t_i)\big) \ (5.5.c)$$

The g(t, n(t)) is the function of n and time. The i is an index, which changes in the range of $i = 1 \ldots i_{MAX}$, where i_{MAX} is the maximum value for which $t_i = t_d$. Δt represents a time step. In the case presented in this work the differential equations are changed into this set of equations of differences:

$$n_{MLi+1} = n_{MLi} + \Delta t \cdot \left[J_{ML} \cdot \left(1 - \frac{n_{MLi}}{n_{0ML}} - \frac{n_{Li}}{n_{0L}} \right) - \frac{n_{MLi}}{\tau_{ML}} - f \sigma_{ML} n_{MLi} \right] \ (5.6.a)$$

$$n_{Li+1} = n_{Li} + \Delta t \cdot \left[f \sigma_{ML} n_{MLi} - \frac{n_{Li}}{\tau_L} - f \sigma_L n_{Li} \right] (5.6.b)$$

Where *i* is an index representing consecutive moments of time.

In all presented calculations following starting conditions were applied:

$$n_{ML}(t = 0) = N_{0ML} \ (5.7.a)$$

$$n_L(t = 0) = 0 \ (5.7.b)$$

which describes the situation when the surface is fully covered with precursor molecules and there are no separated ligands (the beam was switched on at t = 0).

The growth rate is defined as previously:

$$R_j(t) = V_j n(t)_j \sigma_j f \ (5.8)$$

where j = ML or L. The calculations were made for a uniform beam, to simplify calculations.

The growth rate will be presented in dependence on dwell time. As n is function of time, each of the growth rate was calculated as an average growth rate per dwell time, using formula:

$$R_j = \frac{V_j f \sigma_j}{t_d} \int_0^{t_d} n_j(t) dt \quad (5.9a)$$

where j = ML or L. For the discrete data used in numerical calculations, the growth rate had a form of a sum instead of integral:

$$R_j = \frac{V_j f \sigma_j}{t_d} \sum_{i=1}^{i:t_{di}=t_d} n_{j,i} \cdot \Delta t \, (5.9b)$$

where j = ML or L. Since the growth rates can be calculated separately for both metal atoms and ligands, the total growth rate is a simple sum of both components. The growth rate is a very important parameter of the single specie FEBID model, as it can be measured directly for certain experimental conditions and can serve later to calculate basic parameters of precursor molecules, like their average desorption time τ or a total cross section for electron-induced dissociation σ. In her PhD dissertation, Aleksandra Szkudlarek introduced a protocol to use series of spot deposit made with different dwell times to derive basic parameters of the precursor [170], which was based on the work of Toth et al. [85].

The generic shape of this function in relative units was showed in a publication of Szkudlarek et al and it is reproduced in Figure 5.6. What can be noticed is that the function is never growing. At its beginning it is almost flat and then first slowly and later rapidly decays, reaching a plateau for long dwell times.

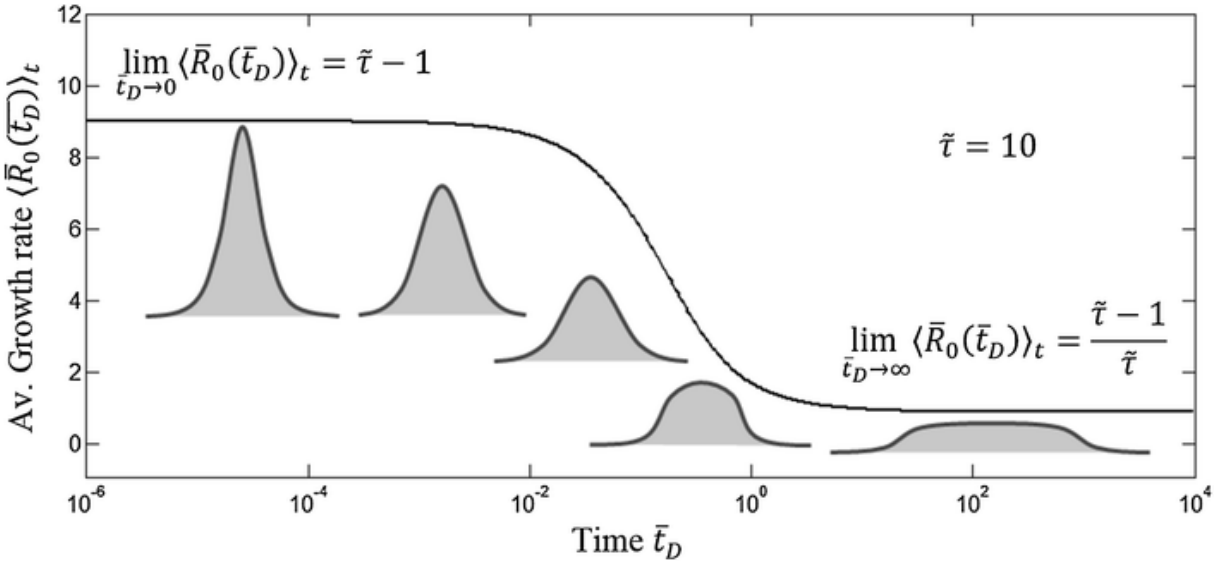

Figure 5.6 Normalised growth rate as function of dwell time in the units of t_{out} calculated with single specie model. $\bar{t}_D$ is a normalised dwell time, defined as for the formula 1.10.c. Taken from [91]

In co-deposition model, the growth rate of ligands is adding to the growth rate of metal atoms. Depending on the characteristic parameters of both pristine precursor molecules and ligands, such as total cross section of electron induced dissociation, average time of thermal desorption, number of sorption sites and volume of metal atoms and deposited parts of ligands. Figure 5.7 depicts the growth rate in function of dwell time for metal atoms, ligands and total (sum of both two). The growth rates were calculated using parameters for $Co_2(CO)_8$ taken from Sanz-Hernandez et al. [92] for precursor molecules and estimated parameters for ligands. The parameters were gathered in Table 5.1. Parameters of ligands were assumed basing on intelligent guesses. Number of sorption sites for ligands was set to be equal to the one of precursor molecules ($N_{0ML} = N_{0L}$), as it is usually the ligands which have higher volume due to the bigger number of atoms and it is their size which limits the number of adsorption sites for molecules. The model itself does not require this assumption. This simplification was used to show the model, which is the closest to real-life case and show some general tendencies, but it can be adjust to fit some other type of molecules. For the same reason their volume was assumed to be higher than the volume of a metal atom and was set as double for the deposited ligand sub-fragment. The precursor molecule contains a metal atom which is heavy, so the volatility of the full molecule is usually lower than the volatility of separated ligand. In the first approach it was then assumed, that ligands have lower average desorption time. Although in next section the influence of changing ligand desorption time will be discussed. The influence of the desorption time will be discussed further in this chapter. The cross section for dissociation of ligands was the hardest to estimate. For the next graph it was assumed to be high-

er than for the precursor molecule, just to show how the growth rate of ligands can affect the total growth rate. However, the influence of the cross section of ligands will be discussed further in this chapter as well.

Table 5.1 Parameters applied to the ligand co-deposition model used in the next part of this chapter. The volume of the deposited fragment corresponds to the metal atom for the molecule and to the deposited sub-fragment of the ligand.

Parameter	**Value for the molecule (ML)**	**Value for the ligand (L)**
Flux of molecules J $\frac{\textbf{molecules}}{\textbf{s}\cdot\textbf{m}^2}$	$1.5 \cdot 10^{21}$	---
Flux of electrons $\frac{\textbf{electrons}}{\textbf{s}\cdot\textbf{m}^2}$	$1.6 \cdot 10^{24}$	same
Number of sorption sites N_0	$2.6 \cdot 10^{18}$	$2.6 \cdot 10^{18}$
Gas supply rate ν_{GAS} $\left(\frac{1}{\text{s}}\right)$	$5.8 \cdot 10^{2}$	$8.0 \cdot 10^{3}$
Average desorption time τ **s**	$7.2 \cdot 10^{-4}$	$7.2 \cdot 10^{-6}$
Desorption rate ν_{DES} $\left(\frac{1}{\text{s}}\right)$	$1.4 \cdot 10^{3}$	$1.4 \cdot 10^{5}$
Cross section for dissociation σ $\textbf{m}^2$	$5 \cdot 10^{-21}$	$2 \cdot 10^{-18}$
Dissociation rate ν_{DISS} $\left(\frac{1}{\text{s}}\right)$	$8.0 \cdot 10^{3}$	$3.2 \cdot 10^{6}$
Volume of deposited part V $\textbf{m}^3$	$8 \cdot 10^{-30}$	$16 \cdot 10^{-30}$

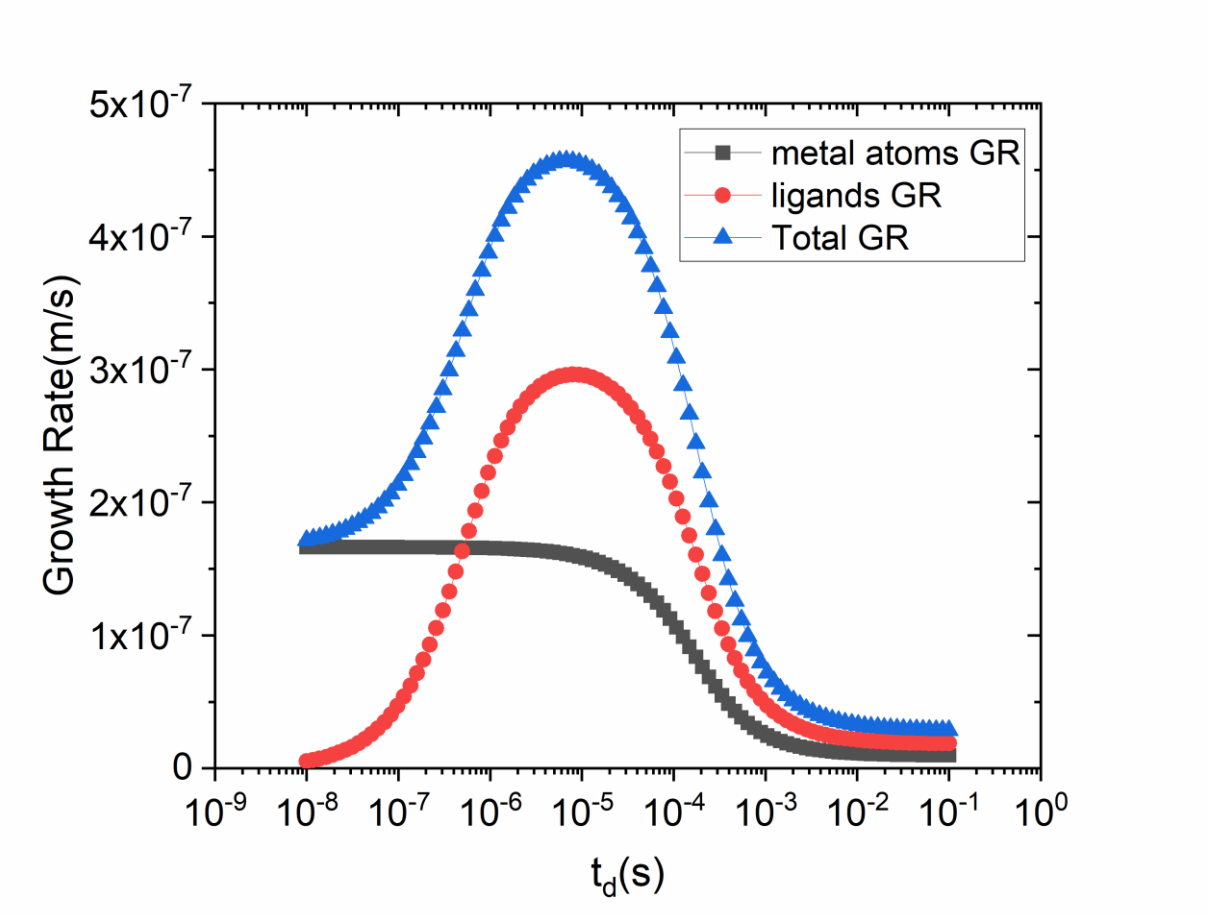

Figure 5.7 Calculated growth rate functions versus electron beam dwell time for metal atoms, ligands and total. Cross section of dissociation of ligand was $2 \cdot 10^{-18}$ m^2. Rates for the precursor molecules ML were equal to: $\nu_{GAS.ML} = 5.8 \cdot 10^2 \frac{1}{s}$, $\nu_{DES.ML} = 1.4 \cdot 10^3 \frac{1}{s}$, $\nu_{DISS.ML} = 8.0 \cdot 10^3 \frac{1}{s}$; and for ligands L: $\nu_{GAS.L} = 8.0 \cdot 10^3 \frac{1}{s}$ (it is equal to dissociation rate of ML), $\nu_{DES.L} = 1.4 \cdot 10^5 \frac{1}{s}$, $\nu_{DISS.L} = 3.2 \cdot 10^6 \frac{1}{s}$.

As can be seen, the growth rate for metal atoms behaves the same way as the growth rate function for the single specie deposition model: starts from a nearly flat region, then rapidly decreases, reaching plateau with increasing dwell time of electron beam. The ligand growth rate, on the other hand, grows rapidly with the dwell time and can exceed the growth rate of precursor molecules. The explanation lays in the difference of dissociation cross sections: in the modelled example, the σ_L is three orders of magnitude higher than σ_{ML} and was equal to $2 \cdot 10^{-18}$ m^2. The Figure 5.7 can help in understanding better the properties of the deposit, depending on the dwell time. From the point of view of the speed of the process, the most favourable are dwell times around 10^{-5} s. On the other hand, at these dwell times the growth rate of ligands dominate over the growth rate of molecules. This situation leads to low metal content deposits as more ligand atoms are incorporated into chemisorbed material than metal atoms. It is an important information in context of optimisation of deposition. In the application where the purity is the most important property, like plasmonics or mask corrections it is

preferable to use shortest dwell times even though the deposition process will probably take long due to small growth rate. For some structures, in which purity does not play the most significant role, it may be an advantage to use longer dwell times to fasten the deposition. To fully understand it, it is crucial to examine the influence of the cross section on a total growth rate dwell time dependence. It is depicted in Figure 5.8. All the parameters used for calculations were the same as listed in Table 5.1, except of cross section for dissociation of ligands, which varied. What can be noticed is that with decreasing the cross section for dissociation of ligands, the peak of the total growth rate decreases as well, and moves towards longer dwell times. Calculating the ν_{dissL} using the changing σ_L values it can be noticed, that the local maximum of the growth rate moves until $\nu_{dissL} > \nu_{dissML}$. For $\sigma_L = 7.2 \cdot 10^{-19}$ m^2 and $\sigma_L = 7.2 \cdot 10^{-20}$ m^2 the peak is at the same position on dwell time scale, $t_d = 1.79 \cdot 10^{-5}$ s. For the next $\sigma_L = 7.2 \cdot 10^{-21}$ m^2, which is an order of magnitude lower than σ_{ML}, the peak of ligands disappears and the total growth rate takes the shape, as for the metal atoms (but not the absolute values). Presented behaviour is very intuitive, as with lowering the cross section for dissociation the characteristic frequency of dissociation lowers, meaning, that during one second, less dissociation events of ligands take place. Using longer dwell times helps to provide more electrons in a unit of time, which increases the growth rate, hence the shift of the peak of the function on the time axis.

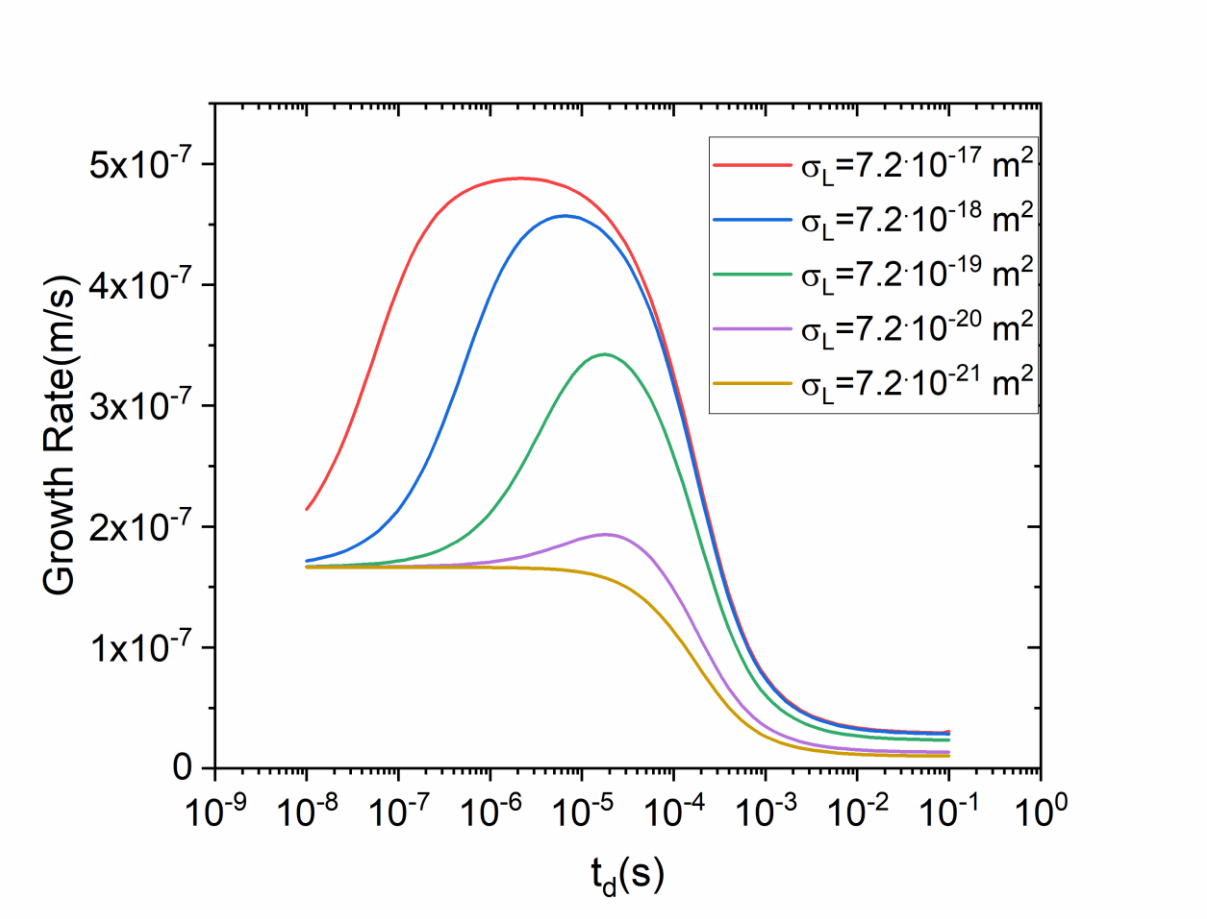

Figure 5.8 Calculated total growth rate in dependence on dwell times for different cross sections for dissociation of ligands. Rates for the precursor molecules ML were equal to: $\nu_{ADS.ML} = 5.8 \cdot 10^2 \frac{1}{s}$, $\nu_{DES.ML} = 1.4 \cdot 10^3 \frac{1}{s}$, $\nu_{DISS.ML} = 8.0 \cdot 10^3 \frac{1}{s}$; and for ligands L: $\nu_{ADS.L} = 8.0 \cdot 10^3 \frac{1}{s}$ (it is equal to dissociation rate of ML), $\nu_{DES.L} = 1.4 \cdot 10^5 \frac{1}{s}$, $\nu_{DISS.L} = 3.2 \cdot 10^7 - 3.2 \cdot 10^3 \frac{1}{s}$.

Another important parameter besides the cross section for dissociation is the average desorption time. Dissociation and desorption are competitive processes in the context of the growth of the deposit. Higher the cross section for dissociation of the precursor, more material grow on the surface. Higher the desorption (shorter average desorption time), less molecules stay on the surface to be dissociated with the electron beam. Moreover, when less precursor molecules are dissociated, less ligands are created, hence the growth rate of ligands should also be quenched. It means, that average desorption time is a limiting factor for both growth rate of metal atoms and ligands.

In the Figure 5.9 the influence of average desorption time of ligands on the total growth rate was depicted for two values of cross section for dissociation of ligands. What can be noticed, is that with decreasing ligand desorption time the total growth rate also decreases. It is intuitive, as faster desorption lowers the number of ligand atoms on the surface which are availa-

ble to be dissociated and deposited with e-beam. Interestingly, this effect seems to have a threshold – for long ligands desorption times, at least an order of magnitude longer than this value for full molecule, the growth rate is the same, despite changing τ_L. For $\sigma_L = 2 \cdot 10^{-17}\mathrm{m}^2$, the threshold is below $\tau_L = 7.2 \cdot 10^{-6}$ s; for $\sigma_L = 2 \cdot 10^{-21}$ m^2 the threshold is below $\tau_L = 7.2 \cdot 10^{-2}$ s. It is then probable, that the influence of the average desorption time of ligands on the growth rate is limited by the cross section for dissociation of ligands. Using the value of the electron flux, the characteristic rate of dissociation of ligands can be calculated: $\nu_{DISS.L} = \sigma_L f$. For $\sigma_L = 2 \cdot 10^{-17}\mathrm{m}^2$, $\nu_{DISS.L} = 3.2 \cdot 10^7 \frac{1}{\mathrm{s}}$ and for $\sigma_L = 2 \cdot 10^{-21}$ m^2, $\nu_{dissL} = 3.2 \cdot 10^3 \frac{1}{\mathrm{s}}$. Characteristic rate of desorption of ligands is an inverse average desorption time $\nu_{DES.L} = \frac{1}{\tau_L}$. The characteristic rate for desorption of ligands values are: $\nu_{DES.L} = 1.4 \cdot 10^7 \frac{1}{\mathrm{s}}$ for $\sigma_L = 2 \cdot 10^{-17}$ m^2 and $\nu_{desL} = 1.4 \cdot 10^3 \frac{1}{\mathrm{s}}$ for $\sigma_L = 2 \cdot 10^{-21}$ m^2. It can be concluded, that the desorption starts affecting the growth rate when $\nu_{DES.L} \geq \nu_{DISS.L}$.

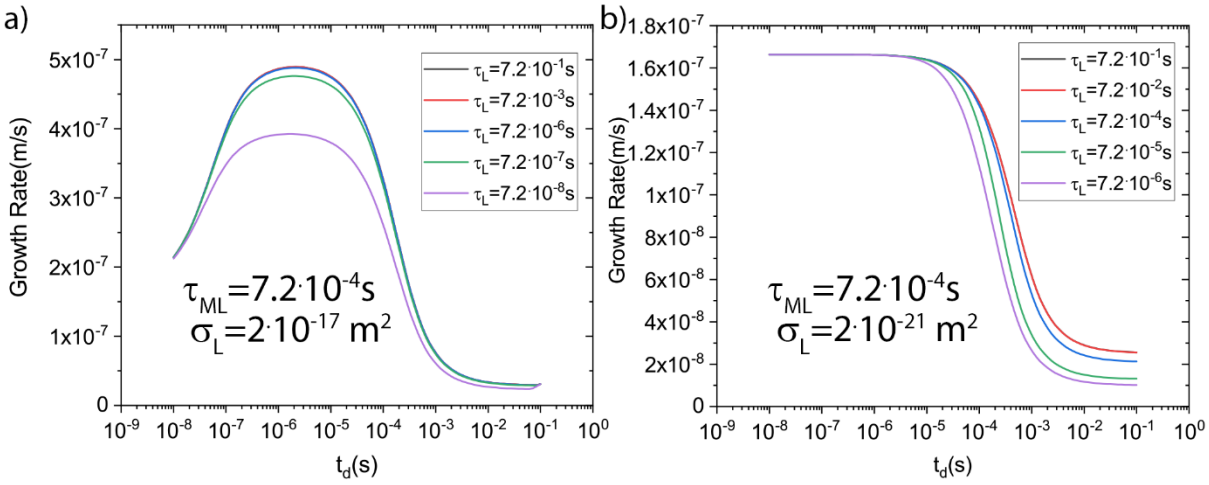

Figure 5.9 Calculated total growth rates in function of dwell times for two different cross section of dissociation of ligands a) $\sigma_L = 2 \cdot 10^{-17}$ m^2 and b) $\sigma_L = 2 \cdot 10^{-21}$ m^2 , in dependence on different average desorption time of ligands.

5.2.2 Deposition yields

Co-deposition model can be used to estimate composition of a deposit. In order to do that, a variable called deposition yield is introduced. The yield is a unitless measure of a growth of deposit, which shows how many molecule fragments (or atoms) have been deposited per incoming electron. Yield can be defined as:

$$Y = \frac{R}{V \cdot f} \quad (5.10)$$

Where R is a deposition rate, V is a volume of deposited molecule fragments and f is a flux of electrons. For ligand co-deposition model yield can be defined separately for precursor ML and ligand L.

$$Y_{ML} = \frac{R}{V_{ML} \cdot f} \quad (5.11.a)$$

$$Y_L = \frac{R}{V_L \cdot f} \quad (5.11.b)$$

Metal content can be estimated as a share of a Y_{ML} in total yield defined as sum: $Y_{ML} + Y_L$:

$$C = \frac{Y_{ML}}{Y_{ML} + Y_L} \quad (5.12)$$

The yields for two different cross-sections for dissociations of ligands are depicted in Figure 5.10 (a) $\sigma_L = 2 \cdot 10^{-18}$ m^2 and (b) $\sigma_L = 2 \cdot 10^{-21}$ m^2. Other parameters are listed in Table 5.1. In both graphs, right axis (coloured blue) depicts the ration between deposition yield of ligands to molecules $\frac{Y_L}{Y_{ML}}$. Figure 5.10 c and d present the metal content for both cross sections.

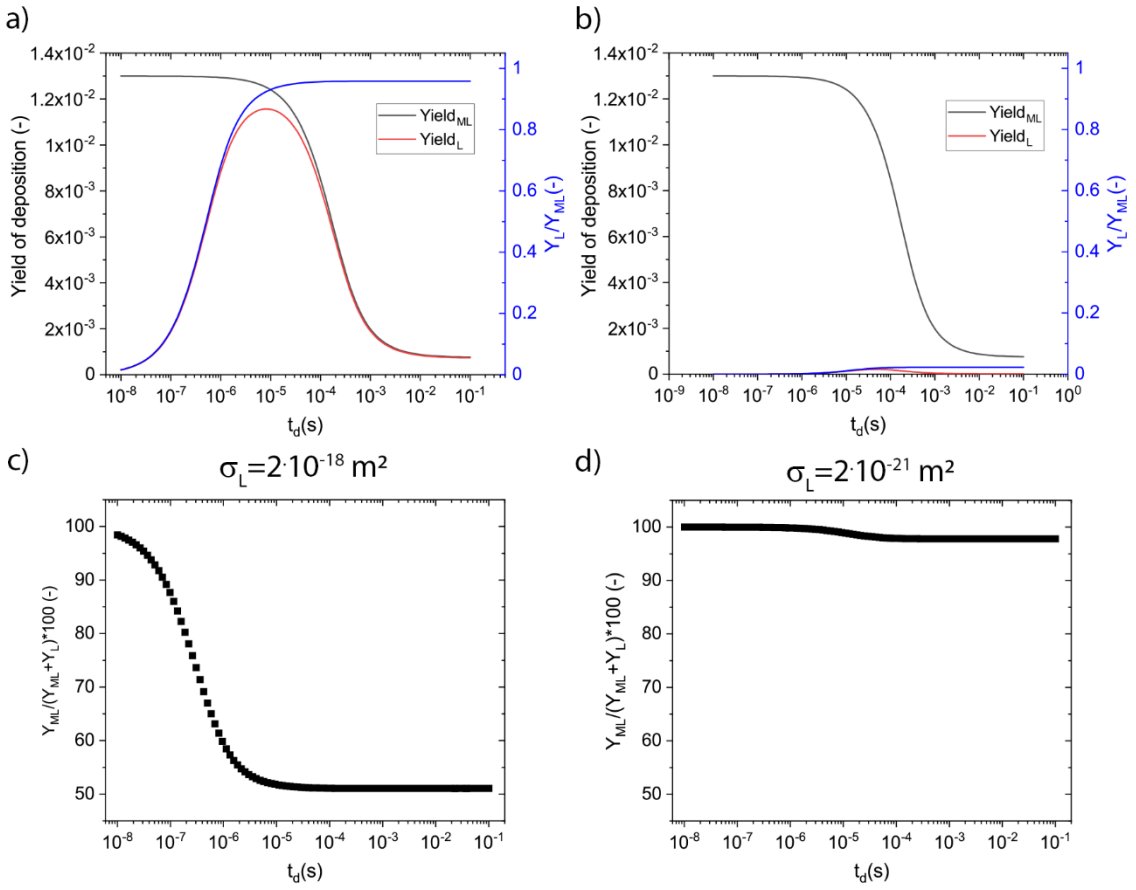

Figure 5.10 Yields of deposition of metal and ligands and their ratio for a) $\sigma_L = 2 \cdot 10^{-18}$ m^2 and b) $\sigma_L = 2 \cdot 10^{-21}$ m^2. Estimated metal contents for c) $\sigma_L = 2 \cdot 10^{-18}$ m^2 and d) $\sigma_L = 2 \cdot 10^{-21}$ m^2.

Figures 5.10.a is similar, in shape, to figure 5.7 from the beginning of this chapter. The yields are dimensionless, so the influence of the volumes of deposited core atoms (M) and ligands (L) do not enter into the shape of the curves. The ratio between yields first grows, to stabilise above 0.9. It suggest growing influence of ligands in the composition of the deposit. Ratio of yields stabilises, at the exact moment, when both yields, of precursor and ligands equalises. It indicates that with increasing dwell time, there will be no change in composition of the deposit. Comparing the yield ratios from Figure 5.10.a and b it can be noticed a huge influence of cross section for dissociation of ligands on the deposition yields. In case of Figure 5.10.b the yield ratio is only around 0.025, suggesting very low influence of ligands on deposits composition. It is worth noticing that it is impossible to achieve $\frac{Y_L}{Y_{ML}} > 1$, as in the presented model, with used parameters listed in table 5.1, there is only one ligand per metal atom. Figures 5.c and d show the metal content for two values of cross section for dissociation of ligands. In both cases, the highest metal contents were achieved for the shortest dwell times. Metal con-

tent curves are mirror reflections of yield ratio curves: the best metal contents are achieved, when $\frac{Y_L}{Y_{ML}}$ is the lowest, which is very intuitive.

It has to be also noticed, that proposed measure of metal content is limited only to the case, when a deposited part of a ligand contains only one atom, as it for metal carbonyl, where electron induced reaction leads to fragmentation of a ligand into volatile oxygen atom and non-volatile carbon: $CO \xrightarrow{e^-} C \downarrow + O \uparrow$. For multi-atomic ligands, a factor β has to be added to, which corrects the C value of equation 5.11 to the number of contaminant atoms contained in the deposited fragment of the ligand:

$$C = \frac{Y_{ML}}{Y_{ML} + \beta Y_L} \quad (5.13)$$

5.2.3 Experimental evidence

In the following we will apply the new co-deposition model to show the origins of larger metal content in halo than in the centre of the deposit, which was observed for both silver and gold and FEBID growth rate measurements of $Cr(CO)_6$ as function of dwell time.

Halo deposits are the result of dissociation of adsorbed molecules by backscattered electrons and their generated secondary electrons. Using distributions of PE and BSE electrons from Figure 3.1.8.a, it is possible to simulate the metal contents in these regions using the ligand co-deposition model. As the spots have been deposited using a continuous irradiation for five minutes, the analytical solutions for yields proposed by Brockhuis [169] for $t_d \to \infty$ were used:

$$\lim_{t_d \to \infty} Y_{ML}(t_d) = \sigma_{ML} \cdot \left[\frac{J_{ML}\left(\frac{1}{\tau_L} + f\sigma_L\right)}{\left(\frac{1}{\tau_L} + f\sigma_L\right) \cdot \left(\frac{J_{ML}}{n_{0ML}} + \frac{1}{\tau_{ML}} + f\sigma_{ML}\right) + \left(\frac{J_{ML} f \sigma_{ML}}{n_{0ML}}\right)} \right] \quad (5.14a)$$

$$\lim_{t_d \to \infty} Y_L(t_d) = \sigma_L \cdot \left[\frac{J_{ML} f \sigma_{ML}}{\left(\frac{1}{\tau_L} + f\sigma_L\right) \cdot \left(\frac{J_{ML}}{n_{0ML}} + \frac{1}{\tau_{ML}} + f\sigma_{ML}\right) + \left(\frac{J_{ML} f \sigma_{ML}}{n_{0ML}}\right)} \right] \quad (5.14)$$

Results of the simulation are presented in Figure 5.11. The simulations were prepared using following parameters: $J_{ML} = 4.5 \cdot 10^{19}\ \frac{\text{molecules}}{\text{m}^2\text{s}}$, $\sigma_{ML} = 5 \cdot 10^{-20}\ \text{m}^2$, $\tau_{ML} = 7.2 \cdot 10^{-6}\ \text{s}$, $N_{0ML} = N_{0L} = 2.6 \cdot 10^{18}\ \frac{1}{\text{m}^2}$. The range stands for the radial distance from the centre of the beam. The dependence of the electron flux on the range was the same as the BSEs distribution

presented in Figure 3.1.8.a and it is shown with dashed blue line on the right axis. The graph presented in Figure 5.11.a shows results simulated with $\tau_L = 7.2 \cdot 10^{-6}$ s and $\sigma_L = 2 \cdot 10^{-15} \ldots 2 \cdot 10^{-18}$ m^2, where the σ_L was changing by the factor of 0.1. Figure 5.11.b presents the results while changing the $\tau_L = 7.2 \cdot 10^{-4} \ldots 7.2 \cdot 10^{-7}$ s by factor of 0.1 and was constant $\sigma_L = 2 \cdot 10^{-16}$ m^2.

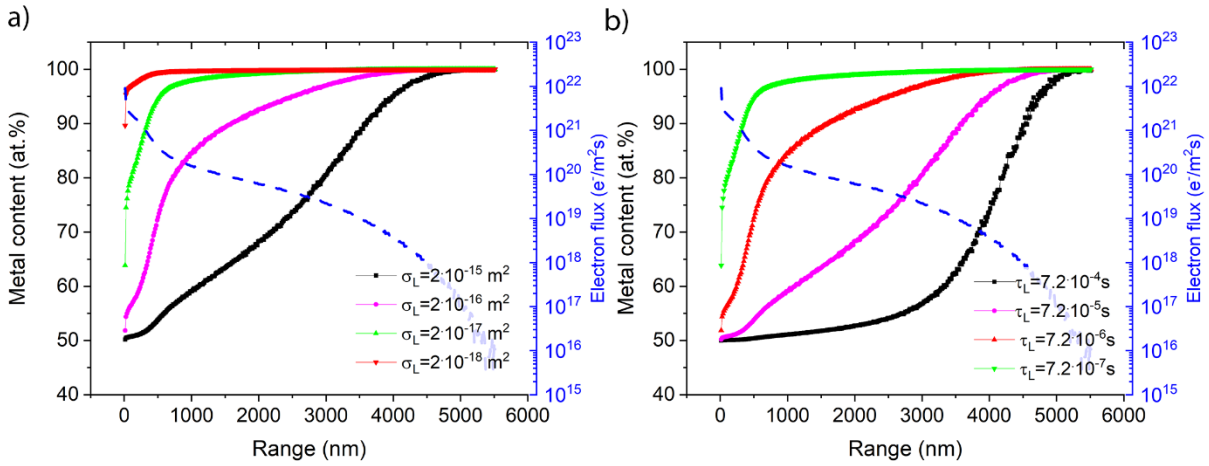

Figure 5.11 Metal contents and electron fluxes in dependence on the distance from the beam centre while changing the a) ligand cross section of dissociation $\sigma_L = 2 \cdot 10^{-15} \ldots 2 \cdot 10^{-18}$ m^2 and b) ligands desorption time $\tau_L = 7.2 \cdot 10^{-4} \ldots 7.2 \cdot 10^{-7}$ s.

The characteristic feature of both graphs is the clear dependence between metal content and the electron flux. In the centre, where the flux is the highest, the metal content is always the lowest. Increase of the distance from the beam centre and hence decrease of electron flux results in increase of the metal content. Such dependence was observed experimentally for spot deposits prepared with silver carboxylates presented in chapter 3.1.4 and gold deposits shown in chapter 3.3.4. Changing of σ_L and τ_L values change only the shape of the curve, but not its general dependence. Of the note is the fact, that both ligand cross section of dissociation and average desorption time are correlated – increase of one can be compensated with decrease of the other. It is clearly visible comparing graphs from Figure 5.11.a and b. Decrease of σ_L gives similar result as decrease of τ_L, they both lead to more efficient desorption of intact ligands. The metal content slope increases faster, reaching the plateau around 100 at.%.

Both graphs starts at 50 at.% because the metal content was calculated using formula 5.12. Y_L cannot be higher than Y_{ML} because dissociation of metal-ligand molecules is the only source of ligands and in the simulated case only one ligand per metal atom was considered. It means that per one atom of deposited metal maximum one atom of ligand can be deposited, hence the metal content cannot be lower than 50 at.%. To properly simulate the metal content values

of a real deposit, exact pathways of dissociation would have to be known. In future, this can be obtained by systematic research combining the FEBiMS with EDX and WDS, and gas and condensed phase measurements.

The growth rate experiment, performed using Zeiss prototype tool, consisted of creating the series of pulsed-exposure spot deposits starting with 50 ns, ending on 0.1 s. The refreshment time was set to 1 ms. All of the spots were deposited with the same dose of electrons. The precursor was $Cr(CO)_6$. The spots were deposited on the Si piece with a native oxide layer. Their height was measured with AFM. Considering the deposition time, the height of the deposit was used to calculate the growth rate. Function of growth rate vs dwell time is plotted with rectangles in Figure 5.12. The lines between dots were added for clarity. The measured growth rates were depicted alongside the calculated growth rates for different σ_L from Figure 5.7.

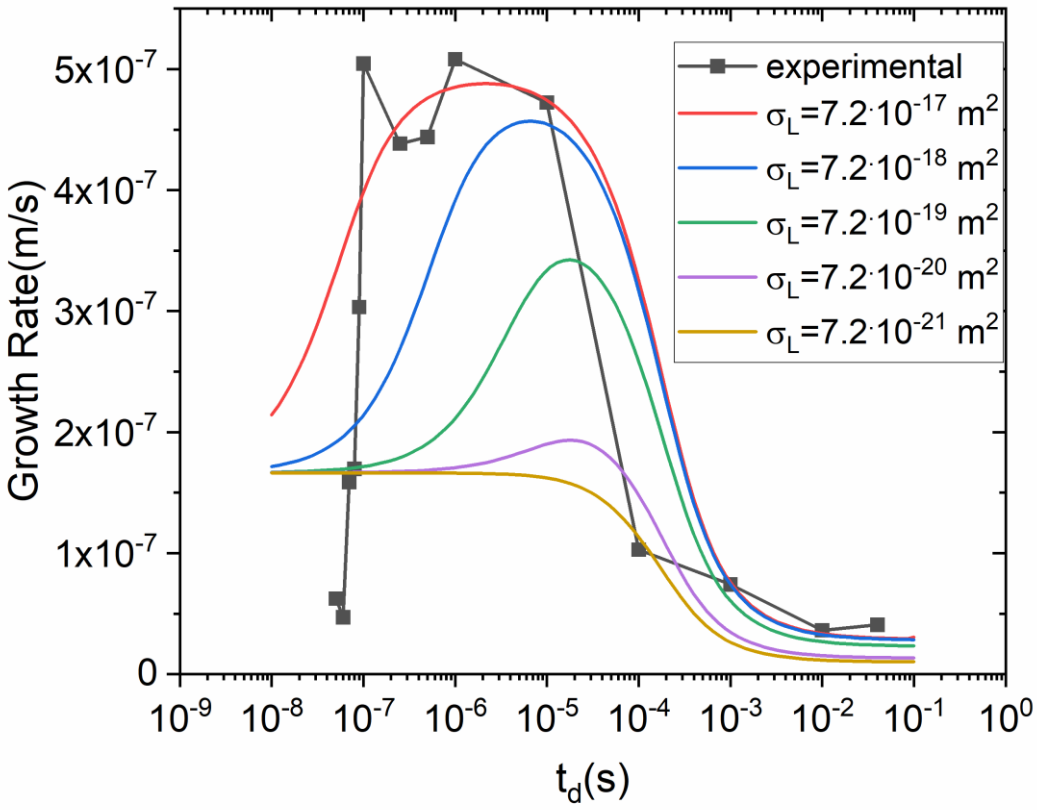

Figure 5.12 Growth rates in function of dwell times from Figure 5.7, compared to experimental results.

What can be noticed is that the experimental results are qualitatively comparable to the calculated functions, especially for the one obtained for $\sigma_L = 2 \cdot 10^{-17}$ m^2. The first difference is

the growth rate for the shortest dwell times, which was much smaller for the experimental curve than for calculated. This can be explain by difference in initial coverage. For simulation, the full monolayer coverage with molecules of the surface was assumed, whereas in the performed experiment it was most probably not the case. Also, it has to be noted, that although the values on the graph seem to be comparable for the experimental points and for calculated curve with $\sigma_L = 2 \cdot 10^{-17}$ m^2 the results have to be compared only qualitatively. The actual values depend to deeply on the parameters of both precursor and ligands. However, the main feature, namely the peak in the experimental growth rate, is adequately reproduced by the ligand co-deposition model. Such a feature cannot be obtained in single species and two species (co-injection of two gases) models published so far. In the two species model, the growth rates for both gases are non-growing functions, with plateau regions for low dwell times [40]. The sum of such function would never result in a peak, in contrast to the experimental results shown in Figure 5.12.

5.2.4 Discussion of the model

The qualitative agreement between the calculated and measured shape of the growth rate vs. dwell time function shows the applicability of the presented ligand co-deposition model. As it shows the mutual dependence between the growth rates of ligands and metal atoms it can be potentially used to predict and even tune the metal content of the deposit by applying the proper dwell times. For now, the presented model does not include the influence of the surface diffusion, which in certain cases may play significant role. The influence of diffusion on the shape of the deposited structure was considered in several works [85, 91]. In their work about the influence of molecular gas flow on the shape of deposits Winkler et al. presented the dependence between the dwell time and the ratio of surface diffusion replenishment and gas phase replenishment [20]. Their results showed, that the influence of diffusion is negligible for very short (<1 μs) or very long (>100 μs). As ligand co-deposition model does not concern diffusion, it will give the most accurate results in similar dwell time ranges. However, the exact values of dwell time ranges may depend the parameters of molecules and FEBIS process. This model is more complex than the one used up to now and it requires knowing twice more parameters, one set for the injected gas molecule and one for the separated ligand. It is already not trivial to measure the cross section for deposition and desorption time for the precursor, see chapters 1.7 and 1.8, not mentioning estimating these values separately for separated ligands. To measure the cross section and desorption time for the separated ligand it

may be profitable to examine FEBID of a compound which is the closest to the used ligand, e.g. a carboxylic acid for a metal carboxylate or carbon oxide for carbonyls. However, the FEBID experiments with ligand-like organic compounds may not exactly correspond to the conditions at which ligands are co-deposited during a FEBID of metalorganic. First, it requires that the metal – ligand bond is cleaved as a first step by the e-beam and that the ligands stay physisorbed intact, until they desorb or are dissociated. It is possibly valid for short ligand chains, like carbonyls, for which in FEBiMS the mass peak of the full ligand fragment has been spotted (see chapter 4). On the other hand, the same measurements performed on grains of carboxylates showed presence of many kinds of different C_xF_y groups, proving the e-beam is non-selective towards bonds and "chopping" the bonds along carboxylate chain as well as metal-ligand bond. It is unknown, which bond was cleaved first, so it is impossible to say for now, if the experiment with carboxylic acid would help understanding the behaviour of a carboxylate ligand cleaved from the metal atom. There is also a certain limitation of the model in its possibilities to predict the composition of the deposit. In the model, the one non-volatile part is considered a metal and the other a ligand sub-fragment, but the ligand may contain few different atoms. To properly predict the metal content of the deposit it has to be known exactly which part of the ligand is deposited. This can be obtained by combining a FEBiMS method presented in chapter 4 with the EDX and WDS methods.

Despite the disadvantage of a larger parameter input for the simulation, the proposed ligand co-deposition model can be a powerful tool to analyse and predict the results of FEIBD experiment. Further experiments would be desirable to both prove the model and to examine its other possible weak points and limits.

5.2.5 Further extension of model

It is possible to extend the model further to describe also heteroleptic compounds and to consider different dissociation pathways. Instead of a set of two differential equations, now set of N_{ML} equations has to be considered, where N_{ML} is the number of different dissociation channel.

$$\frac{\partial n_{ML}}{\partial t} = J_{ML}\left(1 - \sum_{i}^{N_k} \frac{n_i}{n_{0i}}\right) - \frac{n_{ML}}{\tau_{ML}} - \sum_{i}^{N_{ML}} \sigma_{MLi} f n_{ML} \quad (5.15a)$$

$$\left\{\frac{\partial n_{Lk}}{\partial t} = \sigma_{MLk} f n_{MLk} - \frac{n_{Lk}}{\tau_{Lk}} - \sum_{j}^{N_j} \sigma_{Lk} f n_{Lk}\right\} \times N_k \quad (5.15b)$$

Where:

N_{ML} – maximum number of dissociation pathways of precursor molecule

N_k –number of created ligands

N_j – number of dissociation pathway of a *k* ligand

This kind of model would be the most complete, as it can analyse different dissociation pathways of both precursor molecule and ligands and thus cover a larger number of FEBID precursors. On the other hand this model requires more detailed input for the various dissociation pathways and fragments.

5.3 Summary of the modelling

Previous chapter shown two novel directions of modelling of FEBID process: 1) extension of characteristic rate maps to include resolution parameter and influence of surface diffusion and 2) the ligand co-deposition model, to properly simulate and analyse the fate of ligands adsorbed on the surface. Rate maps are a tool, which can be used to plan FEBID experiments and later to analyse their results, as they nicely illustrate the 6 dimensional parameter space ($\nu_{gas}, \nu_{des}, \nu_{diss}, \nu_{diff}, \nu_{GR}, \varphi$) and the relation to the deposition regimes. Adding the resolution parameters makes it easier to connect experimental results with theoretical calculations, which may be used to design experiments allowing for estimation of basic parameters of the precursor, like its cross section for dissociation and the characteristic rate of desorption (average desorption time).

The ligand co-deposition model is a first attempt to model not only the precursor molecule, but also the fate of ligands. It is a new powerful approach, which may have many applications, including prediction of composition of the deposit in dependence of dwell time. The theoretical predictions of the ligand co-deposition model were supported with results from growth rate measurements of $Cr(CO)_6$ and metal content variations in spot deposits with silver carboxylates.

6 Summary and Conclusions

This PhD work focused on determining the viability of novel FEBID precursors by performing a range of complimentary investigations, from *in situ* precursor screening, through deposit characterisation, up to mathematical data analysis and model fitting.

The study includes systematic investigations of ten different metalorganic complexes, coming from four different chemical groups: carboxylates, heteroleptic compounds with allyl, carbonyls and halogen ligands, halogenated NHC complexes and carbonyls. The highest metal content in the deposits was achieved for silver carboxylates, especially $Ag_2(\mu\text{-}O_2CCF_3)_2$ and $Ag_2(\mu\text{-}O_2CC_2F_5)_2$, for which it reached 76 at.% of silver. These two compounds were the most thermally stable and exhibited a metallic type of electrical conductivity of the deposits. From all the tested precursors, these two had the lowest number of carbons in the molecule. Furthermore, $Ag_2(\mu\text{-}O_2CCF_3)_2$ and $Ag_2(\mu\text{-}O_2CC_2F_5)_2$ have the fastest desorbing ligands from among all the examined carboxylates, judging from the fact that, unlike the other carbonyls, the metal content in the halo region was not higher than in the deposit. It can be then concluded that it is more preferable to use shorter, fluorinated carboxylate ligands bonded to silver atoms to deposit high-metal content 3D silver structures. Examined ruthenium complexes were depositing much lower metal contents, below 26 at.%. From all the ligands attached to the metal atom, the easiest one to separate and to desorb from the substrate were carbonyl groups. Attaching an allyl group and a bromide atom directly to a metal atom seems less favourable, as they tend to stay on the substrate, lowering the metal content in the final deposit. NHC carbenes seem the least favourable ligands among all those investigated. In this study, only 16 at.% of gold content was achieved from them, which was lower than for other novel compounds presented in this work.

The work performed in the scope of this Thesis enabled the development of a new approach for FEBIP investigations. Firstly, analysing the halo, which is an unwanted effect during FEBID, provided an opportunity to investigate electron beam induced processes in different deposition regimes. Due to the large change in electron flux, it was possible to look into the mass transport limited regime in the e-beam centre and the reaction rate limited regime at the halo region. Studying different deposition regimes within one deposit is a novelty, being only described in publications prepared as a part of this PhD work. Furthermore, it showed the advantages of combining WDS and EDX for deposit composition analysis. These methods are not often used together, especially for FEBID deposits.

Another part of this PhD work consisted of presenting novel strategies of compound investigations. Vacuum thermogravimetry was shown to be a fast and easy-to-apply pre-screening technique for low volatility compounds, useful to determine both their thermal stability, as well as the preferable GIS temperature range for FEBID. Using VTGA on silver carboxylates, it was proven that fluorinated compounds are more thermally stable than non-fluorinated complexes, therefore deeming them to be potentially better choice to be used as silver FEBID precursors.

The next novel method, developed during this PhD project, was focused electron beam induced mass spectrometry, FEBiMS. It provides information about precursor fragmentation pathways, induced by electron beam irradiation and it can be used to determine which part of the dissociated ligand is co-deposited alongside the metal atom. Knowing this, the volume of the deposited fragment can be estimated, which is crucial for growth rate estimation. The composition of the deposited fragment, which can be deduced from the mass spectrum, is crucial to determine and model the metal content in the deposit. FEBiMS was used to test the effects of electron irradiation of three solid state and one gaseous compound adsorbed on the substrate's surface. The method is very promising and the results obtained provide new insight into electron-induced surface processes. It does not require post-ionisation so it provides information about the exact species created due to electron-induced dissociation under lithographic and FEBID-like exposure conditions. The method requires further work and development, as the origin of the signal, in the case of *in-situ* FEBiMS during $W(CO)_6$ FEBID, was not quantifiable, however, it can serve as a complementary method to the gas and condensed phase studies currently used.

The theory developed within this Thesis presents a novel way for mathematically describing FEBID processes. Firstly, the rate (frequency) maps were extended to include the resolution parameter. This serves to better position the FEBID experiment in the five $(\nu_{gas}, \nu_{des}, \nu_{diss}, \nu_{diff}, \nu_{GR}, \varphi)$ dimensional parameter space. Furthermore, the influence of surface diffusion on the characteristic rates and the size of the deposits was shown. Direct improvement of the deposits' lateral resolution, due to increased surface diffusion rate, was presented. Secondly, this study presents the co-deposition model, as a novel way to trace the fate of the ligand via the introduction of the second equation considering the number of ligands adsorbed to the surface. It implies a need to extend the usually used set of parameters to include variables for ligands such as cross-section of dissociation, number of adsorption sites and average desorption. It can therefore describe and predict composition changes in FEBID

structures as a function of electron or molecule flux, as well as improve deposit growth rate prediction as the function of beam dwell time. Qualitative trends of FEBID experiments revealed in this PhD Thesis were reproduced with the ligand co-deposition model, namely the increased metal content in the halo deposit regions (observed for silver and gold deposits) and the experimentally observed peak of the growth rate function for $Cr(CO)_6$, with the increase in beam exposure time. To obtain quantitative results and to use the predictive power of the model further experiments are needed, in particular to specify the input for the ligand comprising its cross section and average residence (desorption) time.

Appendix

A1 Measurement of the beam size and profile

The beam profile was measured using a knife-edge method. It utilises a sharp edge, positioned perpendicular to the beam propagation direction. In this work, lacy carbon TEM grid were used, as they provide a sharp contrast at the edges of the holes. The linear intensity profile was measured perpendicular to the edge. Assuming a Gaussian-shape beam, the intensity profile has a shape of an error function [171], which first derivate gives the beam shape

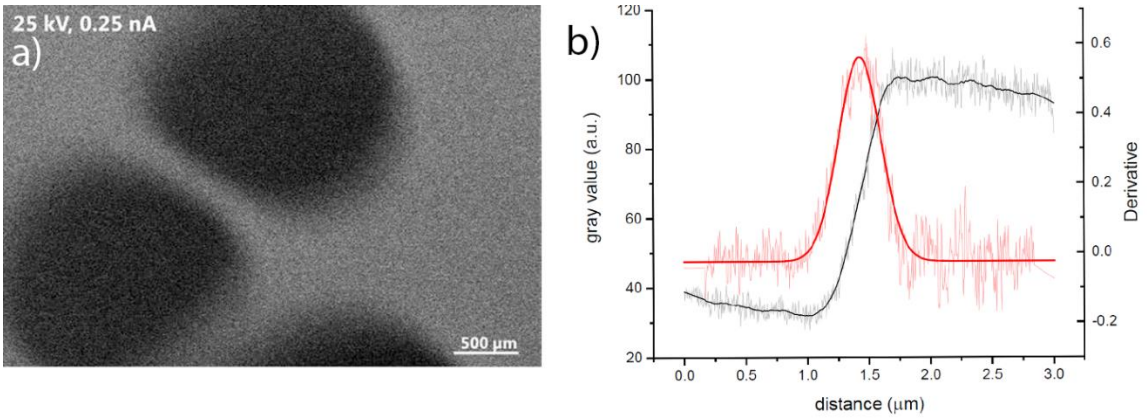

Figure A 1 a) SEM image of a lacy carbon grid. b) Intensity profile measured perpendicular to the edge of the hole (gray curve) and derived Gaussian beam profile (red curve). Taken from the supporting information of joint publication of Berger et al. [35]

Figure A1 presents the high magnification SEM micrograph of a lacy carbon grid and corresponding intensity profile measured using ImageJ software. The line was smoothened with a built-in Origin function and the Gaussian profile was derived. For 20 kV of the acceleration voltage the beam FWHM was 180 nm, which corresponds to 450 nm of FW(99.9%).

A2 BSE profile for thin SiNx film.

BSE distribution profile was simulated using a Monte Carlo simulations software Casino [37]. The density of the SiN_x was assumed to be 3.17 g/cm^3. The thickness of the film was 50 nm, the same as in the thickness of the film used in the TEM grids from this study. The beam acceleration voltage was 20 kV, the beam size (FW(99.9%)) 450 nm and the trajectories of 10 millions primary electrons were simulated. The radial BSE distribution can is presented in Figure A2,

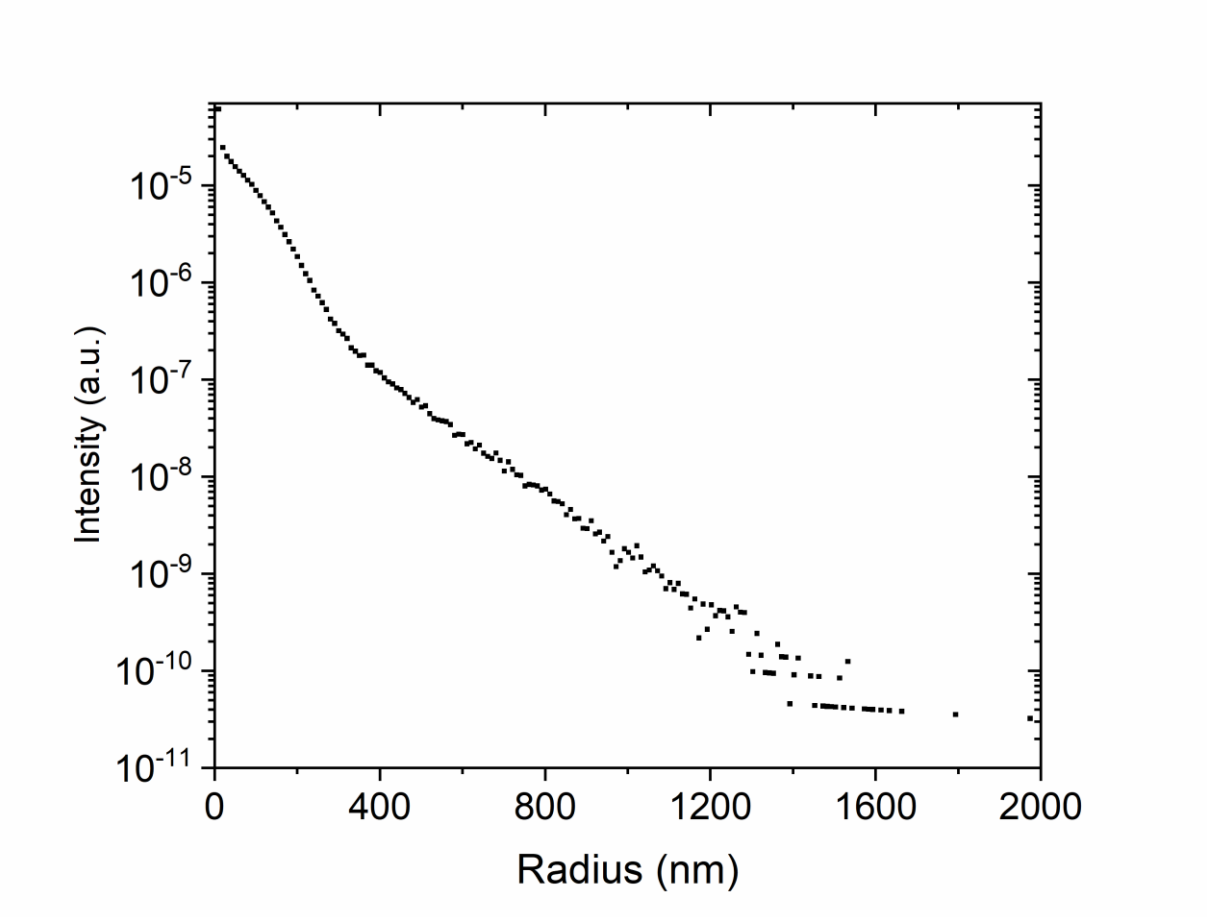

Figure A 2 Radial distribution of BSE electrons generated from 50 nm thick SiN_x film 20 kV beam acceleration voltage and 450 nm beam diameter; simulated using Casino software.

A3 Calculation of the influence of the diffusion on characteristic rate maps

To calculate the influence of the diffusion on the characteristic rate maps, the analytical solution of FEBID equation for the rotational symmetry was used:

$$\theta(r) = \frac{1}{n_0} n_{out} \left[\tilde{\tau}^{-1} + C I_0 \left(\frac{r}{\rho_{in}} \right) \right] \quad (A1)$$

where I_0 is a modified Bessel function and n_{out}, $\tilde{\tau}$ and ρ_{in} are defined with the following formulas:

$$n_{out} = \frac{J}{\nu_{gas} + \nu_{des}} \quad (A1)$$

$$\tilde{\tau} = 1 + \frac{\sigma f(0)}{\nu_{des} + \nu_{gas}} \quad (A2)$$

$$\rho_{in} = \left(D \frac{1}{\nu_{gas} + \nu_{des} + \nu_{diss}} \right)^{\frac{1}{2}} \quad (A3).$$

The constant C is derived using the following formula:

$$C = K_1(\tilde{\rho}_{out}^{-1}) \cdot \frac{1 - \tilde{\tau}^{-1}}{I_0(\tilde{\rho}_{in}^{-1})K_1(\tilde{\rho}_{out}^{-1}) + \tilde{\tau} I_1(\tilde{\rho}_{in}^{-1})K_0(\tilde{\rho}_{out}^{-1})} \quad (A4).$$

The K_n and I_n stand for modified Bessel functions and $\tilde{\rho}_x = \frac{\rho}{FWHM_B}$, where $FWHM_B$ is the full width at half maximum of the beam. ρ_{out} is defined as:

$$\rho_{out} = \left(D \frac{1}{\nu_{gas} + \nu_{des}} \right)^{\frac{1}{2}} \quad (A5)$$

The formulas were adapted from the review of Utke et al. [2].

References

[1] M. Huth, F. Porrati, O.V. Dobrovolskiy, Focused electron beam induced deposition meets materials science, Microelectronic Engineering 185-186 (2018) 9-28.

[2] I. Utke, P. Hoffmann, J. Melngailis, Gas-assisted focused electron beam and ion beam processing and fabrication, Journal of Vacuum Science & Technology B: Microelectronics and Nanometer Structures Processing, Measurement, and Phenomena 26(4) (2008) 1197-1276.

[3] W.F. van Dorp, C.W. Hagen, P.A. Crozier, P. Kruit, Growth behavior near the ultimate resolution of nanometer-scale focused electron beam-induced deposition, Nanotechnology 19(22) (2008) 225305.

[4] L. Keller, M.K.I. Al Mamoori, J. Pieper, C. Gspan, I. Stockem, C. Schröder, S. Barth, R. Winkler, H. Plank, M. Pohlit, J. Müller, M. Huth, Direct-write of free-form building blocks for artificial magnetic 3D lattices, Scientific Reports 8(1) (2018) 6160.

[5] R. Winkler, F.-P. Schmidt, U. Haselmann, J.D. Fowlkes, B.B. Lewis, G. Kothleitner, P.D. Rack, H. Plank, Direct-Write 3D Nanoprinting of Plasmonic Structures, ACS Applied Materials & Interfaces 9(9) (2017) 8233-8240.

[6] J.D. Fowlkes, Simulation guided 3D nanomanufacturing via focused electron beam induced deposition, ACS Nano 10 (2016).

[7] R. Winkler, J.D. Fowlkes, P.D. Rack, G. Kothleitner, H. Plank, Shape Evolution and Growth Mechanisms of 3D-printed Nanowires, Additive Manufacturing (2021) 102076.

[8] L.M. Seewald, R. Winkler, G. Kothleitner, H. Plank, Expanding 3D Nanoprinting Performance by Blurring the Electron Beam, Micromachines 12(2) (2021).

[9] I. Utke, P. Hoffmann, J. Melngailis, Gas-assisted focused electron beam and ion beam processing and fabrication, J. Vac. Sci. Technol. B Microelectron. Nanom. Struct. 26 (2008).

[10] A. Belianinov, M.J. Burch, A. Ievlev, S. Kim, M.G. Stanford, K. Mahady, B.B. Lewis, J.D. Fowlkes, P.D. Rack, O.S. Ovchinnikova, Direct Write of 3D Nanoscale Mesh Objects with Platinum Precursor via Focused Helium Ion Beam Induced Deposition, Micromachines 11(5) (2020).

[11] S. He, R. Tian, W. Wu, W.-D. Li, D. Wang, Helium-ion-beam nanofabrication: extreme processes and applications, International Journal of Extreme Manufacturing 3(1) (2021) 012001.

[12] A.D. Dubner, A. Wagner, J. Melngailis, C.V. Thompson, The role of the ion-solid interaction in ion-beam-induced deposition of gold, Journal of Applied Physics 70(2) (1991) 665-673.
[13] P. Orús, R. Córdoba, J.M. De Teresa, Focused ion beam induced processing, Nanofabrication, IOP Publishing, 2020, pp. 5-1-5-58.
[14] A. Salvador-Porroche, S. Sangiao, P. Philipp, P. Cea, J.M. Teresa, Optimization of Pt-C Deposits by Cryo-FIBID: Substantial Growth Rate Increase and Quasi-Metallic Behaviour, Nanomaterials 10(10) (2020).
[15] R. Córdoba, A. Ibarra, D. Mailly, J.M. De Teresa, Vertical Growth of Superconducting Crystalline Hollow Nanowires by He+ Focused Ion Beam Induced Deposition, Nano Letters 18(2) (2018) 1379-1386.
[16] M. Shimojo, K. Mitsuishi, M. Tanaka, M. Han, K. Furuya, Application of transmission electron microscopes to nanometre-sized fabrication by means of electron beam-induced deposition, Journal of Microscopy 214(1) (2004) 76-79.
[17] T. Lukasczyk, M. Schirmer, H.-P. Steinrück, H. Marbach, Electron-Beam-Induced Deposition in Ultrahigh Vacuum: Lithographic Fabrication of Clean Iron Nanostructures, Small 4(6) (2008) 841-846.
[18] M. Drost, F. Tu, L. Berger, C. Preischl, W. Zhou, H. Gliemann, C. Wöll, H. Marbach, Surface-Anchored Metal–Organic Frameworks as Versatile Resists for Gas-Assisted E-Beam Lithography: Fabrication of Sub-10 Nanometer Structures, ACS Nano 12(4) (2018) 3825-3835.
[19] Gas Injection Systems - Orsay Physics. https://www.orsayphysics.com/gas-injection-systems, (accessed 27.01.2021).
[20] R. Winkler, J. Fowlkes, A. Szkudlarek, I. Utke, P.D. Rack, H. Plank, The Nanoscale Implications of a Molecular Gas Beam during Electron Beam Induced Deposition, ACS Applied Materials & Interfaces 6(4) (2014) 2987-2995.
[21] A. Fernández-Pacheco, R. Streubel, O. Fruchart, R. Hertel, P. Fischer, R.P. Cowburn, Three-dimensional nanomagnetism, Nature Communications 8(1) (2017) 15756.
[22] A. Fernández-Pacheco, Three dimensional magnetic nanowires grown by focused electron-beam induced deposition, Sci. Rep. 3 (2013).
[23] M. Gabureac, L. Bernau, I. Utke, G. Boero, Granular Co–C nano-Hall sensors by focused-beam-induced deposition, Nanotechnology 21(11) (2010) 115503.

[24] I. Utke, F. Cicoira, G. Jaenchen, P. Hoffmann, L. Scandella, B. Dwir, E. Kapon, D. Laub, P. Buffat, N. Xanthopoulos, H.J. Mathieu, Focused Electron Beam Induced Deposition of High Resolution Magnetic Scanning Probe Tips, MRS Proceedings 706 (2001) Z9.24.1.
[25] G. Arnold, R. Winkler, M. Stermitz, A. Orthacker, J.-H. Noh, J.D. Fowlkes, G. Kothleitner, M. Huth, P.D. Rack, H. Plank, Tunable 3D Nanoresonators for Gas-Sensing Applications, Advanced Functional Materials 28(19) (2018) 1707387.
[26] H. Plank, R. Winkler, C.H. Schwalb, J. Hütner, J.D. Fowlkes, P.D. Rack, I. Utke, M. Huth, Focused Electron Beam-Based 3D Nanoprinting for Scanning Probe Microscopy: A Review, Micromachines 11(1) (2020).
[27] T. Bret, T. Hofmann, K. Edinger, Industrial perspective on focused electron beam-induced processes, Applied Physics A: Materials Science & Processing 117(4) (2014) 1607-1614.
[28] J.H. Noh, M.G. Stanford, B.B. Lewis, J.D. Fowlkes, H. Plank, P.D. Rack, Nanoscale electron beam-induced deposition and purification of ruthenium for extreme ultraviolet lithography mask repair, Applied Physics A 117(4) (2014) 1705-1713.
[29] P.-y. Yan, E. Spiller, P. Mirkarimi, Characterization of ruthenium thin films as capping layer for extreme ultraviolet lithography mask blanks, Journal of Vacuum Science & Technology B: Microelectronics and Nanometer Structures Processing, Measurement, and Phenomena 25(6) (2007) 1859-1866.
[30] L. Reimer, Introduction, in: L. Reimer (Ed.), Scanning Electron Microscopy: Physics of Image Formation and Microanalysis, Springer Berlin Heidelberg, Berlin, Heidelberg, 1998, pp. 1-12.
[31] L. Reimer, Emission of Backscattered and Secondary Electrons, in: L. Reimer (Ed.), Scanning Electron Microscopy: Physics of Image Formation and Microanalysis, Springer Berlin Heidelberg, Berlin, Heidelberg, 1998, pp. 135-169.
[32] Low-Energy Electrons: Fundamentals and Applications, 1st ed., Jenny Stanford Publishing, Boca Raton, 2019.
[33] K. Kanaya, S. Okayama, Penetration and energy-loss theory of electrons in solid targets, Journal of Physics D: Applied Physics 5(1) (1972) 43-58.
[34] K. Höflich, J. Jurczyk, Y. Zhang, M.V. Puydinger dos Santos, M. Götz, C. Guerra-Nuñez, J.P. Best, C. Kapusta, I. Utke, Direct Electron Beam Writing of Silver-Based Nanostructures, ACS Applied Materials & Interfaces 9(28) (2017) 24071-24077.

[35] L. Berger, K. Madajska, I.B. Szymanska, K. Höflich, M.N. Polyakov, J. Jurczyk, C. Guerra-Nuñez, I. Utke, Gas-assisted silver deposition with a focused electron beam, Beilstein Journal of Nanotechnology 9 (2018) 224-232.
[36] L. Berger, J. Jurczyk, K. Madajska, T.E.J. Edwards, I. Szymańska, P. Hoffmann, I. Utke, High-Purity Copper Structures from a Perfluorinated Copper Carboxylate Using Focused Electron Beam Induced Deposition and Post-Purification, ACS Applied Electronic Materials 2(7) (2020) 1989-1996.
[37] H. Demers, N. Poirier-Demers, A.R. Couture, D. Joly, M. Guilmain, N. de Jonge, D. Drouin, Three-dimensional electron microscopy simulation with the CASINO Monte Carlo software, Scanning 33(3) (2011) 135-146.
[38] A. Botman, J.J.L. Mulders, C.W. Hagen, Creating pure nanostructures from electron-beam-induced deposition using purification techniques: a technology perspective, Nanotechnology 20(37) (2009) 372001.
[39] A. Botman, J.J.L. Mulders, R. Weemaes, S. Mentink, Purification of platinum and gold structures after electron-beam-induced deposition, Nanotechnology 17(15) (2006) 3779-3785.
[40] L. Bernau, M. Gabureac, R. Erni, I. Utke, Tunable Nanosynthesis of Composite Materials by Electron-Impact Reaction, Angewandte Chemie International Edition 49(47) (2010) 8880-8884.
[41] W.G. Carden, H. Lu, J.A. Spencer, D.H. Fairbrother, L. McElwee-White, Mechanism-based design of precursors for focused electron beam-induced deposition, MRS Communications 8(2) (2018) 343-357.
[42] W.F. van Dorp, X. Wu, J.J.L. Mulders, S. Harder, P. Rudolf, J.T.M. De Hosson, Gold Complexes for Focused-Electron-Beam-Induced Deposition, Langmuir 30(40) (2014) 12097-12105.
[43] S. Barth, M. Huth, F. Jungwirth, Precursors for direct-write nanofabrication with electrons, Journal of Materials Chemistry C 8(45) (2020) 15884-15919.
[44] I. Utke, P. Swiderek, K. Höflich, K. Madajska, J. Jurczyk, P. Martinović, I.B. Szymańska, Coordination and organometallic precursors of group 10 and 11: Focused electron beam induced deposition of metals and insight gained from chemical vapour deposition, atomic layer deposition, and fundamental surface and gas phase studies, Coordination Chemistry Reviews, In Press (2021).

[45] S. Matsui, K. Mori, New selective deposition technology by electron-beam induced surface reaction, Journal of Vacuum Science & Technology B: Microelectronics Processing and Phenomena 4(1) (1986) 299-304.
[46] S. Matsui, T. Ichihashi, M. Mito, Electron beam induced selective etching and deposition technology, Journal of Vacuum Science & Technology B: Microelectronics Processing and Phenomena 7(5) (1989) 1182-1190.
[47] S. Ketharanathan, R. Sharma, P.A. Crozier, J. Drucker, Electron beam induced deposition of pure, nanoscale Ge, Journal of Vacuum Science & Technology B: Microelectronics and Nanometer Structures Processing, Measurement, and Phenomena 24(2) (2006) 678-681.
[48] Y. Liebes-Peer, V. Bandalo, Ü. Sökmen, M. Tornow, N. Ashkenasy, Fabrication of nanopores in multi-layered silicon-based membranes using focused electron beam induced etching with XeF2 gas, Microchimica Acta 183(3) (2016) 987-994.
[49] A. Perentes, G. Sinicco, G. Boero, B. Dwir, P. Hoffmann, Focused electron beam induced deposition of nickel, Journal of Vacuum Science & Technology B: Microelectronics and Nanometer Structures Processing, Measurement, and Phenomena 25(6) (2007) 2228-2232.
[50] J.D. Barry, M. Ervin, J. Molstad, A. Wickenden, T. Brintlinger, P. Hoffman, J. Meingailis, Electron beam induced deposition of low resistivity platinum from Pt(PF3)4, Journal of Vacuum Science & Technology B: Microelectronics and Nanometer Structures Processing, Measurement, and Phenomena 24(6) (2006) 3165-3168.
[51] C. O'Regan, A. Lee, J.D. Holmes, N. Petkov, P. Trompenaars, H. Mulders, Electrical properties of platinum interconnects deposited by electron beam induced deposition of the carbon-free precursor, Pt(PF3)4, Journal of Vacuum Science & Technology B 31(2) (2013) 021807.
[52] A. Fernández-Pacheco, J.M. de Teresa, R. Córdoba, M.R. Ibarra, Magnetotransport properties of high-quality cobalt nanowires grown by focused-electron-beam-induced deposition, Journal of Physics D: Applied Physics 42(5) (2009) 055005.
[53] M. Huth, D. Klingenberger, C. Grimm, F. Porrati, R. Sachser, Conductance regimes of W-based granular metals prepared by electron beam induced deposition, New Journal of Physics 11(3) (2009) 033032.
[54] M. Weber, H.W.P. Koops, M. Rudolph, J. Kretz, G. Schmidt, New compound quantum dot materials produced by electron-beam induced deposition, Journal of Vacuum Science &

Technology B: Microelectronics and Nanometer Structures Processing, Measurement, and Phenomena 13(3) (1995) 1364-1368.
[55] F. Porrati, M. Pohlit, J. Müller, S. Barth, F. Biegger, C. Gspan, H. Plank, M. Huth, Direct writing of CoFe alloy nanostructures by focused electron beam induced deposition from a heteronuclear precursor, Nanotechnology 26(47) (2015) 475701.
[56] D. Spoddig, K. Schindler, P. Rödiger, J. Barzola-Quiquia, K. Fritsch, H. Mulders, P. Esquinazi, Transport properties and growth parameters of PdC and WC nanowires prepared in a dual-beam microscope, Nanotechnology 18(49) (2007) 495202.
[57] C. Mansilla, Y. Zondag, J.J.L. Mulders, P.H.F. Trompenaars, Comparison of Pd electron beam induced deposition using two precursors and an oxygen purification strategy, Nanotechnology 28(37) (2017) 375302.
[58] D.R. Diercks, B.P. Gorman, J.J.L. Mulders, Electron Beam-Induced Deposition for Atom Probe Tomography Specimen Capping Layers, Microscopy and Microanalysis 23(2) (2017) 321-328.
[59] A. Luisier, I. Utke, T. Bret, F. Cicoira, R. Hauert, S.W. Rhee, P. Doppelt, P. Hoffmann, Comparative Study of Cu-Precursors for 3D Focused Electron Beam Induced Deposition, Journal of The Electrochemical Society 151(9) (2004) C590-C593.
[60] M.V. Puydinger dos Santos, A. Szkudlarek, A. Rydosz, C. Guerra-Nuñez, F. Béron, K.R. Pirota, S. Moshkalev, J.A. Diniz, I. Utke, Comparative study of post-growth annealing of Cu(hfac)2, Co2(CO)8 and Me2Au(acac) metal precursors deposited by FEBID, Beilstein Journal of Nanotechnology 9 (2018) 91-101.
[61] A. Szkudlarek, A. Rodrigues Vaz, Y. Zhang, A. Rudkowski, C. Kapusta, R. Erni, S. Moshkalev, I. Utke, Formation of pure Cu nanocrystals upon post-growth annealing of Cu–C material obtained from focused electron beam induced deposition: comparison of different methods, Beilstein Journal of Nanotechnology 6 (2015) 1508-1517.
[62] C. Haverkamp, G. Sarau, M.N. Polyakov, I. Utke, M.V. Puydinger dos Santos, S. Christiansen, K. Höflich, A novel copper precursor for electron beam induced deposition, Beilstein Journal of Nanotechnology 9 (2018) 1220-1227.
[63] Y. Ochiai, J.i. Fujita, S. Matsui, Electron-beam-induced deposition of copper compound with low resistivity, Journal of Vacuum Science & Technology B: Microelectronics and Nanometer Structures Processing, Measurement, and Phenomena 14(6) (1996) 3887-3891.
[64] T. Bret, I. Utke, A. Bachmann, P. Hoffmann, In situ control of the focused-electron-beam-induced deposition process, Applied Physics Letters 83(19) (2003) 4005-4007.

[65] T. Bret, I. Utke, C. Gaillard, P. Hoffmann, Periodic structure formation by focused electron-beam-induced deposition, Journal of Vacuum Science & Technology B: Microelectronics and Nanometer Structures Processing, Measurement, and Phenomena 22(5) (2004) 2504-2510.
[66] I. Utke, A. Luisier, P. Hoffmann, D. Laub, P.A. Buffat, Focused-electron-beam-induced deposition of freestanding three-dimensional nanostructures of pure coalesced copper crystals, Applied Physics Letters 81(17) (2002) 3245-3247.
[67] A. Folch, J. Tejada, C.H. Peters, M.S. Wrighton, Electron beam deposition of gold nanostructures in a reactive environment, Applied Physics Letters 66(16) (1995) 2080-2082.
[68] A. Folch, J. Servat, J. Esteve, J. Tejada, M. Seco, High-vacuum versus ‘‘environmental’’ electron beam deposition, Journal of Vacuum Science & Technology B: Microelectronics and Nanometer Structures Processing, Measurement, and Phenomena 14(4) (1996) 2609-2614.
[69] S. Graells, R. Alcubilla, G. Badenes, R. Quidant, Growth of plasmonic gold nanostructures by electron beam induced deposition, Applied Physics Letters 91(12) (2007) 121112.
[70] K. Höflich, R.B. Yang, A. Berger, G. Leuchs, S. Christiansen, The Direct Writing of Plasmonic Gold Nanostructures by Electron-Beam-Induced Deposition, Advanced Materials 23(22-23) (2011) 2657-2661.
[71] J.J.L. Mulders, L.M. Belova, A. Riazanova, Electron beam induced deposition at elevated temperatures: compositional changes and purity improvement, Nanotechnology 22(5) (2010) 055302.
[72] I. Utke, M.G. Jenke, C. Röling, P.H. Thiesen, V. Iakovlev, A. Sirbu, A. Mereuta, A. Caliman, E. Kapon, Polarisation stabilisation of vertical cavity surface emitting lasers by minimally invasive focused electron beam triggered chemistry, Nanoscale 3(7) (2011) 2718-2722.
[73] O. Sqalli, I. Utke, P. Hoffmann, F. Marquis-Weible, Gold elliptical nanoantennas as probes for near field optical microscopy, Journal of Applied Physics 92(2) (2002) 1078-1083.
[74] I. Utke, B. Dwir, K. Leifer, F. Cicoira, P. Doppelt, P. Hoffmann, E. Kapon, Electron beam induced deposition of metallic tips and wires for microelectronics applications, Microelectronic Engineering 53(1) (2000) 261-264.
[75] M.G. Jenke, D. Lerose, C. Niederberger, J. Michler, S. Christiansen, I. Utke, Toward Local Growth of Individual Nanowires on Three-Dimensional Microstructures by Using a Minimally Invasive Catalyst Templating Method, Nano Letters 11(10) (2011) 4213-4217.

[76] I. Utke, P. Hoffmann, B. Dwir, K. Leifer, E. Kapon, P. Doppelt, Focused electron beam induced deposition of gold, Journal of Vacuum Science & Technology B: Microelectronics and Nanometer Structures Processing, Measurement, and Phenomena 18(6) (2000) 3168-3171.
[77] J.J.L. Mulders, J.M. Veerhoek, E.G.T. Bosch, P.H.F. Trompenaars, Fabrication of pure gold nanostructures by electron beam induced deposition with Au(CO)Cl precursor: deposition characteristics and primary beam scattering effects, Journal of Physics D: Applied Physics 45(47) (2012) 475301.
[78] H. Plank, J.H. Noh, J.D. Fowlkes, K. Lester, B.B. Lewis, P.D. Rack, Electron-Beam-Assisted Oxygen Purification at Low Temperatures for Electron-Beam-Induced Pt Deposits: Towards Pure and High-Fidelity Nanostructures, ACS Applied Materials & Interfaces 6(2) (2014) 1018-1024.
[79] B. Geier, C. Gspan, R. Winkler, R. Schmied, J.D. Fowlkes, H. Fitzek, S. Rauch, J. Rattenberger, P.D. Rack, H. Plank, Rapid and Highly Compact Purification for Focused Electron Beam Induced Deposits: A Low Temperature Approach Using Electron Stimulated H2O Reactions, The Journal of Physical Chemistry C 118(25) (2014) 14009-14016.
[80] M.M. Shawrav, P. Taus, H.D. Wanzenboeck, M. Schinnerl, M. Stöger-Pollach, S. Schwarz, A. Steiger-Thirsfeld, E. Bertagnolli, Highly conductive and pure gold nanostructures grown by electron beam induced deposition, Scientific Reports 6 (2016) 34003.
[81] M.V. Puydinger dos Santos, M.F. Velo, R.D. Domingos, Y. Zhang, X. Maeder, C. Guerra-Nuñez, J.P. Best, F. Béron, K.R. Pirota, S. Moshkalev, J.A. Diniz, I. Utke, Annealing-Based Electrical Tuning of Cobalt–Carbon Deposits Grown by Focused-Electron-Beam-Induced Deposition, ACS Applied Materials & Interfaces 8(47) (2016) 32496-32503.
[82] C. Elbadawi, M. Toth, C.J. Lobo, Pure Platinum Nanostructures Grown by Electron Beam Induced Deposition, ACS Applied Materials & Interfaces 5(19) (2013) 9372-9376.
[83] E. Begun, O.V. Dobrovolskiy, M. Kompaniiets, R. Sachser, C. Gspan, H. Plank, M. Huth, Post-growth purification of Co nanostructures prepared by focused electron beam induced deposition, Nanotechnology 26(7) (2015) 075301.
[84] W.F. van Dorp, T.W. Hansen, J.B. Wagner, J.T.M. De Hosson, The role of electron-stimulated desorption in focused electron beam induced deposition, Beilstein Journal of Nanotechnology 4 (2013) 474-480.
[85] M. Toth, C. Lobo, V. Friedli, A. Szkudlarek, I. Utke, Continuum models of focused electron beam induced processing, Beilstein Journal of Nanotechnology 6 (2015) 1518-1540.

[86] P. de Vera, M. Azzolini, G. Sushko, I. Abril, R. Garcia-Molina, M. Dapor, I.A. Solov'yov, A.V. Solov'yov, Multiscale simulation of the focused electron beam induced deposition process, Scientific Reports 10(1) (2020) 20827.
[87] R.M. Thorman, R. Kumar T. P, D.H. Fairbrother, O. Ingólfsson, The role of low-energy electrons in focused electron beam induced deposition: four case studies of representative precursors, Beilstein Journal of Nanotechnology 6 (2015) 1904-1926.
[88] M. Zlatar, M. Allan, J. Fedor, Excited States of Pt(PF3)4 and Their Role in Focused Electron Beam Nanofabrication, The Journal of Physical Chemistry C 120(19) (2016) 10667-10674.
[89] S. Massey, A.D. Bass, L. Sanche, Role of Low-Energy Electrons (<35 eV) in the Degradation of Fe(CO)5 for Focused Electron Beam Induced Deposition Applications: Study by Electron Stimulated Desorption of Negative and Positive Ions, The Journal of Physical Chemistry C 119(22) (2015) 12708-12719.
[90] J.D. Fowlkes, R. Winkler, B.B. Lewis, A. Fernández-Pacheco, L. Skoric, D. Sanz-Hernández, M.G. Stanford, E. Mutunga, P.D. Rack, H. Plank, High-Fidelity 3D-Nanoprinting via Focused Electron Beams: Computer-Aided Design (3BID), ACS Applied Nano Materials 1(3) (2018) 1028-1041.
[91] A. Szkudlarek, W. Szmyt, C. Kapusta, I. Utke, Lateral resolution in focused electron beam-induced deposition: scaling laws for pulsed and static exposure, Applied Physics A 117(4) (2014) 1715-1726.
[92] D. Sanz-Hernández, A. Fernández-Pacheco, Modelling focused electron beam induced deposition beyond Langmuir adsorption, Beilstein Journal of Nanotechnology 8 (2017) 2151-2161.
[93] R.F. Egerton, The Scanning Electron Microscope, in: R.F. Egerton (Ed.), Physical Principles of Electron Microscopy, Springer Science+Business Media, Inc., United States of America, 2005.
[94] J. Ltd., Schottky-emission electron gun, SE electron gun. https://www.jeol.co.jp/en/words/semterms/search_result.html?keyword=Schottky-emission%20electron%20gun, 2021).
[95] TESCAN, MIRA3 High performance field emission scanning electron microscope, in: TESCAN (Ed.) TESCAN, Brno, Czech republic, 2018.
[96] J. Ltd., Thermionic-emission gun. https://www.jeol.co.jp/en/words/semterms/search_result.html?keyword=thermionic-emission%20gun, 2021).

[97] J.I. Goldstein, D.E. Newbury, P. Echlin, D.C. Joy, C.E. Lyman, E. Lifshin, L. Sawyer, J.R. Michael, Generation of X-Rays in the SEM Specimen, in: J.I. Goldstein, D.E. Newbury, P. Echlin, D.C. Joy, C.E. Lyman, E. Lifshin, L. Sawyer, J.R. Michael (Eds.), Scanning Electron Microscopy and X-ray Microanalysis: Third Edition, Springer US, Boston, MA, 2003, pp. 271-296.
[98] R.F. Egerton, ANALYTICAL ELECTRON MICROSCOPY, in: R.F. Egerton (Ed.), Physical Principles of Electron Microscopy An Introduction to TEM, SEM, and AEM, Springer Science+Business Media, Inc., United States of America, 2005.

[99] D.E. Newbury, N.W.M. Ritchie, Performing elemental microanalysis with high accuracy and high precision by scanning electron microscopy/silicon drift detector energy-dispersive X-ray spectrometry (SEM/SDD-EDS), Journal of Materials Science 50(2) (2015) 493-518.
[100] EDAX, Octane Elect EDS System. https://www.edax.com/products/eds/octane-elect-eds-system, 2021).
[101] J. Jurczyk, C.R. Brewer, O.M. Hawkins, M.N. Polyakov, C. Kapusta, L. McElwee-White, I. Utke, Focused Electron Beam-Induced Deposition and Post-Growth Purification Using the Heteroleptic Ru Complex (η3-C3H5)Ru(CO)3Br, ACS Applied Materials & Interfaces 11(31) (2019) 28164-28171.
[102] StrataGEM, samX, rue Galilée, 78280 Guyancourt, France.
[103] D. Ricci, P.C. Braga, Recognizing and Avoiding Artifacts in AFM Imaging, in: D. Ricci, P.C. Braga (Eds.), Atomic Force Microscopy Biomedical Methods and Applications, Humana Press, 2004.

[104] R. Bottom, Thermogravimetric Analysis, in: P. Gabbott (Ed.), Principles and Applications of Thermal Analysis, 2008.
[105] M.I. Zaki, M.A. Hasan, L. Pasupulety, K. Kumari, Thermochemistry of manganese oxides in reactive gas atmospheres: Probing catalytic MnOx compositions in the atmosphere of CO+O2, Thermochimica Acta 311(1) (1998) 97-103.
[106] E.N. Coker, The oxidation of aluminum at high temperature studied by Thermogravimetric Analysis and Differential Scanning Calorimetry, United States, 2013.
[107] C.J. Rao, S. Ningshen, C. Mallika, U.K. Mudali, Molten salt corrosion behavior of structural materials in LiCl-KCl-UCl3 by thermogravimetric study, Journal of Nuclear Materials 501 (2018) 189-199.

[108] E.C. Ashby, P. Claudy, J. Bousquet, J. Etienne, High vacuum DTA-TGA instrumentation for air-sensitive compounds, Journal of Chemical Education 52(9) (1975) 618.
[109] G. Zhou, S. Roby, T. Wei, N. Yee, Fuel Heat of Vaporization Values Measured with Vacuum Thermogravimetric Analysis Method, Energy & Fuels 28(5) (2014) 3138-3142.
[110] M. Auinger, A. Vogel, D. Vogel, M. Rohwerder, Early stages of oxidation observed by in situ thermogravimetry in low pressure atmospheres, Corrosion Science 86 (2014) 183-188.
[111] L. Du, W. Chu, H. Miao, C. Xu, Y. Ding, Synthesis, characterization, thermal properties of silicon(iv) compounds containing guanidinato ligands and their potential as CVD precursors, RSC Advances 5(88) (2015) 71637-71643.
[112] G.V. Kunte, S.A. Shivashankar, A.M. Umarji, Thermogravimetric evaluation of the suitability of precursors for MOCVD, Measurement Science and Technology 19(2) (2008) 025704.
[113] A. Jakob, H. Schmidt, P. Djiele, Y. Shen, H. Lang, Phosphane/phosphite silver(I) carboxylates as CVD precursors, Microchimica Acta 156(1) (2006) 77-81.
[114] M.A. Siddiqi, B. Atakan, Combined experiments to measure low sublimation pressures and diffusion coefficients of organometallic compounds, Thermochimica Acta 452(2) (2007) 128-134.
[115] E. Szłyk, I. Łakomska, A. Grodzicki, Thermal and spectroscopic studies of the Ag(I) salts with fluorinated carboxylic and sulfonic acid residues, Thermochimica Acta 223 (1993) 207-212.
[116] F. Ferreira da Silva, R.M. Thorman, R. Bjornsson, H. Lu, L. McElwee-White, O. Ingólfsson, Dissociation of the FEBID precursor cis-Pt(CO)2Cl2 driven by low-energy electrons, Physical Chemistry Chemical Physics 22(11) (2020) 6100-6108.
[117] J.A. Spencer, S.G. Rosenberg, M. Barclay, Y.-C. Wu, L. McElwee-White, D. Howard Fairbrother, Understanding the electron-stimulated surface reactions of organometallic complexes to enable design of precursors for electron beam-induced deposition, Applied Physics A 117(4) (2014) 1631-1644.
[118] J.D. Wnuk, J.M. Gorham, S.G. Rosenberg, W.F. van Dorp, T.E. Madey, C.W. Hagen, D.H. Fairbrother, Electron Induced Surface Reactions of the Organometallic Precursor Trimethyl(methylcyclopentadienyl)platinum(IV), The Journal of Physical Chemistry C 113(6) (2009) 2487-2496.
[119] J.A. Spencer, J.A. Brannaka, M. Barclay, L. McElwee-White, D.H. Fairbrother, Electron-Induced Surface Reactions of η3-Allyl Ruthenium Tricarbonyl Bromide [(η^3-

C_3H_5)Ru(CO)$_3$Br]: Contrasting the Behavior of Different Ligands, The Journal of Physical Chemistry C 119(27) (2015) 15349-15359.
[120] M. Rohdenburg, H. Boeckers, C.R. Brewer, L. McElwee-White, P. Swiderek, Efficient NH3-based process to remove chlorine from electron beam deposited ruthenium produced from (η3-C3H5)Ru(CO)3Cl, Scientific Reports 10(1) (2020) 10901.
[121] J.A. Whitby, F. Östlund, P. Horvath, M. Gabureac, J.L. Riesterer, I. Utke, M. Hohl, L. Sedláček, J. Jiruše, V. Friedli, M. Bechelany, J. Michler, High Spatial Resolution Time-of-Flight Secondary Ion Mass Spectrometry for the Masses: A Novel Orthogonal ToF FIB-SIMS Instrument with *In Situ* AFM, Advances in Materials Science and Engineering 2012 (2012) 180437.
[122] L. Pillatsch, F. Östlund, J. Michler, FIBSIMS: A review of secondary ion mass spectrometry for analytical dual beam focussed ion beam instruments, Progress in Crystal Growth and Characterization of Materials 65(1) (2019) 1-19.
[123] V.R. Deline, W. Katz, C.A. Evans, P. Williams, Mechanism of the SIMS matrix effect, Applied Physics Letters 33(9) (1978) 832-835.
[124] A. Benninghoven, Surface analysis by Secondary Ion Mass Spectrometry (SIMS), Surface Science 299-300 (1994) 246-260.
[125] A. Priebe, T. Xie, G. Bürki, L. Pethö, J. Michler, The matrix effect in TOF-SIMS analysis of two-element inorganic thin films, Journal of Analytical Atomic Spectrometry 35(6) (2020) 1156-1166.
[126] BRUKER AFM Probes - RTESPA-300. https://www.brukerafmprobes.com/p-3907-rtespa-300.aspx).
[127] S.I. Bozhevolnyi, J.B. Khurgin, The case for quantum plasmonics, Nature Photonics 11(7) (2017) 398-400.
[128] K. Kneipp, M. Moskovitz, H. Kneipp, Surface-Enhanced Raman Scattering, 1 ed., Springer-Verlag Berlin Heidelberg2006.
[129] M. Moskovits, Surface-Enhanced Raman Spectroscopy: a Brief Perspective, in: K. Kneipp, M. Moskovits, H. Kneipp (Eds.), Surface-Enhanced Raman Scattering: Physics and Applications, Springer Berlin Heidelberg, Berlin, Heidelberg, 2006, pp. 1-17.
[130] L.E. Ocola, A. Joshi-Imre, C. Kessel, B. Chen, J. Park, D. Gosztola, R. Divan, Growth characterization of electron-beam-induced silver deposition from liquid precursor, Journal of Vacuum Science & Technology B 30(6) (2012) 06FF08.
[131] E. Szłyk, P. Piszczek, A. Grodzicki, M. Chaberski, A. Goliński, J. Szatkowski, T. Błaszczyk, CVD of AgI Complexes with Tertiary Phosphines and Perfluorinated

Carboxylates—A New Class of Silver Precursors, Chemical Vapor Deposition 7(3) (2001) 111-116.
[132] J. Jurczyk, K. Madajska, L. Berger, L. Brockhuis, T.E.J. Edwards, K. Höflich, C. Kapusta, I. Szymanska, I. Utke, Ligand size and chain length study of silver carboxylates in focused electron beam induced deposition, Prepreints, 2021.
[133] P. Piszczek, E. Szłyk, M. Chaberski, C. Taeschner, A. Leonhardt, W. Bała, K. Bartkiewicz, Characterization of Silver Trimethylacetate Complexes with Tertiary Phosphines as CVD Precursors of Thin Silver Films, Chemical Vapor Deposition 11(1) (2005) 53-59.
[134] M.J. Shapiro, W.J. Lackey, J.A. Hanigofsky, D.N. Hill, W.B. Carter, E.K. Barefield, Chemical vapor deposition of silver films for superconducting wire applications, Journal of Alloys and Compounds 187(2) (1992) 331-349.
[135] E. Szłyk, P. Piszczek, M. Chaberski, A. Goliński, Studies of thermal decomposition process of Ag(I) perfluorinated carboxylates with temperature variable IR and MS, Polyhedron 20(22) (2001) 2853-2861.
[136] J. Jurczyk, C. Glessi, K. Madajska, L. Berger, J.I.K. Nyrud, I. Szymańska, C. Kapusta, M. Tilset, I. Utke, Vacuum versus ambient pressure inert gas thermogravimetry: a study of silver carboxylates, Journal of Thermal Analysis and Calorimetry (2021).
[137] T. Bret, S. Mauron, I. Utke, P. Hoffmann, Characterization of focused electron beam induced carbon deposits from organic precursors, Microelectronic Engineering 78-79 (2005) 300-306.
[138] C.J. Gommes, Ostwald ripening of confined nanoparticles: chemomechanical coupling in nanopores, Nanoscale 11(15) (2019) 7386-7393.
[139] K. Janerka, J. Jezierski, M. Stawarz, J. Szajnar, Method for Resistivity Measurement of Grainy Carbon and Graphite Materials, Materials 12(4) (2019).
[140] D.R. Smith, F.R. Fickett, Low-Temperature Properties of Silver, Journal of research of the National Institute of Standards and Technology 100(2) (1995) 119-171.
[141] C. Kittel, Chapter 6: Free Electron Fermi Gas, in: C. Kittel (Ed.), Introduction to Solid State Physics, Wiley India Pvt. Limited2007.
[142] K. Höflich, J.M. Jurczyk, K. Madajska, M. Götz, L. Berger, C. Guerra-Nuñez, C. Haverkamp, I. Szymanska, I. Utke, Towards the third dimension in direct electron beam writing of silver, Beilstein Journal of Nanotechnology 9 (2018) 842-849.
[143] R.M. Thorman, P.A. Jensen, J.-C. Yu, S.J. Matsuda, L. McElwee-White, O. Ingólfsson, D.H. Fairbrother, Electron-Induced Reactions of Ru(CO)4I2: Gas Phase, Surface, and

Electron Beam-Induced Deposition, The Journal of Physical Chemistry C 124(19) (2020) 10593-10604.

[144] R.M. Thorman, J.A. Brannaka, L. McElwee-White, O. Ingólfsson, Low energy electron-induced decomposition of (η^3-C_3H_5)$Ru(CO)_3Br$, a potential focused electron beam induced deposition precursor with a heteroleptic ligand set, Physical Chemistry Chemical Physics 19(20) (2017) 13264-13271.

[145] V. Friedli, I. Utke, GIS Simulator, EMPA, https://www.empa.ch/web/s206/febip-codes, 2015.

[146] V. Friedli, I. Utke, Optimized molecule supply from nozzle-based gas injection systems for focused electron- and ion-beam induced deposition and etching: simulation and experiment, Journal of Physics D: Applied Physics 42(12) (2009) 125305.

[147] M. Rohdenburg, J.E. Fröch, P. Martinović, C.J. Lobo, P. Swiderek, Combined Ammonia and Electron Processing of a Carbon-Rich Ruthenium Nanomaterial Fabricated by Electron-Induced Deposition, Micromachines 11(8) (2020).

[148] V. Friedli, I. Utke, K. Mølhave, J. Michler, Dose and energy dependence of mechanical properties of focused electron-beam-induced pillar deposits from Cu(C5HF6O2)2, Nanotechnology 20(38) (2009) 385304.

[149] I.S. Beloborodov, A.V. Lopatin, F.W.J. Hekking, R. Fazio, V.M. Vinokur, Thermal transport in granular metals, Europhysics Letters (EPL) 69(3) (2005) 435-441.

[150] T.B. Tran, I.S. Beloborodov, X.M. Lin, T.P. Bigioni, V.M. Vinokur, H.M. Jaeger, Multiple Cotunneling in Large Quantum Dot Arrays, Physical Review Letters 95(7) (2005) 076806.

[151] C. Glessi, A. Mahgoub, C.W. Hagen, M. Tilset, Gold(I) N-heterocyclic carbene precursors for focused electron beam-induced deposition, Beilstein Journal of Nanotechnology 12 (2021) 257-269.

[152] H. Sangeetha, W.H. Cornelis, V. Thomas, K. Pieter, Size and shape control of sub-20 nm patterns fabricated using focused electron beam-induced processing, Journal of Micro/Nanolithography, MEMS, and MOEMS 13(3) (2014) 1-7.

[153] D. Zhao, A. Han, M. Qiu, Ice lithography for 3D nanofabrication, Science Bulletin 64(12) (2019) 865-871.

[154] S. Yasin, D.G. Hasko, H. Ahmed, Comparison of MIBK/IPA and water/IPA as PMMA developers for electron beam nanolithography, Microelectronic Engineering 61-62 (2002) 745-753.

[155] R. Córdoba, J. Sesé, J.M. De Teresa, M.R. Ibarra, High-purity cobalt nanostructures grown by focused-electron-beam-induced deposition at low current, Microelectronic Engineering 87(5) (2010) 1550-1553.
[156] D.S. McPhail, R.J. Chater, L. Li, Applications of focused ion beam SIMS in materials science, Microchimica Acta 161(3) (2008) 387-397.
[157] A. Priebe, L. Pethö, E. Huszar, T. Xie, I. Utke, J. Michler, High Sensitivity of Fluorine Gas-Assisted FIB-TOF-SIMS for Chemical Characterization of Buried Sublayers in Thin Films, ACS Applied Materials & Interfaces 13(13) (2021) 15890-15900.
[158] A. Priebe, J.-P. Barnes, T.E.J. Edwards, L. Pethö, I. Balogh, J. Michler, 3D Imaging of Nanoparticles in an Inorganic Matrix Using TOF-SIMS Validated with STEM and EDX, Analytical Chemistry 91(18) (2019) 11834-11839.
[159] V. Scheuer, H. Koops, T. Tschudi, Electron beam decomposition of carbonyls on silicon, Microelectronic Engineering 5(1) (1986) 423-430.
[160] L. Berger, J. Jurczyk, K. Madajska, I.B. Szymańska, P. Hoffmann, I. Utke, Room Temperature Direct Electron Beam Lithography in a Condensed Copper Carboxylate, Micromachines 12(5) (2021).
[161] S.G. Rosenberg, M. Barclay, D.H. Fairbrother, Electron induced reactions of surface adsorbed tungsten hexacarbonyl (W(CO)6), Physical Chemistry Chemical Physics 15(11) (2013) 4002-4015.
[162] Y. Wang, F. Gao, M. Kaltchev, W.T. Tysoe, The effect of electron beam irradiation on the chemistry of molybdenum hexacarbonyl on thin alumina films in ultrahigh vacuum, Journal of Molecular Catalysis A: Chemical 209(1) (2004) 135-144.
[163] C. Hauchard, C. Pépin, P. Rowntree, Fe(CO)5 Thin Films Adsorbed on Au(111) and on Self-Assembled Organic Monolayers: I. Structure, Langmuir 21(20) (2005) 9154-9165.
[164] C. Hauchard, P.A. Rowntree, Low-energy electron-induced decarbonylation of Fe(CO)5 films adsorbed on Au(111) surfaces, Canadian Journal of Chemistry 89(10) (2011) 1163-1173.
[165] R.D. Ramsier, M.A. Henderson, J.T. Yates, Electron induced decomposition of Ni(CO)4 adsorbed on Ag(111), Surface Science 257(1) (1991) 9-21.
[166] M. Neustetter, E. Jabbour Al Maalouf, P. Limão-Vieira, S. Denifl, Fragmentation pathways of tungsten hexacarbonyl clusters upon electron ionization, The Journal of Chemical Physics 145(5) (2016) 054301.

[167] K. Wnorowski, M. Stano, C. Matias, S. Denifl, W. Barszczewska, Š. Matejčík, Low-energy electron interactions with tungsten hexacarbonyl – W(CO)6, Rapid Communications in Mass Spectrometry 26(17) (2012) 2093-2098.
[168] J. Pablo-Navarro, D. Sanz-Hernández, C. Magén, A. Fernández-Pacheco, J.M. de Teresa, Tuning shape, composition and magnetization of 3D cobalt nanowires grown by focused electron beam induced deposition (FEBID), Journal of Physics D: Applied Physics 50(18) (2017) 18LT01.
[169] L. Brockhuis, Advances in FEBID modelling and in-situ mass measurements, Faculty of Physics and Applied Computer Sciences, AGH - University of Science and Technology in Krakow, Krakow, 2020, p. 69.
[170] A. Szkudlarek, Surface Kinetics Fundamentals of Focused-Electron-Beam-Induced-Deposition, Faculty of Physics and Applied Computer Sciences, AGH University of Science and Technology, Krakow, 2014, p. 138.
[171] M.A. de Araújo, R. Silva, E. de Lima, D.P. Pereira, P.C. de Oliveira, Measurement of Gaussian laser beam radius using the knife-edge technique: improvement on data analysis, Applied Optics 48(2) (2009) 393-396.

List of author's publications

1. Höflich, K.; **Jurczyk, J**.; Zhang, Y.; Puydinger dos Santos, M. V.; Götz, M.; Guerra-Nuñez, C.; Best, J. P.; Kapusta, C.; Utke, I., Direct Electron Beam Writing of Silver-Based Nanostructures. *ACS Applied Materials & Interfaces* **2017,** *9* (28), 24071-24077. DOI: 10.1021/acsami.7b04353

2. Berger, L.; Madajska, K.; Szymanska, I. B.; Höflich, K.; Polyakov, M. N.; **Jurczyk, J**.; Guerra-Nuñez, C.; Utke, I., Gas-assisted silver deposition with a focused electron beam. *Beilstein Journal of Nanotechnology* **2018,** *9*, 224-232. DOI: 10.3762/bjnano.9.24

3. Höflich, K.; **Jurczyk, J**. M.; Madajska, K.; Götz, M.; Berger, L.; Guerra-Nuñez, C.; Haverkamp, C.; Szymanska, I.; Utke, I., Towards the third dimension in direct electron beam writing of silver. *Beilstein Journal of Nanotechnology* **2018,** *9*, 842-849. DOI: 10.3762/bjnano.9.78

4. **Jurczyk, J**.; Brewer, C. R.; Hawkins, O. M.; Polyakov, M. N.; Kapusta, C.; McElwee-White, L.; Utke, I., Focused Electron Beam-Induced Deposition and Post-Growth Purification Using the Heteroleptic Ru Complex (η3-C3H5)Ru(CO)3Br. *ACS Applied Materials & Interfaces* **2019,** *11* (31), 28164-28171. DOI: 10.1021/acsaelm.0c00282

5. Berger, L.; **Jurczyk, J**.; Madajska, K.; Edwards, T. E. J.; Szymańska, I.; Hoffmann, P.; Utke, I., High-Purity Copper Structures from a Perfluorinated Copper Carboxylate Using Focused Electron Beam Induced Deposition and Post-Purification. *ACS Applied Electronic Materials* **2020,** *2* (7), 1989-1996. DOI: 10.1021/acsaelm.0c00282

6. **Jurczyk, J**.; Glessi, C.; Madajska, K.; Berger, L.; Nyrud, J. I. K.; Szymanska, I.; Kapusta, C.; Tilset, M.; Utke, I., Vacuum versus ambient pressure inert gas thermogravimetry: a study of silver carboxylates. *Journal of Thermal Analysis and Calorimetry* **2021,** https://doi.org/10.1007/s10973-021-10616-6.

7. Utke I.; Swiderek P.; Höflich K.; Madajska K.; **Jurczyk J**.; Martinovic P.; Szymanska I., Coordination and organometallic precursors of group 10 and 11: Focused electron beam induced deposition of metals and insight gained from chemical vapour deposition, atomic layer deposition, and fundamental surface and gas phase studies, *Coordination Chemistry Reviews* **2021**, in press

8. Widmer R.; Bischof D.; **Jurczyk J**.; Michler M.; Schwiedrzik J.; Michler J., Smooth or Not: Robust Fused Silica Micro-Components by Femtosecond-Laser-Assisted Etching, *Materials & Design*, **2021**, 204, 109670, DOI: 10.3390/mi12050580

9. Goc, K.; Przewoźnik, J.; Witulska, K.; Chlubny, L.; Tokarz, W.; Strączek, T.; Michalik, J.M.; **Jurczyk, J**.; Utke, I.; Lis, J.; Kapusta, C. Structure, Morphology, Heat Capacity, and Electrical Transport Properties of $Ti_3(Al,Si)C_2$ Materials. *Materials* **2021**, *14*, 3222. https://doi.org/10.3390/ma14123222

10. L. Berger, **J. Jurczyk,** K. Madajska, I.B. Szymańska, P. Hoffmann, I. Utke, Room Temperature Direct Electron Beam Lithography in a Condensed Copper Carboxylate, Micromachines 12(5) (2021). DOI: 10.3390/mi12050580

Accepted

1. Priebe A.; Sastre, J; Futscher M.; **Jurczyk J**.; Puydinger dos Santos M.; Romanyuk Y.; Michler J., Detection of Au^+ ions during fluorine gas-assisted TOF-SIMS for complete elemental characterization of microbatteries, *ACS, applied Materials and Interfaces*, **2021**, accepted

Preprint

1. **Jurczyk J**.; Madajska K.; Berger L.; Brockhuis L.; Edwards TEJ.; Höflich K.; Kapusta Cz.; Szymanska I.; Utke I., Ligand Size and Chain Length Study of Silver Carboxylates in Focused Electron Beam Induced Deposition, **2021** *Preprints server*.